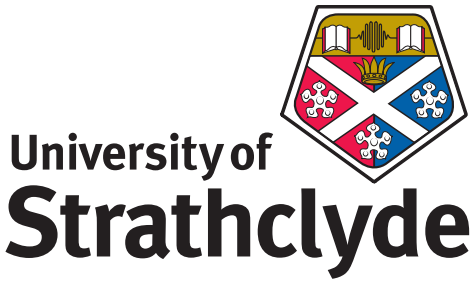

Modelling coagulation in industrial spray drying: An efficient one-dimensional population balance approach

Jonathan Wells

Department of Mathematics & Statistics,

University of Strathclyde, Glasgow, UK.

October 2018

This thesis is submitted to the University of Strathclyde for the degree of Doctor of Philosophy in the Faculty of Science.

This thesis is the result of the author's original research. It has been composed by the author and has not been previously submitted for examination which has led to the award of a degree.

Signed:

Date:

Acknowledgements

This thesis owes a lot to the amazing help and support I've had from my supervisors John MacKenzie and Wilson Lamb at Strathclyde. Huge thanks to them for taking the time to share their knowledge with me and for the much appreciated encouragement (and patience!) along the way.

The project was funded by an Engineering and Physical Sciences Research Council (EPSRC) Industrial CASE studentship set up by the Industrial Mathematics KTN and the Smith Institute. The project was jointly funded by Procter and Gamble and the EPSRC. Thanks to all involved for the support along the way and to Melvin Brown of the Smith Institute, for his help in bringing all parties involved together.

Special thanks to everyone at the Procter and Gamble innovation centre — namely Luis Martin de Juan, Hossein Ahmadian and Dusan Djurdjevic. Their help and enthusiasm towards this project was brilliant and much appreciated.

Similarly, thanks to Andrew Bayly of University of Leeds for sharing his spray drying expertise, and for all the help and guidance along the way.

Abstract

This thesis examines the effects of coagulation on the droplet size distribution within the hollow cone sprays used by industrial spray dryers. A simple model is presented that incorporates the spray's conical shape, droplet transport and coagulation. Both a suitable droplet velocity profile and a coagulation success rate are selected — with the coagulation rate being dependent upon both the size and velocity of colliding droplets. A population balance equation is used to describe how the droplet size distribution is affected by coagulation and this is combined with a conservation equation to capture the droplet transport within the spray. The resulting nonlinear partial integro-differential equation is solved numerically using the cell-average sectional method for the non-local coagulation terms and an essentially non-oscillatory scheme for droplet transport terms.

To our knowledge, this is the first time the cell average technique has been applied to the specific conical sprays found within spray drying. A key achievement of our approach is the significant reduction in computational time that it requires to simulate the droplet size distribution throughout the spray. In comparison, alternative computational fluid mechanics techniques take considerably longer to converge on a steady state solution, as they rely on tracking the trajectory of every

individual droplet within the system.

Numerical results obtained from our model show that coagulation does play an important role within these sprays. Moreover, investigations into the influence of the atomiser nozzle on the extent of coagulation reveal that an increased amount of coagulation occurs in thin, flattish sprays, whilst very little coagulation is observed in widely dispersed sprays.

The model is later extended to include the effects of droplet evaporation. In this case, an increase in the number of smaller droplets near the bottom of the spray is clearly observed in the numerical simulations.

Finally, the model's predictions are validated against experimental data obtained from a series of trials conducted within an industrial-scale dryer tower. Once calibrated, the model's predictions are shown to be in very good agreement with the experimental data.

Contents

Chapter 1

Background

1.1 Industrial motivation

In powder production industries, coagulation of small particles and droplets is used to great effect to influence the final physical properties of the powder itself. These properties may include the powder's size, its moisture content and its physical morphology. Spray drying is one of the most widely used processes for the manufacture of powders within these industries. Its popularity is partly due to the fact that a single spray dryer is capable of producing many different types of powder, each with different physical properties, without the need for investment in additional machinery. Examples of spray dried products range from high value pharmaceutical powders, to consumables such as washing-up powders and powdered foods like milk. The work presented in this thesis will be focused on the production of detergent powders. However the models presented may be applied to any spray drier operation, and potentially to several other fields where atomised sprays are involved.

In spray drying, a slurry is atomised at the top of a tower and allowed to fall

within a flow of drying air. The slurry droplets dry and stick together (coagulate) as they fall, and the final powder is collected at the bottom of the tower.

The production of small, atomised droplets at the top of the tower is deliberate and is due to the fact that, for a set volume of slurry, the smaller the volume of the droplets, the greater the total surface area of slurry that is available for drying. Thus the small initial droplets serve to reduce the slurry's overall drying time. However, one downside of these small droplets is that they are usually deemed too fine to exist within the final powder, and so their coagulation with others is relied upon to create droplets of a larger, more desirable, physical size. This coagulation leads to a significant reduction in dust formation, meaning fewer fine particles (fines), and subsequently makes the finished powder much easier to handle.

When producing detergent powders, the aim is generally to produce a final dried powder of uniform size — usually within the range of 300–500 µm in diameter [1]. In addition to this, the dissolution rate of the powder and its flow-ability must both be maximized, whilst the production of fines kept to a minimum. Here, the dissolution rate is the rate at which the final powder dissolves in water during use (a better dissolution rate avoids clumps of undissolved powder being left after a wash cycle), and the flow-ability is simply the ease at which the final product flows for transportation to its final destination in retail packaging. In designing a drying operation, the combination of atomiser nozzle type, spray pressure, slurry consistency and airflow must be carefully chosen to achieve these aims. Rising energy costs, and consumer demand for high quality powders, mean that it is becoming increasingly important to optimise the operating conditions within spray drying operations.

Despite their importance to the industry, the modelling of the physics within

dryers is still relatively poorly developed. Historically, powder production has generally relied on past experience, and trial and error approaches, to produce powders possessing the desired physical properties. More recently, thanks to modern developments in computational power, computational fluid dynamics (CFD) software has been able to help model the droplet distribution throughout the length of these sprays. The downside of the CFD approach is that it still requires the entire trajectory of each droplet within the spray to be tracked and the addition of a coagulation model adds considerable time to an already computationally intensive process. Thus there is considerable motivation to develop simpler approaches that can approximate the powder's size distributions more efficiently.

Our main aim is to develop some simplified models that achieve exactly this. Using a simple one-dimensional approach we predict the droplet size distribution throughout the length of the spray dryer, both accurately and efficiently. The end result will allow engineers to input a particular apparatus configuration, and quickly approximate the size distribution of their final product. The coagulation models we generate have the potential to be integrated into CFD codes, or larger scale models of a spray dryer, in order to do the job of handling the coagulation effects.

1.2 Spray drying

1.2.1 Dryer design

In its most basic form, a spray dryer consists of a cylindrical tower, with one or more atomiser nozzles mounted at specific heights inside it. A slurry is pumped through each atomiser nozzle and fired into a flow of air as shown in Figure 1.1.

The atomised slurry droplets coagulate with others in the spray and dry as they fall, producing a dried powder that is then collected at the bottom of the tower. Finer dried powder particles will generally become entrained in the airflow, and these will exit the dryer tower with the air at the air exhaust ports, where they can be collected and either recycled or disposed of.

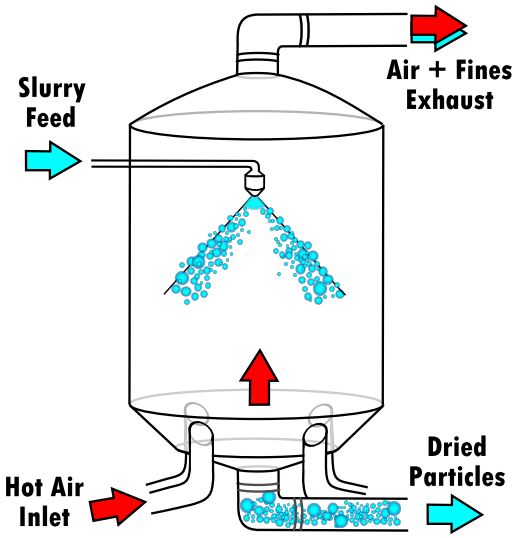

Figure 1.1: A simplified illustration of a counter-current spray dryer, based on the pilot scale dryer used by Procter and Gamble (P&G).

There are two main designs of spray drying tower. These are tall-form and short-form dryers, and are characterised by their height-to-width aspect ratios of taller than 5:1 and around 2:1, respectively [2]. The short-form driers are more popular, due to the fact they can accommodate the wide, flatter, spray trajectory produced by many rotary atomiser nozzles. However the airflow pattern within short-form driers is generally more complex, due to longer gas residency times and shorter plug flow zones than those seen in the tall-form alternatives [3]. Here, plug flow zones are simply regions where the velocity of the gas is constant across the region's entire cross-section. The longer gas residence times, when compared with tall-form dryers, are due to increased turbulence within the short-form design.

This turbulence leads to the drying gas following a far less linear path through the tower and often results in increased zones of recirculating flow when compared to a tall-form design.

A further distinction between dryers lies in the direction of the drying airflow. This air is generally hot, and may either be travelling in the same direction as the spray or flowing, as in Figure 1.1, in the opposing direction to the spray. These two airflow set-ups are termed co-current and counter-current, respectively. Co-current dryers are by far the most common within the industry, and the vast majority of spray drying literature is focused on this particular set-up [4]. Of the two designs, the co-current dryer has the higher rate of instantaneous drying, due to the high temperature of the inlet air around the atomiser nozzle (usually around 150 — $220°C$ [5]). This rapid evaporation increases the tendency for particles to expand (or puff), and so powders produced in this way generally have more porous, non-spherical morphologies. The fact that the hottest air is focused around the top of the tower, means the driest particles are then surrounded by the coolest air, and so this method is ideal for the production of thermo-sensitive materials [6, Chapter 2]. However, the co-current set-up is relatively energy inefficient in comparison to a counter-current design, which offers greater thermal efficiency, as the slurry and hot air enter at opposite ends of the dryer [4]. Since hot air rises, the counter-current design minimises potential for heat energy to be lost through the exhaust pipes at the top of the tower, before the hot air has even made contact with droplets in the spray. Thus, due to a demand for efficiency and cost savings, recent years have seen more research activity focused around further developing the counter-current design.

The counter-current design slows the downward flow of droplets, which sub-

sequently increases the residence time of each droplet within both short and tall-form driers. This, in turn, allows more time for drying and coagulation to take place, which facilitates the production of larger dried particles. The slower drying rate also reduces the tendency for droplets to puff, and so the final product will have a lower porosity than powder produced by co-current means. The main downside of this technique is that the driest particles are exposed to the hottest air at the bottom of the tower, and this can often lead to unwanted burning or charring of the final product. So counter-current drying is generally only viable for products that are not heat sensitive. Generally, washing up detergents are manufactured in counter-current towers, often making use of multiple spray nozzles that may be positioned at different heights within the dryer itself.

1.2.2 Atomiser nozzles

The atomiser nozzle is the heart of a spray dryer and so selection of an appropriate nozzle to match production needs is a key stage in dryer design. There are various ways in which a spray can be created. The main requirement is that a large relative velocity exists between the slurry being atomised, and the surrounding airflow. This may be achieved in several ways, including exposing the slurry to a high velocity airflow within the nozzle itself, or by discharging the slurry, at high velocity, from the edges of a spinning disc or cup that forms part of the nozzle. The method of spray creation is unique to each atomiser nozzle, with each nozzle type having different characteristics that may make it more desirable for specific processes. For example, the spray shape may take many forms, including a flat vertical sheet, hollow cone or a full cone, which will, in turn, influence the extent of liquid-gas mixing and the initial droplet size distribution of the spray.

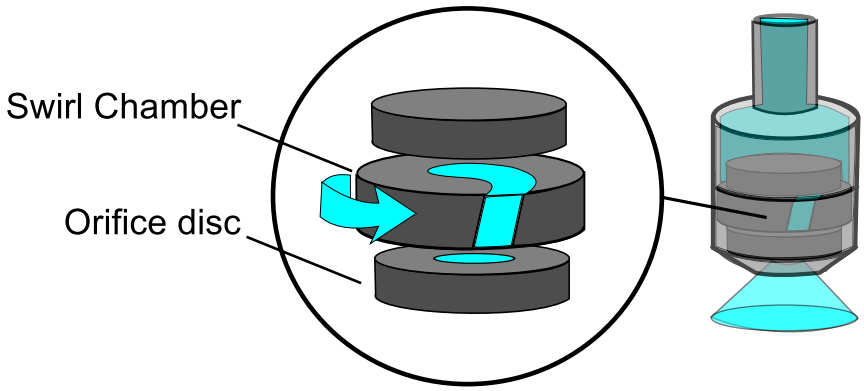

Figure 1.2: Simplified illustration of a pressure swirl atomiser nozzle, based upon illustrations in [7, Chapter 4] and [8].

The three main atomiser nozzles used by the spray drying industry are the pressure-swirl, the rotary spinning disc and the rotary cup atomisers. These are usually chosen due to their ability to create conical spray patterns, which lead to the most thorough liquid-gas mixing of all the nozzle designs available.

We will focus on the pressure-swirl atomiser, which consists of a swirl chamber that precedes a circular orifice, as pictured in Figure 1.2. The slurry is pumped into the swirl chamber through tangential holes or slots within the nozzle body, and this, in turn, creates pressure that is used to make the swirl chamber rotate. The rotating swirl chamber creates a core of air at the centre of the spray as it is discharged from the nozzle orifice, and the slurry is ejected as an annular sheet, that spreads rapidly outwards to form a hollow conical spray [7, Chapter 1].

The spray sheet which exits the nozzle first breaks up into ligaments, before eventually forming individual droplets at some distance further away. This is termed sheet break-up and is a result of aerodynamic waves forming within the sheet. These waves are caused by the combined forces of pressure, surface tension, centrifugal force and drag acting on the sheet as it widens and falls. Further details on the physics, together with different models for sheet break-up, can be found in

[9, 10].

The benefits of using the pressure-swirl atomiser are that it is both simple and cheap and can produce a wide range of spray angles ($30 - 180°$). These rotary atomisers also tend to produce the most uniform initial droplet size distribution.

1.2.3 Spray characteristics

There are several unique spray characteristics that will be dictated by the choice of nozzle used, as well as the physical properties of the slurry itself. In the case of the pressure-swirl atomiser, the first of these is the spray angle. This is widely accepted in the literature [7, Chapter 7] as the angle at the vertex of the cone formed by the two outermost surfaces of the spray, as illustrated in Figure 1.3. The spray angle will vary, depending on the internal geometry of the nozzle being used, and the pressure at which the slurry is being pumped through the atomiser. For example, both the swirl chamber and nozzle orifice can be interchanged to produce different shape sprays. In general terms, the higher the pressure of the slurry feed, the larger the spray angle and finer the resulting atomised droplets.

Any changes to the nozzle geometry and flow rate will also affect the initial

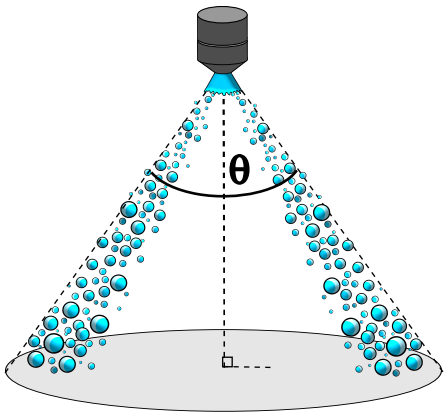

Figure 1.3: Illustration of the spray angle of a hollow conical spray.

droplet size distribution created at the point of complete sheet break-up. The size of the droplets at the point of sheet break-up will never be exactly uniform and so the distribution of droplet sizes will be unique to the spray nozzle set-up being used. Within the particle size literature, it is commonplace to assume droplets are spherical, and use droplet diameter in microns as the main measurement of size. The initial droplet size distribution may then be fitted to some mathematical distribution function of two parameters — the first being a measure of the mean droplet diameter, and the second a measure of the spread of droplet size within the spray. This approach assumes we have a uni-modal inlet distribution, and the most commonly used distributions for this purpose are the log-normal and modified Rosin-Rammler distributions [7, Chapter 3]. The log-normal distribution used takes the form

$$f(D) = \frac{1}{\sqrt{2\pi} D S_g} \exp\Big[-\frac{1}{2S_g^2}\Big(\log D - \log D_{ng}\Big)^2\Big], \tag{1.1}$$

where $f(D)$ is the number density function for droplets of diameter D, and D_{ng} and S_g are the mean diameter and the standard deviation parameters, respectively. The Rosin-Rammler distribution was originally developed for powders, and takes the form

$$f(D) = \frac{k}{\lambda_{rr}}\Big(\frac{D}{\lambda_{rr}}\Big)^{k-1} \exp\Big[-\Big(\frac{D}{\lambda_{rr}}\Big)^{k}\Big], \tag{1.2}$$

where λ_{rr} and k are distribution constants, representing measures of mean and spread, respectively. This is essentially a Weibull probability density function, however Rosin and Rammler were the first to apply it in the context of particulate systems when they used it to describe the cumulative distribution of coal particles [11]. When presented in the literature, the Rosin-Rammler is usually given as a

cumulative distribution function rather than the probability density function, and takes the form [12],

$$F(D) = 1 - \exp(-D/\lambda_{rr})^k. \tag{1.3}$$

Examples of other droplet size distributions that can be used, such as the Nukiyama-Tanasawa, can be found in [13].

To further quantify a spray's characteristics, it is usual for some measure of average droplet size to be quoted as well. The most common of these are the Sauter mean diameter D_{32} and the median diameter $D_{v0.5}$ (diameter of the median droplet volume). The Sauter mean diameter is defined by the formula

$$D_{32} = \frac{\int_{D_{min}}^{D_{max}} D^3 f(D)\, dD}{\int_{D_{min}}^{D_{max}} D^2 f(D)\, dD} \ , \tag{1.4}$$

where $D_{min/max}$ are the minimum/maximum drop diameters respectively [14]. The Sauter mean diameter represents the diameter of a droplet that has the same volume-to-surface-area ratio as the entire system of droplets, and is widely accepted as the best measure of a spray's fineness for atomisation processes. The standard arithmetic mean (summation of all droplet diameters divided by the total number) can often become skewed if there is a large number of smaller droplets within a system, despite the fact that these smaller droplets only make up a small proportion of the total volume. Thus, for processes like spray drying, where the surface area, or the fineness of the spray will be a critical factor, the Sauter mean gives a much better measure of which spray will be the most effective [7]. The diameters $D_{v0.1}$ and $D_{v0.9}$ will generally appear here as well, and represent the droplet diameters below which 10% and 90% of the distribution's total volume lies, respectively. One final measure is the span of the size distribution, which is

given by the equation

$$\text{Span} = \frac{D_{v0.9} - D_{v0.1}}{D_{v0.5}}, \tag{1.5}$$

and provides a quantitative description of the distribution's width.

1.2.4 Dryer phenomena

The following section provides an overview of the many complex physical phenomena that feature within an industrial spray drying operation. The list presented below is by no means exhaustive, but does aim to touch upon the main effects present within the drying chamber itself, as this is the area this thesis focuses upon. Not all of these effects will be incorporated into the dryer tower models that we develop, as our goal is to predict the final droplet distribution in a computationally efficient manner. Our reason for discussing them here is to highlight the inherent difficulties and challenges involved in producing a simple model that can predict accurately the droplet distributions throughout the length of the drying tower.

Coagulation

Coagulation is a physical phenomenon that appears within the dynamics of dispersed systems of droplets. It is the process by which droplets collide and become stuck together to form one larger droplet. During this process, the original droplets become an indistinguishable part of the new one. Coagulation is present in all aerosol systems where there exists a population of droplets that are free to move about in space and interact with each other. Examples of these include cloud formations, liquid mixtures and atomised sprays, many of which are commonplace in powder

production.

In the same dispersed systems, droplets may also spontaneously break up into smaller droplets — this reverse process is referred to as fragmentation. If colliding droplets do not coagulate, they may simply bounce of each other, or alternatively the collision may lead to fragmentation.

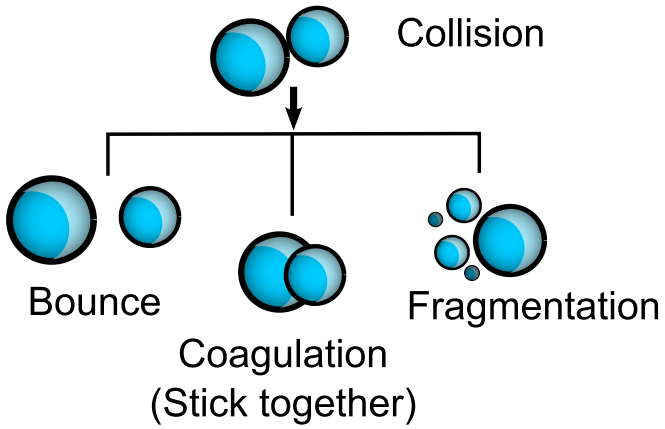

Figure 1.4: In a particulate system, particles are free to move about and collide. Often these collisions will result in successful coagulation of the colliding droplets. Alternatively the droplets may simply bounce off of one another. Occasionally, individual droplets may spontaneously fragment, or do so as the direct result of a collision.

In the literature, mechanisms for coagulation have received significantly more attention than their fragmentation counterparts [15]. Within the context of the models we develop later, it will be assumed that no fragmentation occurs (after the point of initial sheet break-up).

Airflow

Completely quantifying the airflow within a spray dryer is a very complex process that, as stated earlier, generally requires the use of highly computer intensive

CFD simulations. A comprehensive model needs to account for the effects of all interactions between the discrete droplets and the continuous gas phase, whilst also accounting for turbulence and the effects of coagulation and evaporation events among the droplets. Within a dryer it is often found that there will be zones of recirculating gas at the tower walls, and near the atomiser nozzle itself. The use of different atomiser nozzles, with varying inlet swirl, may also lead to the creation and collapse of eddies within the gas flow. A good insight into these flow patterns can be found in [16], where smoke plumes and laser sheets are used to show experimentally the existence of areas of recirculation, flow instabilities, and, in some cases, large-scale drifting of droplets within the dryer.

Slurry rheology

Slurries used for detergent production are viscous, non-Newtonian mixtures, containing large amounts of suspended solids, both organic and inorganic, and held together by a binder fluid [17]. This construction allows the slurry to behave like a thick fluid and, as such, it can be pumped to, and sprayed through, an atomiser nozzle. Laundry detergent slurries are often white in colour, and very similar in appearance to the gritty toothpastes that are widely available to the public.

It is noted that whilst no attempt will be made to incorporate the slurry and its rheology in our models, the slurry's characteristics do have an influence on the model input parameters used later on within this thesis — namely the droplet distribution and velocity at sheet breakup — and so it is of interest to provide a brief summary of slurries here.

The slurry's rheology will play a role in determining the physical properties of both the atomised droplets and the final dried product — influencing the density,

size, drying rate and morphology of each. The slurry pumped to the atomiser nozzle should be as consistent as possible in all influential variables, including temperature, moisture content, viscosity and aeration levels. In this context, the aeration of the slurry involves the introduction of air into the mixture, whilst it is stored. This air results in mixing as it rises through the slurry, and subsequently keeps the slurry in a pumpable state. Monitoring all these variables ensures that atomisation is both consistent and uniform for all production runs and for each different batch of slurry [18]. Thus, characterisation of a slurry's construction is essential in maintaining a consistent spray drying operation.

Wall deposition

Wall deposition is commonly encountered in spray drying. However, due to the challenges involved in modelling it, in this thesis we will make no attempt at incorporating the phenomenon into any models. It is, however, of relevance when analysing experimental data later on, and so it is beneficial to include the brief summary of it provided below.

Depending on the stickiness of the slurry droplets, the tower operating parameters and the physical properties of the wall itself, the contact of slurry droplets with the wall often results in an accumulation of product deposits upon the dryer wall. This build-up is commonly referred to as wall deposition. The build-up often sits on the wall for some indefinite period of time, however it may also become re-entrained within the dryer's airflow. This usually occurs when the aerodynamic drag forces acting on the wall deposits overcome the pull of the adhesive forces holding the deposits to the wall [19]. As a result, when present, wall deposition is generally responsible for creating the majority of the larger droplets present within

the end product, as it increases the residence time of droplets within the dryer. It may also lead to undesirable events. For example, the deposition may catch fire, or, if not re-entrained, the build-up will reduce the throughput of powder and often requires the tower to be shut down frequently to enable removal of blockages.

Many factors affect the amount of wall deposition observed within a dryer. In [20], it is demonstrated that decreasing swirl in the inlet air flow and decreasing the spray angle will both minimize wall depositions within a dryer. In [21] it is shown how the droplet stickiness level affects the rate of wall deposition for a dryer producing powdered milk. In [22], a comprehensive experimental review of wall deposition mechanisms within a counter-current dryer is given, and it is found that wall deposits that have become re-entrained within the airflow account for more than $12-20\%$ in mass of the final product. Thus, in systems where wall deposition occurs, the larger clusters produced by re-entrainment may lead to a second peak in the particle size distribution of the end product, with the first peak being due to smaller clusters that have had no interaction with the walls of the dryer.

1.3 Mathematical models of spray drying

Various approaches to spray dryer modelling have been presented within the literature, from plug flow models to full CFD simulations, a good review of which can be found in [23]. These provide varying levels of detail from the model predictions, with the most detailed also generally requiring the longest calculation times. To help classify the different models, the following hierarchy was introduced in [24], with each level producing more detailed results than the one preceding it.

1. Level 0 — Heat and mass balances.

2. Level 1— Heat and mass balances with solid-vapour equilibrium.

3. Level 2A — Rate-based model with simplifying assumptions about droplet motion.

4. Level 2B — Rate-based with simulation of gas flow and droplet motion (CFD).

A model from levels 0–2B above, may then be selected depending on the desired level of accuracy and detail required from the results. For example, a level 2B model would be required if spray tower aerodynamics were being investigated, whilst a lower level, less computationally expensive model may be more appropriate for preliminary process design. We now summarize some existing models from these categories.

1.3.1 Level 0 — Heat and mass balances

These are the simplest of all the modelling approaches and are based on the application of appropriate energy and mass balance equations to the system. Being the simplest type of model, they also require the least computational time, and although limited information can be predicted from them, they prove useful in assessing the thermodynamic feasibility of an operation at the earliest design phase. The main "streams" used to construct these models are the flows of mass through the four main entrance and exit points, into and out of the dryer. These are all illustrated in Figure 1.5. There are two streams letting mass flow into the dryer — the liquid slurry feed through the atomizer nozzle (FEED) and the gas inlet pipes (IN-GAS), through which the flow of drying air is pumped. Then, two streams allowing mass to exit the dryer — the exhaust gas pipes (EX-GAS) and the pipe

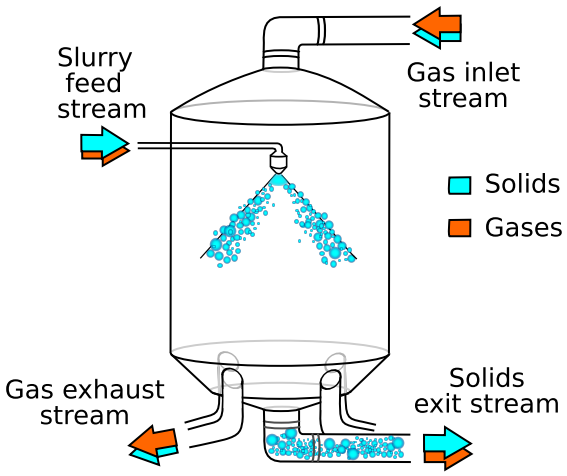

Figure 1.5: Illustration of the different streams entering and exiting the dryer tower. It is assumed that both solids and gases may enter the tower via each of the two streams. Although obviously some streams, like the gas exhaust and gas inlet pipes, will consist predominently of gases, whilst the slurry feed and solids exit pipes will be predominently solids.

through which the dried solids exit (EX-SOLIDS). Whilst it is perhaps counter-intuitive, there is potential for both solids and gases to travel through each of these four entrances/exits to the dryer tower. For example, in the case of the inlet gas feed, in some drying operations, fine particles which exit the tower through the gas exhaust pipes, are simply fed back into the dryer through the gas inlet pipe. As might be expected, the gas exhaust and gas inlet streams, will consist predominantly of gas, and the slurry feed and solids exit pipes will be predominantly solids. However, by accounting for the fact that gas and solids may travel through any one of these streams, the models make sure all mass is always accounted for.

As explained in [24], the mass balances for solids and gases in these main

streams are:

$$F_{FEED}^{SOLIDS} + F_{IN-GAS}^{SOLIDS} = F_{EX-SOLIDS}^{SOLIDS} + F_{EX-GAS}^{SOLIDS}, \tag{1.6}$$

$$F_{FEED}^{GAS} + F_{IN-GAS}^{GAS} = F_{EX-SOLIDS}^{GAS} + F_{EX-GAS}^{GAS}, \tag{1.7}$$

where F_i^j is the mass flow-rate of component j in stream i (Kg per second). Here, equation (1.6) simply states that the flow of solids into the dryer must be equal to the flow of solids out of the dryer, whilst (1.7) states the same for the flow of gases into and out of the dryer. Using X_i to denote the moisture content of solids in stream i (kg per kg of dry solid), and Y_i for the humidity of the gases in stream i (kg per kg of dry air), a third mass balance can be written for the moisture content entering and exiting the dryer:

$$\begin{aligned}(F_{FEED}^{SOLIDS} X_{FEED} + F_{FEED}^{GAS} Y_{FEED}) \\ + (F_{IN-GAS}^{SOLIDS} X_{IN-GAS} + F_{IN-GAS}^{GAS} Y_{IN-GAS}) \\ = (F_{EX-SOLIDS}^{SOLIDS} X_{EX-SOLIDS} + F_{EX-SOLIDS}^{GAS} Y_{EX-SOLIDS}) \\ + (F_{EX-GAS}^{SOLIDS} X_{EX-GAS} + F_{EX-GAS}^{GAS} Y_{EX-GAS}).\end{aligned} \tag{1.8}$$

This states that moisture entering the system must be equal to the moisture exiting the system. In addition to these mass balances, an overall energy balance for the dryer is given by the equation

$$\begin{aligned}\widehat{F}_{FEED} H_{FEED} + \widehat{F}_{IN-GAS} H_{IN-GAS} \\ = \widehat{F}_{EX-GAS} H_{EX-GAS} + \widehat{F}_{EX-SOLID} H_{EX-SOLID} + Q,\end{aligned} \tag{1.9}$$

where H_i is the specific enthalpy (Joules per unit mass), Q is the heat loss from the dryer (Watts = Joules per second) and $\widehat{F}_i$ is the combined mass flow-rate of gas and solids in stream i. The specific enthalpy is used to quantify the total amount of energy contained within a stream, due to pressure and temperature.

In general, the mass flow-rate, temperature and moisture content of all the inlet streams will be known, along with the moisture content of the exiting solids and gas. Equations (1.6–1.9), can then be used to calculate the energy lost from the dryer, i.e. the dryers thermal efficiency. Similarly, if a certain moisture content is required for the final product, and the heat loss Q is known, these equations may be used to check if the desired moisture content is achievable by, for example, simply fine-tuning the drying air's temperature.

Energy balance equations have been used in [25] to create simple models of both co- and counter-current dryers, and also to assess the effects of slurry inlet mass flow rate and the inlet gas mass flow rate upon the moisture removal capabilities of a dryer. In addition, a heat balance equation played a key role in estimating wasted energy in a survey investigating the energy consumption of a number of industrial spray dryer installations, [26].

1.3.2 Level 1— Heat and mass balances with solid-vapour equilibrium

In these models, the heat and mass balances are extended to include the moisture content within the droplets themselves. This is achieved by the use of curves that represent the equilibrium moisture content of the solid as a function of the gas phase's temperature and composition. These curves are generally referred

to as desorption isotherms and show the variation of the equilibrium moisture content of the droplets with relative humidity at a constant temperature. Here, the equilibrium moisture content of each droplet is deemed to be that at which the droplet is no longer losing (or gaining) moisture and is dynamic in nature, in that it will vary with the relative humidity and temperature of the droplet's surroundings.

The advantage of models including these equilibrium moisture content curves is that they can predict the final moisture content of the particles, rather than relying on it being specified by the user (as in the previous heat and mass balance approach).

Desorption isotherms are widely available in the literature, in the form of both experimentally measured examples and correlations to experimental observations. One example is that suggested in [27], where several correlations were reviewed and the formula

$$X_{eq} = A \exp\Big[-BT \ln\Big(\frac{1}{\Psi}\Big)\Big], \tag{1.10}$$

was proposed. Here X_{eq} is the equilibrium moisture content on a dry basis (in kg water per kg dry material), T is the temperature of the gas (in Kelvin) and Ψ is the relative humidity of the gas. The values of A and B are constants that will be unique to the types of material that make up the solid and liquid phases.

Calculation times for level 1 models are relatively fast, and computationally inexpensive. The shortfalls are the need to determine experimentally the desorption isotherms, and the assumption that the exhaust solid's moisture content is in equilibrium with the surrounding gas. Generally, it is safest to use this approach for smaller droplet sizes, for which the moisture equilibrium will usually be reached

quickly within the dryer tower; see [28].

1.3.3 Level 2A — Rate-based model with simplifying assumptions about droplet motion

This next level of model aims to calculate the rate at which a droplet dries, together with its final moisture content, without requiring the calculation of full gas flow patterns and droplet trajectories via CFD. These models consist of two main components: a droplet drying model, and some method of estimating droplet residence times within the spray.

The drying model often takes the form

$$-M_{DS}\frac{dX}{dt} = N, \tag{1.11}$$

where M_{DS} is the mass of drying solids (kg), X the moisture content (kg per kg dry solid) and N the droplet drying rate (kg moisture per second) [24] [1].

An estimation of the droplet residence time is obtained using a parameter called the "chamber coefficient", which relates droplet residence time to the average gas residence time. The drop residence times τ_{drop} are then calculated by substituting the chamber volume $V_{chamber}$, and the volumetric flow rate of gas through the

[1] Note that the form of the drying rate in (1.11) can be obtained from the growth rate later introduced in (6.2): By multiplying the growth rate $\gamma(x)$ (Volume per second) by the droplet density ρ_{drop} (kg per unit volume) and the corresponding moisture content X (kg per kg dry solid), the moisture lost per second is obtained. A similar conversion may also be applied to the evaporation rate found in (6.60).

chamber $\dot{V}_{gas}$, into the equation

$$\tau_{drop} = \tau_{cc} \times \overbrace{\frac{V_{chamber}}{\dot{V}_{gas}}}^{\text{Mean gas residence time}}, \tag{1.12}$$

where τ_{cc} is the chamber coefficient.

This type of model was used in [29] to describe the drying of single droplets, all of which were assumed to be the same size. It was also assumed that the gas within the system was a single well-mixed mass, and this allowed standard residence time distributions for droplets in a well-mixed reactor to be used. This was used to simulate the droplet drying, and validated using experimental data from the drying of skimmed milk concentrate.

Since the chamber coefficient (or residence times) must be calculated from experimental observations, this type of model proves difficult to use for spray dryer design purposes, as doing so would first require the construction of a prototype dryer in order to obtain the necessary experimental measurements.

1.3.4 Level 2B — Rate-based with simulation of gas flow and droplet motion (CFD)

Full computational fluid dynamics simulations track each droplet's entire trajectory throughout the length of its residency within the dryer, and provide a comprehensive description of flow fields, as well as temperatures and velocities, within a given model.

The main steps involved in the construction of a CFD model are as follows. First a computational grid in the shape of the dryer chamber is created, followed by

the calculation of the gas flow throughout the chamber, using mass and momentum balances for each cell within the grid. This allows energy conservation to be modelled, as well as the effects of turbulence when an appropriate turbulence model is used in the simulation. Next, the droplet trajectories are calculated by solving their equations of motion, taking into account both drag and gravitational forces. At the same time, droplet moisture content and temperature are calculated, often using drying rate curves of the form found in equation (1.11). The combined effect of each droplet's motion, temperature and drying has a resultant effect on the surrounding gas flow field. Subsequently, the gas flow is recalculated to account for this, and the above steps repeated until a measure of convergence is reached.

There have been many attempts within the literature to capture gas/droplet flow patterns using CFD. A good review is provided in [3, 30] and [31], although most of the models presented neglect the effects of coagulation.

A CFD approach that does incorporate coagulation in a spray is presented in [32], where a droplet collision probability, based upon the kinetic theory of gases, is obtained and used to model particle collisions within the dryer. Another CFD based model that includes coagulation effects is given in [33], where a stochastic approach is used to incorporate droplet-droplet collisions and coagulation into a CFD simulation for two overlapping hollow-cone sprays. The results are also verified against experimental data.

Benefits of the use of CFD include the high level of detail returned from the simulations, together with the fact that there are no restrictions on the shape of the spray drying chamber being used. The main downside is that CFD is computationally expensive, and thus may not be warranted if a high level of detail is not required.

1.3.5 EDECAD project

The EDECAD (Efficient DEsign and Control of Agglomeration in spray Drying machines) project was set up in 2001 with the aim of creating a comprehensive, industrially validated computer model, using CFD software to model coagulation and predict the resulting powder size distribution produced by a spray drying tower [34]. The end product of the project is a tool that can be used to predict the properties of the final dried powder, based on the slurry, dryer configuration and operating conditions used.

The EDECAD model uses CFD to resolve the flow field within a dryer, adopting an Euler-Lagrangian viewpoint to simulate the flow of both the continuous and discrete phases. The flow field is combined with three sub-models which simulate the drying, collision and coagulation of droplets. Local temperature and moisture content of the air flow is handled by solving heat and mass balances. Combined, all of these components allow droplet moisture content, temperature, porosity and the structure of droplet clusters to be predicted with reasonable accuracy.

The project makes use of the stochastic approach described in [35] to simulate collision events. The drying sub-model adopted uses an approach outlined in [36], which is applicable to slurry droplets. It also incorporates a mechanism for representing the drying of hollow droplets, which can occur if an expanding (due to heat) air bubble is present within a slurry droplet.

The sub-model for coagulation takes a force balance approach and considers only the viscous forces acting upon colliding droplets, when evaluating coagulation success.

1.4 Coagulation

The following discussion provides a brief outline of the history of mathematical coagulation equations and their applications to dispersed systems of droplets.

1.4.1 Mathematical models of coagulation

One approach for describing coagulation is to concentrate on the statistical behaviour of the large numbers of droplets concentrated together in space. The first person to succeed in using such an approach for coagulation was the Polish-Austrian physicist Smoluchowski [37, 38]. He studied the Brownian motion of particles within a spatially homogeneous, mono-disperse system and derived a model for the binary coagulation of colloidal particles within this system. Here, "mono-disperse" describes a system in which all the constituent droplets are of uniform size, and "binary coagulation" simply means that only two droplets may collide and coagulate at any given time. Smoluchowski's theory of rapid coagulation resulted in the formulation of an infinite set of nonlinear, differential equations given by

$$\frac{dn_i}{dt} = -n_i \sum_{j=1}^{\infty} K_{i,j} n_j + \frac{1}{2} \sum_{j=1}^{i-1} K_{j,i-j} n_j n_{i-j}, \tag{1.13}$$

where $i = 1, 2, 3, \ldots$, and the initial conditions for the mono-disperse system are

$$n_1(0) = n_0, \;\; n_i(0) = 0 \;\; \forall\, i \in \{2, 3, 4 \ldots\}. \tag{1.14}$$

Here, n_i represents the number of clusters made up of i monomers, per unit volume in space, and $K_{i,j}$ is the the coagulation rate constant for a cluster of i monomers successfully coagulating with one of j monomers. These rate constants are non-

negative and symmetric, in that $K_{i,j} \geq 0$ and $K_{i,j} = K_{j,i}$ for all i and j, and are also referred to as the "coagulation rate kernel" or simply the "coagulation kernel". It should also be noted that, in the specific case of $i = 1$, the second sum on the right-hand side (RHS) of (1.13) will be exactly equal to zero. This accounts for the fact that the monomers are the smallest building blocks within the system, and, as such, cannot be created by means of coagulation.

As discussed in [39], this infinite system of ordinary differential equations (ODEs) provides a discrete, mean-field model for binary coagulation, and will be referred to as the discrete Smoluchowski equation. The original Smoluchowski papers [37, 38], written in German, appeared in 1916 and 1917, and detailed summaries, in English, of the derivation of (1.13) can be found in [40, 41]. The discrete size Smoluchowski equation (1.13) was later extended to the continuous size setting by Müller in 1928; see [40, 42, 43]. In this continuous form, the summations in (1.13) are replaced by integrals, resulting in

$$\frac{\partial n(x,t)}{\partial t} = \frac{1}{2}\int_0^x K(x-y,y)\, n(x-y,t)n(y,t)\, dy - \int_0^\infty K(x,y)\, n(x,t)n(y,t)\, dy, \tag{1.15}$$

where $n(x,t)$ is the number density function of droplets of volume x, at time t, within the system, per droplet volume size range, per unit volume in space. Hence,

$$\int_x^{x+\Delta x} n(\zeta,t)d\zeta = \begin{array}{l}\text{Number of droplets with}\\ \text{volumes in } [x, x+\Delta x] \text{ per}\\ \text{unit volume in space.}\end{array}$$

The $\frac{1}{2}$ in the birth term is necessary to avoid double accounting, as the integral includes every possible way of constructing a droplet of volume x twice. Here, the

term "birth" is used to represent the event of a droplet of volume $x-y$ coagulating with a droplet of volume y to create a new droplet of volume x, whilst "death" will be used to represent the loss of a droplet of volume x from the system due to coagulation with another droplet.

Equation (1.15) will be referred to as the continuous Smoluchowski equation. Once again, the coagulation kernel is assumed to be non-negative and symmetric, so that

$$K(x,y) \geq 0 \text{ and } K(x,y) = K(y,x) \ \forall x, y \ \geq \ 0. \tag{1.16}$$

This symmetry property simply captures the fact that the rate of coagulation should be unaffected by the ordering of the colliding droplets. Note that the coagulation rate kernel, $K(x,y)$ in (1.15) or $K_{i,j}$ in (1.13), gives the rate at which successful coagulation of droplets of volume x and y (or i-mers and j-mers) takes place within a dispersed system of droplets. The kernel is dependent on environmental factors within the system, and the selection of a suitable coagulation kernel is generally one of the trickiest parts of modelling coagulation.

$K(x,y)$	Specific usage
$(x^{1/3}+y^{1/3})(x^{-1/3}+y^{-1/3})$	Brownian motion (continuum regime)
$(x^{1/3}+y^{1/3})^2(x^{-1}+y^{-1})^{1/2}$	Brownian motion (free molecular regime)
$(x^{1/3}+y^{1/3})^3$	Shear (linear velocity profile)
$(x^{1/3}+y^{1/3})^2\lvert x^{1/3}-y^{1/3}\rvert$	Gravitational settling
$(x^{1/3}+y^{1/3})(xy)^{1/2}(x+y)^{-3/2}$	Based on kinetic theory

Table 1.1: Table of specific coagulation kernels taken from [44].

Examples of some commonly used kernels for coagulation in flow driven motion, Brownian motion, and gravitational sedimentation, are found in [44] and

presented in Table 1.1. The form each of these kernels takes generally reflects the main mechanisms thought to be responsible the coagulation. For example, in the gravitational settling case, the kernel is proportional to the effective cross-sectional area that is available for collisions, and the relative (terminal) velocity of the two colliding droplets (proportional to the droplet diameter squared).

In our spray drying models, the effects of coagulation will be represented by a modified version of the population balance equation (PBE) (1.15) in which the coagulation kernels are spatially dependent. The kernel we use later (which can be found in (2.41)) is very similar in appearance to the gravitational settling kernel found in Table 1.1. The main difference is that our kernel has an added spatial dependence that is incorporated through the relative velocity of the two colliding droplets at a each point in space. This differs from the gravitational settling case, where the relative velocity is constant, due to the fact the droplets are all assumed to be falling at terminal velocity at every point in space.

1.4.2 Exact solutions of the coagulation equations

The coagulation equations outlined above have very few exact solutions, and consequently the solution of most coagulation problems will require the use of a numerical method. Some of these numerical schemes will be described in Chapter 4. Those analytic solutions that have been derived are only for very specific combinations of coagulation kernel and initial condition.

The analytic solutions to the discrete equation (1.13), for the cases of constant, additive and product kernels, subject to a mono-disperse initial condition can be found in [45]. These are shown in Table 1.2. Similarly, exact solutions to the continuous equation (1.15), for these kernels combined with a negative exponential

initial condition can be found in Table 1.3.

Kernel	Analytic Solution for $n_i(t)$
$K_{i,j} = 1$	$(1 + \frac{t}{2})^{-2}(\frac{t}{2+t})^{i-1},\ \ 0 < t < \infty$
$K_{i,j} = i + j$	$e^{-t}B(1 - e^{-t}, i),\ \ 0 < t < \infty$
$K_{i,j} = ij$	$i^{-1}B(t, i),\ \ 0 < t < 1$

Table 1.2: Table of analytic solutions for the discrete coagulation equation (1.13), subject to a monodisperse initial condition, $n(i, 0) = \delta(i - 1)$, taken from [45]. The three kernels listed are referred to as the constant, additive (or sum) and product kernel, respectively.

In Table 1.2, some of the solutions involve the density function, B, of the Borel distribution, where

$$B(\lambda, i) = \frac{(\lambda i)^{i-1}e^{-\lambda i}}{i!},\ \ i = 1, 2, 3, \ldots, 0 \leq \lambda \leq 1. \tag{1.17}$$

Kernel	Analytic Solution for $n(x, t)$
$K(x, y) = 1$	$\frac{4}{(t+2)^2}\exp[\frac{-2x}{t+2}],\ \ 0 < t < \infty$
$K(x, y) = x + y$	$\frac{(1-\tau)e^{(-x(\tau+1))}}{x\tau^{1/2}} I_1\left(2x\tau^{1/2}\right),\ \ \tau = 1 - e^{-t},\ \ 0 < t < \infty$

Table 1.3: Table of analytic solutions for the continuous coagulation equation, subject to a negative exponential initial condition, $n(x, 0) = e^{-x}$, taken from [46]. Here I_1 is a modified Bessel function of the first kind.

1.4.3 Moments of the number density function

In many applications of PBEs to droplet coagulation, the main measure of interest is often a particular quantity of the droplet volume distribution, such as the average droplet volume within the system. This is where the moments of the droplet number density function can play a valuable role. Particular moments represent

some of the the inherent physical properties of the system, such as total number of droplets and total volume, from which the evolution of properties, such as average droplet volume and mass, can be monitored [47].

By definition, the ν^{th} moment of the number density function $n(x,t)$ is given by

$$M_\nu(t) = \int_0^\infty x^\nu \, n(x,t) \, dx. \tag{1.18}$$

Taking the time derivative of this function, and assuming it is permissible to differentiate under the integral sign, gives

$$M'_\nu(t) = \int_0^\infty x^\nu \, \frac{\partial}{\partial t} n(x,t) \, dx. \tag{1.19}$$

An equation for the time evolution of the moments of a known PBE can then be obtained by using the PBE itself to replace $\frac{\partial n}{\partial t}$. In the case of the continuous Smoluchowski equation, we substitute the RHS of (1.15) for $\frac{\partial n}{\partial t}$. This may then enable the evolution of the moment related quantities, such as average volume, to be obtained without the need for solving the entire PBE, which is usually more complicated.

As a result, this technique of determining the evolution of particular moments is often the one chosen, rather than solving the full PBE. However, in the context of this thesis, our interest is in obtaining the complete droplet volume distribution throughout the length of the spray tower. Simply measuring average droplet volume can make all the droplets appear to be of the ideal volume, but may hide the fact that there are, in fact, a large number of undesirable small droplets and large droplets present in the system. Thus, in the models presented later, we will use the moments for an alternative purpose — as a global measure of the accuracy

of the numerical techniques chosen to handle coagulation. For example, in the absence of a mechanism for mass loss, such as evaporation, we would aim for a model that conserves the total mass of the droplets in the system. This can be done by monitoring the first moment of the system which, as described below, allows the total volume of droplets within the system to be calculated, from which the mass can easily be obtained.

In an isotropic system of droplets, with no spatial dependence, and volume as the droplet's "size coordinate", the first moment corresponds to the total volume of droplets within the system (per unit volume in space). Thus a good check that any given numerical method is handling the coagulation equations well is to verify that the volume of drops within the system, $M_1(t)$, remains constant for all time, i.e. $M_1(t) = M_1(0), \forall\, t \geq 0$. In a system where all droplets have the same density, ρ_{drop}, the total mass of the droplets within the system (per unit volume in space) is simply

$$\text{Total mass} = \rho_{drop} \times M_1(t). \tag{1.20}$$

Together with the first moment, we will also make use of the zeroth moment $M_0(t)$. Here, the zeroth moment represents the total number of particles in an isotropic system at time t. In the case of pure coagulation, it is expected that $M_0(t)$ will decrease as time progresses, since coagulation will cause the total number of individual droplets to be reduced. Subsequently, the average droplet volume, $\bar{x}$, within the system can be found by calculating

$$\bar{x}(t) = \frac{M_1(t)}{M_0(t)}, \tag{1.21}$$

and will be expected to increase as time progresses.

While there are an infinite number of moments of the number density function, we only mention the cases $\nu = 0, 1, 2$ here. These are the moments most commonly mentioned in the literature, due to the fact they are the most physically relevant to a system of particles. The third of these ($\nu = 2$) is the second moment, which represents the volume of each droplet within the system, squared, and then summed over all droplet volumes. The second moment is similar to the variance that appears in statistical contexts and is useful for capturing the spread of the droplet volumes found within the system. Knowing the second moment also allows for an alternative calculation to find the average droplet volume within the system [39, 48], using the equation

$$\bar{x}(t) = \frac{M_2(t)}{M_1(t)}. \tag{1.22}$$

Note that the formula in (1.22) will return a different value for the average droplet size than that obtained from (1.21). However both are still valid interpretations of the average droplet volume.

If we consider the case of coagulation in an isotropic system of particles governed by the continuous Smoluchowski equation (1.15), then, on using (1.18), we

obtain

$$\begin{aligned}
M'_\nu(t) &= \frac{1}{2}\int_0^\infty \int_y^\infty x^\nu\, K(x-y,y)\, n(x-y,t)n(y,t)\, dx\, dy \\
&\qquad - \int_0^\infty \int_0^\infty x^\nu\, K(x,y)\, n(x,t)n(y,t)\, dx\, dy \\
&= \frac{1}{2}\int_0^\infty \int_0^\infty (x+y)^\nu K(x,y)n(x,t)n(y,t)dxdy \\
&\qquad - \int_0^\infty \int_0^\infty x^\nu\, K(x,y)\, n(x,t)n(y,t)\, dx\, dy \\
&= \frac{1}{2}\int_0^\infty \int_0^\infty (x+y)^\nu\, K(x,y)\, n(x,t)n(y,t)\, dx\, dy \\
&\quad - \frac{1}{2}\int_0^\infty \int_0^\infty x^\nu\, K(x,y)\, n(x,t)n(y,t)\, dx\, dy \\
&\qquad - \frac{1}{2}\int_0^\infty \int_0^\infty x^\nu\, K(x,y)\, n(x,t)n(y,t)\, dx\, dy \\
&= \frac{1}{2}\int_0^\infty \int_0^\infty \left\{(x+y)^\nu - x^\nu - y^\nu\right\}\, K(x,y)\, n(x,t)n(y,t)\, dx\, dy, \qquad (1.23)
\end{aligned}$$

where we have used the fact that $K(x,y) = K(y,x)$. This is in agreement with the result shown in [49].

Clearly, if $\nu = 0$, the RHS of (1.23) will be negative for all time (since $n(x,t) \geq 0$ and $K(x,y) \geq \forall t$), and thus $M_0(t)$ will always decrease as time increases. This is in agreement with what we would expect. Similarly, when ν is set to 1, the RHS of equation (1.23) is exactly zero. Again, this agrees with what is expected physically. The first moment represents the total volume of droplets within the system, and with no mechanism for mass loss it is understandable that $M_1(t)$ should be constant. If it were not, it would indicate mass being gained or lost from the system. The exception to this rule is when gelation is present within the system [39]. Gelation occurs when mass conservation fails, and can be characterised physically by the formation of a particle of infinite size within the system. However, since this is unlikely to occur within the context of spray drying,

we won't go into any further details here.

Closed-form expressions for the moments can be obtained for the constant, additive and product coagulation kernels. Calculation of the exact zeroth, first and second moments of the number density function for the constant and additive kernel cases can be found in Appendix A. These will be used to validate the numerical methods developed later for dealing with the coagulation terms in our model.

1.4.4 Self-similar solutions and long-term behaviour

In any model of a physical system that varies with time, it is important to know what happens within the system over long time scales (as time $t \to \infty$). In certain cases, the model equations predict that the solution will ultimately display steady-state behaviour represented by a time-independent solution. In others, it may be possible that the long-term behaviour remains time-dependent, but can be represented in terms of a simple solution, known as a similarity solution.

If we consider the coagulation equation (1.15), then, since this models an irreversible process, no equilibrium solutions can exist. However there have been many investigations which have focused on similarity solutions of the form

$$n_S(x,t) = g(t)\Phi\Big(\frac{x}{S(t)}\Big), \tag{1.24}$$

where g and Φ are functions of a single scalar variable. Here, $S(t)$ is an arbitraty function of time, often referred to as the scaling function and which usually represents the typical size of droplets within the system. Detailed accounts of the use of similarity solutions can be found in [48, 50, 51], where it will be seen that

attention is restricted to homogeneous kernels of the form

$$K(ax, ay) = a^{\lambda} K(x, y). \tag{1.25}$$

Here, a may be any positive real number, and $\lambda \in (-\infty, 2]$ is some fixed exponent that represents the degree of homogeneity of K, [52]. Hence, for some function β,

$$K(x, y) = x^{\lambda} K\Big(1, \frac{y}{x}\Big) = x^{\lambda} \beta\Big(\frac{y}{x}\Big). \tag{1.26}$$

An additional assumption is that

$$K(x, y) \sim x^{\mu} y^{\nu} \text{ for } y \gg x, \text{ where } \mu + \nu = \lambda \text{ and } \nu \ll 1. \tag{1.27}$$

The physical reasoning behind the restriction on λ is that, for a large droplet of volume y to increase at a rate not greater than its volume, we require $K(y, y) = y^{\lambda} K(1, 1) \leq y^2 K(1, 1)$; see [51].

Note that the kernels in Table 1.1 satisfy these assumptions. For example, if we examine

$$K(x, y) = (x^{1/3} + y^{1/3})(x^{-1/3} + y^{-1/3}),$$

then we can write

$$K(x, y) = \Big(1 + \Big(\frac{y}{x}\Big)^{1/3}\Big(1 + \Big(\frac{y}{x}\Big)^{-1/3}\Big),$$

and so $\lambda = 0$ and $\beta(z) = (1 + z^{1/2})(1 + z^{-1/2})$. Also, for $y >> x$, $K(x, y) \sim y^{1/3} x^{-1/3}$. Consequently $\nu = \frac{1}{3}$ and $\mu = -\frac{1}{3}$.

The form taken by the function g in (1.24) can be established if we assume

that the total mass in the system is conserved. This means that the first moment, M_1, is constant for all time, and consequently

$$\begin{aligned} M_1 &= \int_0^\infty x\, n_S(x,t)\, dx \\ &= g(t) \int_0^\infty x\Phi\Big(\frac{x}{S(t)}\Big)\, dx \\ &= g(t)S^2(t) \int_0^\infty \eta\Phi(\eta)\, d\eta, \ \text{ where } \ \eta = \frac{x}{S(t)}. \end{aligned}$$

It follows that

$$g(t) = \frac{M_1}{S^2(t)\int_0^\infty \eta\Phi(\eta)\, d\eta},$$

and assuming the integral is finite, we can choose Φ so that $\int_0^\infty \eta\Phi(\eta)\, d\eta = M_1$ to obtain

$$g(t) = \frac{1}{S^2(t)}.$$

Thus, when dealing with equation (1.15), we look for a similarity solution in the form

$$n_S(x,t) = \frac{1}{S^2(t)}\Phi\Big(\frac{x}{S(t)}\Big), \tag{1.28}$$

where $S(t)$ is some representation of the mean droplet size.

As discussed in [50, 51], equations for S and Φ can now be derived by substituting (1.28) into (1.15), and using the homogeneity condition (1.25). After some lengthy, but routine, manipulations, we arrive at

$$S'(t) = \omega S^\lambda(t),$$

and

$$-\omega[2\Phi(x)+x\Phi'(x)] = \frac{1}{2}\int_0^x K(y,x-y)\Phi(y)\Phi(x-y)\,dy - \int_0^\infty K(x,y)\Phi(x)\Phi(y)\,dy,$$

where ω is a separation constant for the x and the t dependence.

Establishing the existence of such similarity solutions for the coagulation equation is a non-trivial problem, but some progress has been made in recent years; for example, see [53]. The role of self-similarity for coagulation arising in physical applications is also nicely demonstrated in [54], where the coagulation and settling of particles in Lake Zurich is examined and the resulting number flux distribution of particles is shown to be self-similar with depth.

As mentioned earlier, a primary motivation for seeking similarity solutions is that these provide information on the long-term behaviour of other solutions. In connection with this is the "scaling hypothesis" for coagulation equations with homogeneous kernels [48]. In essence, this hypothesis asserts that solutions emanating from a suitable initial distribution will evolve into a self-similar solution, of the type discussed above, that is independent of the initial distributions. One consequence of this is that similarity solutions have been employed as a means of assessing the accuracy and efficiency of numerical algorithms designed to solve (1.15).

1.5 Outline of thesis

This thesis presents a novel, simplified and robust approach for the simulation of droplet coagulation within the sprays produced by the atomiser nozzles of a spray drying tower. This is achieved by coupling an existing PBE for coagulation with spatial derivative terms in order to simulate the transport of droplets throughout the spray. In later chapters, we further develop this novel coupling, with the addition of droplet evaporation to the model.

The resulting integro-differential equations are solved numerically, using the cell average technique for the coagulation terms and Kurgano-Tadmor's high resolution, central difference scheme for the transport terms. To our knowledge, this is the first instance that these two techniques have been combined and successfully applied in a spray dryer model.

Another key part of this work, is the validation of its accuracy via comparison against experimental results.

In Chapter 2, we construct a simple one-dimensional model for coagulation and transport within the hollow-cone spray of a spray drying tower. The model is based upon a population balance approach, and aims to predict the droplet number distribution throughout the length of a steady-state spray. The resulting nonlinear partial integro-differential equation combines coagulation with spatial transport, and uses a coagulation kernel that is dependent on both a droplet's size and spatial position.

In Chapter 3, we explore the possibility of applying any existing mathematical theory on coagulation to our governing equation.

In Chapter 4, the one-dimensional model is discretised, using the cell average

technique and Kurganov Tadmor discretisations for the coagulation and transport terms respectively.

In Chapter 5, the predictions of the numerical schemes are verified by using the schemes to solve a series of test problems, and, where possible, comparing the predictions to known analytic solutions.

Having established that the coagulation-transport model provides a reasonable agreement to the experimental data, we extend the model to incorporate the effects of evaporation in Chapter 6. This is done by the addition of a growth term to the existing model, and the selection of an appropriate numerical technique to discretise this new evaporation term.

We then go on to compare the predictions of the model against experimentally obtained data in Chapter 7. In doing so, the coagulation kernel efficiency parameter is optimised for the different slurries used in the experimental trials.

Conclusions and potential future investigations are given in Chapter 8.

Chapter 2

A 1-D model for coagulation and transport in a hollow cone spray

2.1 Derivation of a one-dimensional model

In this chapter, a model is presented for coagulation and droplet transport within a spray dryer's hollow conical spray. The model is "one-dimensional" in that all spray properties are defined relative to a single axis in space, rather than relying on a three-dimensional coordinate system. The main advantage of this approach is that results can be obtained relatively quickly and in a computationally efficient manner. Our approach uses a PBE to describe the coagulation and transport of droplets throughout the spray, whilst at the same time accounting for the spreading conical shape of the spray sheet.

2.1.1 Set-up, variables and modelling assumptions

Before deriving the equations behind our model, we first set the scene. Here, we introduce the physical configuration of the dryer tower we are investigating,

along with the variables and assumptions used in constructing our one-dimensional model.

Physical set-up of the spray dryer

The spray drying tower being modelled consists of a cylindrical tower with a single atomiser nozzle mounted centrally in the upper portion of the tower. The nozzle is angled vertically downwards, perpendicular to the base of the tower, as pictured in Figure 1.1 and is of the pressure-swirl variety introduced in Section 1.2.2, which is designed to produce a hollow conical spray.

Model geometry

The vertical z-axis, illustrated in Figure 2.1, is the single axis that will quantify location within the spray. It has its origin at the nozzle orifice and is used as a reference axis for the displacement of droplets throughout the length of the spray. The axis runs from the centre of the spray-nozzle tip, to the base of the dryer tower so that the positive $z-$direction is vertically downwards. It is assumed that the slurry exits the nozzle as a conical sheet, axially-symmetric about the $z-$axis and subsequently breaks up completely into individual droplets at a distance $z = z_0$ from the nozzle. The model will focus on a spray which has a total length L in the vertical direction.

Spray shape

As mentioned in Section 1.2.2, the spray starts life as a thin, conical sheet at the nozzle, breaks up into (ligaments and then) droplets at $z = z_0$ and subsequently spreads and increases in thickness as z increases. This phenomenon is referred

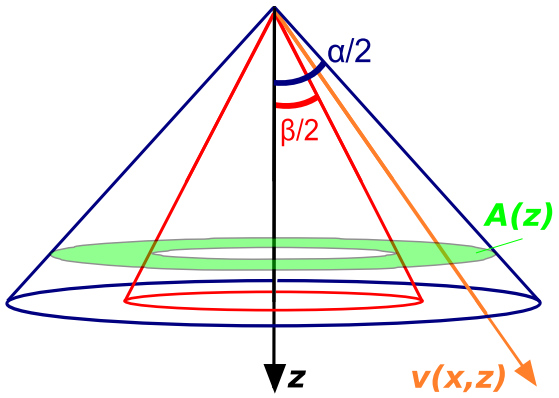

Figure 2.1: Illustration of the set-up used to derive the governing equations for the model of coagulation and transport in the hollow conical spray system.

to as spray spreading, and, for simplicity, this is captured by assuming that the spray takes the shape of the volume enclosed between the red inner and blue outer surfaces in Figure 2.1. The blue and red surfaces are assumed to be cones with cone angles α and β respectively, such that $\beta < \alpha$. The blue cone will be referred to as the spray's outer surface, whilst the red cone will be the spray's inner surface. The angles $\alpha/2$ and $\beta/2$ are assumed to remain constant throughout the length of the spray.

To incorporate the spreading of the spray within the model, we will make use of the horizontal cross-sectional area of the spray at each distance z. This area is highlighted in green in Figure 2.1 and will be denoted by $A(z)$.

Population balance fundamentals — continuous/discrete phases

At this point, it is important to outline some key features of the population balance framework used in our model. The system being modelled consists of droplets (the discrete phase) dispersed within a flow of air, which shall be referred to as the continuous phase. The way in which the droplets interact with the continuous

phase will vary from droplet to droplet depending on a number of unique characteristics associated with individual droplets. These characteristics are contained within, what is referred to as, the discrete droplet phase vector and each characteristic can be either continuous or discrete in nature. In the context of a spray dryer, continuous characteristics are by far the most common type encountered, and examples of these include droplet temperature, droplet position and droplet volume. The continuous air phase vector describes the continuous air phase of the system. This continuous phase vector is assumed to satisfy the traditional transport equations and, as such, these will be coupled with the PBE proposed later for coagulation.

Internal and external coordinates

The basis of the PBE assumes that the length scale of the discrete droplet phase is considerably smaller than the length scale associated with the continuous air phase. This is true for the spray we are modelling, as the atomised droplets are typically 10 – 600 µm in diameter [55, Chapter 4], [56], whilst the dried particles are in the range 100 – 2300 µm [57]. Both are considerably smaller than the height of the spray tower, which is in excess of 3 m. Here it is important to highlight the difference between internal and external droplet coordinates that will feature in our PBEs. External coordinates are those used to distinguish a droplet's position within the continuous air phase. In the spray model, the external coordinate used will simply be the vertical displacement in the tower, measured in metres, and given by the droplet's z-coordinate. Internal coordinates are those associated with the droplet itself. Here, the internal coordinate used will be the droplet's volume, denoted by x, and measured in μm^3. Subsequently, the droplet phase vector for

this model will only have one component, and this will be the droplet volume x. The domains of these internal and external variables will be the intervals Ω_x and Ω_z, respectively, where Ω_x represents the range of droplet volumes found in the spray and $\Omega_z = [z_0, L]$.

To specify the state of a droplet within our model, we require both its volume and location. Consequently, the droplet state domain is given by $\Omega_x \times \Omega_z$, with the droplet state coordinates taking the form (x, z).

Quantitative representations of the droplet population

The main quantity of interest will often be the total number of droplets of a particular volume, at a certain distance down the spray. To calculate this quantity, we assume there exists an average droplet number density function, n, defined on the particle state space, as outlined in [58]. Here, $n(x, z, t)$ is the number density function, for $x \in \Omega_x$, $z \in \Omega_z$ and time $t \geq 0$. The number density function itself represents the number of droplets of volume x, per unit droplet volume, per unit volume in space, at distance z down the spray, at time t. Subsequently, $n(x, z, t)$ has units of number, per (internal) droplet volume range, per (external) volume in space. Since internal droplet volume and external volume in space are measured in μm^3 and m^3, respectively, the number density will be in units $\mu m^{-3}\, m^{-3}$.

Another useful measure is the droplet number concentration, denoted by $N(x, z, t)$. This is defined by the formula

$$N(x, z, t) = \int_x^{x+\Delta x} n(\xi, z, t)\, d\xi, \tag{2.1}$$

and gives the number of droplets, at time t, with volume in $[x, x + \Delta x]$, per unit

volume of physical space. This number concentration has units of number per unit volume in space, i.e. m^{-3}.

The number of droplets with volume in $[x, x+\Delta x]$ and position in $[z, z+\Delta z]$ at time t, is then given by

$$\int_z^{z+\Delta z} A(\zeta) \int_x^{x+\Delta x} n(\xi, \zeta, t)\, d\xi d\zeta, \tag{2.2}$$

where

$$A(z) = \pi z^2 \big[\tan^2 \frac{\alpha}{2} - \tan^2 \frac{\beta}{2}\big] \tag{2.3}$$

is the cross-sectional area of the spray at position z. Alternatively, (2.2) may be calculated from the number concentration (2.1), by evaluating the integral

$$\int_z^{z+\Delta z} A(\zeta) N(x, \zeta, t) d\zeta. \tag{2.4}$$

The number density function also allows for the calculation of the total number of droplets in the entire system at time t. This is given by

$$\text{Total no. of drops at time } t = \int_{\Omega_z} \int_{\Omega_x} n(x, z, t) A(z)\, dx\, dz. \tag{2.5}$$

Droplet velocities

For simplicity, we will assume that the spray has reached steady state and that all droplets of a given volume x and position z have the same velocity for all time, denoted $\mathbf{v}(x, z)$. Thus, droplet velocity has no time dependence and is simply a function of droplet volume and position. It is assumed that the direction of this velocity lies along the spray sheet's centreline, halfway between the inner and outer

spray sheets, at an angle $\frac{\alpha+\beta}{4}$ to the z-axis, as illustrated in Figure 2.2.

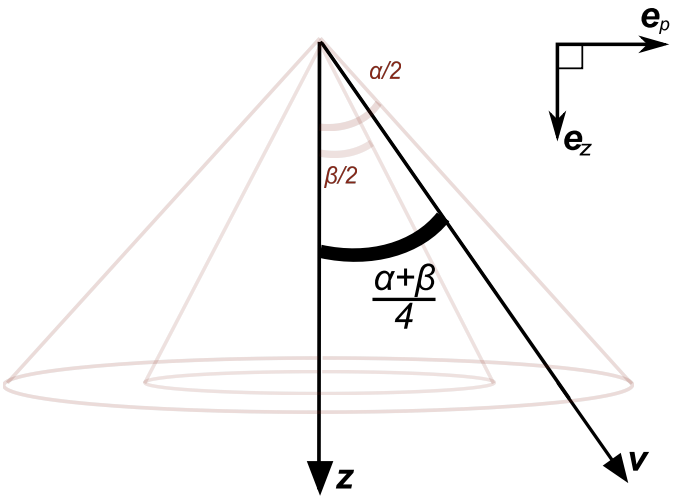

FIGURE 2.2: Illustration of the basis vectors $\mathbf{e_z}$ and $\mathbf{e_p}$ used to write the velocity vector $\mathbf{v}(x, z)$ in its component form.

.

As a vector in component form, the droplet velocity is written as

$$\mathbf{v}(x, z) = u(x, z)\mathbf{e}_z + w(x, z)\mathbf{e}_p, \tag{2.6}$$

where $\mathbf{e}_z$ and $\mathbf{e}_p$ are the vertical and horizontal basis vectors shown in Figure 2.2. Denoting the magnitude of the droplet velocity as

$$v(x, z) = |\mathbf{v}(x, z)|, \tag{2.7}$$

we can write

$$\mathbf{v}(x, z) = v(x, z)\Big[\cos\Big(\frac{\alpha+\beta}{4}\Big)\mathbf{e}_z + \sin\Big(\frac{\alpha+\beta}{4}\Big)\mathbf{e}_p\Big]. \tag{2.8}$$

Equating (2.6) and (2.8) shows that $u(x, z)$, the component of the droplet's velocity

in the z-direction, is

$$u(x,z) = v(x,z)\cos\Big(\frac{\alpha+\beta}{4}\Big). \tag{2.9}$$

The speed $u(x,z)$ will be referred to as the magnitude of axial velocity, and will later be used in the calculation of the droplet flux in the z-direction.

At the top of the spray, all droplets are assumed to be travelling at the same speed when they leave the nozzle and this speed will be denoted v_{inlet}. Likewise, all droplets will have the same axial velocity at the inlet, the magnitude of which will be denoted as u_0. The inlet axial velocity is determined by the pressure drop across the nozzle and the ratio of the nozzle orifice to air-core diameter, as outlined in [59]. The zero flux of droplets across the inner and outer surfaces of

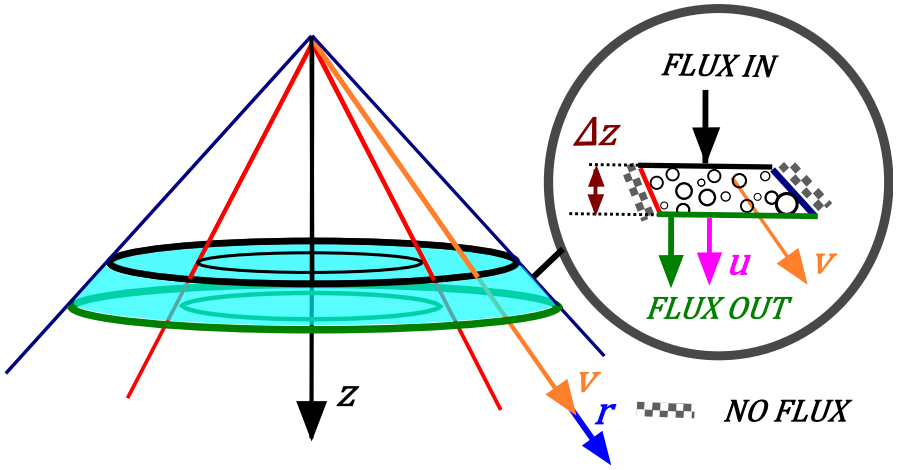

FIGURE 2.3: One of the modelling assumptions is that there is zero flux through the inner and outer surfaces of the spray, as pictured above.

.

the hollow cone, illustrated in Figure 2.3, follows from the previous assumption that all droplets are assumed to move in the direction of $\mathbf{v}(\mathbf{x},\mathbf{z})$, and agrees with that observed experimentally in [60].

2.1.2 Conservation equation for coagulation and transport within the spray

Now that the physical set-up and variables have been introduced, the next step is to construct an equation incorporating both coagulation and the movement of droplets down the spray, together with the spray's shape. This is done by looking at the conservation of droplets within a thin slice of the spray.

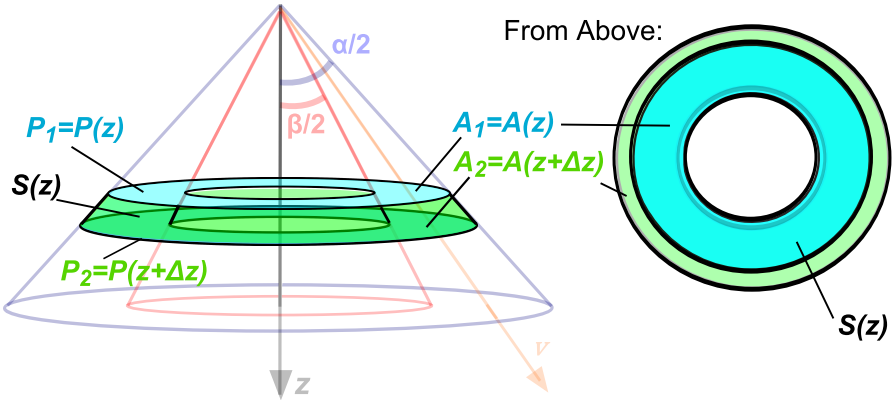

Figure 2.4: The change in droplet number concentration within the slice $S(z)$, due to coagulation and advection, is equal to the number flux of droplets into the slice through the plane P_1 minus the flux of droplets out of the slice through the plane P_2, plus the number born, and minus that lost, due to coagulation. The horizontal surface areas of the spray at planes P_1 and P_2 are given by A_1 and A_2 respectively, as illustrated.

The slice used in this derivation, labelled $S(z)$, is enclosed between the planes P_1 and P_2 in Figure 2.4. Here, $P(z)$ represents the horizontal, cross-sectional annular plane of the spray at distance z. We define planes $P_1 = P(z)$ and $P_2 = P(z + \Delta z)$ to be the upper and lower surfaces of the slice $S(z)$, respectively, and denote their corresponding cross-sectional areas as $A_1 = A(z)$ and $A_2 = A(z+\Delta z)$. As zero flux is assumed through the inner/outer surfaces of the hollow cone, all droplet movement must be across the planes P_1 and P_2, as illustrated in Figure

2.5.

The change in the number of droplets of volume x within this slice will be equal to the difference between the number of droplets transported into and out of the slice at P_1 and P_2 respectively, plus the number of new droplets of volume x born due to coagulation, minus the number of droplets of volume x lost due to coagulation with others.

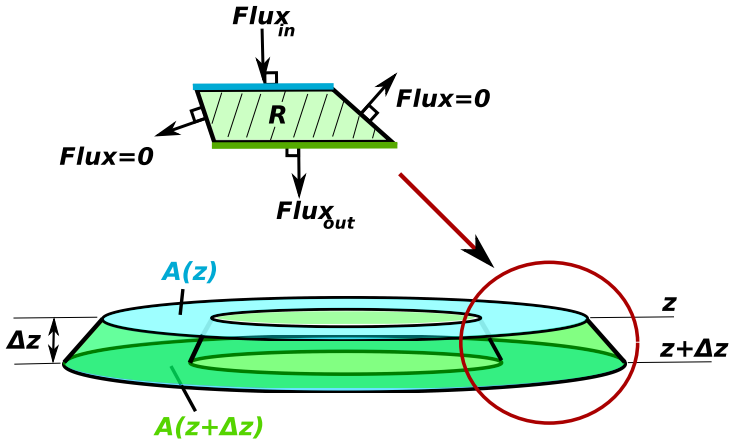

FIGURE 2.5: The slice $S(z)$ of the spray and the flux at each of its four different surfaces. The region R is a vertical cross-section of the slice S.

Let $f(x, z, t)$ denote the number density flux of droplets of volume x crossing the top surface P_1, at time t. That is,

$$f(x, z, t) = A(z)u(x, z)n(x, z, t), \tag{2.10}$$

which has units of number per droplet volume range, per unit time. The number of droplets with volume between x and $x + \Delta x$, entering the slice $S(z)$ through

the upper surface over a period of time, Δt, is then given by

$$\int_t^{t+\Delta t} \int_x^{x+\Delta x} f(\xi, z, \tau) d\xi d\tau. \tag{2.11}$$

Likewise, the number of these droplets exiting the slice through the lower surface P_2 is given by

$$\int_t^{t+\Delta t} \int_x^{x+\Delta x} f(\xi, z + \Delta z, \tau) d\xi d\tau. \tag{2.12}$$

Thus, the change in droplet number density within $S(z)$ due to advection is given by the difference between (2.11) and (2.12). This change is equal to

$$\int_t^{t+\Delta t} \int_x^{x+\Delta x} \Big(f(\xi, z, \tau) - f(\xi, z + \Delta z, \tau) \Big) d\xi d\tau. \tag{2.13}$$

The change in the number of droplets in the slice $S(z)$ over the same, small time period Δt is given by

$$\overbrace{\int_z^{z+\Delta z} \int_x^{x+\Delta x} A(\zeta)\, n(\xi, \zeta, t + \Delta t) d\xi d\zeta}^{\text{No. drops at time } t + \Delta t} - \overbrace{\int_z^{z+\Delta z} \int_x^{x+\Delta x} A(\zeta)\, n(\xi, \zeta, t) d\xi d\zeta}^{\text{No. drops at time } t}. \tag{2.14}$$

The expression in (2.14) must be equal to that in (2.13), plus the number of droplets born and lost due to coagulation. Hence, using the standard coagulation equation (1.15), but now allowing the coagulation kernel to be dependent on spatial position z, the change in the number of drops with volume between x and $x + \Delta x$

in the slice $S(z)$, due to coagulation over the same time period Δt, is given by

$$\int_t^{t+\Delta t}\int_z^{z+\Delta z}\int_x^{x+\Delta x} A(\zeta)\Big[\frac{1}{2}\int_0^{\xi} K(\xi-y,y,\zeta)n(\xi-y,\zeta,\tau)n(y,\zeta,\tau)dy - \int_0^{\infty} K(\xi,y,\zeta)n(\xi,\zeta,\tau)n(y,\zeta,\tau)dy\Big]d\xi d\zeta d\tau. \quad (2.15)$$

When combined, the expressions (2.13), (2.14) and (2.15) produce the conservation equation

$$\overbrace{\int_z^{z+\Delta z}\int_x^{x+\Delta x} A(\zeta)\,n(\xi,\zeta,t+\Delta t)d\xi d\zeta}^{\text{No. drops in } S(z) \text{ at time } t+\Delta t} - \overbrace{\int_z^{z+\Delta z}\int_x^{x+\Delta x} A(\zeta)n(\xi,\zeta,t)d\xi d\zeta}^{\text{No. drops in } S(z) \text{ at time } t} = \underbrace{\int_t^{t+\Delta t}\int_x^{x+\Delta x} f(\xi,z,\tau)d\xi d\tau}_{\text{No. drops entering slice}} - \underbrace{\int_t^{t+\Delta t}\int_x^{x+\Delta x} f(\xi,z+\Delta z,\tau)d\xi d\tau}_{\text{No. drops exiting slice}}$$
$$+ \overbrace{\int_t^{t+\Delta t}\int_z^{z+\Delta z}\int_x^{x+\Delta x} A(\zeta)\Big[\frac{1}{2}\int_0^{\xi} K(\xi-y,y,\zeta)n(\xi-y,\zeta,\tau)n(y,\zeta,\tau)dy}^{\text{No. drops born due to coagulation}} - \underbrace{\int_0^{\infty} K(\xi,y,\zeta)n(\xi,\zeta,\tau)n(y,\zeta,\tau)dy\Big]d\xi d\zeta d\tau}_{\text{No. drops lost due to coagulation}}. \quad (2.16)$$

Combining integrals in (2.16) gives

$$\int_z^{z+\Delta z}\int_x^{x+\Delta x} A(\zeta)\big[n(\xi,\zeta,t+\Delta t)-n(\xi,\zeta,t)\big]d\xi d\zeta = \int_t^{t+\Delta t}\int_x^{x+\Delta x}\big[f(\xi,z,\tau)-f(\xi,z+\Delta z,\tau)\big]d\xi d\tau + \int_t^{t+\Delta t}\int_z^{z+\Delta z}\int_x^{x+\Delta x} A(\zeta)\Big[\frac{1}{2}\int_0^{\xi} K(\xi-y,y,\zeta)n(\xi-y,\zeta,\tau)n(y,\zeta,\tau)dy - \int_0^{\infty} K(\xi,y,\zeta)n(\xi,\zeta,\tau)n(y,\zeta,\tau)dy\Big]d\xi d\zeta d\tau. \quad (2.17)$$

Assuming Δz, Δx and Δt are very small, each of the integral terms in (2.17) can be approximated as follows. For the term on the LHS, the transport term and the coagulation integral terms on the RHS, respectively, we have:

$$\int_z^{z+\Delta z}\int_x^{x+\Delta x} A(\zeta)\big[n(\xi,\zeta,t+\Delta t)-n(\xi,\zeta,t)\big]d\xi d\zeta \simeq A(z)\Big[n(x,z,t+\Delta t)-n(x,z,t)\Big]\Delta x\Delta z \ , \quad (2.18)$$

$$\int_t^{t+\Delta t}\int_x^{x+\Delta x} \big[f(\xi,z,\tau)-f(\xi,z+\Delta z,\tau)\big]d\xi d\tau \simeq \big[f(x,z,t)-f(x,z+\Delta z,t)\big]\Delta x\Delta t \ , \quad (2.19)$$

$$\begin{aligned}\text{and} \quad \int_t^{t+\Delta t}\int_z^{z+\Delta z}\int_x^{x+\Delta x} A(\zeta)\Big[\frac{1}{2}\int_0^{\xi} K(\xi-y,y,\zeta)n(\xi-y,\zeta,\tau)n(y,\zeta,\tau)dy \\ -\int_0^{\infty} K(\xi,y,\zeta)n(\xi,\zeta,\tau)n(y,\zeta,\tau)dy\Big]d\xi d\zeta d\tau \\ \simeq A(z)\big[\frac{1}{2}\int_0^{x} K(x-y,y,z)n(x-y,z,t)n(y,z,t)dy \\ -\int_0^{\infty} K(x,y,z)n(x,z,t)n(y,z,t)dy\big]\Delta x\Delta z\Delta t. \quad (2.20)\end{aligned}$$

Combining the approximations in (2.18), (2.19) and (2.20), equation (2.17) can be

approximated, to first-order, by

$$\begin{aligned}\frac{A(z)\times\big[n(x,z,t+\Delta t)-n(x,z,t)\big]}{\Delta t} &\\ = -\frac{\big[f(x,z+\Delta z,t)-f(x,z,t)\big]}{\Delta z}\big] &\\ + A(z)\Big[\frac{1}{2}\int_0^x K(x-y,y,z)n(x-y,z,\tau)n(y,z,\tau)dy &\\ -\int_0^\infty K(x,y,z)n(x,z,\tau)n(y,z,\tau)dy\Big]. \quad (2.21)\end{aligned}$$

Letting Δz and Δt tend to zero, and using (2.10), we arrive at the equation

$$\begin{aligned}\overbrace{\frac{\partial}{\partial t}\Big[A(z)n(x,z,t)\Big]}^{\text{Transport \& Spray Shape}} + \overbrace{\frac{\partial}{\partial z}\Big[A(z)u(x,z)n(x,z,t)\Big]}^{} &\\ = A(z)\times\Big[\underbrace{\frac{1}{2}\int_0^x K(x-y,y,z)n(x-y,z,t)n(y,z,t)\,dy}_{\text{Birth of droplets}} &\\ \underbrace{-\int_0^\infty K(x,y,z)n(x,z,t)n(y,z,t)\,dy}_{\text{Loss of droplets}}\Big]. \quad (2.22)\end{aligned}$$

This equation combines the movement of droplets within the spray, the spray shape and the effects of coagulation.

2.1.3 Airflow velocity

The air velocity profile within the spray dryer will generally be complicated and thus difficult to give an accurate mathematical representation. This is due to the fact that it will depend upon various different factors, such as the type and shape of air intakes, exhausts and dimensions of the tower used. It will also be affected by the flow of the spray, with momentum transfer between the droplets and the

gas flow, and there is also the fact that it may not be axially symmetric about the z axis. Interaction with the droplets may also lead to recirculating regions within the airflow close to the spray nozzle.

In this thesis, we will make use of three different approaches to define the airflow velocity mathematically. The simplest of these is to set the air velocity to be zero throughout the length of the spray. Secondly, the airflow velocity may be set to follow the axial velocity of a decaying jet, using the relation

$$u_{air}(z) = z_0 \times \frac{u_{air}(z_0)}{z}, \tag{2.23}$$

where $u_{air}(z)$ is the magnitude of air velocity at position z and z_0 is the point of complete sheet break up. Here, the airflow is assumed to be purely in the z-direction and the value of $u_{air}(z_0)$ is assumed to be known. The third approach used is to define the airflow velocity by fitting its magnitude to that observed using experimental data.

2.1.4 Equation for droplet velocities

To calculate droplet velocities within the spray, the approach used in [35, 61] is adopted. This approach assumes that the droplet velocity for each representative droplet size follows a time dependent force balance equation. In doing so, it is assumed that a droplet's deceleration is due to aerodynamic drag, buoyancy and gravity alone. The droplet velocities can then be defined in terms of a droplet's volume and position in the spray.

The droplet velocity equation is derived by considering the sum of all forces acting on a droplet of volume x at position z within the spray. This gives the

equation

$$\begin{aligned} \text{Droplet mass} \;\times\; \text{Droplet acceleration} &= \sum \text{Forces} \\ \implies \rho_{drop}\, x \times \frac{dv(x,z)}{dt} &= \sum \text{Forces}, \end{aligned} \tag{2.24}$$

where ρ_{drop} is the density of the droplets. We recall, from (2.7) and (2.9), that the magnitude of droplet velocity, and the component in the z-direction, are denoted by $v(x,z)$ and $u(x,z)$, respectively. Using these, the acceleration of a droplet of volume x can be written as

$$\frac{dv(x,z)}{dt} = \frac{\partial v(x,z)}{\partial z}\frac{dz}{dt} \;=\; u(x,z)\,\frac{\partial v(x,z)}{\partial z}. \tag{2.25}$$

Resolving (2.24) in the z-direction, and using the standard formulae for drag, buoyancy and gravitational forces, the vertical force balance equation is

$$\begin{aligned} &\rho_{drop}\, x \times u(x,z)\,\frac{\partial u(x,z)}{\partial z} \\ &\qquad = \overbrace{\frac{1}{2}\rho_{air} C_{D_x}(z)[\frac{\pi}{4}d^2(x)] \times (u(x,z) - u_{air}(z))|u(x,z) - u_{air}(z)|}^{\text{Drag}} \\ &\qquad\qquad + \underbrace{g\rho_{drop}\, x}_{\text{Gravity}} - \underbrace{g\rho_{air}\, x}_{\text{Buoyancy}}\ , \end{aligned} \tag{2.26}$$

where ρ_{air} is the density of the air, g is the magnitude of acceleration due to gravity and $d(x)$ is the diameter of a droplet of volume x. The term $C_{D_x}(z)$ is the coefficient of drag associated with a droplet of volume x, at position z and its value will depend upon the droplet's Reynolds number at that position within the spray. We define the Reynolds number for a droplet of volume x at position z, to

be

$$Re_x(z) = \frac{\rho_{air} d(x) \left| u(x,z) - u_{air}(z) \right|}{\mu}, \tag{2.27}$$

where μ is the dynamic viscosity of the air; see [62, 61]. The Reynolds number and drag coefficient are both functions of z, as they depend upon the droplet/air relative velocity which varies at different z positions within the spray.

For low Reynolds numbers ($Re_x(z) < 0.3$), the drag coefficient for a sphere is calculated via Stokes law as in [63] such that

$$C_{D_x}(z) = \frac{24}{Re_x(z)}. \tag{2.28}$$

When the droplet Reynolds number is intermediate ($0.3 \leq Re_x(z) \leq 500$), the drag coefficient is given by the Schiller-Naumann equation [61, 64] which states that

$$C_{D_x}(z) = \frac{24}{Re_x(z)}(1 + 0.15[Re_x(z)]^{0.687}). \tag{2.29}$$

Noting that the droplet volume x can be written in terms of the droplet diameter $d(x)$, as

$$x = \frac{\pi}{6}(d(x))^3, \tag{2.30}$$

equation (2.26) can be rewritten as

$$u(x,z)\,\frac{\partial u(x,z)}{\partial z} = \overbrace{-C_{D_x}(z)\frac{3}{4}\frac{\rho_{air}}{\rho_{drop}}\frac{(u(x,z)-u_{air}(z))|u(x,z)-u_{air}(z)|}{d(x)}}^{\text{Drag}} + \underbrace{g}_{\text{Gravity}} - \underbrace{\frac{g\,\rho_{air}}{\rho_{drop}}}_{\text{Buoyancy}}, \tag{2.31}$$

This is the governing equation we will use for droplet axial velocities within our model, and matches that found in [61].

It should be noted that we are assuming that droplets of the same volume all share the same velocity at a given distance down the spray. Likewise, the air velocity at a particular z point will be pre-defined and fixed under the steady-state assumption. Here, droplet collisions will have no effect on the droplet velocities and as such, in this model, there is no explicit mechanism for the conservation of droplet momentum.

2.1.5 Size and velocity dependent coagulation kernel

The coagulation kernel that we use is derived from the kinetic theory of gases and can be found in [61, 65]. The kernel takes into account both the total cross-sectional area available to a droplet for collisions and the relative velocity of colliding droplets.

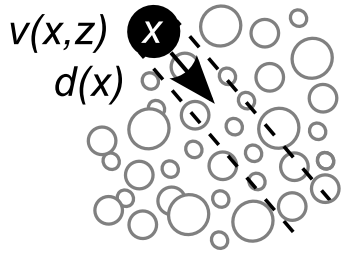

Figure 2.6: Illustration of the volume swept out (and hence available for collisions) by a droplet of diameter $d(x)$ travelling through a field of droplets with velocity $\mathbf{v}(x, z)$.

It is assumed that all droplets in the path swept out by a droplet are available for collision and possible coagulation. In Figure 2.6, we illustrate this path for a droplet of volume x, with diameter $d(x)$, travelling through a field of droplets with

velocity $\mathbf{v}(x, z)$.

The basic idea behind the derivation of the kernel is then as follows. When a droplet of volume x enters the slice $S(z)$, it is travelling with an initial velocity $\mathbf{v}(x, z)$ in the r-direction, as illustrated in Figures 2.3 and 2.4. Here, the r-direction is simply the centreline of the spray, at angle $\frac{\alpha+\beta}{4}$ to the z-axis. In the absence of any collisions, after a period of time Δt has elapsed, the droplet will have travelled a distance Δr, where

$$\Delta r = v(x, z)\Delta t, \tag{2.32}$$

and $v(x, z)$ is once again the magnitude of the velocity $\mathbf{v}(x, z)$. This assumes Δt is small enough that a constant velocity approximation is reasonable. Then, assuming all droplets are approximately spherical, with a droplet of volume x having diameter

$$d(x) = \Big(\frac{6x}{\pi}\Big)^{1/3}, \tag{2.33}$$

the volume, $\Delta V(x, z)$, that is swept out by such a droplet in time Δt can be approximated by

$$\Delta V(x, z) \simeq \frac{\pi}{4}\Big(d(x)\Big)^2 \underbrace{v(x, z)\Delta t}_{\Delta r}. \tag{2.34}$$

Subsequently, this can be rearranged to give

$$\frac{\Delta V(x, z)}{\Delta t} = \frac{\pi}{4}\Big(d(x)\Big)^2 v(x, z). \tag{2.35}$$

$$\implies \frac{\Delta V(x, z)}{\Delta z}\frac{\Delta z}{\Delta t} = \frac{\pi}{4}\Big(d(x)\Big)^2 v(x, z). \tag{2.36}$$

Then, on letting $\Delta t \to 0$, we obtain

$$\dot{V} = \frac{\partial V}{\partial z}\frac{dz}{dt} = \frac{\pi}{4}\Big(d(x)\Big)^2 v(x, z), \tag{2.37}$$

which is in agreement with [61].

If every droplet of volume x collides and agglomerates with every droplet of volume y found in the volume swept out along its flight path, then the agglomeration rate is simply the product $n(y,z,t)\dot{V}$ of the droplet number density $n(y,z,t)$ and the swept out volume. The total number of these collisions, accounting for every droplet of volume x in the flow, is then simply

$$\frac{1}{2}n(x,z,t)n(y,z,t)\dot{V}.$$

This is the number of collisions for one droplet, multiplied by the number density of droplets of volume x and divided by two. Here, the factor of $\frac{1}{2}$ is necessary to ensure each collision is counted only once.

The total number of collisions, $C(x,y,z)$, between droplets of volumes x and y in the slice $S(z)$ will thus depend upon the diameters $d(x)$ and $d(y)$, the relative velocity $v(x,z)-v(y,z)$, and the number densities $n(x,z,t)$ and $n(y,z,t)$. Basing the swept out volume $\dot{V}$ on that of a droplet of diameter $d(x)+d(y)$, we then have

$$\begin{aligned} C(x,y,z) &= \frac{1}{2}n(x,z,t)n(y,z,t)\ \times \dot{V} \\ &= \frac{1}{2}n(x,z,t)n(y,z,t)\ \times\ \frac{\pi}{4}(d(x)+d(y))^2|v(x,z)-v(y,z)|. \end{aligned} \quad (2.38)$$

If only a proportion λ^* of all collisions result in successful coagulation, then we modify (2.38) accordingly to arrive at the following expression for the rate of coagulation of droplets of volumes x and y at position z down the spray:

$$\frac{1}{2}\lambda^* n(x,z,t)n(y,z,t)\ \times\ \frac{\pi}{4}(d(x)+d(y))^2|v(x,z)-v(y,z)|. \quad (2.39)$$

Then, in keeping with the form of (2.22), the coagulation rate kernel we use is

$$K(x,y,z) = \frac{2\lambda^* C(x,y,z)}{n(x,z,t)n(y,z,t)} = \lambda^* \frac{\pi}{4}(d(x)+d(y))^2|v(x,z)-v(y,z)| \tag{2.40}$$

$$= \lambda\Big(x^{1/3}+y^{1/3}\Big)^2|v(x,z)-v(y,z)|, \tag{2.41}$$

where

$$\lambda = \lambda^* \pi^{1/3}(3/4)^{2/3}. \tag{2.42}$$

This kernel has units of volume in space per unit time. Subsequently, since we have opted to use different scales for the droplet diameters and spatial lengths, the parameter λ must have dimensions of spatial length scale squared per droplet length scale squared. Note that if the units chosen for the droplet length scale and the spatial length were the same, then λ would not need a scaling factor.

Throughout this thesis, λ will be set to be constant, however, in reality its value is likely to depend on the volume of the two droplets colliding.

2.2 Dimensionless model

Before investigating the modified coagulation equation (2.22) and transport equation (2.31), non-dimensional versions of these are derived using an approach similar to that found in [66]. Within the model we have constructed, there exist large variances in the scales used to quantify the different parameters. For example, the μm^3 scale associated with droplet volumes is around 10^9 times smaller than the m^3 scale associated with the spatial volume of the dryer tower itself. Thus, from solutions in a dimensional form, it may not be obvious how variations in one parameter affects the overall system. However, by converting the equation to a dimensionless

form, we reduce the complexity of the problem, and obtain a better insight into the fundamental scales within the system. In the simplified, non-dimensional form, it is also often easier to spot cases to which existing mathematical techniques may be applied to simplify the solution process.

In the case of this model, making the equations dimensionless allows an insight into which of the time-scales is the dominant time-scale for the system. That is, whether coagulation or advection is the dominant force influencing the droplet volume distribution throughout the spray.

2.2.1 Dimensionless coagulation-transport equation

The coagulation-transport equation (2.22) is non-dimensionalised using the dimensionless variables introduced below. The dimensionless form of each variable will be distinguished from the dimensional form by the use of an over-bar.

Since the spray is assumed to be in steady state, the inlet drop size distribution will be constant for all time. Hence, at the inlet, at position $z = z_0$, the total number of droplets and total volume of droplets (per unit volume in space) are given respectively by

$$N_0(t) = \int_0^\infty n(x, z_0, t)\, dx \ , \ V_0(t) = \int_0^\infty x\, n(x, z_0, t)\, dx. \tag{2.43}$$

Due to the steady state assumption, both of these are independent of time, t; i.e. $N_0(t) \equiv N_0$ and $V_0(t) \equiv V_0$ for all $t \geq 0$. Using (2.43), the mean droplet volume at the inlet is defined to be

$$x_0 = \frac{V_0}{N_0}. \tag{2.44}$$

This is then used to produce non-dimensional versions, $\bar{x}$ and $\bar{y}$, of the droplet

volume variables x and y, given by

$$x = x_0\bar{x} \quad \text{and} \quad y = x_0\bar{y}. \tag{2.45}$$

To non-dimensionalise the spatial variable, z, we use the length, L, of the spray, as described in Section 2.1.1, and define $\bar{z}$ via

$$z = L\bar{z}. \tag{2.46}$$

For the coagulation kernel, we set

$$K(x, y, z) = K_0\bar{K}(\bar{x}, \bar{y}, \bar{z}), \tag{2.47}$$

where

$$K_0 = \frac{1}{x_0^2}\int_0^\infty \int_0^\infty K(x, y, z_0 + \epsilon_z)\, dxdy \tag{2.48}$$

is the average rate of coagulation at distance $z_0 + \epsilon_z$ down the spray. We have assumed there is no coagulation at z_0 and so must use the $z_0 + \epsilon_z$ term ($\epsilon_z \ll 1$) to evaluate the average coagulation rate as close to the separation distance z_0 as possible.

For the droplet velocity, we set

$$u(x, z) = u_0\bar{u}(\bar{x}, \bar{z}), \quad v(x, z) = u_0\bar{v}(\bar{x}, \bar{z}), \tag{2.49}$$

where u_0 is the constant axial speed in the z-direction at which all droplets leave the spray nozzle.

To obtain an explicit form for $\bar{K}(\bar{x}, \bar{y}, \bar{z})$, we use (2.41), (2.47) and (2.49) to

write

$$\begin{aligned}\bar{K}(\bar{x},\bar{y},\bar{z}) &= \frac{1}{K_0}K(x_0\bar{x},x_0\bar{y},L\bar{z}) \\ &= \frac{\lambda}{K_0}x_0^{2/3}u_0(\bar{x}^{1/3}+\bar{y}^{1/3})^2|\bar{v}(\bar{x},\bar{z})-\bar{v}(\bar{y},\bar{z})|. \end{aligned} \tag{2.50}$$

Noting that

$$\begin{aligned}K_0 &= \frac{1}{x_0^2}\int_0^\infty\int_0^\infty K(x,y,z_0+\epsilon_z)\ dxdy \\ &= \frac{1}{x_0^2}\int_0^\infty\int_0^\infty K(x_0\bar{x},x_0\bar{y},L(z_0+\epsilon_z))x_0^2\ d\bar{x}d\bar{y} \\ &= \lambda u_0\int_0^\infty\int_0^\infty x_0^{2/3}(\bar{x}^{1/3}+\bar{y}^{1/3})^2|\bar{v}(\bar{x},\overline{z_0}+\overline{\epsilon_z})-\bar{v}(\bar{y},\overline{z_0}+\overline{\epsilon_z})|\ d\bar{x}d\bar{y} \\ &= \lambda u_0 x_0^{2/3}\int_0^\infty\int_0^\infty(\bar{x}^{1/3}+\bar{y}^{1/3})^2|\bar{v}(\bar{x},\overline{z_0}+\overline{\epsilon_z})-\bar{v}(\bar{y},\overline{z_0}+\overline{\epsilon_z})|\ d\bar{x}d\bar{y}, \end{aligned} \tag{2.51}$$

(2.50) reduces to

$$\bar{K}(\bar{x},\bar{y},\bar{z}) = C\times(\bar{x}^{1/3}+\bar{y}^{1/3})^2|\bar{v}(\bar{x},\bar{z})-\bar{v}(\bar{y},\bar{z})|, \tag{2.52}$$

where C is some constant.

The cross-sectional area of the spray is non-dimensionalised by setting

$$A(z) = A_L\bar{A}(\bar{z}), \tag{2.53}$$

where $A_L = A(L)$ is the cross-sectional area at the end of the spray. Recalling from (2.3) that

$$A(z) = \pi z^2\big[\tan^2\Big(\frac{\alpha}{2}\Big)-\tan^2\Big(\frac{\beta}{2}\Big)\big], \tag{2.54}$$

it follows that

$$\bar{A}(\bar{z}) = \frac{z^2}{L^2} = \bar{z}^2. \tag{2.55}$$

We note that $\frac{1}{N_0 K_0}$ and $\frac{L}{u_0}$ have units of time; the former being the time-scale associated with coagulation, whilst the latter is that associated with droplet advection. To non-dimensionalise the time variable, either one of these time-scales could be used. In order to determine which is the best choice, we would identify which of the time-scales is dominant within the spray. For example, if coagulation effects happen faster than advection can remove the droplets from the system, we will non-dimensionalise time using the coagulation time-scale.

Here, we assume coagulation is the dominant time-scale and, for the time variable, we set

$$t = \bar{t} \,/\, N_0 K_0, \tag{2.56}$$

and define the dimensionless number density $\bar{n}$ by

$$x_0 n(x, z, t) = N_0 \bar{n}(\bar{x}, \bar{z}, \bar{t}), \tag{2.57}$$

where N_0, K_0, x_0, $\bar{x}$ and $\bar{z}$ are as described above. We could equally have assumed that advection was the dominant time-scale, however, since we are interested in coagulation effects, we have chosen to use the corresponding timescale to non-dimensionalise the time variable. We also point out that, in terms of the dimensionless variables, the following relationships are true

$$\int_0^\infty \bar{n}(\bar{x}, \bar{z}, \bar{t}) \; d\bar{x} = 1, \;\; \text{and} \;\; \int_0^\infty \bar{x}\, \bar{n}(\bar{x}, \bar{z}, \bar{t}) \; d\bar{x} = \frac{V_0}{N_0 x_0} = 1. \tag{2.58}$$

From (2.46) and (2.56),

$$\frac{\partial}{\partial z} = \frac{\partial}{\partial \bar{z}}\frac{d\bar{z}}{dz} = \frac{1}{L}\frac{\partial}{\partial \bar{z}} \quad \text{and} \quad \frac{\partial}{\partial t} = \frac{\partial}{\partial \bar{t}}\frac{d\bar{t}}{dt} = N_0\, K_0 \frac{\partial}{\partial \bar{t}}.$$

Substituting these expressions into (2.22), and changing the limits on the y integrals, leads to the equation

$$\begin{aligned} N_0\, K_0 \frac{\partial}{\partial \bar{t}}\Big[A_L \bar{A}(\bar{z})\frac{N_0}{x_0}\bar{n}(\bar{x},\bar{z},\bar{t})\Big] \;+\; \frac{1}{L}\frac{\partial}{\partial \bar{z}}\Big[A_L \bar{A}(\bar{z}) u_0 \bar{u}(\bar{x},\bar{z})\frac{N_0}{x_0}\bar{n}(\bar{x},\bar{z},\bar{t})\Big] = \\ A_L \bar{A}(\bar{z}) \times \Big[\frac{1}{2}\int_0^{\bar{x}} K_0 \bar{K}(\bar{x}-\bar{y},\bar{y},\bar{z})\frac{N_0}{x_0}\bar{n}(\bar{x}-\bar{y},\bar{z},\bar{t})\frac{N_0}{x_0}\bar{n}(\bar{y},\bar{z},\bar{t})\, x_0 d\bar{y} \\ - \int_0^{\infty} K_0 \bar{K}(\bar{x},\bar{y},\bar{z})\frac{N_0}{x_0}\bar{n}(\bar{x},\bar{z},\bar{t})\frac{N_0}{x_0}\bar{n}(\bar{y},\bar{z},\bar{t})\, x_0 d\bar{y}\Big]. \end{aligned} \quad (2.59)$$

Grouping all the constants together, this becomes

$$\begin{aligned} \frac{A_L \bar{A}(\bar{z}) N_0^2 K_0}{x_0}\frac{\partial[\bar{n}(\bar{x},\bar{z},\bar{t})]}{\partial \bar{t}} + \frac{A_L u_0 N_0}{L x_0}\frac{\partial[\bar{A}(\bar{z})\bar{u}(\bar{x},\bar{z})\bar{n}(\bar{x},\bar{z},\bar{t})]}{\partial \bar{z}} = \\ A_L \bar{A}(\bar{z}) \times \frac{K_0 N_0^2}{x_0}\Big[\frac{1}{2}\int_0^{\bar{x}} \bar{K}(\bar{x}-\bar{y},\bar{y},\bar{z})\bar{n}(\bar{x}-\bar{y},\bar{z},\bar{t})\bar{n}(\bar{y},\bar{z},\bar{t})\, d\bar{y} \\ - \int_0^{\infty} \bar{K}(\bar{x},\bar{y},\bar{z})\bar{n}(\bar{x},\bar{z},\bar{t})\bar{n}(\bar{y},\bar{z},\bar{t})\, d\bar{y}\Big]. \end{aligned} \quad (2.60)$$

Simplifying (2.60), and using (2.55), produces the non-dimensional form of the coagulation-transport equation (2.22):

$$\begin{aligned} \frac{\partial}{\partial \bar{t}}\Big[\bar{z}^2 \bar{n}(\bar{x},\bar{z},\bar{t})\Big] + \frac{u_0}{N_0 K_0 L}\frac{\partial}{\partial \bar{z}}\Big[\bar{z}^2 \bar{u}(\bar{x},\bar{z})\bar{n}(\bar{x},\bar{z},\bar{t})\Big] = \\ \bar{z}^2 \times \Big[\frac{1}{2}\int_0^{\bar{x}} \bar{K}(\bar{x}-\bar{y},\bar{y},\bar{z})\bar{n}(\bar{x}-\bar{y},\bar{z},\bar{t})\bar{n}(\bar{y},\bar{z},\bar{t})\, d\bar{y} \\ - \int_0^{\infty} \bar{K}(\bar{x},\bar{y},\bar{z})\bar{n}(\bar{x},\bar{z},\bar{t})\bar{n}(\bar{y},\bar{z},\bar{t})\, d\bar{y}\Big]. \end{aligned} \quad (2.61)$$

Dropping the bars for notational convenience, (2.61) can be written as

$$\frac{\partial}{\partial t}\Big[z^2 n(x,z,t)\Big] + q_0 \frac{\partial}{\partial z}\Big[z^2 u(x,z) n(x,z,t)\Big] = z^2 \times \Big[\frac{1}{2}\int_0^x K(x-y,y,z)n(x-y,z,t)n(y,z,t)\,dy - \int_0^\infty K(x,y,z)n(x,z,t)n(y,z,t)\,dy\Big], \quad (2.62)$$

$$\text{where } x,\ y \in \Omega_x,\ z \in \Omega_z \text{ and } t \in [0,\infty),$$

$$q_0 = \frac{u_0}{N_0 K_0 L} \qquad \Big(= \frac{\text{Coagulation time-scale}}{\text{Advection time-scale}}\Big), \quad (2.63)$$

$$\text{and } K(x,y,z) = C \times (x^{1/3} + y^{1/3})^2 |v(x,z) - v(y,z)|. \quad (2.64)$$

Note that q_0 is the ratio of the two different time-scales associated with coagulation and advection. It is observed that if $q_0 \ll 1$, we have coagulation dominating. On the other hand, if $q_0 \gg 1$, the opposite is true and we have convection dominating.

2.2.2 Dimensionless velocity equation

The next step is to put the droplet velocity equation into a similar dimensionless form. Starting from equation (2.31), which stated that

$$u(x,z)\frac{\partial u(x,z)}{\partial z} = \overbrace{-C_{D_x}(z)\frac{3}{4}\frac{\rho_{air}}{\rho_{drop}}\frac{(u(x,z)-u_{air}(z))|u(x,z)-u_{air}(z)|}{d(x)}}^{\text{Drag}} + \overbrace{g}^{Gravity} - \overbrace{\frac{g\,\rho_{air}}{\rho_{drop}}}^{Buoyancy}, \quad (2.65)$$

it is clear that the ratio ρ_{air}/ρ_{drop} is already dimensionless. Similarly, the drag coefficient, C_{D_x}, is dimensionless by definition. The magnitude of acceleration due

to gravity, g, has units of length in space per unit time squared, $\mathrm{m\,s^{-2}}$, whilst the velocities $u(x,z)$ and $u_{air}(z)$ have units of length in space per unit time, $\mathrm{m\,s^{-1}}$.

First, we divide both sides of equation (2.65) by g to produce

$$\frac{u(x,z)}{g}\frac{\partial u(x,z)}{\partial z} = -C_{D_x}(z)\frac{3}{4}\frac{\rho_{air}}{\rho_{drop}}\frac{(u(x,z)-u_{air}(z))|u(x,z)-u_{air}(z)|}{g\,d(x)} + 1 - \frac{\rho_{air}}{\rho_{drop}}, \quad (2.66)$$

and note that the last two terms on the RHS are now dimensionless.

To eliminate the dimensions from the other terms, we introduce the following dimensionless variables. Again, the bar above the variable is used to distinguish the dimensionless form of a variable from the original. For the droplet velocity, we again use (2.49), and, for the air velocity, we set

$$u_{air}(z) = u_0\bar{u}_{air}(\bar{z}), \quad (2.67)$$

where u_0 is the axial speed at which all droplets are assumed to be travelling when they exit the nozzle and , as before, $z = L\bar{z}$.

To non-dimensionalise the droplet diameters, we use

$$d(x) = d(x_0\bar{x}) = \left(\frac{6}{\pi}x_0\bar{x}\right)^{1/3} = x_0^{1/3}d(\bar{x}), \quad (2.68)$$

where x_0 is the same mean droplet volume, per unit spatial volume, at z_0 as in (2.44).

To remove the dimensions from the gravity term, we set

$$gL = (u_0)^2\bar{g}, \quad (2.69)$$

Rewriting equation (2.66) in terms of the new dimensionless variables produces

$$\frac{Lu_0^2}{Lu_0^2}\frac{\bar{u}(\bar{x},\bar{z})}{\bar{g}}\frac{\partial}{\partial\bar{z}}\bar{u}(\bar{x},\bar{z}) = - C_{D_{[x_0\bar{x}]}}(L\bar{z})\frac{3}{4}\frac{\rho_{air}}{\rho_{drop}}\frac{L}{(x_0)^{1/3}}\frac{(\bar{u}(\bar{x},\bar{z})-\bar{u}_{air}(\bar{z}))|\bar{u}(\bar{x},\bar{z})-\bar{u}_{air}(\bar{z})|}{\bar{g}\,d(\bar{x})} + 1 - \frac{\rho_{air}}{\rho_{drop}}, \quad (2.70)$$

where

$$C_{D_{[x_0\bar{x}]}}(L\bar{z}) = \begin{cases} \frac{24}{Re_{[x_0\bar{x}]}(L\bar{z})} & \text{if } Re_{[x_0\bar{x}]}(L\bar{z}) < 0.3, \\ \frac{24}{Re_{[x_0\bar{x}]}(L\bar{z})}\Big(1+0.15\big[Re_{[x_0\bar{x}]}(L\bar{z})\big]^{0.687}\Big) & \text{if } 0.3 \le Re_{[x_0\bar{x}]}(L\bar{z}) \le 500. \end{cases} \quad (2.71)$$

Here, we have

$$Re_{[x_0\bar{x}]}(L\bar{z}) = \frac{\rho_{air}}{\mu}d(x_0\bar{x})|u(x_0\bar{x},L\bar{z})-u_{air}(L\bar{z})|. \quad (2.72)$$

This is only dimensionless, if x_0 and L share the same units. So to reach a fully dimensionless equation, we use the dimensionless terms $\bar{\mu}$ and $\bar{\rho}_{air}$, defined by $\mu = \rho_{air}u_0L\bar{\mu}$ and $\rho_{air} = \rho_{air}\bar{\rho}_{air}$, respectively, to remove dimensions from (2.72) (Note: by this definition, $\bar{\rho}_{air} \equiv 1$). This leads to

$$\begin{aligned} Re_{[x_0\bar{x}]}(L\bar{z}) &= \frac{\rho_{air}}{u_0L\rho_{air}\bar{\mu}}x_0^{1/3}d(\bar{x})u_0|\bar{u}(\bar{x},\bar{z})-\bar{u}_{air}(\bar{z})| \\ &= \frac{x_0^{1/3}}{L}\frac{d(\bar{x})|\bar{u}(\bar{x},\bar{z})-\bar{u}_{air}(\bar{z})|}{\bar{\mu}} \\ &= \frac{x_0^{1/3}}{L}\bar{R}e_{\bar{x}}(\bar{z}), \end{aligned}$$

where

$$\bar{R}e_{\bar{x}}(\bar{z}) = \frac{\bar{d}(\bar{x})|\bar{u}(\bar{x},\bar{z}) - \bar{u}_{air}(\bar{z})|}{\bar{\mu}}.$$

Subsequently, the coefficient of drag can now be written in dimensionless form as

$$\bar{C}_{D_{\bar{x}}}(\bar{z}) = \begin{cases} \frac{L}{x_0^{1/3}} \frac{24}{\bar{R}e_{\bar{x}}(\bar{z})} & \text{if } \frac{x_0^{1/3}}{L}\bar{R}e_{\bar{x}}(\bar{z}) < 0.3, \\ \frac{L}{x_0^{1/3}} \frac{24}{\bar{R}e_{\bar{x}}(\bar{z})}\Big(1 + 0.15\big[\frac{x_0^{1/3}}{L}\bar{R}e_{\bar{x}}(\bar{z})\big]^{0.687}\Big) & \text{if } 0.3 \leq \frac{x_0^{1/3}}{L}\bar{R}e_{\bar{x}}(\bar{z}) \leq 500. \end{cases} \tag{2.73}$$

Note that whilst the drag coefficient is usually dimensionless by definition, the fact that we have chosen two different length scales for z-displacement and droplet diameter (m and µm), means the dimensionless drag coefficient in (2.73) is necessary. If the two length scales for spatial length and droplet diameter are set to be the same, then the drag coefficient in (2.73) simply reduces to the normal drag coefficient equations, found in (2.28) and (2.29).

Dropping bars for all terms apart from $\bar{g}$, and rearranging, leads to the dimensionless equation

$$u(x,z)\frac{\partial}{\partial z}u(x,z) = -\frac{L}{x_0^{1/3}}C_{D_x}(z)\frac{3}{4}\frac{\rho_{air}}{\rho_{drop}}\frac{(u(x,z) - u_{air}(z))|u(x,z) - u_{air}(z)|}{d(x)} + \bar{g} - \bar{g}\,\frac{\rho_{air}}{\rho_{drop}}, \tag{2.74}$$

where $L/(x_0^{1/3})$ is the ratio of spatial and droplet length scales. As g is taken customarily to represent the usual gravitational constant, we retain the bar on the $\bar{g}$ terms.

Chapter 3

Analytical results for coagulation-transport equations

In the previous chapter, we established that the non-dimensional form of the PBE used to model the spray can be written as

$$\frac{\partial}{\partial t}\Big[z^2 n(x,z,t)\Big] + q_0 \frac{\partial}{\partial z}\Big[z^2 u(x,z) n(x,z,t)\Big] = z^2 \times \Big[\frac{1}{2}\int_0^x K(x-y,y,z) n(x-y,z,t) n(y,z,t)\, dy - \int_0^\infty K(x,y,z) n(x,z,t) n(y,z,t)\, dy\Big], \quad (3.1)$$

$$\text{where} \quad x,\, y \in \Omega_x, \quad z \in \Omega_z, \quad t \in [0,\infty), \quad q_0 = \frac{u_0}{N_0 K_0 L},$$

$$\text{and} \;\; K(x,y,z) = C \times (x^{1/3} + y^{1/3})^2 |v(x,z) - v(y,z)|; \quad (3.2)$$

see (2.62) - (2.64). In later chapters, the emphasis will be placed firmly on the application of appropriate numerical techniques to obtain information on the behaviour of solutions to (3.1). However, before we describe these numerical investigations, it is worth exploring the established analytical results on continuous

coagulation equations, to see if any of these can be applied to (3.1).

3.1 Coagulation-transport equation

On setting

$$c(x,z,t) = z^2 n(x,z,t), \text{ and} \tag{3.3}$$

$$k(x,y,z) = \frac{K(x,y,z)}{z^2} = \frac{C}{z^2}(x^{1/3}+y^{1/3})^2|v(x,z)-v(y,z)|, \tag{3.4}$$

equation (3.1) becomes

$$\frac{\partial}{\partial t}c(x,z,t) + q_0\cos\Big(\frac{\alpha+\beta}{4}\Big)\frac{\partial}{\partial z}\Big[v(x,z)c(x,z,t)\Big] = \frac{1}{2}\int_0^x k(x-y,y,z)c(x-y,z,t)c(y,z,t)\,dy - \int_0^\infty k(x,y,z)c(x,z,t)c(y,z,t)\,dy\,, \tag{3.5}$$

where we have used the fact that $u(x,z) = \cos\Big(\frac{\alpha+\beta}{4}\Big)v(x,z)$. Note that (3.5) is a spatially inhomogeneous coagulation equation incorporating (1-D) spatial transport. The cone angles α, β appear in the coefficient of the transport term, as do u_0, N_0, K_0, and L. Here, the terms α, β, u_0, N_0, K_0 and L are all input parameters for the model.

If we assume that $v(x,z)$ is known a priori, then there are some existence and uniqueness results within the literature that can be applied to equations of the form (3.5). However as far as we are aware, none of them deal with a spatially and size-dependent coagulation kernel such as (3.2).

A typical uniqueness/existence result is that given in [67, Chapter 11]. Here,

the spatially inhomogeneous equation that is considered takes the form

$$\frac{\partial}{\partial t}\, c(x,z,t) + \frac{\partial}{\partial x}\Big[r(x)c(x,z,t)\Big] + \operatorname{div}_z\Big(v(x,z)\, c(x,z,t)\Big) = \frac{1}{2}\int_0^x k(x-y,y)\, c(x-y,z,t)\, c(y,z,t)dy - c(x,z,t)\int_0^\infty k(x,y)\, c(y,z,t)dy, \quad (3.6)$$

where $r(x)$ is a rate of condensation. Here, z is not restricted to being a scalar variable, as it is in our model, and instead may represent any position in $3D$ space, such that $z \in \mathbb{R}^3$. However, as (3.6) uses a coagulation kernel $k(x,y)$ which does not depend on spatial position, the results in [67] are not directly applicable to equation (3.5).

Other existence/uniqueness results are provided in [68]. Here an equation incorporating coagulation, fragmentation and spatial diffusion is considered, and takes the form

$$\frac{\partial}{\partial t}\, c(x,z,t) + \mathcal{A}(x,z,t)c(x,z,t) = \frac{1}{2}\int_0^x k(x-y,y,z,t)\, c(x-y,z,t)\, c(y,z,t)dy - c(x,z,t)\int_0^\infty k(x,y,z,t)\, c(y,z,t)dy + f(x,v,z,t) + h(x,z,t), \quad (3.7)$$

where $f(x,v,z,t)$ and $h(x,z,t)$ are fragmentation and source terms respectively.

Here,

$$\mathcal{A}(x,z,t)c \equiv -\operatorname{div}_z\Big(a(x,z,t)\operatorname{grad}_z c + \underline{a}(x,z,t)c\Big) + \underline{b}(x,z,t)\cdot\operatorname{grad}_z c + a_0(x,z,t)c,$$

where a is the diffusion matrix, $\underline{a}$ and $\underline{b}$ are drift vectors and a_0 is the absorption rate.

The general nature of equation (3.7) means that it does indeed include coagulation-transport equations with size and spatially dependent coagulation kernels as a specific case. However the existence/uniqueness results that are established require the coagulation kernel to be bounded, which is not the case for the kernel given by (3.2).

3.2 Steady-state equation

When we later solve equation (3.1) numerically, we assume that sufficient time has elapsed for a steady-state system to be achieved throughout the length of the spray. Thus, in this section, we investigate if there are any existing analytical results that may be used to support the assumption that such a steady-state solution to (2.62) may be achieved.

On setting the time derivative to zero in (3.5), we obtain the steady-state

equation

$$\frac{\partial}{\partial z}\Big(v(x,z)\,c_s(x,z)\Big) = \frac{1}{q_0\cos\Big(\frac{\alpha+\beta}{4}\Big)}\Big\{\frac{1}{2}\int_0^x k(x-y,y,z)\,c_s(x-y,z)\,c_s(y,z)dy - \int_0^\infty k(x,y,z)\,c_s(x,z)\,c_s(y,z)dy\Big\}, \quad (3.8)$$

where

$$k(x,y,z) = \frac{C}{z^2}(x^{1/3}+y^{1/3})^2|v(x,z)-v(y,z)|.$$

If we put $f(x,z) = v(x,z)c_s(x,z)$, (3.8) simplifies to

$$\frac{\partial}{\partial z}f(x,z) = \frac{1}{2}\int_0^x \widetilde{k}(x-y,y,z)\,f(x-y,z)\,f(y,z)dy - \int_0^\infty \widetilde{k}(x,y,z)\,f(x,z)\,f(y,z)dy, \quad (3.9)$$

where

$$\widetilde{k}(x,y,z) = \frac{\sec\Big((\alpha+\beta)/4\Big)}{q_0}\frac{k(x,y,z)}{v(x,z)\,v(y,z)} = \frac{C\,\sec\Big((\alpha+\beta)/4\Big)}{q_0 z^2}\frac{|v(x,z)-v(y,z)|(x^{1/3}+y^{1/3})^2}{v(x,z)\,v(y,z)}. \quad (3.10)$$

If we regard z as a "time-like" variable, then (3.9) can be regarded as a non-autonomous Smoluchowski equation, for which a small number of analytic results are available; for example, see [69, 70].

In [70], the coagulation-fragmentation equation considered takes the form

$$\frac{\partial f(x,t)}{\partial t} = \frac{1}{2}\int_0^x K(y, x-y, t) f(y,t) f(x-y,t) dy - f(x,t)\int_0^\infty K(x,y,t) f(y,t) dy + \text{fragmentation terms}, \quad (3.11)$$

where K is a time-dependent coagulation kernel. Under certain hypotheses, it is shown in [70] that a unique solution exists. However, whilst (3.9) may be obtained from (3.11) if fragmentation is set to zero, one of the hypotheses in [70] stipulates that the coagulation kernel is bounded. Since our kernel is unbounded, the results presented in [70] cannot be applied to our equation.

Similarly, in [69], the existence of a unique, global, non-negative solution to an equation of the form (3.11) is established. However, for the results in [69] to hold, the coagulation kernel is again required to be bounded. Subsequently, these results are also not applicable to our spray-drying coagulation model, due to our choice of kernel.

3.3 A simplified steady-state problem

In the previous section, we highlighted the fact that, to the best of our knowledge, existing analytic results on non-autonomous coagulation equations cannot be applied to the steady-state equation (3.8) because of the form of our coagulation kernel. However some progress can be made if we make an additional simplifying assumption on the velocity $v(x, z)$.

More specifically, suppose that $v(x,z)$ is separable and can be written as

$$v(x,z) = v_1(x)v_2(z), \quad \text{where} \quad v_1(x) > 0, \quad v_2(z) > 0, \quad \forall\, x, z.$$

Then, from (3.10), we obtain

$$\begin{aligned}\widetilde{k}(x,y,z) &= \frac{C\,\sec\Big((\alpha+\beta)/4\Big)}{q_0}\,\frac{(x^{1/3}+y^{1/3})^2|v_1(x)-v_1(y)|}{v_1(x)\,v_1(y)\,z^2 v_2(z)} \\ &= \widetilde{k}_1(x,y)\times\widetilde{k}_2(z),\end{aligned}$$

where

$$\widetilde{k}_1(x,y) = \frac{C\,\sec\Big((\alpha+\beta)/4\Big)}{q_0}\,\frac{(x^{1/3}+y^{1/3})^2|v_1(x)-v_1(y)|}{v_1(x)\,v_1(y)}, \tag{3.12}$$

and

$$\widetilde{k}_2(z) = \frac{1}{z^2 v_2(z)}. \tag{3.13}$$

The steady-state equation (3.9) is then

$$\begin{aligned}\frac{\partial}{\partial z}f(x,z) = \widetilde{k}_2(z)\Big\{\frac{1}{2}\int_0^x \widetilde{k}_1(x-y,y)f(x-y,z)f(y,z)dy \\ -\int_0^\infty \widetilde{k}_1(x,y)f(x,z)f(y,z)dy\Big\}.\end{aligned} \tag{3.14}$$

The benefit to be gained from having the steady-state equation in this form is that we can now rescale z to obtain an autonomous Smoluchowski equation. To achieve this, we set

$$s = \Theta(z) \equiv \int_{z_0}^{z} \widetilde{k}_2(\sigma)d\sigma, \tag{3.15}$$

and assume that $\widetilde{k}_2$ satisfies the following conditions:

1. $\widetilde{k}_2 \in \mathcal{C}\Big([z_0, \infty)\Big)$;

2. $\Theta(z) \to \infty$ as $z \to \infty$.

It follows that Θ is a strictly increasing, differentiable function from $[z_0, \infty)$ onto $[0, \infty)$. Consequently Θ is invertible, with inverse Θ^{-1} mapping $[0, \infty)$ onto $[z_0, \infty)$. We use Θ^{-1} to define a function ω by

$$\omega(x, s) = f(x, \Theta^{-1}(s)). \tag{3.16}$$

Given that f satisfies (3.14), it follows that

$$\begin{aligned}
\frac{\partial}{\partial s}\omega(x,s) &= \frac{\partial}{\partial s}\Big[f\Big((x, \Theta^{-1}(s)\Big)\Big] \\
&= \frac{\partial}{\partial z} f(x, \Theta^{-1}(s)) \frac{d}{ds}\Theta^{-1}(s) \\
&= \frac{\widetilde{k}_2(\Theta^{-1}(s))}{\frac{d\Theta}{dz}(\Theta^{-1}(s))}\Big\{\frac{1}{2}\int_0^x \widetilde{k}_1(x-y,y) f(x-y, \Theta^{-1}(s)) f(y, \Theta^{-1}(s)) dy \\
&\qquad\qquad - \int_0^\infty \widetilde{k}_1(x,y) f(x, \Theta^{-1}(s)) f(y, \Theta^{-1}(s)) dy\Big\} \\
&= \frac{\widetilde{k}_2(\Theta^{-1}(s))}{\widetilde{k}_2(\Theta^{-1}(s))}\Big\{\frac{1}{2}\int_0^x \widetilde{k}_1(x-y,y)\omega(x-y,s)\omega(y,s) dy \\
&\qquad\qquad - \int_0^\infty \widetilde{k}_1(x,y)\omega(x,s)\omega(y,s) dy\Big\}.
\end{aligned}$$

$$\begin{aligned}
\Rightarrow \frac{\partial}{\partial s}\omega(x,s) = \frac{1}{2}\int_0^x \widetilde{k}_1(x-y,y)\omega(x-y,s)\omega(y,s) dy \\
- \int_0^\infty \widetilde{k}_1(x,y)\omega(x,s)\omega(y,s) dy,
\end{aligned} \tag{3.17}$$

where $\widetilde{k}_1$ is given by (3.12). From (3.16), we also have that

$$\begin{aligned}\omega(x,s) = f(x,\Theta^{-1}(s)) &= v(x,\Theta^{-1}(s))\; c_s(x,\Theta^{-1}(s)) \\ &= (\Theta^{-1}(s))^2\; v(x,\Theta^{-1}(s))\; n_s(x,\Theta^{-1}(s)),\end{aligned} \tag{3.18}$$

where $n_s(x,z)$ is the steady-state solution to our original problem (3.1). We can then work backwards from any steady-state solution of (3.17) to get the corresponding steady-state solution to (3.1), using the relationship

$$\begin{aligned} n_s(x,\Theta^{-1}(s)) &= \frac{\omega(x,s)}{(\Theta^{-1}(s))^2\, v(x,\Theta^{-1}(s))} \\ \implies n_s(x,z) &= \frac{\omega(x,\Theta(z))}{z^2 v(x,z)}, \;\text{ where }\; \Theta(z) = \int_{z_0}^{z} \widetilde{k}_2(\sigma)\, d\sigma. \end{aligned}$$

Since equation (3.17) is an autonomous Smoluchowski equation, there are many more analytic results available; for example, see [71]. However, before these can be considered, we require some a priori information on the function v_1, since this features in the kernel $\widetilde{k}_2$. Even then, there is no guarantee that the kernel will satisfy the conditions under which the analytic results hold. However, if we make a further simplifying assumption, namely that the droplets in the tower are falling vertically at their terminal velocity, then the scaling theory, described briefly in Section 1.4.4, can be applied. This is explained in the next section.

3.4 Simpler model: droplets at terminal velocity

The steady-state equation can be simplified further if it is assumed that the droplets are falling at their terminal velocity within the dryer tower. This as-

sumption removes spatial z dependence from the droplet velocities, leaving us with velocities $U_{TERM}(x)$ that only depend upon droplet volume.

Here, we assume that, for z sufficiently large, the radial component of any droplet's trajectory is zero. Subsequently, for large z, the droplet will simply fall vertically downwards at its terminal velocity $U_{TERM}(x)$, as illustrated in Figure 3.1.

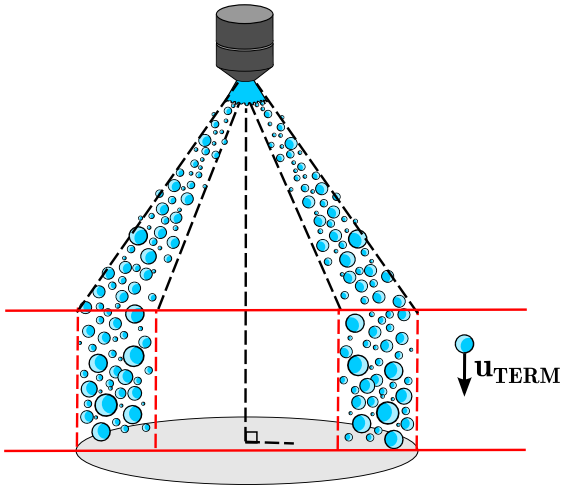

FIGURE 3.1: Illustration of the bell shape taken by a hollow conical spray as $z \to \infty$, and droplets simply fall vertically downwards, after a certain z position in space.

The terminal velocity of the droplets can be obtained by setting the spatial derivative to zero on the LHS of (2.74). This results in the following equation for U_{TERM}:

$$\begin{aligned} U_{TERM}(x) &= \sqrt{\frac{4}{3}\frac{x_0^{1/3}}{LC_{D_{x,TERM}}} g d(x) \left(1 + \frac{\rho_{air}}{\rho_{drop}}\right)} + u_{air} \\ &= \sqrt{\frac{4}{3}\frac{x_0^{1/3}}{LC_{D_{x,TERM}}} g \left(\frac{6x}{\pi}\right)^{1/3} \left(1 + \frac{\rho_{air}}{\rho_{drop}}\right)} + u_{air} \end{aligned}$$

where $C_{D_{x,TERM}}$ is the dimensionless drag coefficient of a droplet of volume x

travelling at its terminal velocity. For this particular case, we assume the air velocity u_{air} is constant. Subsequently, we can say that $U_{TERM}(x)$ behaves like $x^{1/6}$ for large x.

Since the droplets are now all falling vertically, the spray's cross-sectional area, $A(z)$, will be constant and therefore,

$$\exists z_1 : A(z) = A(z_1) = z_1^2 \ \forall \ z \geq z_1.$$

Thus, for $z \geq z_1$, equation (3.1) simply becomes

$$z_1^2 \frac{\partial}{\partial t}\Big[n(x,z,t)\Big] + q_0 z_1^2 U_{TERM}(x) \frac{\partial}{\partial z}\Big[n(x,z,t)\Big] = z_1^2 \times \Big[\frac{1}{2}\int_0^x K(x-y,y,z)n(x-y,z,t)n(y,z,t)\,dy - \int_0^\infty K(x,y,z)n(x,z,t)n(y,z,t)\,dy\Big]. \quad (3.19)$$

At steady state, let $n(x,z,t) = n_s(x,z)$ be the steady state droplet number density. Here, the time derivative is zero and the constants in (3.19) cancel out to give the steady state equation

$$\frac{\partial}{\partial z}\Big[U_{TERM}(x)n_s(x,z)\Big] = \frac{1}{q_0}\Big[\frac{1}{2}\int_0^x K(x-y,y,z)n_s(x-y,z)n_s(y,z)\,dy - \int_0^\infty K(x,y,z)n_s(x,z)n_s(y,z)\,dy\Big]. \quad (3.20)$$

If we then set $f(x,z) = U_{TERM}(x)n_s(x,z)$, we have the steady-state equation

$$\frac{\partial}{\partial z}f(x,z) = \Big[\frac{1}{2}\int_0^x \widetilde{k}_1(x-y,y)f(x-y,z)f(y,z)\,dy - \int_0^\infty \widetilde{k}_1(x,y)f(x,z)f(y,z)\,dy\Big], \quad (3.21)$$

$$\text{where} \quad \widetilde{k}_1(x,y) = \gamma \times (x^{1/3}+y^{1/3})^2 \frac{|U_{TERM}(x) - U_{TERM}(y)|}{U_{TERM}(x)U_{TERM}(y)}, \quad (3.22)$$

with

$$\gamma = \frac{C}{q_0}. \quad (3.23)$$

It follows that, for large droplet sizes, the coagulation kernel $\widetilde{k}_1$ behaves like

$$Q(x,y) = \gamma(x^{1/3}+y^{1/3})^2\,|y^{-1/6} - x^{-1/6}|. \quad (3.24)$$

Note that

$$Q(ax,ay) = a^{2/3-1/6}Q(x,y) = a^{1/2}Q(x,y),$$

and, for $y \gg x$,

$$Q(x,y) \propto y^{2/3}x^{-1/6}.$$

Consequently, Q is a kernel of the type considered in Section 1.4.4, and satisfies the assumptions (1.25) and (1.27) with $\lambda = \frac{1}{2}$, $\mu = -\frac{1}{6}$ and $\nu = \frac{2}{3}$. Also, since

$$Q(x,y) = \lim_{a\to\infty} a^{-1/2}\,\widetilde{k}_1(ax,ay),$$

$\widetilde{k}_1$ is asymptotically homogeneous of degree $\frac{1}{2}$ (see [48, p107]) and therefore the corresponding coagulation equation can be investigated using the scaling and self-similar solutions approach described in [48].

However, since our interests lie with the less specialised case of droplets falling non-vertically and at non-terminal velocities, we do not pursue this special case any further here.

In summary, due to the unbounded and spatially dependent nature of our coagulation kernel, we have shown that none of the existing analytic results for coagulation-fragmentation equations can be applied to our spray model. Instead, most of the existing work focuses on kernels that depend only upon the size of the coagulating droplets. This inevitably means that the results cannot be applied to spatially or temporally dependent kernels. There are a few results which are applicable to spatially and temporally dependent kernels, however all of these require the kernel to be bounded in nature, which ours is not. Even in the simplified case of a steady-state system, the established results once again specify that the kernel must be bounded. Subsequently, due to the absence of applicable analytic solutions, we now proceed to validate our model numerically in Chapter 4.

Chapter 4

Numerical techniques for coagulation-transport equations

This chapter introduces some numerical methods that have been specifically designed to handle coagulation and transport. We show how these techniques can be combined to discretise a general coagulation-transport equation of the form (2.62), given by the equation

$$\frac{\partial}{\partial t}\Big[A(z)n(x,z,t)\Big] + q_0\frac{\partial}{\partial z}\Big[A(z)u(x,z)n(x,z,t)\Big] = A(z)\times\Big[\frac{1}{2}\int_0^x K(x-y,y,z)n(x-y,z,t)n(y,z,t)\,dy - \int_0^\infty K(x,y,z)n(x,z,t)n(y,z,t)\,dy\Big],$$
$$x,\, y\, \in \Omega_x, \quad z \in \Omega_z, \quad t \in [0,\infty). \quad (4.1)$$

Once the discrete system of equations has been established, we go on to describe how they are solved numerically and illustrate the advantages of the methods we have chosen by solving a series of test problems. For these test cases, we focus our

attention on the specific case where $A(z) \equiv 1$ and $q_0 = 1$, as appropriate analytic solutions are available within the literature.

4.1 Numerical discretisation

4.1.1 Partitioned droplet size domain

In order to produce a discrete system of equations, the first step is to partition the droplet volume domain, Ω_x, as illustrated in Figure 4.1. The range between adjacent points, v_i and v_{i+1}, is referred to as the i^{th} cell and the droplet population in this cell is represented by a single volume x_i, such that $v_i < x_i < v_{i+1}$ and $1 \leq i \leq I$. Here v_1 and v_{I+1} correspond to the largest and smallest droplet volumes considered. The point x_i is termed the i^{th} pivot point or representative droplet volume and its value may be assigned differently depending on the numerical technique being used. Throughout the remainder of this thesis, we will simply set the pivot points to be the midpoints of the respective i^{th} cells.

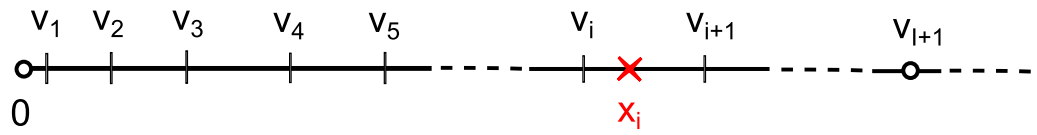

Figure 4.1: Partitioning of the droplet size domain. The i^{th} cell covers the range of droplet volumes between v_i and v_{i+1}, and v_{I+1} represents the largest droplet size considered.

The spacing of the points v_i is arbitrary and the following methods will work for any partition. These could be equally spaced along the droplet size domain;

however we have opted to use a geometric grid given by

$$v_{i+1} = r\, v_i, \tag{4.2}$$

where $r > 1$ is a constant grid ratio, and we set $v_1 = \epsilon$, where $\epsilon\,(> 0)$ is small. Careful choice of the constant r then allows the grid to be engineered to span a specific size range. Here, this range is from the smallest droplet volume v_1, up to the largest v_{I+1}. To achieve this, with a total of I grid points, the grid ratio is set to be

$$r = \left(\frac{v_{I+1}}{v_1}\right)^{1/I}. \tag{4.3}$$

Due to the decreased number of grid points needed to cover a given volume range, the use of a geometric grid proves less computationally expensive in comparison to a uniform grid. This will be especially relevant later, when applied to the droplet volumes within a spray dryer, as these will generally cover several orders of magnitude from around $15 - 2000\,\mu\text{m}$ in diameter. The geometric grid also allows for increased accuracy in the smaller droplet volume ranges, which will be covered by a finer resolution set of grid points. This is important, as it is anticipated that the vast majority of droplets will have volumes concentrated around the smaller volume size ranges.

4.1.2 Partitioned spatial domain

The next step is to partition the spatial domain, Ω_z. This is done using a uniform grid, which splits the range of dimensionless z values between $z = 0$ and $z = 1$ into J equal cells of size Δz. The j^{th} spatial cell, Ω_{z_j}, is then the range $z \in [z_{j-1/2}, z_{j+1/2}]$, where $z_{j-1/2}$ and $z_{j+1/2}$ are the cell boundaries. We assign z_j to be

the representative distance for Ω_{z_j}, and all droplets within the cell are assumed to be concentrated at this point in space. For simplicity, these z_j points are assigned to the cell midpoints. A non-uniform grid could also have been chosen, however we have opted to use a uniform grid for simplicity, and to minimise potential error due to numerical diffusion.

Combined with the discretised droplet volume range, we now have the grid upon which the general coagulation-transport equation (4.1) may be discretised. This grid is illustrated in Figure 4.2 and we use the notation Ω_{ij} to represent the domain of a grid cell such that

$$\begin{aligned} \Omega_{ij} \equiv & [v_i, v_{i+1}] \times [z_{j-1/2}, z_{j+1/2}], \\ & \text{where } \; i = 1, \ldots, I, \;\; \text{and } \; j = 1, \ldots, J. \end{aligned} \tag{4.4}$$

4.1.3 Discretisation of the coagulation-transport equation

Having defined the computational mesh, the aim is now to approximate the droplet number concentration in each of the grid cells Ω_{ij}. To achieve this, it is convenient to use a piecewise constant approximation to the number concentration in each cell, such that the number concentration at every distance in the cell Ω_{ij} is assumed to be approximately equal to the concentration at the cell centre z_j. The approximate number concentration $N_{ij}(t)$, in the cell Ω_{ij} at time t, then takes the form

$$N_{ij}(t) \simeq \int_{v_i}^{v_{i+1}} n(x, z_j, t) dx = N_i(z_j, t), \tag{4.5}$$

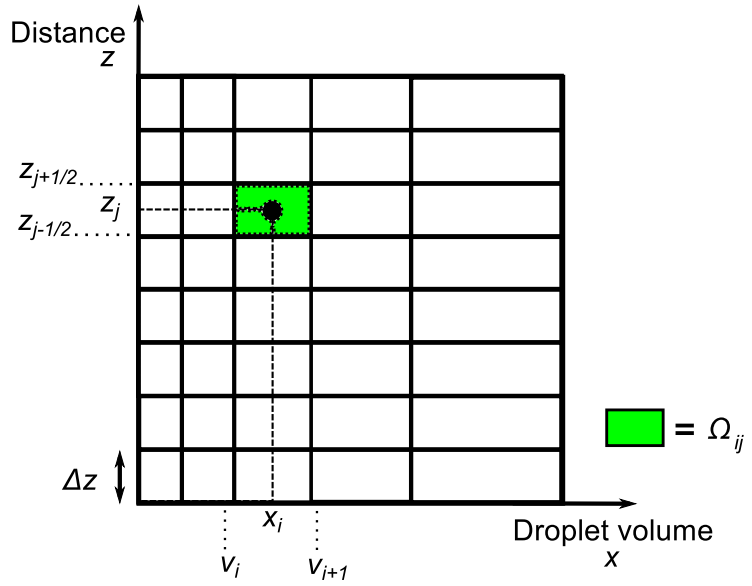

FIGURE 4.2: Computational mesh used to discretise the coagulation-transport equation (4.1). The cell with the black dot will be referred to as Ω_{ij}.

where $N_i(z,t)$ denotes the droplet number concentration in the droplet volume range $[v_i, v_{i+1}]$ at distance z down the spray at time t. By definition, $N_i(z,t)$ is given by

$$N_i(z,t) \equiv \int_{v_i}^{v_{i+1}} n(x,z,t)\,dx. \tag{4.6}$$

If we assume that all the droplets in the volume-range $[v_i, v_{i+1}]$ are concentrated at the representative volume x_i, then this allows us to approximate the droplet number density $n(x,z,t)$ over the i^{th} droplet volume cell by

$$n(x,z,t) \simeq \sum_{i=1}^{I} N_i(z,t)\delta(x_i - x). \tag{4.7}$$

This approximation will be a key step in producing a system of numerically tractable equations for $N_{ij}(t)$, as this will require a way of expressing the $n(x,z,t)$ terms of the governing equations as functions of the $N_{ij}(t)$ terms.

To begin, we take the general coagulation-transport equation, (4.1), and integrate over the grid cell Ω_{ij}, which results in the equation

$$\begin{aligned}
&\int_{z_{j-1/2}}^{z_{j+1/2}} \int_{v_i}^{v_{i+1}} \frac{\partial}{\partial t}\Big[A(z)n(x,z,t)\Big]\,dx\,dz \\
&\quad = \overbrace{\frac{1}{2}\int_{z_{j-1/2}}^{z_{j+1/2}} A(z) \int_{v_i}^{v_{i+1}} \int_0^x K(x-y,y,z)n(x-y,z,t)n(y,z,t)\,dy\,dx\,dz}^{\text{Influx of droplets due to coagulation}} \\
&\qquad \overbrace{-\int_{z_{j-1/2}}^{z_{j+1/2}} A(z) \int_{v_i}^{v_{i+1}} n(x,z,t) \int_0^\infty K(x,y,z)n(y,z,t)\,dy\,dx\,dz}^{\text{Outflux of droplets due to coagulation}} \\
&\qquad\qquad \underbrace{- q_0 \int_{z_{j-1/2}}^{z_{j+1/2}} \int_{v_i}^{v_{i+1}} \frac{\partial}{\partial z}\Big[A(z)u(x,z)n(x,z,t)\Big]\,dx\,dz}_{\text{Transport term: Loss/gain of droplets due to advection}}\,. \qquad (4.8)
\end{aligned}$$

We then note that the term on the left-hand side (LHS) of (4.8) can be written as

$$\int_{z_{j-1/2}}^{z_{j+1/2}} \int_{v_i}^{v_{i+1}} \frac{\partial}{\partial t}\Big[A(z)n(x,z,t)\Big]\,dx\,dz = \frac{d}{dt}\int_{z_{j-1/2}}^{z_{j+1/2}} A(z)N_i(z,t)\,dz. \qquad (4.9)$$

Using the midpoint rule for the z integral, leads to the approximation

$$\int_{z_{j-1/2}}^{z_{j+1/2}} \int_{v_i}^{v_{i+1}} \frac{\partial}{\partial t}\Big[A(z)n(x,z,t)\Big]\,dx\,dz \simeq \frac{d}{dt}\Big[V_j N_{ij}(t)\Big], \qquad (4.10)$$

where

$$V_j \equiv \Delta z A(z_j) \qquad (4.11)$$

is the approximate spatial volume of the system being modelled, lying within the spatial cell Ω_{z_j}. Using the expression in (4.10), equation (4.8) can now be written as

$$V_j \frac{dN_{ij}(t)}{dt} \simeq [\,B_{ij}(t) - D_{ij}(t)\,] - T_{ij}(t), \qquad (4.12)$$

where $B_{ij}(t)$, $D_{ij}(t)$ and $T_{ij}(t)$ are the birth, death and transport terms highlighted in (4.8). In what follows, approximations to these terms are calculated, and distinguished from the exact values by the use of an over tilde, i.e. $\widetilde{B}_{ij}(t)$, $\widetilde{D}_{ij}(t)$ and $\widetilde{T}_{ij}(t)$.

In (4.12), we now have an equation where $N_{ij}(t)$ appears on the LHS but not on the RHS and as such, cannot be solved for $N_{ij}(t)$ without first rewriting the birth, death and transport terms on the RHS in terms of $N_{ij}(t)$. To achieve this, we make use of the approximation in (4.7), among others, to convert the birth, death and transport terms into functions of $N_{ij}(t)$ that can then be combined and allow (4.8) to be solved numerically.

4.1.4 The Kurganov-Tadmor scheme for the transport term

We first consider the transport term in equation (4.8)

$$T_{ij}(t) = q_0 \int_{z_{j-1/2}}^{z_{j+1/2}} \int_{v_i}^{v_{i+1}} \frac{\partial}{\partial z}\Big[A(z)u(x,z)n(x,z,t)\Big]dxdz,$$

which we want to rewrite in terms of $N_{ij}(z,t)$. We can use the discrete approximation for $n(x,z,t)$ and $u(x,z)$ to approximate $T_{ij}(t)$ as

$$T_{ij}(t) \simeq q_0 \int_{z_{j-1/2}}^{z_{j+1/2}} \frac{\partial}{\partial z}\Big[A(z)u_i(z)N_i(z,t)\Big]dz, \tag{4.13}$$

where

$$u_i(z) \equiv u(x_i, z) \tag{4.14}$$

is the velocity of a droplet of volume x_i at distance z. Carrying out the integration in (4.13) leads to the equation

$$T_{ij}(t) \simeq q_0 A(z_{j+1/2}) u_i(z_{j+1/2}) N_i(z_{j+1/2}, t) - q_0 A(z_{j-1/2}) u_i(z_{j-1/2}) N_i(z_{j-1/2}, t). \tag{4.15}$$

The RHS of (4.15) is simply the difference between the number flux of droplets into and out of the cell Ω_{ij} due to advection. However, due to the way we have set up our computational mesh, the droplet number concentrations at the cell edges, $N_i(z_{j\pm1/2}, t)$, are currently unknown.

This is overcome by using the upwind, central differencing scheme of Kurganov and Tadmor [72]. The technique is a modification of the Nessyahu-Tadmor scheme [73] and satisfies the total variation diminishing property [74]. The scheme allows us to approximate the fluxes at the cell edges, using the information about the droplet number concentration from the cell centres, and is implemented as follows. By setting

$$\phi(z,t) = A(z) N_i(z,t) \quad \text{and} \quad f(z, \phi(z,t)) = q_0 u_i(z) \phi(z,t), \tag{4.16}$$

equation (4.15) can be rewritten as

$$\begin{aligned} T_{ij}(t) &\simeq f\Big(z_{j+1/2}, \phi(z_{j+1/2}, t)\Big) - f\Big(z_{j-1/2}, \phi(z_{j-1/2}, t)\Big), \\ &\simeq F_{j+1/2}(t) - F_{j-1/2}(t), \end{aligned} \tag{4.17}$$

where the numerical flux terms $F_{j\pm1/2}(t)$ are defined as

$$F_{j\pm1/2}(t) = \frac{1}{2}[f(z_{j\pm1/2}, \phi^{+}_{j\pm1/2}(t)) + f(z_{j\pm1/2}, \phi^{-}_{j\pm1/2}(t))] - \frac{a_{j\pm1/2}(t)}{2}[\phi^{+}_{j\pm1/2}(t) - \phi^{-}_{j\pm1/2}(t)]. \quad (4.18)$$

Here, $a_{j\pm1/2}(t)$ is the maximal local speed of propagation at the cell boundary $z_{j\pm1/2}$. Since we know the droplet velocities and number concentrations at the cell centres, intermediate values $\phi^{\pm}_{j+1/2}(t)$ are given by the equations

$$\phi^{+}_{j+1/2}(t) = \phi_{j+1}(t) - \frac{\Delta z}{2}\Big(\frac{\partial \phi}{\partial z}\Big)\Big|_{z_{j+1}},$$

and

$$\phi^{-}_{j+1/2}(t) = \phi_{j}(t) + \frac{\Delta z}{2}\Big(\frac{\partial \phi}{\partial z}\Big)\Big|_{z_{j}}. \quad (4.19)$$

These intermediate values $\phi^{+}_{j+1/2}(t)$ and $\phi^{-}_{j+1/2}(t)$ are slope limited extrapolations, approximating the value of $\phi(z_{j+1/2}, t)$, using the known droplet velocity and number density information from the cell centres z_j and z_{j+1}, respectively. Approximations to the spatial derivatives used in (4.19), are then given by the formula

$$\Big(\frac{\partial \phi}{\partial z}\Big)\Big|_{z_j} := \text{minmod}\Big(\theta\frac{\phi_j - \phi_{j-1}}{\Delta z}, \frac{\phi_{j+1} - \phi_{j-1}}{2\Delta z}, \theta\frac{\phi_{j+1} - \phi_j}{\Delta z}\Big), \quad (4.20)$$

where $1 \leq \theta \leq 2$, and the multivariable min-mod slope limiter function takes the form

$$\text{minmod}(x_1, x_2, ...) = \begin{cases} \min\{x_j\} & \text{if } x_j > 0 \quad \forall j, \\ \max\{x_j\} & \text{if } x_j < 0 \quad \forall j, \\ 0, & \text{otherwise.} \end{cases} \tag{4.21}$$

The local speed of propagation at the cell boundaries, $a_{j+1/2}(t)$, is then calculated as

$$a_{j+1/2}(t) := \max\Big[\Big(\frac{\partial f}{\partial \phi}(z_{j+1/2}, \phi^+_{j+1/2}(t))\Big), \Big(\frac{\partial f}{\partial \phi}(z_{j-1/2}, \phi^-_{j+1/2}(t))\Big)\Big].$$

In our case,

$$a_{j+1/2}(t) = \left.\frac{\partial f}{\partial \phi}\right|_{z_j} = q_0 u_i(z_j). \tag{4.22}$$

Putting the above together, the discrete transport term is simply

$$\widetilde{T}_{ij}(t) = F_{j+1/2}(t) - F_{j-1/2}(t), \tag{4.23}$$

where the numerical flux terms, $F_{j\pm1/2}(t)$, are defined in (4.18).

Whilst we have chosen to use the Kurganov-Tadmor scheme for this approximation, there are many other existing techniques that could have been used here. These include first-order upwinding, the Lax-Friedrichs scheme, and second-order methods such as the Beam-Warming or Lax-Wendroff method [75, 76, 77]. In later sections, we will perform some numerical experiments to demonstrate why we have made this choice.

4.1.5 Discrete death term

We now consider how to discretise the birth and death terms in equation (4.8), starting with the death term

$$D_{ij}(t) = -\int_{z_{j-1/2}}^{z_{j+1/2}} A(z) \int_{v_i}^{v_{i+1}} n(x,z,t) \int_0^\infty K(x,y,z) n(y,z,t)\, dy\, dx\, dz. \quad (4.24)$$

Approximating the z integral using the midpoint rule, this term becomes

$$D_{ij}(t) \simeq -\overbrace{(z_{j+1/2} - z_{j-1/2}) A(z_j)}^{=V_j} \int_{v_i}^{v_{i+1}} n(x,z_j,t) \int_0^\infty K(x,y,z_j) n(y,z_j,t)\, dy\, dx. \quad (4.25)$$

The y integral can be written as a sum of integrals so that

$$D_{ij}(t) \simeq -V_j \int_{v_i}^{v_{i+1}} \Big[n(x,z_j,t) \sum_{k=1}^{I} \int_{v_k}^{v_{k+1}} K(x,y,z_j) n(y,z_j,t)\, dy \Big] dx. \quad (4.26)$$

Here, the summation up to $i = I$ is to account for v_{i+1} being the largest droplet volume in the system. Replacing the $n(x,z_j,t)$ terms by the approximation given in (4.7), we obtain the new approximation

$$\widetilde{D}_{ij}(t) = -V_j \sum_{k=1}^{I} K_{i,j,k} N_i(z_j,t) N_k(z_j,t), \quad (4.27)$$

where

$$K_{i,j,k} = K(x_i, x_j, z_k).$$

4.1.6 Discrete birth term

We next consider the birth term in (4.8),

$$B_{ij}(t) = \frac{1}{2}\int_{z_{j-1/2}}^{z_{j+1/2}} A(z) \int_{v_i}^{v_{i+1}} \int_0^x K(x-y,y,z)n(x-y,z,t)n(y,z,t)\,dy\,dx\,dz. \tag{4.28}$$

Using the midpoint rule for the z integration,

$$B_{ij}(t) \simeq \frac{1}{2}\overbrace{(z_{j+1/2}-z_{j-1/2})A(z_j)}^{=V_j} \int_{v_i}^{v_{i+1}} \int_0^x K(x-y,y,z_j)n(x-y,z_j,t)n(y,z_j,t)\,dy\,dx. \tag{4.29}$$

Splitting the y integral into the sum of two separate integrals, we obtain

$$\begin{aligned} B_{ij}(t) \simeq \frac{V_j}{2}\Big[&\int_{v_i}^{v_{i+1}} \int_0^{v_i} K(x-y,y,z_j)n(x-y,z_j,t)n(y,z_j,t)\,dy\,dx \\ &+ \int_{v_i}^{v_{i+1}} \int_{v_i}^{x} K(x-y,y,z_j)n(x-y,z_j,t)n(y,z_j,t)\,dy\,dx\Big], \end{aligned} \tag{4.30}$$

which is then rewritten, with the first y integral replaced by the corresponding sum of integrals, such that

$$\begin{aligned} B_{ij}(t) \simeq \frac{V_j}{2}\Big[&\int_{v_i}^{v_{i+1}} \Big[\sum_{k=1}^{i-1} \int_{v_k}^{v_{k+1}} K(x-y,y,z_j)n(x-y,z_j,t)n(y,z_j,t)\,dy\Big]\,dx \\ &+ \int_{v_i}^{v_{i+1}} \int_{v_i}^{x} K(x-y,y,z_j)n(x-y,z_j,t)n(y,z_j,t)\,dy\,dx\Big]. \end{aligned} \tag{4.31}$$

Replacing the $n(x,z_j,t)$ terms by the approximation

$$n(x,z_j,t) \simeq \sum_{l=1}^{I} N_l(z_j,t)\delta(x-x_l), \tag{4.32}$$

we obtain the approximation to the birth term

$$\widetilde{B}_{ij}(t) = \frac{V_j}{2}\Big[\int_{v_i}^{v_{i+1}}\Big[\sum_{k=1}^{i-1}\int_{v_k}^{v_{k+1}} K(x-y,y,z_j)\times\sum_{l=1}^{I}[N_l(z_j,t)\delta(x-y-x_l)] \times\sum_{m=1}^{I}[N_m(z_j,t)\delta(y-x_m)]\,dy\Big]\,dx + \int_{v_i}^{v_{i+1}}\int_{v_i}^{x} K(x-y,y,z_j)\times\sum_{l=1}^{I}[N_l(z_j,t)\delta(x-y-x_l)] \times\sum_{m=1}^{I}[N_m(z_j,t)\delta(y-x_m)]\,dy\,dx\Big]. \quad (4.33)$$

As with the transport term, the tilde over the variable is used to emphasise that this is now an approximation to the birth term.

To allow us to simplify (4.33), we change the order of integration for the second integral term so that

$$\widetilde{B}_{ij}(t) = \frac{V_j}{2}\Big[\int_{v_i}^{v_{i+1}}\Big[\sum_{k=1}^{i-1}\int_{v_k}^{v_{k+1}} K(x-y,y,z_j)\times\sum_{l=1}^{I}[N_l(z_j,t)\delta(x-y-x_l)] \times\sum_{m=1}^{I}[N_m(z_j,t)\delta(y-x_m)]\,dy\Big]\,dx + \int_{v_i}^{v_{i+1}}\int_{y}^{v_{i+1}} K(x-y,y,z_j)\times\sum_{l=1}^{I}[N_l(z_j,t)\delta(x-y-x_l)] \times\sum_{m=1}^{I}[N_m(z_j,t)\delta(y-x_m)]\,dx\,dy\Big]. \quad (4.34)$$

Now applying the sifting property of the Dirac-delta function to the integrals in (4.34), we have that

$$\widetilde{B}_{ij}(t) = \frac{V_j}{2}\Big[\int_{v_i}^{v_{i+1}}\Big[\sum_{k=1}^{i-1} K(x-x_k, x_k, z_j)\times\sum_{l=1}^{I}[N_l(z_j,t)\delta(x-x_k-x_l)]\times N_k(z_j,t)\Big]\,dx + \int_{v_i}^{v_{i+1}} K(x-x_i, x_i, z_j)\times\sum_{l=1}^{I}[N_l(z_j,t)\delta(x-x_i-x_l)]\times N_i(z_j,t)dx\Big]. \quad (4.35)$$

To proceed further, it is noted that

$$\int_{v_i}^{v_{i+1}}\delta(x-x_j-x_k)dx = \int_{v_i}^{v_{i+1}}\delta(x-(x_j+x_k))dx = \begin{cases} 1, \text{ if } x_j+x_k \in [v_i, v_{i+1}], \\ 0, \text{ if } x_j+x_k \notin [v_i, v_{i+1}], \end{cases}$$

and, as such, we only get a contribution to the birth term from the first integral when $x_k + x_l \in [v_i, v_{i+1}]$. Likewise, in the second integral, we only get a contribution to the birth term when $x_i + x_l \in [v_i, v_{i+1}]$. Thus the birth term from (4.35) can be simplified to

$$\widetilde{B}_{ij}(t) = \frac{V_j}{2}\Big[\sum_{k=1}^{i-1} N_k(z_j,t)\underbrace{\sum_{v_i\le x_k+x_l<v_{i+1}}}_{\text{Sum over } l=1 \text{ to } I.} K(x_l, x_k, z_j)N_l(z_j,t) + \underbrace{\sum_{v_i\le x_k+x_l<v_{i+1}}}_{\text{Sum over } l=1 \text{ to } I.} K(x_l, x_i, z_j)N_l(z_j,t)N_i(z_j,t)\Big]. \quad (4.36)$$

We can then add the two terms on the RHS of (4.36) together, being careful not to count terms twice. Since $K(x_k, x_j, z_j)$ is symmetric ($K(x_k, x_j, z_j) = K(x_j, x_k, z_j)$), each term $K(x_k, x_j, z_j)N_j(z_j,t)N_k(z_j,t)$ has a corresponding identical term $K(x_j, x_k, z_j)N_k(z_j,t)N_j(z_j,t)$ except for the case when $l = k$. Thus if we add

the two sum terms on the RHS of (4.36) and specify that $l \geq k$, then we avoid counting these identical terms twice. However, we still end up double counting the terms where $l = k$ and so these terms need to be removed. This is done using the Kronecker delta term, $\delta_{l,k}$, to remove the duplicates and (4.36) becomes

$$\begin{aligned} \widetilde{B}_{ij}(t) &= V_j \sum_{v_i \leq x_k + x_l < v_{i+1}}^{l \geq k} (1 - \frac{1}{2}\delta_{l,k}) K(x_l, x_k, z_j) N_l(z_j, t) N_k(z_j, t), \\ \implies \widetilde{B}_{ij}(t) &= V_j \sum_{v_i \leq x_k + x_l < v_{i+1}}^{l \geq k} (1 - \frac{1}{2}\delta_{l,k}) K_{l,k,j} N_{l,j}(t) N_{k,j}(t). \end{aligned} \tag{4.37}$$

From this point, there are a number of different numerical methods that we could use to proceed, such as the fixed pivot method of [78] or a finite volume scheme as used in [79]. However, on weighing up the advantages and disadvantages of the available methods, we have chosen to use the cell average technique proposed in [80]. Whilst the fixed pivot is currently the most widely used of all existing techniques, the cell average technique provides a more accurate prediction of the number density of larger droplet sizes and so it is the best choice for our model. Both these sectional methods are more general and flexible than the other existing discretised techniques in the literature, with each allowing for any choice of numerical grid, being compatible with both multiple and binary coagulation and allowing the accurate evolution of any two desired moments of choice.

Before we focus our efforts on the cell average technique, we will quickly outline the fundamental difference between the two schemes and the effect this subtle change has on the predictions of droplet number density and integral moments obtained from each method.

4.1.7 Sectional methods

The cell average and fixed pivot techniques are sectional methods developed specifically for application to coagulation and fragmentation processes. Both are designed to work with a general partition of the droplet size domain, and each aims to accurately evolve any two desired moments of the droplet volume distribution. The fundamental difference between the two techniques is simply the way in which the birth term is handled. Rather than assuming all droplets born in the range v_i to v_{i+1} are of size x_i, the methods distribute a fraction of these newborn droplets to each of the neighbouring representative volumes. However, they both perform this distribution slightly differently, and this subtle difference has a significant effect on the subsequent predictions made by each method.

The cell average technique was developed by Kumar et al. [80] as a more accurate evolution of its predecessor the fixed pivot method [78]. Using the fixed pivot method, *each newborn droplet* within a cell is considered separately and a fraction of that droplet is allocated to each of the neighbouring pivot points, so that the two desired moments of the droplet size distribution are evolved accurately. These pivot points are assigned to be the representative droplet volumes, x_i. The idea behind the cell average technique is to calculate the *average* volume of *ALL* newborn droplets within a cell and to assign a fraction of this *average droplet volume* to the neighbouring representative volumes such that any two properties of interest can be accurately evolved. In the case of the spray drier model, the two properties of interest we want to evolve accurately are the total mass of the system and the droplet number density.

When using the cell average technique, the net birth in Ω_{x_i}, the i^{th} droplet volume

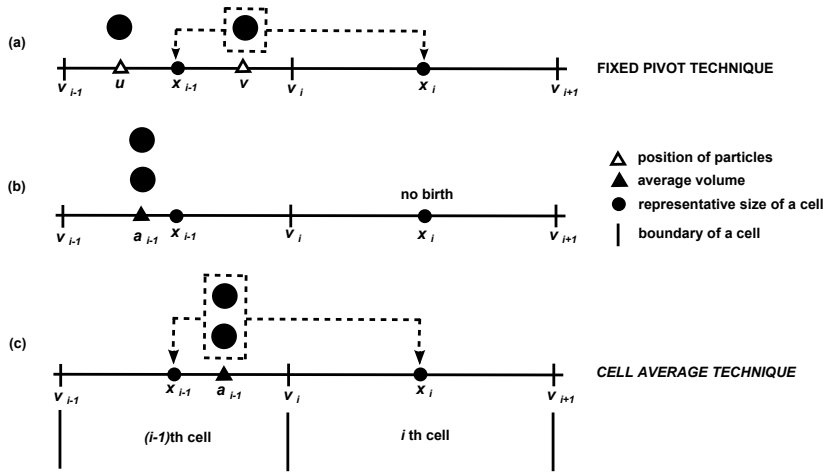

FIGURE 4.3: Illustration of the assignment of droplets born in the $(i-1)^{th}$ cell to the neighbouring representative size x_i, via (a) the fixed pivot method, (b) the cell average technique where $a_{i-1} < x_{i-1}$ and (c) the cell average techniqie when $a_{i-1} > x_{i-1}$. Here, a_{i-1} is the average volume of a new born droplet in the $(i-1)^{th}$ cell.

cell, is calculated using the volume average of all newborn droplets due to coagulation within the three neighbouring cells; $\Omega_{x_{i-1}}$, Ω_{x_i} and $\Omega_{x_{i+1}}$. The newborn droplets are then assigned to nearby representative volumes depending on the position of this average value. The difference between these two concepts for allocation of the newborn droplets is illustrated in Figure 4.3.

The main disadvantage of the fixed pivot technique is that while the two moments are evolved accurately, it consistently overpredicts the droplet number density. This is especially obvious for the larger droplet sizes when using a coarse numerical grid, and so, in general, a finer grid has to be used to maintain accuracy with the fixed pivot technique. Another weakness is that the fixed pivot method can only be used for coagulation and breakage, unlike the cell average technique which can still be used when growth and nucleation are present within the system being

modelled [81].

The problem is, that in the context of a spray dryer, the finer droplets generally far outnumber the larger ones. This means that it is beneficial to use some form of geometrically stretched grid, that will allow the full size range to be covered efficiently, ensuring high accuracy for the fine droplets, yet not neglecting the larger ones. This is where the newer cell average technique prevails. On the same geometrically stretched grid, the new technique improves the overall accuracy of the numerical predictions for both the intermediate and large droplet size ranges, yet still maintains the accuracy over the finer droplet sizes and moments, seen with the fixed pivot technique.

4.1.8 Fixed pivot technique

The theory behind the fixed pivot technique is fairly simple — consider two droplets that collide and coagulate to form a new droplet of volume v at distance z within the spray. If this droplet's volume lies between the representative volumes x_i and x_{i+1}, then we simply assign a fraction of the newborn droplet to x_i and the remaining fraction to x_{i+1}.

If the newly formed droplet has volume exactly equal to one of the representative volumes, it is simply allocated solely to that representative volume and consequently all physical properties, such as mass, will be preserved. When a newly born droplet's volume does not correspond to one of these representative volumes, we must assign it to neighbouring representative volumes in such a way that the moments of choice are preserved. To achieve this, the formation of a droplet of volume v in the range (x_i, x_{i+1}) is handled by assigning fractions $a(v, x_i)$ and $b(v, x_i)$ to the representative volumes at x_i and x_{i+1} respectively. The represent-

ative volume x_i then gains a fraction $a(v, x_i)$ from the droplets born in the range (x_i, x_{i+1}) and a fraction $b(v, x_i)$ from the range (x_{i-1}, x_i), where $a(v, x_i)$ and $b(v, x_i)$ are calculated as shown below.

If we are to conserve the ζ^{th} and μ^{th} moments, then for a droplet v born in the range (x_i, x_{i+1}), the fractions a and b must satisfy the following equations:

$$\begin{aligned} a(v, x_i)x_i^{\zeta} + b(v, x_{i+1})x_{i+1}^{\zeta} &= v^{\zeta} \\ a(v, x_i)x_i^{\mu} + b(v, x_{i+1})x_{i+1}^{\mu} &= v^{\mu}. \end{aligned} \tag{4.38}$$

The fractions $a(v, x_i)$ and $b(v, x_i)$ are then found to be

$$a(v, x_i) = \frac{v^{\zeta}x_{i+1}^{\mu} - v^{\mu}x_{i+1}^{\zeta}}{x_i^{\zeta}x_{i+1}^{\mu} - x_i^{\mu}x_{i+1}^{\zeta}} \tag{4.39}$$

$$b(v, x_i) = \frac{v^{\zeta}x_{i-1}^{\mu} - v^{\mu}x_{i-1}^{\zeta}}{x_i^{\zeta}x_{i-1}^{\mu} - x_i^{\mu}x_{i-1}^{\zeta}}. \tag{4.40}$$

From (4.37), our approximation to the birth term of the equation is currently

$$\widetilde{B}_{ij}(t) = V_j \sum_{v_i \le x_k + x_l < v_{i+1}}^{l \ge k} (1 - \frac{1}{2}\delta_{l,k}) K_{l,k,j} N_{l,j}(t) N_{k,j}(t). \tag{4.41}$$

This is then further approximated to give the modified fixed pivot birth term for the birth in the cell Ω_{ij}. Since the representative volume x_i gains a fraction $a(v, x_i)$ from the droplets in the range (x_i, x_{i+1}) and a fraction $b(v, x_i)$ from the range (x_{i-1}, x_i), the modified birth term is

$$\widehat{B}_{ij}^{FP} = \sum_{\substack{l,k \\ x_{i-1} \le (x_k + x_l) \le x_{i+1}}}^{l \ge k} (1 - \frac{1}{2}\delta_{l,k})\, \eta(v)\, K_{l,k,j} N_{k,j}(t) N_{l,j}(t) \tag{4.42}$$

where

$$v = x_l + x_k,$$

$$\eta(v) = \begin{cases} \dfrac{v^\zeta x_{i+1}^\mu - v^\mu x_{i+1}^\zeta}{x_i^\zeta x_{i+1}^\mu - x_i^\mu x_{i+1}^\zeta}, & x_i \leq v \leq x_{i+1} \\ \dfrac{v^\zeta x_{i-1}^\mu - v^\mu x_{i-1}^\zeta}{x_i^\zeta x_{i-1}^\mu - x_i^\mu x_{i-1}^\zeta}, & x_{i-1} \leq v \leq x_i. \end{cases}$$

Note that in the above, $\eta(v)$ is simply the fraction $a(v, x_i)$ when $x_i \leq v \leq x_{i+1}$ and the fraction $b(v, x_i)$ when $x_{i-1} \leq v \leq x_i$.

The exact preservation of numbers and mass is achieved by setting $\zeta = 0$ and $\mu = 1$ as in [78] and by doing so, the expression for $\eta(v)$ simplifies to the linear hat function

$$\eta(v) = \begin{cases} \dfrac{x_{i+1} - v}{x_{i+1} - x_i}, & x_i \leq v \leq x_{i+1} \\ \dfrac{v - x_{i-1}}{x_i - x_{i-1}}, & x_{i-1} \leq v \leq x_i. \end{cases}$$

4.1.9 Cell average technique

Now focusing on the cell average technique from [80], we take the same birth term approximation (4.37) that the fixed pivot method began with, and modify it accordingly, to get the corresponding modified birth term. From (4.37), we have that

$$\widetilde{B}_{ij}(t) = V_j \sum_{v_i \leq x_k + x_l < v_{i+1}}^{l \geq k} (1 - \frac{1}{2}\delta_{l,k}) K_{l,k,j} N_{l,j}(t) N_{k,j}(t), \tag{4.43}$$

where this is interpreted as the total number of new droplets born due to coagulation, whose volume lies within the range Ω_{x_i} at distance z_j down the spray. The net volume of newborn droplets in the cell Ω_{ij} as a direct result of coagulation will thus be equal to the number of new droplets $\widetilde{B}_{ij}(t)$ multiplied by their respective

volumes. This volume is labelled $M_{ij}(t)$ and given by the equation

$$M_{ij}(t) = V_j \sum_{v_i \le x_k + x_l < v_{i+1}}^{l \ge k} (1 - \frac{1}{2}\delta_{l,k}) K_{l,k,j} N_{l,j}(t) N_{k,j}(t)(x_l + x_k). \tag{4.44}$$

From (4.43) and (4.44), the average volume of newborn droplets in Ω_{ij} can be calculated. Denoting this average volume as $\bar{a}_{ij}(t)$, it is calculated by simply dividing the total volume of newborn droplets by the total number of newborn droplets and thus, we have the equation

$$\bar{a}_{ij}(t) = \frac{M_{ij}(t)}{\widetilde{B}_{ij}(t)}. \tag{4.45}$$

Using the cell average technique it is now assumed that all newborn droplets in the cell Ω_{ij} are temporarily of volume $\bar{a}_{ij}(t)$ and these droplets are subsequently divided between the neighbouring pivot points (representative volumes), depending on the position of $\bar{a}_{ij}(t)$. As with the fixed pivot technique, this division of newborn droplets between pivot points is done so as to accurately evolve both the number and total mass of droplets in the system.

Suppose that the volume $\bar{a}_{ij}(t)$ lies between x_i and x_{i+1}, and let a and b represent the number of the newborn droplets assigned to the pivot points x_i and x_{i+1} respectively, at distance z_j within the spray. Thus for the correct evolution of both number and mass, we require

$$a + b = \widetilde{B}_{ij}(t), \tag{4.46}$$

$$a x_i + b x_{i+1} = \widetilde{B}_{ij}(t)\bar{a}_{ij}(t). \tag{4.47}$$

Solving (4.46) and (4.47) for a and b, results in

$$a(\bar{a}_{ij}(t)) = \frac{\widetilde{B}_{ij}(t)(\bar{a}_{ij}(t) - x_{i+1})}{x_i - x_{i+1}} \text{ and } b(\bar{a}_{ij}(t)) = \frac{\widetilde{B}_{ij}(t)(\bar{a}_{ij}(t) - x_i)}{x_{i+1} - x_i}. \tag{4.48}$$

Now if we look to model the birth due to coagulation in the cell Ω_{ij}, then at position z_j in the spray, the volume pivot point x_i gains contributions equal to

$$\begin{aligned} a(\bar{a}_{ij}(t)) \text{ if } \bar{a}_{ij}(t) \in [x_i, x_{i+1}], \qquad & b(\bar{a}_{ij}(t)) \text{ if } \bar{a}_{ij}(t) \in [x_{i-1}, x_i], \\ a(\bar{a}_{i+1,j}) \text{ if } \bar{a}_{i+1,j}(t) \in [x_i, x_{i+1}] \text{ and } \quad & b(\bar{a}_{i-1}) \text{ if } \bar{a}_{i-1,j}(t) \in [x_{i-1}, x_i]. \end{aligned}$$

Thus, by introducing λ_i^+ and λ_i^-, where

$$\lambda_i^{\pm}(x) = \frac{x - x_{i\pm1}}{x_i - x_{i\pm1}},$$

we can rewrite the functions a and b as

$$a(\xi) = \widetilde{B}_{ij}(t)\lambda_i^+(\xi) \qquad \text{and} \qquad b(\xi) = \widetilde{B}_{ij}(t)\lambda_{i+1}^-(\xi).$$

Using these, the cell average approximation to the birth term for cell Ω_{ij} can then be written in the form of [80, Equation 17], which states

$$\begin{aligned} \widehat{B}_{ij}^{CA}(t) = \widetilde{B}_{i-1,j}(t)\, \lambda_i^-(\bar{a}_{i-1,j}(t))H(\bar{a}_{i-1,j}(t) - x_{i-1}) + \widetilde{B}_{ij}(t)\lambda_i^-(\bar{a}_{ij}(t))H(x_i - \bar{a}_{ij}(t)) \\ + \widetilde{B}_{ij}(t)\lambda_i^+(\bar{a}_{ij}(t))H(\bar{a}_{ij}(t) - x_i) + \widetilde{B}_{i+1,j}\lambda_i^+(\bar{a}_{i+1,j}(t))H(x_{i+1} - \bar{a}_{i+1,j}(t)) \end{aligned} \tag{4.49}$$

where $H(x)$ is the Heaviside function

$$H(x) = \begin{cases} 1, & x > 0 \\ \frac{1}{2}, & x = 0 \\ 0, & x < 0. \end{cases}$$

The first term in (4.49) represents the contribution to the pivot point x_i due to birth in the cell $\Omega_{i-1,j}$. Such a contribution occurs when $\bar{a}_{i-1,j}(t)$, the volume of the average newborn droplet in the cell $\Omega_{i-1,j}$, lies in the range $[x_{i-1}, x_i]$. As a result, we then have a fraction λ_{i-1}^{-} of the total number of droplets born ($\widetilde{B}_{i-1,j}(t)$) in the cell $\Omega_{i-1,j}$ assigned to the pivot x_i. The Heaviside function is simply there to tell us whether we get a contribution or not. If $\bar{a}_{ij}(t) < x_i$ lies out with $[x_{i-1}, x_i]$ we will have no contribution. The Heaviside function reflects this and takes the value zero if this average lies outwith this range.

The other three terms in (4.49) act in the same way — representing the contribution to the pivot point x_i^{th} of the cell Ω_{ij} if:

- the average volume of new droplets born in Ω_{ij} lies in the range $[x_{i-1}, x_i]$;
- the average volume of new droplets born in Ω_{ij} lies in the range $[x_i, x_{i+1}]$;
- the average volume of new droplets born in $\Omega_{i+1,j}$ lies in the range $[x_i, x_{i+1}]$.

The Heaviside function is chosen with $H(0) = \frac{1}{2}$ to avoid double counting, since, if the average birth in the Ω_{ij} is exactly equal to x_i, then we find we have a contribution to the birth at x_i from both the second and third terms in (4.49). Had the standard definition whereby $H(0) = 1$ been used, we would have allocated double the number of droplets to the representative volume x_i.

So from (4.49), when applying the cell average technique, our discrete birth term becomes

$$\widehat{B}_{ij}^{CA}(t) = \widetilde{B}_{i-1,j}(t)\,\lambda_i^-(\bar{a}_{i-1,j}(t))H(\bar{a}_{i-1,j}(t)-x_{i-1})+\widetilde{B}_{ij}(t)\lambda_i^-(\bar{a}_{ij}(t))H(x_i-\bar{a}_{ij}(t)) + \widetilde{B}_{ij}(t)\lambda_i^+(\bar{a}_{ij}(t))H(\bar{a}_{ij}(t)-x_i) + \widetilde{B}_{i+1,j}\lambda_i^+(\bar{a}_{i+1,j}(t))H(x_{i+1}-\bar{a}_{i+1,j}(t)), \tag{4.50}$$

where

$$\widetilde{B}_{ij}(t) = V_j \sum_{v_i \le x_k + x_l < v_{i+1}}^{l \ge k} (1 - \frac{1}{2}\delta_{l,k})K_{l,k,j}N_{l,j}(t)N_{k,j}(t)$$

Combining the discrete transport, birth and death terms, (4.23), (4.50) and (4.27) with equation (4.8), results in the coupled system of ordinary differential equations

$$\frac{d}{dt}N_{ij}(t) = \frac{1}{V_j}\Big[\widehat{B}_{ij}^{CA}(t) + \widetilde{D}_{ij}(t) - \widetilde{T}_{ij}(t)\Big], \tag{4.51}$$

where

$$1 \le i \le I \text{ and } 1, \le j \le J. \tag{4.52}$$

4.2 Numerical solution of the discretised system of equations

To solve (4.51), we first create a vector $\mathbf{N}(t)$, which takes the form

$$\mathbf{N}(t) = \Big(N_{1\,1}(t), N_{1\,2}(t), \ldots, N_{ij}(t), \ldots, N_{2\,1}(t), N_{2\,2}(t), \ldots, N_{IJ}(t)\Big)^T, \tag{4.53}$$

and then solve

$$\frac{d}{dt}\mathbf{N}(t) = \mathbf{G}(\mathbf{N}(t)), \tag{4.54}$$

where $\mathbf{G}$ is a vector corresponding to the RHS of (4.51).

The system (4.54) is solved numerically using an explicit, fourth order Runge-Kutta method with adaptive time-step control (MATLAB's `ode45`). We are interested in being able to quantify the droplet volume distribution within a steady state spray, where the temporal effects of atomiser start up are negligible. As such the approach described here is specific to the solution of steady state problems. For the solution of (4.51), the system is treated as a time-dependent system of equations, and the Runge-Kutta scheme is used to return the droplet number concentration throughout the length of the spray at a time where the spray has established its steady state. That is, we integrate the system of equations forward in time until the computed approximation of $\mathbf{N}$ takes on a steady state value. To test for convergence towards a steady state, we evaluate the L_1 norm of the differences in the approximation to $\mathbf{N}$ between time-steps, given by

$$E_\tau = \sum_{j=1}^{J}\sum_{i=1}^{I}\left|N_{ij}^{\tau} - N_{ij}^{\tau-1}\right|, \tag{4.55}$$

where the superscript τ denotes the time step at which the temporal differences has been calculated. Time integration proceeds until

$$E_\tau < \kappa, \tag{4.56}$$

for a chosen tolerance κ and/or when some maximum time, t_{max} has been exceeded.

4.3 Test problems

We now look to see how the combined numerical methods perform in a group of test problems. In these, we run a series of simulations of advection and coagulation in isolation, followed by the case of coagulation with constant advection. To check the accuracy of these simulations, the predicted results are verified against known analytic solutions for the test problem used.

4.3.1 Constant advection and no coagulation

To illustrate the Kurganov-Tadmor scheme's ability to resolve sharp advecting fronts, we consider the following model problem of constant advection with no coagulation,

$$\frac{\partial N_1}{\partial t} = U_d \frac{\partial N_1}{\partial z}, \tag{4.57}$$

where

$$N_1(z,0) = \begin{cases} 100 & \text{if } z = 0, \\ 0 & \text{if } z \neq 0, \end{cases}$$

$$U_d > 0, \quad z \in [0,1],$$

and

$$N_1(0,t) = 100, \quad \forall\ t.$$

This PDE models a constant influx of monomers at $z = 0$, advecting at constant speed U_d through an initially empty region where all monomers are initially concentrated at the inlet. Here, U_d is the constant advecting field and, for this example, is set to be $U_d = 0.006$.

Equation (4.57) has been approximated using the Beam-Warming [76], Lax-

Wendroff [77] and first-order upwind schemes [75, Chapter 4], and the results are shown in Figure 4.4. The equations were solved using a uniform spatial grid. The grid point spacing is denoted by Δz and the process was repeated using grids of both 40 and 160 points.

To ensure stability of these methods, it is essential that the size of the time steps, Δt, satisfies the Courant-Friedrichs-Levy (CFL) condition [82]. For stability of the first-order upwind and the Lax-Wendroff schemes, the following inequality must be satisfied [83, Chapter 17]

$$\text{CFL number} \quad = \quad \frac{U_d \, \Delta t}{\Delta z} \quad \leq \quad 1. \tag{4.58}$$

In order to achieve this, we set the time step size to be

$$\Delta t = 0.1 \times \frac{\Delta z}{U_d}, \tag{4.59}$$

and subsequently, the number of time steps used to be $t_{max}/\Delta t$.

Similarly, for the second-order Beam-Warming scheme, the CFL condition requires [83, Chapter 17]

$$\frac{U_d \, \Delta t}{\Delta z} \quad \leq \quad 2, \tag{4.60}$$

whilst, for the Kurganov-Tadmor scheme [72],

$$\frac{U_d \, \Delta t}{\Delta z} \quad \leq \quad \frac{1}{8}. \tag{4.61}$$

Figure 4.4 shows the computed solutions using each method at time $t_{max} = 100$. The analytic solution at this time is a step function, dropping from 100

to 0 at $z = 0.6$. We can see that both the Beam-Warming and Lax-Wendroff schemes capture the steep advecting front well, but both methods give rise to unwanted oscillations. In a particulate system, any oscillations in these solutions may result in unrealistic, negative droplet number concentrations and so they must be avoided at all costs. The first-order upwind scheme has none of these oscillations, but instead sees significant numerical diffusion and, as a result, it fails to resolve the steep advecting front. The Kurganov-Tadmor scheme does the best job of capturing the steep advecting front. In comparison to the other techniques, there is very little numerical diffusion and there are no unwanted oscillations.

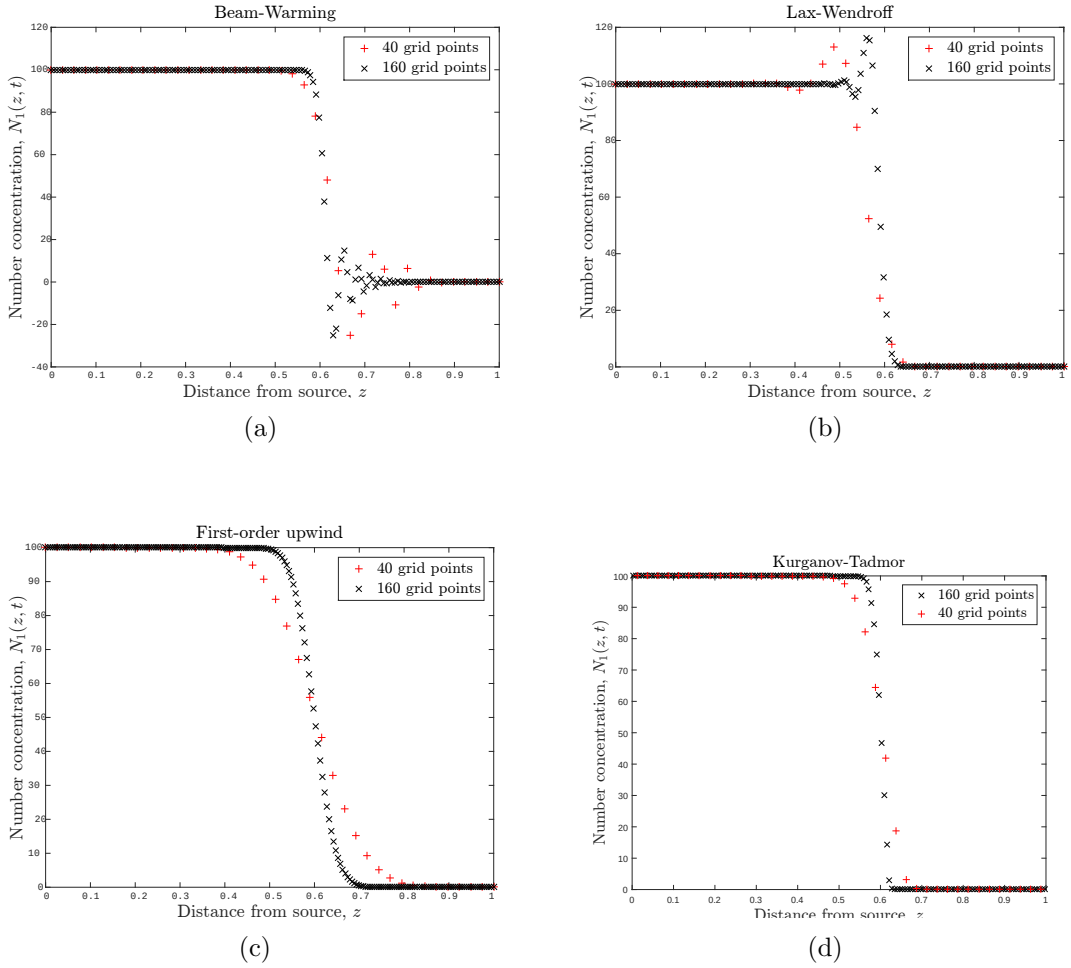

Figure 4.4: Numerical approximations for constant advection with no coagulation. Comparison of results produced using the following schemes: (a) Beam-Warming scheme [76]; (b) Lax-Wendroff scheme [77]; (c) First-order upwind scheme [75]; (d) Kurganov-Tadmor scheme [72].

To investigate the estimated order of convergence (EOC) of the Kurganov Tadmor scheme, equation (4.57) was solved using the initial condition

$$N_1(z,0) = 50\Big[1 + \tanh\Big(\frac{z_0 - z}{\epsilon_d}\Big)\Big],$$

where we set $\epsilon_d = 0.1$ and $z_0 = 0$. The equation was solved using grids of increasing

resolution for the spatial range, with 20, 40, 80, 160 and finally 320 grid points. The results for the 160 point run are shown in figure 4.5, where we have integrated forward in until time $t_{max} = 100$. We solve using an explicit Runge-Kutta method, with adaptive time-stepping and very small tolerances. With such fine tolerances, the assumption can then be made that any error in the results is due to the discretisation of the advection term, and so these errors can be used to estimate a numerical method's order of convergence. The error in the numerical results was

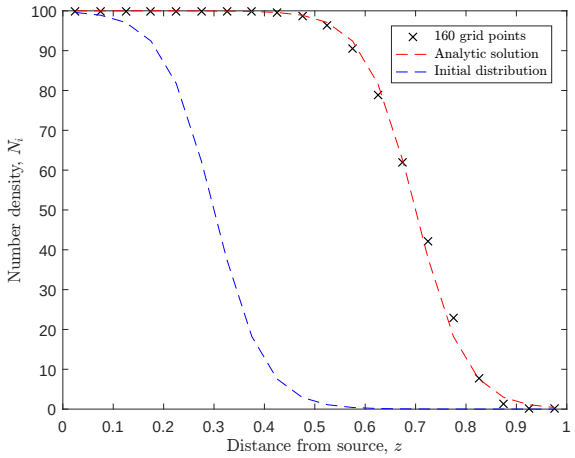

Figure 4.5: Illustration of the smooth initial condition used for calculating the EOC results for constant advection case. The predicted results are also shown for a grid of 160 points.

measured at $t = t_{max}$ using the norm

$$E_J = \sum_{j=1}^{J} (z_{j+1/2} - z_{j-1/2}) \Big| N_1(z_j, t_{max}) - N_{1j}(t_{max}) \Big|. \tag{4.62}$$

Here, $N_{1j}(t_{max})$ is the numerical approximation to the number of monomers of volume x_1 at distance $z = z_j$ in space. From this, the EOC was calculated using the formula

$$\text{EOC} = \frac{\ln\left[E_J / E_{2J}\right]}{\ln(2)}, \tag{4.63}$$

and the results are shown in Table 4.1. We can see that the EOC for the Kurganov-

J	E_J	EOC Rate
20	9.03×10^{-1}	—
40	3.20×10^{-1}	1.50
80	8.11×10^{-2}	1.98
160	2.00×10^{-2}	2.02
320	4.99×10^{-3}	2.00

Table 4.1: Estimated order of convergence results for the numerical solution of equation (4.57) for constant advection and zero coagulation.

Tadmor scheme is displaying second-order convergence as the number of spatial grid points is increased. This is consistent with what we would expect, as the scheme is designed to be a second-order accurate numerical method when the exact solution is smooth. Subsequently, we can conclude that the discretisation of the advection terms from our model is functioning as desired.

Based on the observations from Figure 4.4 and Table 4.1, it is clear that the Kurganov-Tadmor scheme will be one of the most accurate and best suited for our purposes. The scheme has also been successfully applied to the solution of spatially dispersed coagulation PBEs, as in [84], where the hydrodynamic interactions of liquid-liquid dispersions are modelled. The scheme effectively combines the best characteristics of first-order methods with benefits of second-order central difference techniques in that it does not suffer from unwanted oscillations, or numerical diffusion and does a very good job of reproducing a steep advecting front. The scheme is also second-order convergent for smooth solutions.

There are of course other equally capable numerical schemes available. How-

ever, the alternatives, such as second-order upwind schemes, generally require a complicated characteristic decomposition of the convective flux, using approximate Riemann solvers, which is both time-consuming and computationally expensive [84]. Thus, in keeping with the aim of this thesis, to construct a computationally inexpensive tool for the prediction of droplet size distributions, the Kurganov-Tadmor scheme is a far better fit for our goals.

4.3.2 Coagulation with no advection: Fixed pivot vs cell average

Next, we test the numerical approximation of a pure coagulation process using known analytic solutions to the coagulation equation (1.15) for two simple kernels. Since we have no spatial dependence, we let $N_i(t)$ represent the number concentration of droplets in the i^{th} droplet volume range and $n(x,t)$ the number density of droplets of size x at time t. We assume an exponential initial droplet size distribution

$$n(x,0) = e^{-x}, \tag{4.64}$$

and solve (1.15) for both the constant kernel and sum kernel

$$K(x,y) = 1, \qquad \text{and} \qquad K(x,y) = x + y, \tag{4.65}$$

respectively. The numerical results are plotted against the analytic solutions presented in Table 1.3. The results for the constant kernel case are shown in Figure 4.6, whilst those for the sum kernel case are shown in Figure 4.7.

For the results in Figures 4.6 and 4.7, we have used the grid from (4.2) with the grid ratio (4.3), and set $v_{min} = 1 \times 10^{-3}$ and $v_{max} = 1 \times 10^{5}$, for a total of $I = 80$ grid points. The simulations were run until a final time $t_{max} = 0.8$ for both cases. The droplet number concentration results shown in Figures 4.6(a) and 4.7(a) have been plotted on a log-log scale to highlight the difference in accuracy between each technique.

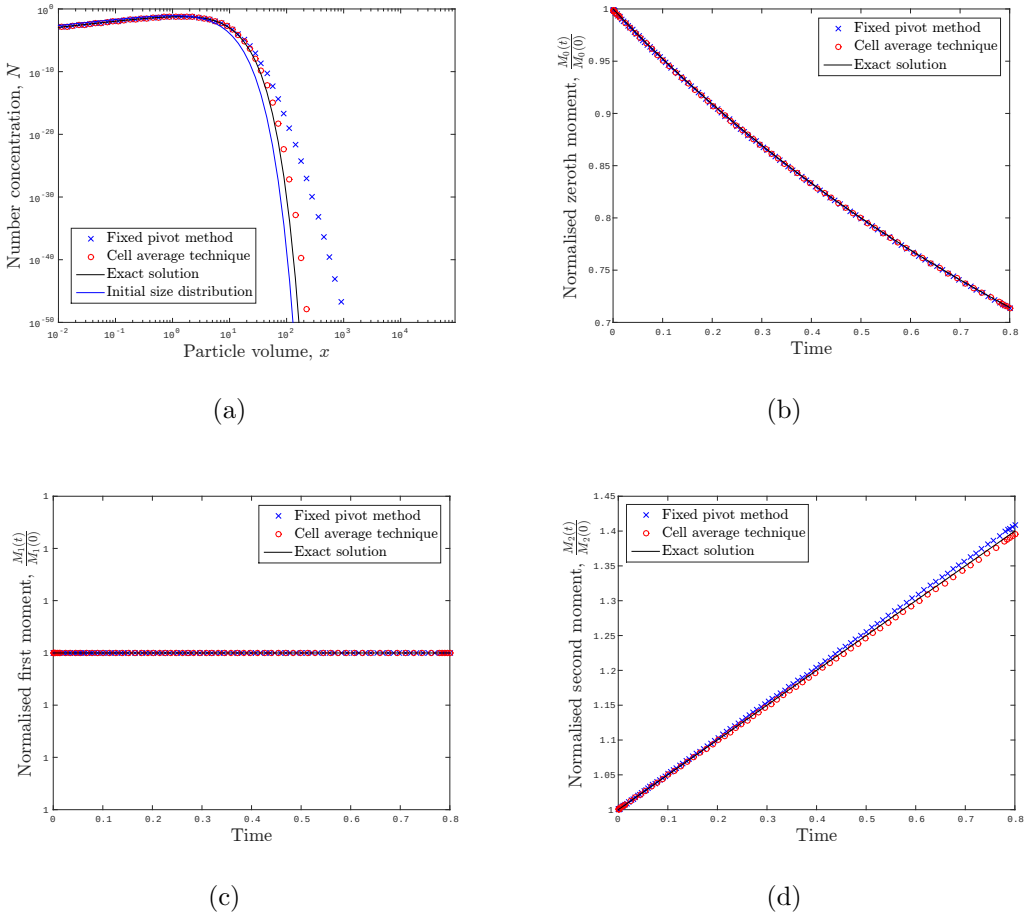

Figure 4.6: Comparison of cell average technique and fixed pivot technique for coagulation, using the constant kernel $K(x, y) = 1$, and the exponential initial droplet number density given by (4.64). The plots show:(a) droplet number concentration (log-log axis scales); (b) normalised zeroth moment; (c) normalised first moment; and, (d) normalised second moment.

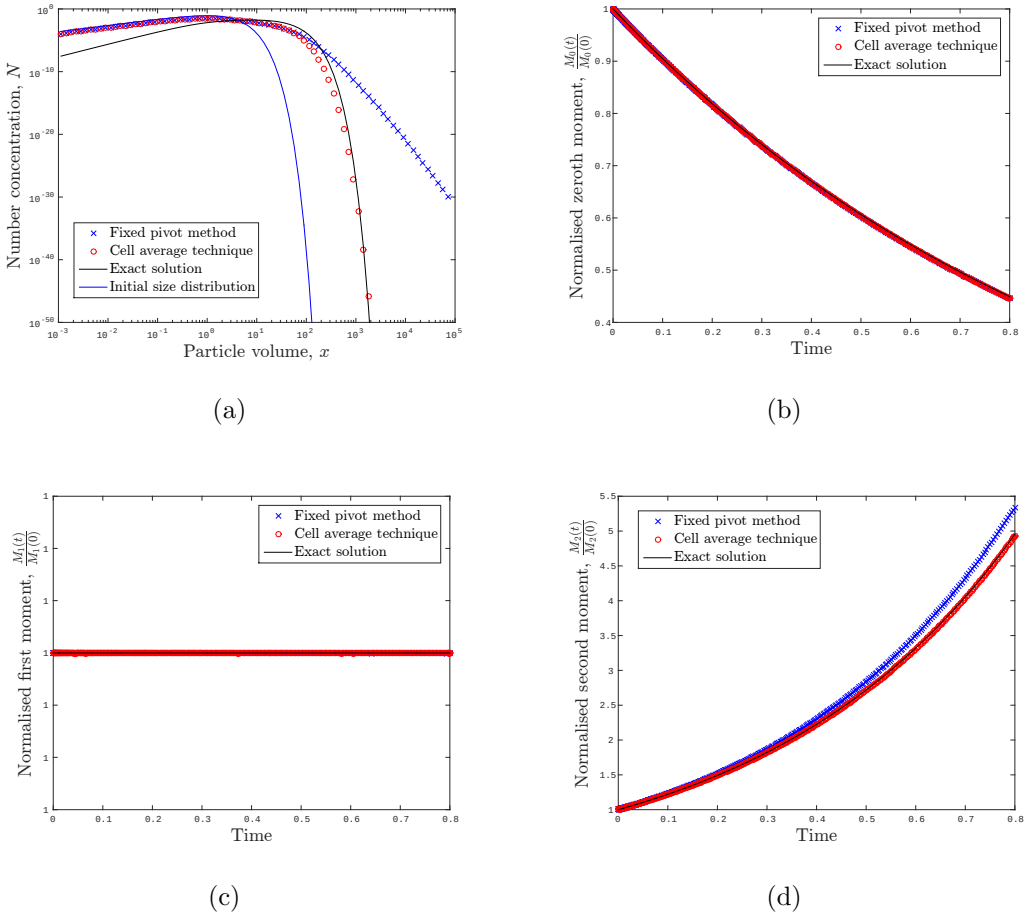

Figure 4.7: Comparison of cell average technique and fixed pivot technique for coagulation, using the sum kernel $K(x, y) = x+y$, and the exponential initial droplet number density given by (4.64). The four plots show:(a) droplet number concentration (log-log axis scales); (b) normalised zeroth moment; (c) normalised first moment; and, (d) normalised second moment.

It can be clearly seen in Figures 4.6(a) and 4.7(a) that the fixed pivot method overpredicts the number concentration of larger droplets, whilst the cell average results are much closer to the analytic solution in both cases. Both techniques do a good job of evolving the zeroth moment and the first moment result is very accurate for both methods, with it remaining constant at one as expected. The second moment results are reasonable for the fixed pivot method, however those

from the cell average technique are excellent in comparison and clearly outperform the fixed pivot more and more, as time progresses.

To investigate the EOC for both the fixed pivot and cell average techniques, the same test problem was solved, using grids of increasing resolution for the droplet volume range. This time, the geometric grid was defined using equations (4.2), with grid ratio (4.3), where $v_1 = 10^{-3}$ and $v_I = 10^5$. The number of grid points looked at were 20, 40, 80 and finally 160.

The error in the numerical results was measured at $t = t_{max}$, $z = z_0$, using the norm

$$E_I = \sum_{i=1}^{I} \Big| N(x_i, z_0, t_{max}) - N_{i0}(t_{max}) \Big|. \tag{4.66}$$

Here, $N_{i0}(t_{max})$ is the numerical approximation to the number of droplets of size x_i in the system, at distance $z = 0$ (since we have no advection in this test case). From this, the EOC was calculated using the formula

$$\text{EOC} = \frac{\ln\big[E_I / E_{2I}\big]}{\ln(2)}, \tag{4.67}$$

and the results are shown in Tables 4.2 and 4.3. From Figure 4.2 it can clearly be seen that the estimated order of convergence for the fixed pivot technique is converging towards a value of two for both the constant kernel and sum kernel cases. This is consistent with results found in [85], that show the fixed pivot method is second-order accurate on a non-uniform, smooth grid. Similarly, for the cell average technique, Table 4.3 clearly shows the method is second-order accurate for the sum kernel case. For the constant kernel case, there appears to be some oscillation in the EOC rate, however, it does still converge to a value of two. This is again agreement with [80], and so we can conclude that the cell average is also

	Constant Kernel		Sum Kernel	
I	E_I	EOC Rate	E_I	EOC Rate
20	2.35×10^{-2}	—	5.41×10^{-2}	—
40	6.50×10^{-3}	1.85	1.44×10^{-2}	1.91
80	1.73×10^{-3}	1.91	3.69×10^{-3}	1.96
160	4.52×10^{-4}	1.94	9.34×10^{-4}	1.98
320	1.14×10^{-4}	1.99	2.34×10^{-4}	2.00

Table 4.2: EOC results for the numerical solution of the pure coagulation equation using the fixed pivot technique.

	Constant Kernel		Sum Kernel	
I	E_I	EOC Rate	E_I	EOC Rate
20	7.86×10^{-3}	—	5.34×10^{-2}	—
40	2.34×10^{-3}	1.75	1.48×10^{-2}	1.85
80	1.62×10^{-3}	0.53	4.08×10^{-3}	1.86
160	2.52×10^{-4}	2.68	1.05×10^{-3}	1.96
320	6.651×10^{-5}	1.92	2.63×10^{-4}	2.00

Table 4.3: EOC results for the numerical solution of the pure coagulation equation using the cell average technique.

second-order convergent using a non-uniform, smooth grid.

Here, we have seen that both the fixed pivot method and cell average technique are second-order accurate on the non-uniform smooth mesh used in our model. However, as per Figures 4.6 and 4.7, it is clear that the cell average technique predicts the moments of the droplet number density function with greater accuracy than the fixed pivot method as time progresses. Thus, on this basis, we will only

use the cell average technique to discretise the coagulation terms throughout the remainder of this thesis.

4.3.3 Coagulation and constant advection

We next consider combined coagulation and advection for the simple case of constant advection, which takes the form

$$\frac{\partial n(x,z,t)}{\partial t} + U_d \frac{\partial n(x,z,t)}{\partial z} = \frac{1}{2}\int_0^x K(x-y,y,z)n(x-y,z,t)n(y,z,t)dy - \int_0^\infty K(x,y,z)n(x,z,t)n(y,z,t)dy, \tag{4.68}$$

where U_d is the constant speed of advection.

For these test cases, we will again use an exponential distribution for the droplet number density at the inlet and presume that initially all droplets are concentrated at $z = 0$, such that the rest of the system is empty. That is:

$$n(x,0,t) = e^{-x}, \quad \forall\ t, \quad \text{and} \tag{4.69}$$

$$n(x,z,0) = 0 \ \ \forall z \in (0,L]. \tag{4.70}$$

For simple kernels, such as the constant and sum kernels, analytic solutions to (4.68) can be calculated using the change of variable technique presented by Attarakih [84]. When $t = L/U_d$, the leading droplets will have reached position $z = L$, and the droplet number density will subsequently have reached a steady state for all $z < U_d t = L$. When $t \geq L/U_d$, the leading droplets will have passed

the end of the spray. If we therefore set $\bar{t} = t - \frac{L}{U_d}$, then

$$\frac{\partial n(x,z,\bar{t})}{\partial \bar{t}} = 0, \quad \forall\ \bar{t} \geq 0.$$

This change of variable allows us to now write (4.68) as the equation

$$\frac{\partial n(x,z,\bar{t})}{\partial z} = \frac{1}{2}\int_0^x \frac{K(x-y,y,z)}{U_d} n(x-y,z,\bar{t})n(y,z,\bar{t})dy - \int_0^\infty \frac{K(x,y,z)}{U_d} n(x,z,\bar{t})n(y,z,\bar{t})dy. \quad (4.71)$$

Equation (4.71) can then be written in the form of a standard coagulation equation, where z plays the role of time and we have a modified coagulation kernel $\bar{K}(x,y,z) = K(x,y,z)/U_d$. This gives the equation

$$\frac{\partial n(x,z,\bar{t})}{\partial z} = \frac{1}{2}\int_0^x \bar{K}(x-y,y,z) n(x-y,z,\bar{t})n(y,z,\bar{t})dy - \int_0^\infty \bar{K}(x,y,z) n(x,z,\bar{t})n(y,z,\bar{t})dy. \quad (4.72)$$

Analytic solutions to (4.72) using the inlet condition (4.69) can be found in the paper by Scott [46], for both the constant and sum kernel cases. We can then work backwards from these to obtain the analytic solution for the droplet number density function corresponding to each test case.

Constant kernel with constant advection

The first case we look at is that of the constant kernel $K(x,y,z) = C$. Here, we are interested in solving (4.68) to find the system's steady-state solution. To do so, we integrate the equation far enough in time, so as to make sure a steady state

system has been reached — in this case any physical time $t\,\frac{L}{U_d}$ will be sufficient to achieve this.

For the constant kernel, the modified coagulation kernel in equation (4.72) is then

$$\bar{K}(x, y, z) = \frac{C}{U_d}, \tag{4.73}$$

and hence, using the analytic solutions in [46], we have the steady-state solution

$$n(x, z) = \frac{4}{[\frac{C}{U_d}z + 2]^2} \exp\Big[-2x/\Big(\frac{C}{U_d}z + 2\Big)\Big]. \tag{4.74}$$

Equation (4.68) was solved for the constant kernel case using the Kurganov-Tadmor scheme to discretise the advection term and the cell average technique for the coagulation terms. The calculation was carried out using the geometric grid from (4.2) for the droplet volume size range, with the maximum and minimum droplet volumes set to be $v_1 = 10^{-3}$ and $v_{I+1} = 10^2$. In the z-direction a linearly spaced grid of J points is used, spanning the range between $z = 0$ and $z = 1$. A total of $I = 100$ and $J = 150$ grid points were used, for the droplet volume and spatial distance ranges, respectively. The value of the constant kernel was set to be $K(x, y, z) = 0.75$, the constant speed of advection used was $U_d = 1$, and we integrated in time to $t = 2$, to ensure a steady-state system within the range $z \in [0, 1]$.

Figure 4.8 shows the numerical results for the droplet number concentration plotted against the analytic solution at three points in the z-direction. Observe that as z increases, there is an increase in the number of larger droplets relative to the number observed at shorter z distances. It is clear that the numerical results are in good agreement with the analytic solution, and so, for this case, we can

conclude that our chosen numerical techniques are handling both the coagulation and transport terms correctly.

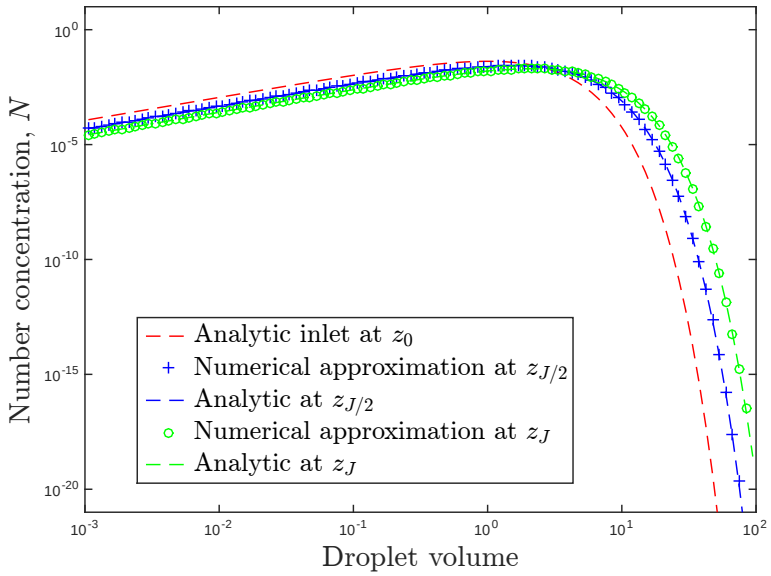

Figure 4.8: Numerical simulation of coagulation and constant advection, using the constant kernel $K(x, y, z) = 0.75$ for coagulation and a constant advecting velocity field of $U_d = 1$.

Sum kernel and constant advection

We next consider the sum kernel $K(x, y, z) = x + y$ and use the same exponential inlet distribution as before (4.69). This time, the modified kernel in equation (4.72) will be

$$\bar{K}(x, y, z) = \frac{x + y}{U_d}. \tag{4.75}$$

Using the change of variable from [84] and solutions from [46], we have the analytic steady state solution

$$n(x, z) = \frac{(1 - \tau)\exp(-x(\tau + 1))}{x\tau^{1/2}} I_1\Big(2x\tau^{1/2}\Big), \tag{4.76}$$

where

$$\tau = 1 - \exp(-z/U_d), \tag{4.77}$$

and $I_1(x)$ is the standard modified Bessel function of the first kind. As before, the steady state solution given by (4.76), is valid for all time t satisfying

$$t \geq \frac{z}{U_d}. \tag{4.78}$$

The same mesh was used, as per the preceding constant kernel case, and the constant advecting speed was again set to be $U_d = 1$.

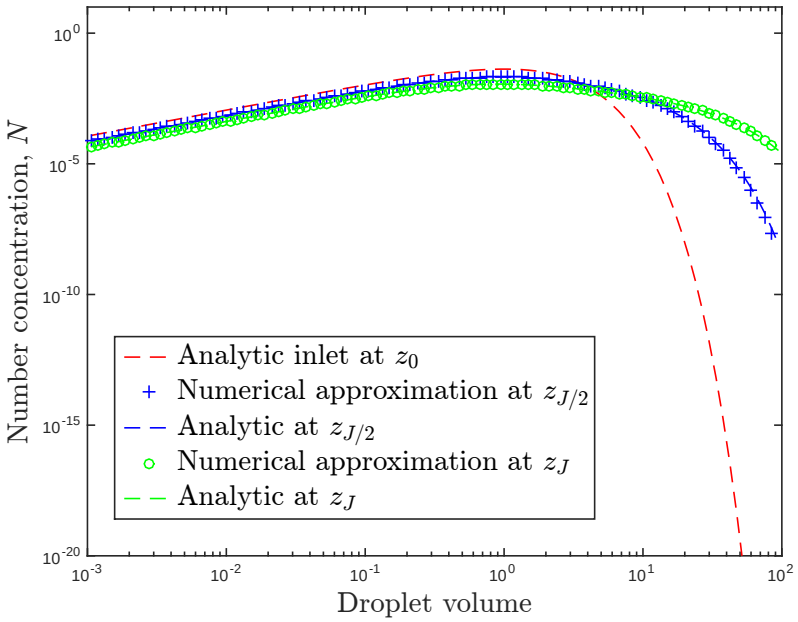

FIGURE 4.9: Numerical simulation of coagulation and constant advection, using the sum kernel $K(x, y, z) = x + y$ for coagulation and a constant advecting velocity field of $U_d = 1$.

The numerical results are plotted in Figure 4.9, against the analytic solution, at three points in the z-direction. Once again, we observe an increase in the number

of larger droplets, as z increases. It is also clear that the numerical results are an excellent match to the analytic solutions, and so, we have yet more evidence that the chosen numerical techniques are handling both the coagulation and transport terms correctly.

To investigate the estimated order of convergence (EOC) for coagulation combined with constant advection, the test problem (4.68) was solved again, using grids of increasing resolution for both the spatial and droplet volume ranges. When varying the number of droplet volume grid points the number of spatial grid points was held fixed at $J = 160$. The error in the numerical solutions was measured at $z = z_J$ using the norm

$$E_I = \sum_{i=1}^{I} \Big| N(x_i, z_J) - N_{iJ} \Big|, \tag{4.79}$$

where $N(x_i, z_j)$ is the exact number concentration found by combining the analytic solution for $n(x, z)$ with (4.5). By doing this, we are fixing a representative value of z, and looking at the value of the error at this point in space, while we refine the droplet volume grid. The estimated order of convergence is then calculated using

$$\text{EOC} = \frac{\ln\big[E_I / E_{2I}\big]}{\ln(2)}. \tag{4.80}$$

Grids with $I = 20$, 40, 80, 160 and 320 were used for the droplet volume range and the results are shown in Table 4.4. This time, a droplet volume range spanning from $v_1 = 1 \times 10^{-3}$ to $v_{I+1} = 1 \times 10^{4}$ was used and the constant kernel was taken to be $K(x, y) = 0.6$. It is clear that second-order convergence is displayed, as the number of droplet volume grid points is refined. Since the spatial grid has been fixed, we expect any error in the solution to be down to the discretisation of the coagulation terms. Subsequently, the results agree with what we would

expect, as the cell average technique has been shown to be second-order accurate on non-uniform smooth grids in [80].

	Constant Kernel		Sum Kernel	
I	E_I	EOC Rate	E_I	EOC Rate
20	7.6×10^{-3}	—	4.17×10^{-2}	—
40	2.89×10^{-3}	1.39	1.15×10^{-2}	1.85
80	7.13×10^{-4}	2.02	3.04×10^{-3}	1.92
160	2.22×10^{-4}	1.68	7.77×10^{-4}	1.96
320	4.75×10^{-5}	2.31	1.88×10^{-4}	2.05

Table 4.4: Estimated order of convergence results for the numerical solution of equation (4.68), when the droplet volume grid is refined, and the total number of spatial grid points is fixed at $J = 160$. Results are for the case of constant advection and coagulation using both the constant and sum kernels.

Similarly, when the number of spatial grid points was varied, the number of droplet volume grid points was fixed at $I = 400$, and the error in the numerical results was measured using the norm

$$E_J = \sum_{j=1}^{J} (z_{j+1/2} - z_{j-1/2}) \Big| N(x_{REF}, z_j) - N_{REF\,j} \Big|, \tag{4.81}$$

where x_{REF} was chosen to be $x_{150} = 7.39 \times 10^{-2}$. By doing this, we are fixing a particular droplet volume x_{150}, as the spatial grid is refined. From this, the EOC was calculated using the formula

$$\text{EOC} = \frac{\ln\big[E_J / E_{2J}\big]}{\ln(2)}. \tag{4.82}$$

Here, grids with $J = 5$, 10, 20, 40 and 80 were used for the spatial range and the results are shown in Table 4.5. This time, a droplet volume range spanning from $v_1 = 1 \times 10^{-3}$ to $v_{I+1} = 1 \times 10^{2}$ was used and the constant kernel was taken to be $K(x, y) = 0.75$.

	Constant Kernel		Sum Kernel	
J	E_J	EOC Rate	E_J	EOC Rate
5	1.07×10^{-5}	—	1.33×10^{-5}	—
10	3.28×10^{-6}	1.71	4.43×10^{-6}	1.61
20	9.53×10^{-7}	1.78	1.29×10^{-6}	1.75
40	2.54×10^{-7}	1.91	3.22×10^{-7}	2.00
80	6.44×10^{-8}	1.97	8.75×10^{-8}	1.88

Table 4.5: Estimated order of convergence results for the numerical solution of equation (4.68), when the spatial grid is refined, and the number of droplet volume grid points is fixed at $I = 400$. Results are for the case of constant advection and coagulation using the both the constant and sum kernels.

The results of refining the uniform spatial grid, while keeping the droplet volume grid fixed, can be seen in Table 4.5. This time, it has been assumed that any error is due mainly to the discretisation of the transport terms. From the table, we see second-order convergence is being displayed, as the spatial grid's resolution is refined. This agrees with what we would expect to see as the Kurganov-Tadmor scheme for advection has been shown to be second-order accurate for uniform grids in [72]. So we can conclude that the Kurganov-Tadmor scheme we have used for the transport terms is also second-order accurate for this particular problem.

Based on the results of Tables 4.5 and 4.4, we can confidently conclude that our chosen numerical methods are functioning as desired.

To allow for comparisons to be made to an alternative numerical technique, we have repeated the experiments used to produce Table 4.5 using a first-order upwind scheme [75, Chapter 4], instead of our chosen Kurganov-Tadmor scheme. The results are shown in Table 4.6. Clearly switching to the first-order scheme for

	Constant Kernel		Sum Kernel	
J	E_J	EOC Rate	E_J	EOC Rate
5	4.65×10^{-5}	—	6.14×10^{-5}	—
10	2.45×10^{-5}	0.92	3.31×10^{-5}	0.89
20	1.26×10^{-5}	0.95	1.71×10^{-5}	0.95
40	6.40×10^{-6}	0.98	8.74×10^{-6}	0.97
80	3.22×10^{-6}	0.99	4.33×10^{-6}	1.01

Table 4.6: Estimated order of convergence results for the numerical solution of equation (4.68), when the spatial grid is refined, and the number of droplet volume grid points is fixed at $I = 400$. Results are for the case of constant advection and coagulation using the both the constant and sum kernels, when a first-order upwind scheme is used to handle the advection terms.

advection results in first-order convergence for both the constant and sum kernel cases. The errors observed when using the first-order scheme also appear to be larger than those encountered when the Kurganov-Tadmor scheme is employed. Thus, we have more evidence here to support our conclusion that the second-order convergent, Kurganov-Tadmor scheme is a better choice for our particular needs.

Chapter 5

Discretisation of the spray model

5.1 Numerical solution of the spray model

Having established that our chosen numerical techniques are working as desired in Chapter 4, we now go on to apply them to equation (2.62), the governing equation for our spray model. From equation (4.51), the discrete equation for our spray is

$$\frac{d}{dt}N_{ij}(t) = \frac{1}{V_j}\Big[\widehat{B}_{ij}^{CA}(t) + \widetilde{D}_{ij}(t) - \widetilde{T}_{ij}(t)\Big], \tag{5.1}$$

where

$$i = 1, 2, \ldots, I, \quad \text{and} \quad j = 1, 2, \ldots, \ J\,.$$

Here

$$V_j \equiv \Delta z A(z_j) \tag{5.2}$$

is the approximate volume of the spray within the spatial cell Ω_{z_j} and as such, the area is

$$A(z) = \pi z^2\big[\tan^2\frac{\alpha}{2} - \tan^2\frac{\beta}{2}\big]. \tag{5.3}$$

In (5.1), the discretised transport, birth and death terms all take the same form as those derived for the general coagulation-transport equation in Chapter 4. Thus we have

$$\widetilde{T}_{ij}(t) = F_{j+1/2}(t) - F_{j-1/2}(t), \tag{5.4}$$

where the numerical flux terms, $F_{j\pm1/2}(t)$, are the same as those defined in (4.18). Our death term is again

$$\widetilde{D}_{ij}(t) = -V_j \sum_{k=1}^{I} K(x_i, x_k, z_j) N_i(z_j, t) N_k(z_j, t),$$

and the discretized, cell-average, birth term is

$$\begin{aligned}\widehat{B}_{ij}^{CA}(t) = \widetilde{B}_{i-1,j}(t)\, \lambda_i^-(\bar{a}_{i-1,j}(t)) H(\bar{a}_{i-1,j}(t) - x_{i-1}) + \widetilde{B}_{ij}(t) \lambda_i^-(\bar{a}_{ij}(t)) H(x_i - \bar{a}_{ij}(t)) \\ + \widetilde{B}_{ij}(t) \lambda_i^+(\bar{a}_{ij}(t)) H(\bar{a}_{ij}(t) - x_i) + \widetilde{B}_{i+1,j} \lambda_i^+(\bar{a}_{i+1,j}(t)) H(x_{i+1} - \bar{a}_{i+1,j}(t)),\end{aligned} \tag{5.5}$$

where

$$\widetilde{B}_{ij}(t) = V_j \sum_{v_i \le x_k + x_l < v_{i+1}}^{l \ge k} (1 - \frac{1}{2}\delta_{l,k}) K_{l,k,j} N_{l,j}(t) N_{k,j}(t).$$

The numerical solution of the discrete spray system described by (5.1) is carried out in exactly the same way as described in Section 4.2, with the only difference being that the values of the area $A(z)$ and the parameter q_0 are now unique to the spray set-up being modelled.

5.2 Coagulation and advection in the spray using size and velocity dependent kernel

Having established the discretised form of our governing equations, we now move on to simulate a full conical spray system. In this section, we run a series of simulations to investigate the effects the various model parameters have on the droplet size distribution within a spray. The parameters considered include the density of the droplets, the thickness of the spray sheet and the droplet inlet velocity. Knowledge of the effects that each parameter has on the droplet distribution of the spray is fundamental to spray dryer design to produce the optimum final product characteristics.

To allow the effects of each change to be easily observed, we first define a base configuration. The droplet distribution produced by these base settings can then be used as a benchmark, against which comparisons can be made and the effects of varying a single parameter may easily be quantified. In the base configuration, all the model's constant parameters, such as densities, velocities and spray angles, are assigned arbitrary, but realistic values. In the following simulations, a log-normal inlet droplet size distribution is used:

$$n(x, z_0, t) = \frac{N_{part}}{x\sigma\sqrt{2\pi}} \exp\Big[-\frac{1}{2\sigma^2}\Big(\log x - \log(x_{50})\Big)^2\Big], \tag{5.6}$$

where the mean droplet volume and spread parameters are set to $x_{50} = 6.545 \times 10^{-12}\text{m}^3$ and $\sigma = \log(2.5)$, respectively. Here N_{part} is the total number of droplets, per unit volume in space, in the initial distribution, and is set to $N_{part} = 1 \times 10^9\text{m}^{-3}$. The x_{50}, σ and N_{part} values and the base settings which follow below, were all arrived

at after discussions with process engineers at Procter and Gamble. The only exception is the value of the coagulation efficiency parameter λ, which is at present has been chosen arbitrarily. This parameter will later be fitted to the particular slurry being used within the spray dryer.

The base settings used in the following simulations are:

$$\rho_{air} = 1.2\,\mathrm{kg\,m^{-3}}, \quad \rho_{drop} = 1000\,\mathrm{kg\,m^{-3}}\ , \quad \mu = 1.8 \times 10^{-5}\ \mathrm{m^2\,s^{-1}},$$
$$L = 1\,\mathrm{m}, \qquad z_0 = 0.2\,\mathrm{m}, \qquad \lambda = 0.75,$$
$$d_{min} = 100\,\mu\mathrm{m}, \qquad d_{max} = 2080\,\mu\mathrm{m}, \qquad \tfrac{\beta}{2} = \tfrac{\pi}{6},$$
$$\tfrac{\alpha}{2} = \tfrac{7\pi}{36}, \qquad u_{inlet} = 40\,\mathrm{m\,s^{-1}}, \qquad u_{air}(z_0) = 7.5\,\mathrm{m\,s^{-1}}\ .$$

This combination simulates a spray of water droplets falling in a co-current flow of air. The sheet break-up length z_0, the smallest and largest droplet diameters $d_{min/max}$ and velocities, are all chosen to be within the usual ranges generally observed experimentally for a hollow cone spray [56, 57]. We integrate in time to $t_{max} = 1$ for all simulations within this chapter, and plot the resulting droplet distribution within the spray.

We are interested in quantifying the number of droplets of volume x at a given distance z within the spray for each simulation. If the thickness of the spray was uniform throughout its length, this would simply require looking at the number concentration N_{ij}. However, since N_{ij} has units of number per unit volume in space, and the cross sectional area $A(z)$ of our spray is increasing with z, we must use a different measure for our comparisons. For example, if N_{ij} were to appear constant for all z, the actual number of droplets of volume x is in fact increasing as z increases. Thus, to avoid confusion, we choose to compare the number of

droplets per unit length in the z direction. This is simply calculated as

$$\text{No. per unit length} = N_{ij} \times A(z_j). \tag{5.7}$$

Figure 5.1 shows the droplet number per unit length distribution obtained when

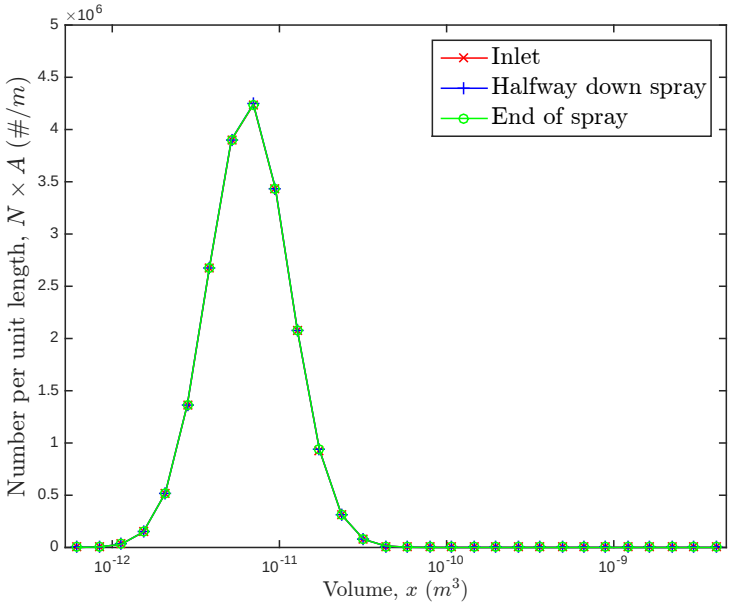

Figure 5.1: Illustrating the droplet number per unit length distribution throughout the spray, for a constant droplet velocity and zero coagulation.

all droplets share the same velocity throughout the spray, with no coagulation. That is to say $u(x, z) = u_{inlet} = 40\,\mathrm{m\,s^{-1}}$, $\forall x,\ z$. As expected, the droplet number per unit length distribution remains constant throughout the length of the spray. The lack of numerical diffusion here is further evidence that the Kurganov-Tadmor scheme is doing a very good job of accurately evolving the transport term from of our system of equations.

5.2.1 Effect of realistic droplet velocity

As mentioned above, we begin by introducing the droplet velocities outlined in Section 2.1.4. These are calculated by solving (2.74) numerically using a Runge-Kutta method. This returns a velocity for each droplet volume size, at each z distance within the system, and these droplet velocities are then assumed to be constant for all time. That is, every single droplet of volume x, at distance z in the spray, will always be assigned exactly the same pre-defined velocity, from the solution of (2.74). Figure 5.2 shows the droplet velocities for various droplet sizes,

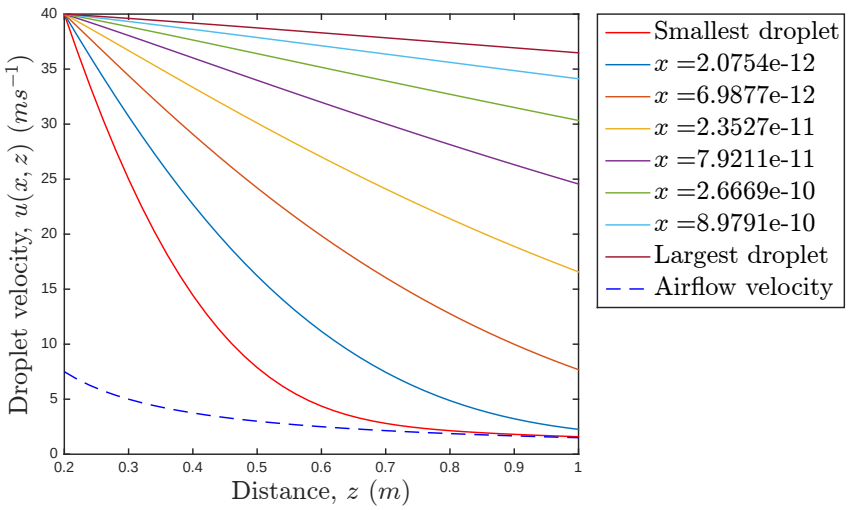

Figure 5.2: Droplet velocities throughout the spray. Here it is assumed the initial velocity of all droplet sizes is the same.

produced by solving equation (2.74). The air velocity used here is co-current, and defined by equation (2.23), with $u_{air}(z_0) = 7.5\,\mathrm{m\,s^{-1}}$ and $z_0 = 0.2\,\mathrm{m}$.

Clearly the velocity of all the droplets decreases as z increases. We observe that the smaller droplets decelerate much faster than the larger droplets. This is due to the fact the larger droplets have the greatest momentum, which lets

them maintain their velocity for longer. The smaller droplets have significantly less momentum, and so aerodynamic drag forces them to decelerate much faster. Note that the velocity of the smallest droplets tends towards the airflow velocity as z increases. This is in agreement with what is observed experimentally, when these fines tend to become entrained within the airflow.

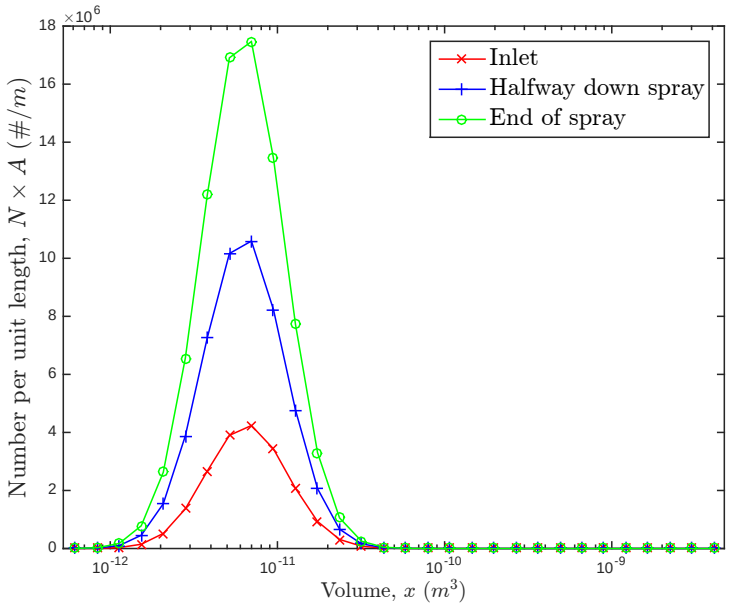

Figure 5.3: Droplet number per unit length distribution throughout the spray, when using realistic droplet velocities, with zero coagulation. A snapshot at $t = t_{max} = 1$.

The effect of using the realistic droplet velocities on the droplet number distribution can clearly be seen in Figure 5.3. Here we see an increase in the number of all droplets at every distance within the spray. This can be explained by the increased residence times caused by the realistic droplet velocities.

On closer inspection, the number of smaller droplets increases very slightly more than that of the larger ones, towards the end of the spray — this can be seen in Figure 5.3 when comparing the distance between the red and green lines

at the outer edges of the bell curves. This increase was observed consistently in multiple simulations for varying inlet velocities and droplet densities, and the trend continued throughout all trials. This can be explained by the increased deceleration of these smaller droplets, which results in them having even longer residence times within the spray. In contrast, the larger droplets maintain more of their velocity as z increases, and so their number decreases slightly less throughout the length of the spray.

5.2.2 Effect of size and velocity dependent kernel

Next, we introduce coagulation to the experiments, in the form of the size and velocity dependent coagulation kernel defined in (2.41) and (2.42). The resulting droplet number distributions can be seen in Figure 5.4.

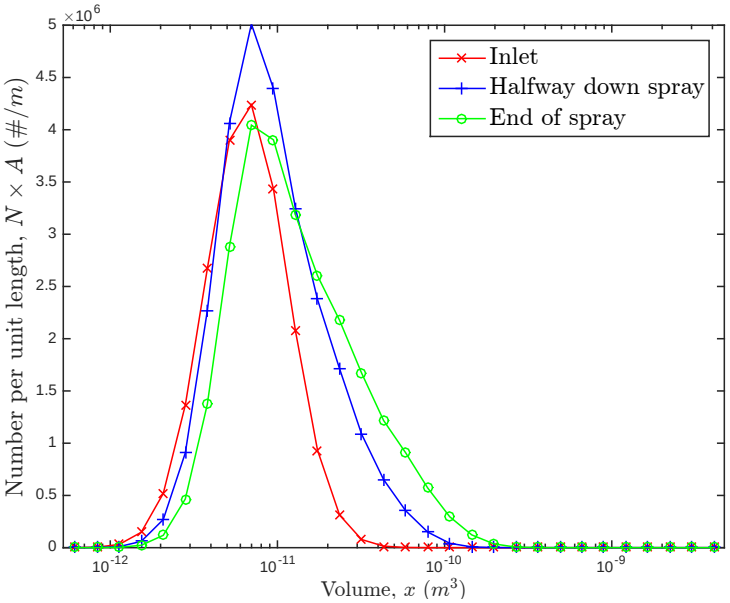

Figure 5.4: Results produced using realistic droplet velocities with the size and velocity dependent coagulation kernel.

This time, we observe a significant increase in the number of larger droplets,

as z increases. This is expected, as using the kernel from (2.41), larger droplets are much more likely to coagulate, as they have both larger diameters and travel at faster velocities than the smaller droplets.

Here, the number of smaller droplets decreases as z increases. However the decrease is not as large as the increase seen in larger drop sizes. This can be explained by the combined effect of their increased residence times, and the fact that these smaller droplets are less likely to coagulate than their larger counterparts.

5.2.3 Effect of varying spray angle

To investigate the effect of varying the spray angle, we increase the air-core angle from $\beta = \pi/3$ to $\beta = 8\pi/9$, whilst keeping the thickness of the spray sheet ($\alpha/2 - \beta/2$) constant at $\pi/36$. The results are plotted in Figure 5.5.

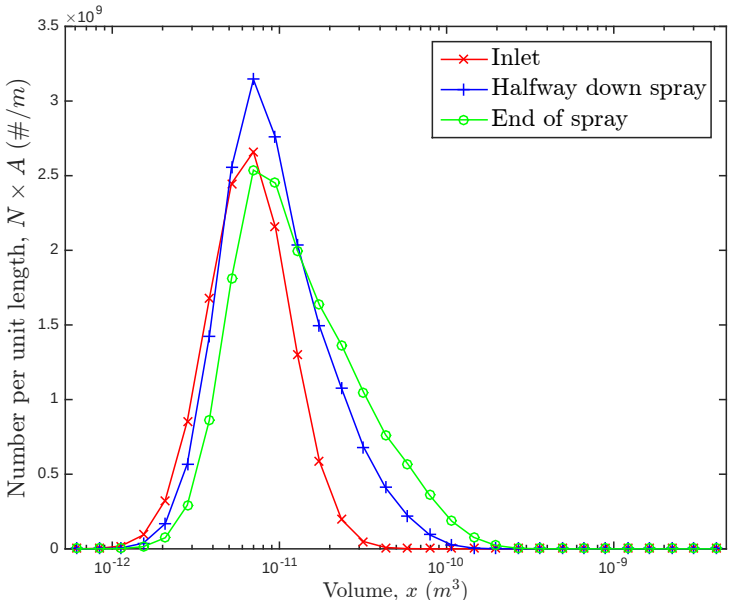

Figure 5.5: Results of increasing the air-core angle from $\beta = \pi/3$ to $\beta = 8\pi/9$, whilst keeping the spray thickness the same. Droplet velocities remain as per Figure 5.2.

Here, we observe an increase in all droplet sizes, as z increases. The increased

air-core angle produces a flatter spray, and reduces the axial velocity of the droplets in the z direction, which leads to increased residence times within the spray for all droplet sizes. The increased angle, with fixed spread angle, also increases the cross-sectional area of the spray, for all z. This results in an increase in the number of droplets per unit length for all points within the spray and the shape of the plot reflects this — it is similar to the plot in Figure 5.4, only translated vertically upwards. So the rates of coagulation are similar to those observed when the air-core angle was smaller. The main result of increasing the air-core angle is simply that the number of droplets per unit length increases at all points within the spray.

5.2.4 Effect of varying spray sheet thickness

Next, we look at the effects of varying the spray sheet thickness. This is done by decreasing the air-core angle to $\beta = \pi/9$, whilst increasing α to $13\pi/9$.

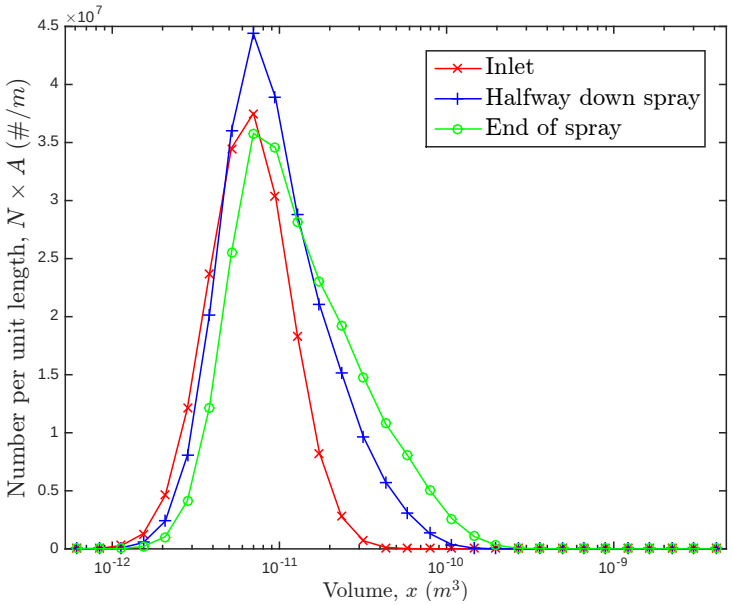

Figure 5.6: Results of increasing the spray sheet thickness. Achieved by decreasing the air-core angle to $\beta = \pi/9$, whilst increasing α to $13\pi/9$. Droplet velocities remain as per Figure 5.2.

The results in Figure 5.6 are similar to the case of increasing the air-core angle. We simply see an increase in the total number of droplets per unit length across all droplet volume ranges. This is explained by the fact the cross-sectional area of the spray is again increased for all z.

5.2.5 Effect of varying droplet density

One of the main design parameters available to process engineers when formulating a new product will be the actual density of the slurry that gets fed into the atomiser nozzle. So here, we investigate the effects of increasing the density from ρ_{drop} =1000 kg m^{-3} to ρ_{drop} =1600 kg m^{-3}.

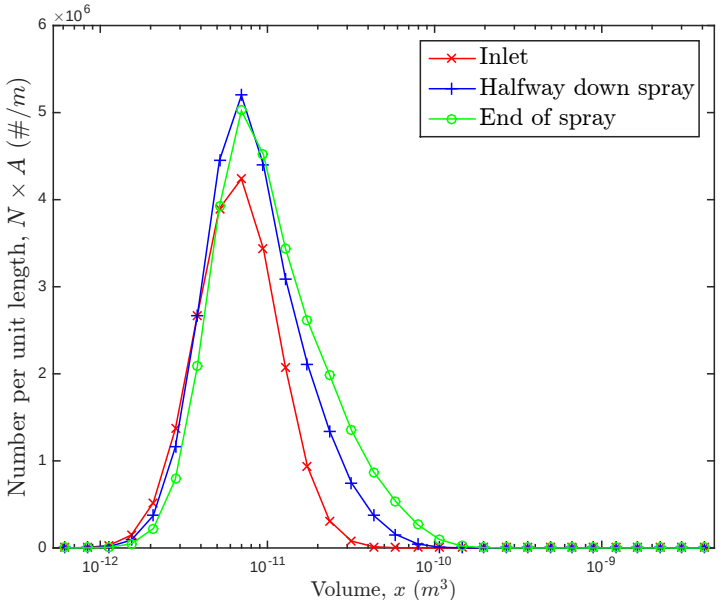

Figure 5.7: Droplet number per unit length distribution throughout the spray resulting from increasing the droplet density from ρ_{drop} =1600 kg m^{-3}.

The resulting number per unit length distribution and droplet velocity profiles are shown in Figures 5.7 and 5.8. From the first of these, it is evident that we still see an increase in smaller droplets toward the end of the spray. The main

difference is the smaller number of larger droplets in comparison to that seen in Figure 5.4. So there is less coagulation taking place when the density of the slurry increases. This decrease in coagulation can be explained by the new droplet velo-

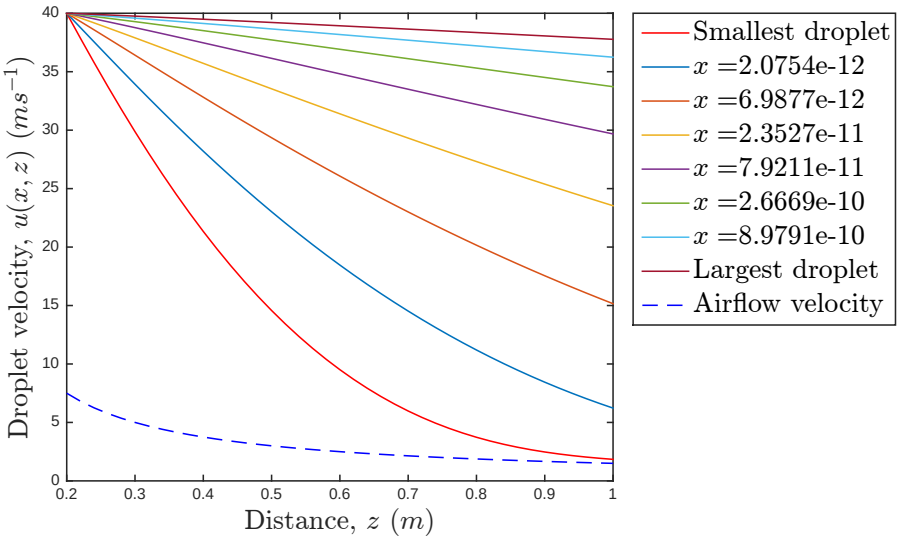

Figure 5.8: Droplet velocities resulting from increasing the droplet density from ρ_{drop} =1600 kg m^{-3}.

city profile pictured in Figure 5.8. Clearly the heavier density droplets maintain their momentum for longer, and so have shorter residence times within the dryer, and thus less time for successful coagulation.

5.2.6 Effect of varying inlet velocity

To investigate the effects of droplet inlet velocity, we reduce the inlet velocity to below that of the inlet air. The results are shown in Figures 5.9 and 5.10.

This agrees with what is observed in Figure 5.9, where there is very little coagulation throughout the length of the spray. These results can be explained by the fact that the droplet velocities converge upon the airflow velocity, and so

the relative velocity between colliding droplets becomes zero. As a result, the coagulation kernel, which depends upon this relative velocity, becomes close to zero, and minimal coagulation events take place.

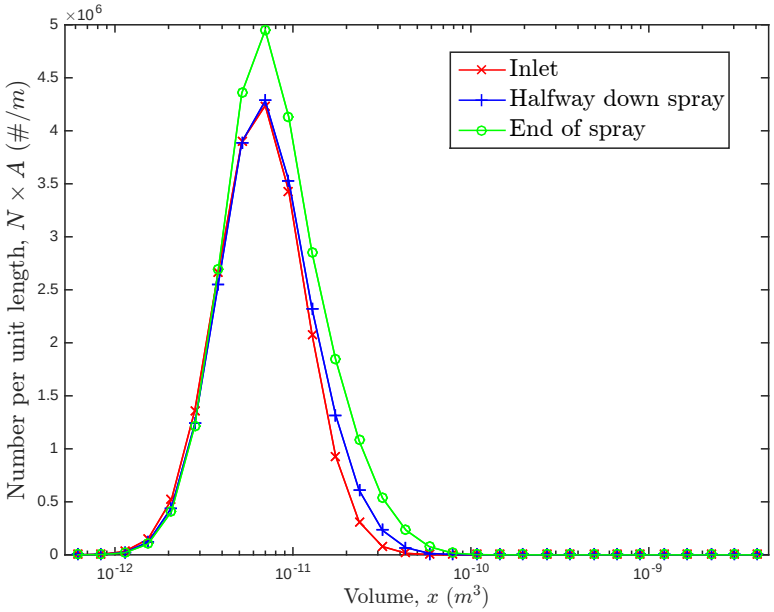

Figure 5.9: Results of decreasing the droplet inlet velocity to $4\,\mathrm{m\,s^{-1}}$. Droplet velocities are shown in Figure 5.10.

From Figure 5.10, we see that all droplet velocities converge upon the airflow's velocity, as z increases.

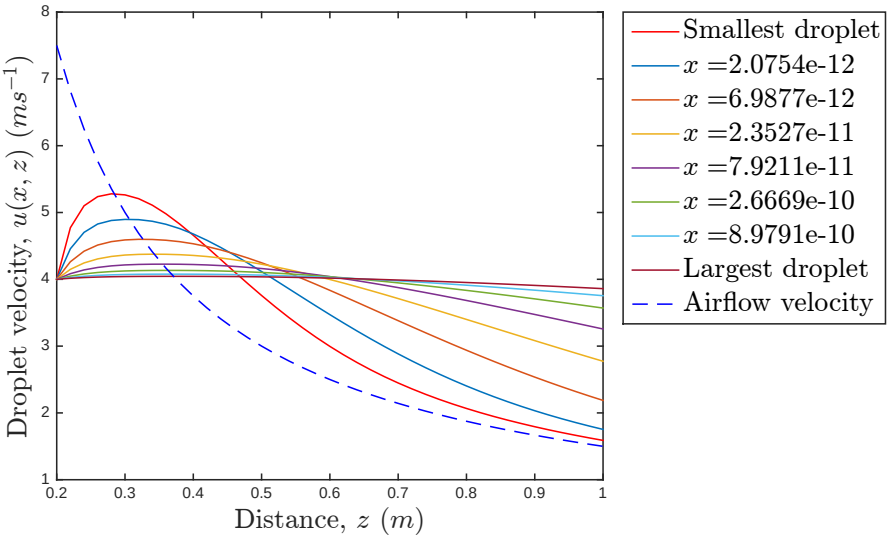

Figure 5.10: New droplet velocities through out the spray when the droplet inlet velocity is decreased to $4\,\mathrm{m\,s^{-1}}$

5.2.7 Effect of varying the efficiency parameter in the coagulation kernel

The last parameter investigation we carry out here is the effect of the efficiency parameter λ from the coagulation kernel (2.41). By its definition, we should expect that an increase in λ would result in increased coagulation within the entire system. So this is another good way to check that the model is functioning correctly.

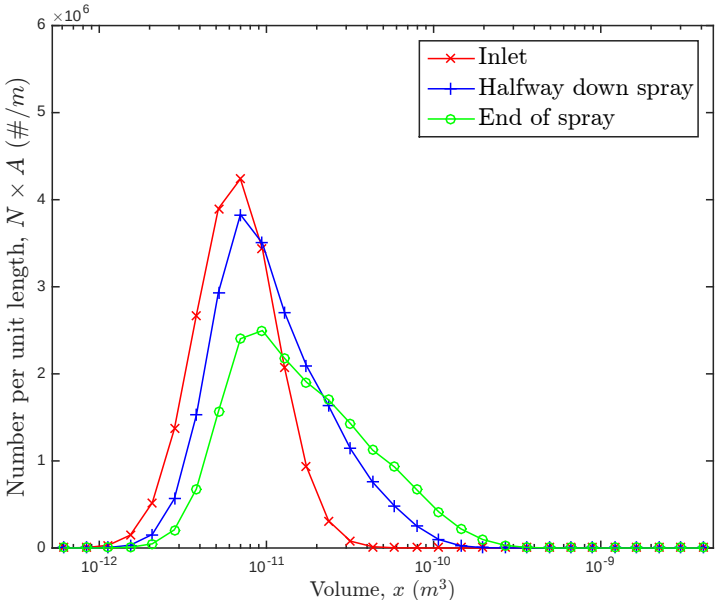

Figure 5.11: Results of increasing the coagulation efficiency parameter from $\lambda = 0.75$ to $\lambda = 1$.

The results are shown in Figure 5.11 where the droplet velocity profile remains identical to that in Figure 5.2. As expected, there is a big increase in larger droplet volumes and a decrease in smaller droplets at the end of the spray. This is an obvious result of increased coagulation within the whole system.

Chapter 6

Incorporation of evaporation

6.1 Modelling growth and coagulation

We next consider the incorporation of evaporation into the spray drying model, to investigate what effect this has on the model's predictions. Since evaporation causes droplets to shrink, it can simply be thought of as droplet growth, with a negative growth rate. So we first investigate the incorporation of growth into the coagulation equation. This is achieved by the addition of a growth term to the LHS of (1.15), and results in the equation

$$\frac{\partial n(x,t)}{\partial t} + \overbrace{\frac{\partial}{\partial x}\Big[\gamma(x)n(x,t)\Big]}^{\text{Growth term}} = \frac{1}{2}\int_0^x K(x-y,y)\,n(x-y,t)n(y,t)\,dy - \int_0^\infty K(x,y)\,n(x,t)n(y,t)\,dy, \quad (6.1)$$

$$\text{where} \quad \gamma(x) = \frac{\partial x}{\partial t}, \;\; x \in \Omega_x, \;\; \text{and} \;\; t \in [0, t_{max}],$$

see [47, 86]. Here, $\gamma(x)$ is the growth (or shrinkage) rate of droplets of volume x and its exact form may be tailored to the particular problem being considered.

This growth rate has units of volume per second, however it may be converted into kg moisture lost per second, to give a rate of the same form as that mentioned earlier in Chapter 1 in equation (1.11).

6.1.1 Exact solutions for the growth-coagulation equation

Similar to the pure coagulation case (1.15), analytic solutions to the growth-coagulation equation (6.1) are only known for a few very specific cases. Most of these make use of either a constant or a linear growth rate, where

$$\gamma(x) = \gamma_0 \ \text{ or } \ \gamma(x) = \gamma_0 x \quad (\gamma_0 \geq 0), \tag{6.2}$$

respectively, [86]. Below, we list some of these known solutions for the case of the negative exponential initial condition given by

$$n(x,0) = \frac{N_0}{x_0} \exp\Big(-\frac{x}{x_0}\Big), \tag{6.3}$$

where N_0 is the initial number of droplets, and x_0 is the mean initial volume of the droplets. The analytic solutions presented will prove useful in evaluating the accuracy of the numerical techniques described later on.

Constant coagulation kernel and linear growth

The first case we look at is that of the constant coagulation kernel, with linear growth, where

$$K(x,y) = K_0, \quad \gamma(x) = \gamma_0\, x,$$

and K_0, γ_0 are positive constants. For the initial condition (6.3), the solution presented in [87, 88] is

$$n(x,t) = \Big[\frac{2}{2+K_0N_0t}\Big]^2 \frac{N_0}{x_0\exp(\gamma_0 t)} \exp\Big[-\frac{2}{2+K_0N_0t}\frac{x}{x_0\exp(\gamma_0 t)}\Big]. \tag{6.4}$$

The zeroth and first moments are

$$M_0(t) = \frac{2N_0}{2+K_0N_0t}, \tag{6.5}$$

$$M_1(t) = N_0x_0\exp(\gamma_0 t). \tag{6.6}$$

Sum coagulation kernel and linear growth

The second case is that of the sum coagulation kernel paired with linear growth. Here,

$$K(x,y) = K_0(x+y), \quad \gamma(x) = \gamma_0\, x,$$

and K_0, γ_0 are again constants. This time, the analytic solution is given in [87, 88] by

$$n(x,t) = \frac{M_0(t)}{x\sqrt{1-M_0(t)/N_0}} \exp\Big[-\frac{M_0(t)}{M_1(t)}\Big(\frac{2N_0}{M_0(t)}-1\Big)x\Big] I_1\Big(2\sqrt{1-\frac{M_0(t)}{N_0}\Big[\frac{N_0x}{M_1(t)}\Big]}\Big), \tag{6.7}$$

where I_1 is the modified Bessel function of the first kind. Here, the corresponding moments at time t take the form

$$M_0(t) = N_0\exp\Big[\frac{K_0N_0x_0}{\gamma_0}\Big(1-\exp(\gamma_0 t)\Big)\Big], \tag{6.8}$$

$$M_1(t) = N_0x_0\exp(\gamma_0 t). \tag{6.9}$$

Constant coagulation kernel and constant growth

The third and final case we look at is that of the constant coagulation kernel, with a constant growth rate, where

$$K(x,y) = K_0, \quad \gamma(x) = \gamma_0,$$

and both K_0 and γ_0 are positive constants. The approximate solution from [87, 88] for this case is

$$n(x,t) = \frac{(M_0(t)^2/M_1(t))}{1 - 2\Lambda x_0(N_0 - M_0(t)/M_1(t))} \times \exp\Big[-\frac{M_0(t)(x - 2\Lambda x_0(N_0/M_0(t) - 1))}{M_1(t)(1 - 2\Lambda x_0(N_0 - M_0(t)/M_1(t)))}\Big], \tag{6.10}$$

where

$$\Lambda = \frac{\gamma_0}{K_0 N_0 x_0},$$

and the zeroth and first moments, respectively, are given by

$$M_0(t) = \frac{2N_0}{2 + K_0 N_0 t}, \tag{6.11}$$

$$M_1(t) = N_0 x_0 \Big[1 - \frac{2\gamma_0}{K_0 N_0 x_0} \ln\Big(\frac{2}{2 + K_0 N_0 t}\Big)\Big]. \tag{6.12}$$

It is important to note here that, for this particular case, the analytic solution is in fact an approximation, and is only valid for larger droplet sizes. This is discussed in [87], and is due to the fact that the solution is derived using a Laplace transform technique which needs to be inverted; however the inverse cannot be determined. Subsequently, to work around this issue, the authors of [87, 88] use a solution which has been approximated using linearisation instead.

6.1.2 Dimensionless growth-coagulation equation

To derive the non-dimensional form of equation (6.1), we use a similar approach to that described in Section 2.2.1. Here, we have no z dependence, so we define the dimensionless variables to be:

$$x = x_0\,\bar{x}, \quad y = x_0\,\bar{y}, \quad t = \frac{\bar{t}}{K_0 N_0}, \quad \text{and} \quad \gamma(x) = x_0 N_0 K_0\,\bar{\gamma}(\bar{x}), \tag{6.13}$$

where

$$N_0 = \int_0^\infty n(x,0)\,dx, \;\; x_0 = \frac{1}{N_0}\int_0^\infty x n(x,0)\,dx, \tag{6.14}$$

and

$$K_0 = \frac{1}{x_0^2}\int_0^\infty\int_0^\infty K(x,y)\,dxdy. \tag{6.15}$$

We can then say that

$$\frac{\partial}{\partial x} = \frac{\partial}{\partial \bar{x}}\frac{\partial \bar{x}}{\partial x} = \frac{1}{x_0}\frac{\partial}{\partial \bar{x}}.$$

Using these non-dimensional variables, equation (6.1) can be rewritten as

$$\begin{aligned} N_0\,K_0\frac{\partial}{\partial \bar{t}}\Big[\frac{N_0}{x_0}\bar{n}(\bar{x},\bar{t})\Big] + \frac{1}{x_0}\frac{\partial}{\partial \bar{x}}\Big[\,x_0 N_0 K_0\,\bar{\gamma}(\bar{x})\,\frac{N_0}{x_0}\bar{n}(\bar{x},\bar{t})\Big] = \\ \frac{1}{2}\int_0^{\bar{x}} K_0\bar{K}(\bar{x}-\bar{y},\bar{y})\frac{N_0}{x_0}\bar{n}(\bar{x}-\bar{y},\bar{t})\frac{N_0}{x_0}\bar{n}(\bar{y},\bar{t})\,x_0\,d\bar{y} \\ -\int_0^\infty K_0\bar{K}(\bar{x},\bar{y})\frac{N_0}{x_0}\bar{n}(\bar{x},\bar{t})\frac{N_0}{x_0}\bar{n}(\bar{y},\bar{t})\,x_0\,d\bar{y}, \end{aligned} \tag{6.16}$$

where, $\bar{K}(\bar{x},\bar{y}) = \frac{1}{K_0} K(x,y)$. Then, on cancelling out the constants and dropping the bars, we end up with the dimensionless equation

$$\frac{\partial n(x,t)}{\partial t} + \frac{\partial}{\partial x}\Big[\gamma(x) n(x,t)\Big] = \frac{1}{2}\int_0^x K(x-y,y)\, n(x-y,t) n(y,t)\, dy - \int_0^\infty K(x,y)\, n(x,t) n(y,t)\, dy. \quad (6.17)$$

Note that with this particular choice of dimensionless variables, the dimensionless equation in (6.17) takes exactly the same form as the original dimensional equation in (6.1).

6.1.3 Previous work — numerical techniques for growth

There have been several attempts to solve (6.1) using cubic splines [89, 90]. However, whilst the results show good agreement with known analytic solutions, the technique is both computationally expensive, and fails to capture the steep advecting fronts commonly found in growth-coagulation problems.

More recent developments have focused on different discretisation techniques for the growth term appearing in (6.1). If we ignore the coagulation terms, we have the pure growth equation

$$\frac{\partial n(x,t)}{\partial t} + \frac{\partial}{\partial x}\Big[\gamma(x) n(x,t)\Big] = 0. \quad (6.18)$$

We define the exact number concentration in the i^{th} droplet volume cell to be

$$N_i^E(t) = \int_{v_i}^{v_{i+1}} n(x,t)\, dx. \quad (6.19)$$

Then, upon integrating (6.18) over the i^{th} droplet volume cell, we arrive at the following equation for the droplet number concentration:

$$\frac{d}{dt}N_i^E(t) = \overbrace{-\Big[\gamma(v_{i+1})n(v_{i+1},t) - \gamma(v_i)n(v_i,t)\Big]}^{\text{Growth Term}}. \tag{6.20}$$

The problem we are faced with here is that the number density is undefined at the cell edges. Thus, the terms $n(v_i,t)$ and $n(v_{i+1},t)$ which appear on the RHS are unknown. To get around this issue, various approximations to the growth term of (6.20) have been presented, some of which are outlined below.

Examples of first and second-order central difference schemes to approximate the growth term have been presented in [91] and [47], respectively. These discretisations take the forms:

$$\text{Growth Term} = \frac{\gamma(v_{i+1})N_{i+1}(t)}{2(v_{i+1}-v_i)} + \frac{\gamma(v_{i+1})-\gamma(v_i)N_i(t)}{2(v_i - v_{i-1})} - \frac{\gamma(v_i)N_{i-1}(t)}{2(v_{i-1}-v_{i-2})} \quad \text{in [91]},$$

$$\text{Growth Term} = \frac{2\gamma(x_i)}{v_i + v_{i+1}}\Big(\frac{v_i v_{i+1}}{v_{i+1}^2 - v_i^2}N_{i-1}(t) + N_i(t) + \frac{v_i v_{i+1}}{v_{i+1}^2 - v_i^2}N_{i+1}(t)\Big) \quad \text{in [47]}.$$

Here, $N_i(t)$ is simply the approximate number concentration in the i^{th} droplet volume cell, such that $N_i(t) \simeq N_i^E(t)$.

The main advantage of these two discretisations is that they are computationally efficient; however both techniques suffer from oscillations where the number density is zero, and also see overpredictions in the tail regions of the droplet number density function due to numerical diffusion.

In [92], an improved discretisation is presented, making use of the method of characteristics for the growth term. This technique produces very accurate results, and avoids both the unwanted oscillations and overpredictions of the techniques

mentioned previously. However the method requires the characteristics used to be known a priori, which is not possible for the majority of particulate processes. For many of these processes, $\gamma(x)$ is not simply a function of x, and will often depend on other unknowns such as temperature and heat transfer coefficients. A more general scheme was later introduced in [86]. Here the cell average technique is used to discretise the growth term; however with careful choice of the approximations used, the technique was shown to reduce to the simple first-order upwind scheme given by

$$\text{Growth term}_i = \gamma(x_{i-1})\,\frac{N_{i-1}(t)}{v_i - v_{i-1}} - \gamma(x_i)\,\frac{N_i(t)}{v_{i+1} - v_i}. \tag{6.21}$$

When it comes to the prediction of the moments, this first-order upwind scheme is only consistent with its predictions of droplet number (zeroth moment), and not mass. However, we will later show how this scheme can be modified to accurately predict the first moment as well. The authors of [86] also commented that (6.21) produces near identical results to those obtained via the cell average technique for the droplet number density.

6.1.4 Discretisation of the growth-coagulation equation

In this section, we present the numerical techniques we later use to discretise the growth term found in (6.17). In doing so, we are interested in formulating a discretisation that accurately predicts both the zeroth and first moments.

At a discrete level, (6.20) is approximated as

$$\frac{d}{dt}\Big(N_i(t)\Big) = -\Big[GP_i(t) - GM_i(t)\Big], \tag{6.22}$$

where

$$GP_i(t) \simeq \gamma(v_{i+1})\, n(v_{i+1}, t), \text{ and } GM_i(t) \simeq \gamma(v_i)\, n(v_i, t). \tag{6.23}$$

Here $GM_i(t)$ and $GP_i(t)$ are the number fluxes of droplets into and out of the i^{th} droplet volume cell due to growth, and hence, for consistency, we assume that

$$GP_i(t) = GM_{i+1}(t). \tag{6.24}$$

The zeroth moment represents the total number of droplets in the system, and so in the case of pure growth, the total number of droplets remains constant; i.e. $\frac{d}{dt}M_0(t) = 0$. Using the relationship (6.24) and summing (6.22) over all i values, the rate of change of the zeroth moment with respect to time can be written as

$$\frac{d}{dt}\,\widetilde{M_0}(t) = \frac{d}{dt}\sum_{i=1}^{I} N_i(t) = GM_1(t) - GP_I(t). \tag{6.25}$$

Here, $\widetilde{M_0}(t)$ is the discrete approximation to the zeroth moment $M_0(t)$. Thus, so long as v_{I+1} is suitably large, such that $n(v_{I+1}, t) \simeq 0$, and $\gamma(v_1) \simeq 0$, then we have the RHS of (6.25) approximately equal to zero. It follows that, no matter how $GM_i(t)$ and $GP_i(t)$ are defined, we will have successfully achieved approximate conservation of the zeroth moment.

Moving on to look at the first moment, if we take the pure growth problem (6.18) and multiply through by x, we have

$$\frac{\partial}{\partial t}\Big(x\, n(x,t)\Big) = -x\,\frac{\partial}{\partial x}\Big[\gamma(x) n(x,t)\Big]. \tag{6.26}$$

Integrating this over the i^{th} cell with respect to x, we have that

$$\begin{aligned}
&\int_{v_i}^{v_{i+1}} \frac{\partial}{\partial t}\Big(x\, n(x,t)\Big)\, dx = -\int_{v_i}^{v_{i+1}} x\, \frac{\partial}{\partial x}\Big[\gamma(x) n(x,t)\Big] dx \\
\implies &\frac{d}{dt}\int_{v_i}^{v_{i+1}} \Big(x\, n(x,t)\Big)\, dx = -\Big[\Big(x\gamma(x) n(x,t)\Big)\Big|_{v_i}^{v_{i+1}} - \int_{v_i}^{v_{i+1}} \Big(\gamma(x) n(x,t)\Big) dx\Big].
\end{aligned}$$

Summing over all i, and using the same assumptions as above, we get the following expression for the rate of change of the first moment with respect to time

$$\frac{d}{dt} M_1(t) \simeq \int_{v_1}^{v_{I+1}} \Big(\gamma(x) n(x,t)\Big) dx. \tag{6.27}$$

At a discrete level, multiplying our approximation for the zeroth moment (6.22) by x_i, and summing over all i values, we arrive at the corresponding approximation for the first moment:

$$\begin{aligned}
\frac{d}{dt}\Big(\widetilde{M}_1(t)\Big) = \sum_{i=1}^{I} \frac{d}{dt}\Big(x_i N_i(t)\Big) &= -\sum_{i=1}^{I} x_i\Big[GP_i(t) - GM_i(t)\Big], \\
&= -\Big[x_1\big(GP_1(t) - GM_1(t)\big) + x_2\big(GP_2(t) - GM_2(t)\big) \\
&\qquad + \ldots + x_I\big(GP_I(t) - GM_I(t)\big)\Big].
\end{aligned} \tag{6.28}$$

The tilde on $\widetilde{M}_1(t)$ is again used to distinguish that this is a discrete approximation to the first moment. Using the relationship in (6.24) and the same assumptions as

before, the sum on the RHS of (6.28) can be written as

$$\begin{aligned}\text{RHS} &= -\Big[x_1 GP_1(t) + x_2\big(GP_2(t) - GP_1(t)\big) + x_3\big(GP_3(t) - GP_2(t)\big) \\ &\qquad\qquad + \ldots + x_I\big(-GP_{I-1}(t)\big)\Big] \\ &= -\Big[-(x_2 - x_1)GP_1(t) - (x_3 - x_2)GP_2(t) \\ &\qquad\qquad - \ldots - (x_I - x_{I-1})GP_{I-1}(t)\Big] \\ &= (x_2 - x_1)GP_1(t) + (x_3 - x_2)GP_2(t) \\ &\qquad + \ldots + (x_I - x_{I-1})GP_{I-1}(t).\end{aligned}$$

Thus, by assuming that there is zero contribution to growth from the boundary terms, we have that

$$\frac{d}{dt}\Big(\widetilde{M}_1(t)\Big) = \sum_{i=1}^{I-1}\big(x_{i+1} - x_i\big)GP_i(t), \tag{6.29}$$

which is clearly an approximation to the integral in (6.27). The choice of $GP_i(t)$ will thus dictate the accuracy of the evolution of the first moment. Whilst there are many possible forms of the growth fluxes $GP_i(t)$ and $GM_i(t)$, we will outline two of the most relevant below.

Modified first-order upwind scheme for growth

The first pairing we present forms the modified first-order upwind scheme outlined in [93], where the authors present a modified version of (6.21) that is designed to accurately predict both the zeroth and the first moments of the droplet size

distribution. For this scheme, we have

$$GP_i(t) = \gamma(x_i)\,\frac{N_i(t)}{x_{i+1} - x_i}, \tag{6.30}$$

$$GM_i(t) = \gamma(x_{i-1})\,\frac{N_{i-1}(t)}{x_i - x_{i-1}}, \tag{6.31}$$

and, as a result, equation (6.29) takes the form

$$\frac{d}{dt}\Big(\widetilde{M}_1(t)\Big) = \sum_{i=1}^{I-1}\big(x_{i+1} - x_i\big)\,\frac{\gamma(x_i)N_i(t)}{x_{i+1} - x_i} = \sum_{i=1}^{I-1}\gamma(x_i)N_i(t). \tag{6.32}$$

The sum on the RHS of (6.32) can be thought of as a mid-point quadrature approximation of the integral in (6.27), with the integral approximated by a sum over each of the sections $[v_i, v_{i+1}]$. Subsequently, this particular choice of $GP_i(t)$ ensures good first and zeroth moment evolution. Due to the approximation only being first-order in nature, we are unlikely to see a good agreement with analytic solutions for the droplet size distribution using this scheme.

In [93], the discretisation (6.30) and (6.31) was combined with finite volume schemes to model coupled problems, involving growth, breakage and coagulation, and the results display good agreement with analytic solutions for the moments. Whilst (6.21) and the sum of the fluxes in (6.30) and (6.31) look very similar, the subtle difference on the denominator makes all the difference to the moments. It is noted, however, that the discretisations are identical for the special case of an equidistant droplet volume grids.

If we combine this modified first-order scheme for growth with the cell average technique for the coagulation terms from [80, 94], we arrive at the discrete growth-

coagulation equation

$$\frac{d}{dt}N_i(t) \;=\; B_i^{CA}(t) \;+\; D_i^{CA}(t) \;+\; \gamma(x_{i-1})\,\frac{N_{i-1}(t)}{x_i - x_{i-1}} \;-\; \gamma(x_i)\,\frac{N_i(t)}{x_{i+1} - x_i}, \quad (6.33)$$

where $B_i^{CA}(t)$ and $D_i^{CA}(t)$ are the cell average birth and death terms, respectively. The full derivation of these can be found in [94, Section 2]. We will later use this discretisation to solve some test problems for combined coagulation and growth.

Second-order upwind scheme for growth

An alternative second-order upwind scheme for growth is outlined in [88, 95]. Using this technique, we again see accurate predictions of the zeroth and first moments, as well as the droplet size distribution. In both papers, however, the scheme is formulated in terms of the mass density of the droplets ($xn(x,t)$), rather than the number density $n(x,t)$ that we have been working with. So here, we outline the form that this second-order scheme takes when applied to the growth term of equation (6.18).

This time, we set the growth fluxes to be

$$\begin{aligned} GP_i(t) &= \gamma(v_{i+1})\left[\frac{N_i(t)}{\Delta x_i} + \frac{\Delta x_i}{2(x_i - x_{i-1})}\Phi(r_i^+(t))\Big(\frac{N_{i+1}(t)}{\Delta x_{i+1}} - \frac{N_i(t)}{\Delta x_i}\Big)\right], \\ GM_i(t) &= \gamma(v_i)\left[\frac{N_{i-1}(t)}{\Delta x_{i-1}} + \frac{\Delta x_{i-1}}{2(x_{i-1} - x_{i-2})}\Phi(r_{i-1}^+(t))\Big(\frac{N_i(t)}{\Delta x_i} - \frac{N_{i-1}(t)}{\Delta x_{i-1}}\Big)\right], \end{aligned} \quad (6.34)$$

where

$$\Phi(r_i^+(t)) = \frac{|r_i^+(t)| + r_i^+(t)}{1 + |r_i^+(t)|}, \quad \text{and} \quad r_i^+(t) = \frac{\left[\frac{N_i(t)}{\Delta x_i} - \frac{N_{i-1}(t)}{\Delta x_{i-1}} + \epsilon\right]}{\left[\frac{N_{i+1}(t)}{\Delta x_{i+1}} - \frac{N_i(t)}{\Delta x_i} + \epsilon\right]}. \quad (6.35)$$

Here, ϵ is some arbitrary, very small number, and has been included to avoid division by zero. The function $\Phi(r_i^+(t))$ is simply a slope limiter function, and this particular form is known as the Van Leer limiter [96].

Note that this time $GP_i(t)$ is a second-order approximation of the growth flux at v_{i+1}. When multiplied by $(x_{i+1} - x_i)$, as per (6.29), we again have a mid-point quadrature approximation to the integral in (6.27), except this time it is summed over the intervals $[x_i, x_{i+1}]$. This time we not only get good first moment evolution, but we also expect a much improved estimate of the droplet size distribution.

Combining (6.34) and (6.35) with the cell average technique for coagulation, we arrive at the following numerical approximation to the growth-coagulation equation (6.1):

$$\frac{d}{dt}N_i(t) = \widetilde{B}_i^{CA}(t) + \widetilde{D}_i^{CA}(t) - \Big[GP_i(t) - GM_i(t)\Big], \tag{6.36}$$

where $\widetilde{B}_i^{CA}(t)$ and $\widetilde{D}_i^{CA}(t)$ are once again the spatially inhomogeneous cell average birth and death terms from [94, Section 2].

We note here, that despite the combination of the cell average technique and the second-order growth scheme being somewhat obvious, it does appear that this may in fact be the first time that they have both been combined to evolve a number density form of the growth-coagulation equation (6.1).

6.1.5 Test cases - combined growth and coagulation

Having established two alternative discretisations for the coagulation-growth equation, we now go on to evaluate the predictions of each using a series of test problems. Here (6.33) and (6.36) are solved numerically using MATLAB's built in Runga-Kutta solver ode45. The results are presented for each of the three cases

outlined in Section 6.1.1 and allow the predictions of the modified first-order upwind scheme to be compared to those of the second-order scheme.

Case 1: Linear growth and constant coagulation

First, we consider the case of linear growth with constant coagulation, where

$$\gamma(x) = x, \text{ and } K(x, y) = 10. \tag{6.37}$$

Since the analytic solution is known for the negative exponential initial distribution in (6.3), we set

$$n(x, 0) = \frac{N_0}{x_0} \exp\Big(-\frac{x}{x_0}\Big), \tag{6.38}$$

and, to allow for comparison with the results presented in [88], we specify

$$N_0 = 5, \text{ and } x_0 = 0.01. \tag{6.39}$$

Equations (6.33) and (6.36) are solved on the geometrically stretched grid defined by (4.2) and (4.3) with parameters

$$v_1 = 1 \times 10^{-5}, \ v_{I+1} = 1 \times 10^{7} \text{ and } I = 200.$$

We have imposed the boundary condition

$$n(x_{min}, t) = n_E(v_1, t), \tag{6.40}$$

where $n_E(v_1, t)$ is the exact analytic solution for the droplets of volume v_1 at time t. By using this boundary condition, we can avoid the discontinuities seen in

the predicted number density of the smaller droplets in [88], and thus establish improved results. The simulations were run until a maximum time of $t_{max} = 10$, and the droplet number density predicted by both the first and second-order schemes have been plotted in Figure 6.1. Plots of the moments can also be seen here, and the corresponding analytic solutions may be found in (6.4), (6.5) and (6.6).

From Figure 6.1, it can be seen that the moments predicted by both the first and second-order schemes are both in excellent agreement with the analytic solutions. Similarly both numerical methods do a very good job of predicting the droplet size distribution, however the first-order scheme clearly loses some of this accuracy as time increases, with the results for $t = 10$ showing some deviation from the exact solution. This is in agreement with the results published in [88], where a similar small loss in accuracy is observed as time progresses. The accuracy has been shown to further improve, however, if the number of grid points I is increased. In comparison, the second-order scheme appears to maintain a superior level of accuracy for all time.

So for this test case, it would appear that the second-order scheme produces the most accurate predictions for all three of these properties of interest.

To investigate the rate of convergence, the above test case was repeated using droplet volume grids of increasing fineness, with $I = 20$, 40, 80, 160, 320 and 640 grid points respectively. For each run, the error in the numerical predictions was then measured using the norm

$$E_I = \sum_{i=1}^{I} \Big| N_i(1) - N_i^E(1) \Big|, \tag{6.41}$$

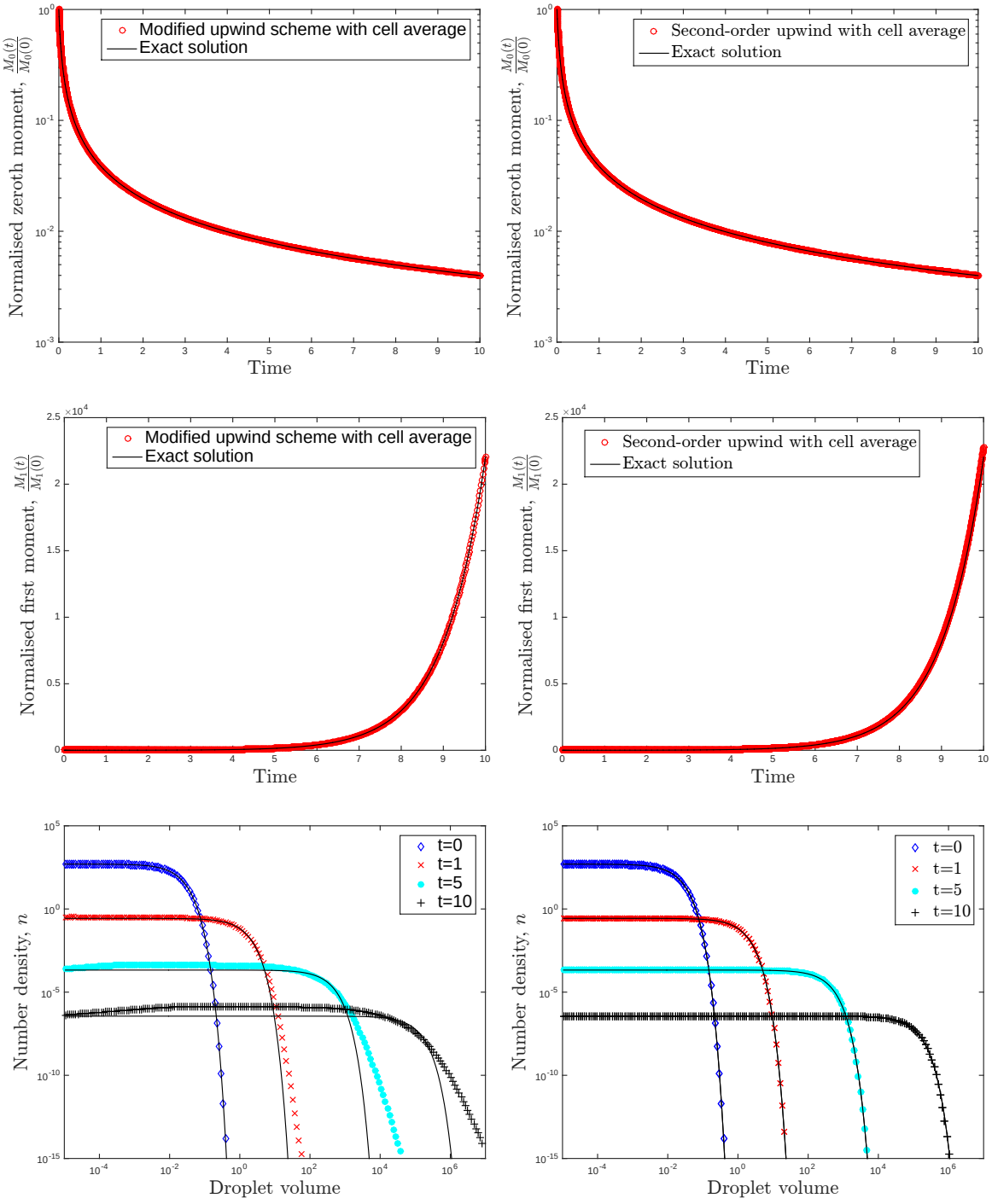

Figure 6.1: Results for linear growth, constant coagulation: $\gamma(x) = x$ and $K(x, y) = 10$. Modified first-order upwind scheme on the left and second-order scheme on the right. Solid lines are analytic solutions.

where $N_i^E(1)$ is the exact number concentration in the i^{th} droplet volume cell, at time $t = 1$, as defined in (6.19). The estimated order of convergence was calculated to be

$$\text{EOC} = \frac{\ln\left[E_I/E_{2I}\right]}{\ln(2)}. \tag{6.42}$$

From Table 6.1, it is clear that the first-order scheme is displaying first-order con-

	First-order scheme		Second-order scheme	
I	E_I	EOC Rate	E_I	EOC Rate
20	2.62×10^{-2}	—	1.92×10^{-2}	—
40	2.07×10^{-2}	0.34	1.62×10^{-2}	0.24
80	1.44×10^{-2}	0.52	4.82×10^{-3}	1.75
160	9.07×10^{-3}	0.67	1.02×10^{-3}	2.24
320	5.38×10^{-3}	0.75	2.23×10^{-4}	2.19
640	3.01×10^{-3}	0.84	5.58×10^{-5}	2.00

Table 6.1: EOC results for the numerical solution of linear growth combined with constant coagulation.

vergence whilst we have second-order convergence for the second-order method. We also note that the error in the second-order scheme's results is smaller than the corresponding error for the first-order scheme for every single value of I. Furthermore, it is observed that this improvement in accuracy increases even more as I is increased, and the grid becomes finer.

Case 2: Linear growth and sum coagulation

Next, we compare the results for the case of linear growth and the sum coagulation kernel, where we set

$$\gamma(x) = x, \text{ and } K(x, y) = x + y. \tag{6.43}$$

We solve equation (6.1) using the same negative exponential initial condition and parameter values defined in (6.38) and (6.39), with the boundary condition (6.40). Here, the geometric grid is defined by

$$v_1 = 1 \times 10^{-5}, \ v_{I+1} = 1 \times 10^4 \text{ and } I = 200. \tag{6.44}$$

In this case, we only integrate in time up until $t_{max} = 3$, as the combined effect of the linear growth with the sum coagulation kernel leads to a quicker increase in the number of larger droplets than in the previous case. The predicted droplet number density has been plotted in Figure 6.2. The corresponding analytic solutions can be found in (6.7), (6.8) and (6.9). From Figure 6.2, it is clear that both first- and second-order schemes capture the evolution of the two moments very well. Similarly, the first-order scheme provides a good estimate of the droplet number density for the smaller volumes, but suffers from slight overpredictions of the larger droplet volumes. We again observe that, in comparison, the second-order scheme does a far better job of resolving the droplet number density, with no loss of accuracy for the larger droplets.

Due to our use of the exact boundary condition (6.40), we see improved results for the smaller droplets, in comparison to those of [88], where the authors simply

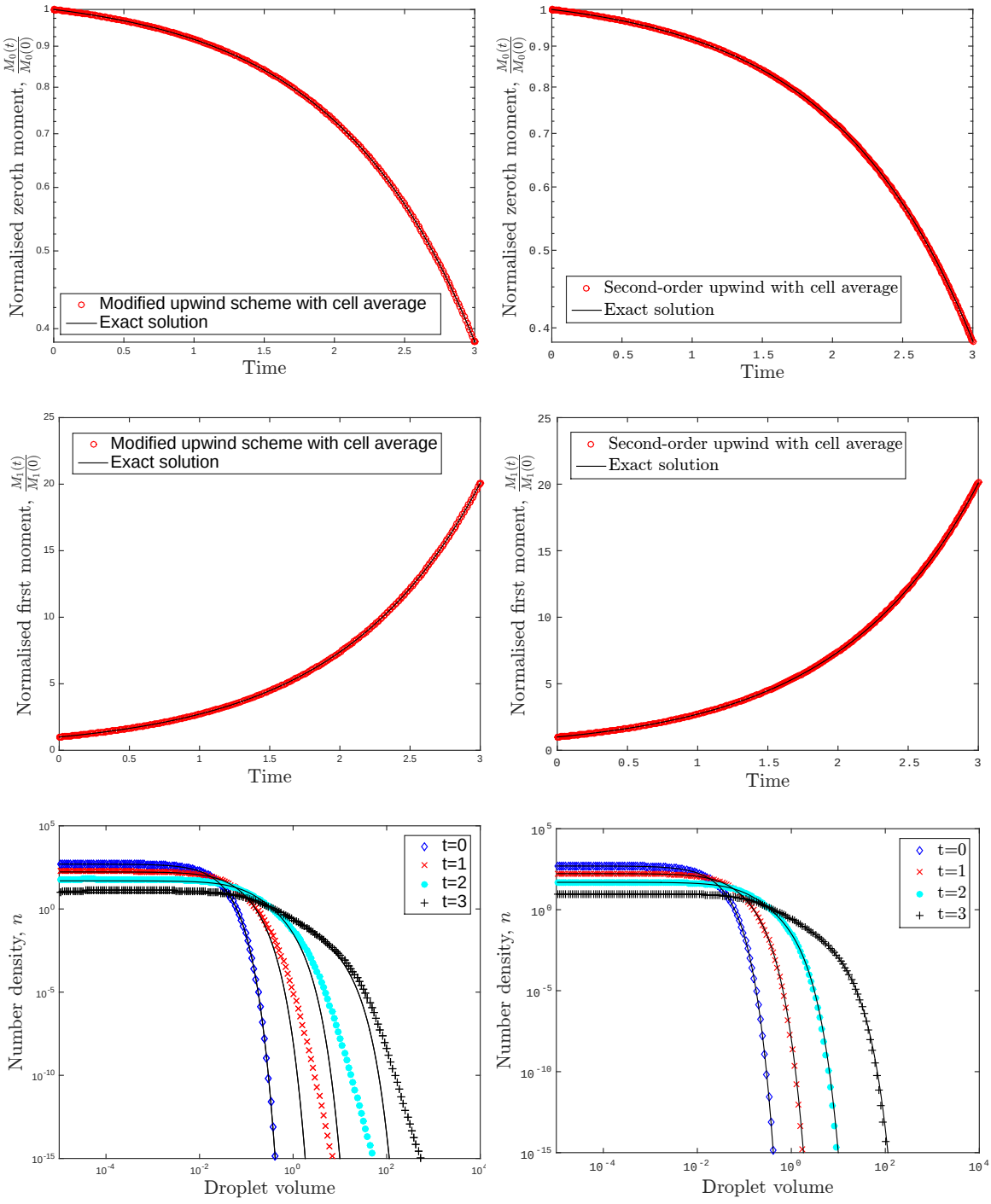

Figure 6.2: Results for linear growth, sum coagulation: $\gamma(x) = x$ and $K(x, y) = x+y$. Modified first-order upwind scheme on the left and second-order scheme on the right. Solid lines are analytic solutions.

set the boundary condition to $n(x_{min}, t) = 0$. It is also noted that the observed overpredictions by the first-order scheme can be reduced by increasing the number of droplet volume grid points used. We have again carried out a convergence

	First-order scheme		Second-order scheme	
I	E_I	EOC Rate	E_I	EOC Rate
20	1.23	—	1.65	—
40	8.60×10^{-1}	0.51	6.07×10^{-1}	1.44
80	5.16×10^{-1}	0.74	1.09×10^{-1}	2.45
160	2.85×10^{-1}	0.86	1.97×10^{-2}	2.46
320	1.51×10^{-1}	0.91	4.20×10^{-3}	2.23
640	7.77×10^{-2}	0.96	9.49×10^{-4}	2.15

Table 6.2: EOC results for the numerical solution of linear growth combined with sum coagulation.

analysis using (6.41) and (6.42), and the results of this can be seen in Table 6.2. Clearly, we again have first and second-order convergence for the respective first and second-order upwind schemes. We also generally observe smaller errors with the second-order scheme.

Case 3: Constant growth and constant coagulation

Finally, we consider the case of constant growth, with constant coagulation. To do so, we solve equation (6.1) for the case of

$$\gamma(x) = 1, \text{ and } K(x, y) = 100. \tag{6.45}$$

We again use the negative exponential initial condition, parameter values and geometric grid as defined in (6.38) and (6.39), combined with the grid parameters

$$v_1 = 1 \times 10^{-5}, \;\; v_{I+1} = 1 \times 10^{6} \;\text{ and }\; I = 200. \tag{6.46}$$

The boundary condition

$$n(x_{min}, t) = 0, \tag{6.47}$$

is imposed, to correspond to that used in [88], and be consistent with the exact solution which becomes zero for $x < t$.

As mentioned previously, in this particular case, the analytic solution is in fact an approximation, and is only valid for larger droplet sizes [87]. Subsequently, we can only assess the predictions of the numerics to plotting accuracy in this case.

The simulations were run until a time of $t_{max} = 10$, and the predicted droplet number density has been plotted in Figure 6.3 at various time steps against the analytic solution (6.10). Plots are also shown of the corresponding normalised zeroth and first moments.

The results in Figure 6.3 show excellent agreement to the analytic solution, for both first- and second-order upwind schemes, for all three of the properties plotted — droplet number density, zeroth and first moments. The predicted droplet size distributions match the analytic solutions at every timestep, for both schemes, with the exception of the smaller droplet sizes, where it is known that the analytic solution is invalid [87, 92]. We also note that the first-order upwind plots match those presented in [88], for the same problem, perfectly. Again we see improved accuracy with the second-order scheme. This is observed by the fact that the jump discontinuity in the droplet number density is resolved better by the second-order

scheme.

Thus, having shown the second-order scheme is consistently more accurate, it is this scheme that we will later incorporate into our model for evaporation in the spray dryer.

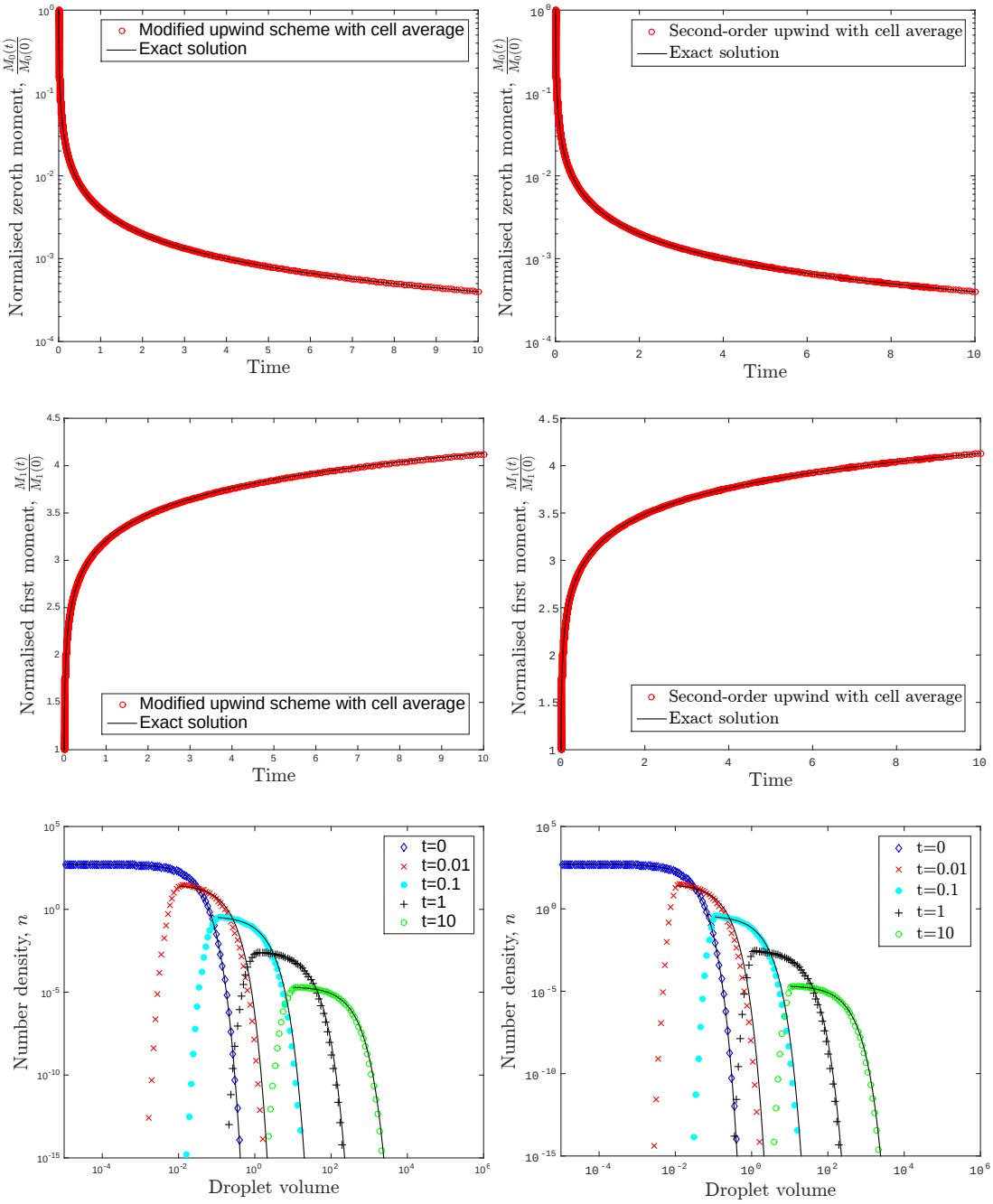

Figure 6.3: Results for constant growth, constant coagulation: $\gamma(x) = 1$ and $K(x, y) = 100$. Modified first-order upwind scheme on the left and second-order scheme on the right. Solid lines are the approximate solutions from (6.10), which are only valid for the larger droplet sizes.

6.2 Evaporation in a spray dryer

As in (6.1), the incorporation of evaporation effects into the spray model is achieved via the introduction of a convective term along the droplet volume range x to equation (2.22) along with the specification of a growth rate $\gamma(x, z)$, where

$$\gamma(x, z) = \frac{\partial x}{\partial t} = \frac{\partial}{\partial t}(\text{Droplet Volume}), \tag{6.48}$$

is the rate of growth/shrinkage of a droplet of volume x within the spray. The addition of this evaporation/growth term results in the new governing PBE for the spray model:

$$\frac{\partial[A(z)n(x,z,t)]}{\partial t} + \overbrace{\frac{\partial[A(z)u(x,z)n(x,z,t)]}^{\text{Transport \& Spray Shape}}}{\partial z} + \overbrace{\frac{\partial[A(z)\gamma(x,z)n(x,z,t)]}^{\text{Evaporation}}}{\partial x} =$$
$$A(z) \times \Big[\frac{1}{2} \underbrace{\int_0^x K(x-y,y,z)n(x-y,z,t)n(y,z,t)\,dy}_{\text{Birth of droplets}}$$
$$- \underbrace{\int_0^\infty K(x,y,z)n(x,r,t)n(y,z,t)\,dy}_{\text{Loss of droplets}} \Big]. \tag{6.49}$$

6.2.1 Derivation of an evaporation rate

Before we go onto solve (6.49) numerically, we must first specify an evaporation rate $\gamma(x, z)$. The form we have opted for is similar to that presented in [97], and is derived below.

For conservation of mass during evaporation, we require

$$\rho_{drop}\,\Delta V_{drop} \;=\; \rho_{gas}\,\Delta V_{gas}, \tag{6.50}$$

where ΔV_{drop} is the change in volume of the evaporating liquid droplet, and ΔV_{gas} is the corresponding change in volume of gas vapour due to evaporation. Here ρ_{gas} is the density of the gas produced by the evaporation.

The change in volume as a function of the liquid droplet's diameter $D = d(x)$ is given by

$$\Delta V_{gas} - \Delta V_{drop} = \Delta\Big(\frac{\pi}{6}D^3\Big). \tag{6.51}$$

Dividing (6.51) by some change in time Δt, we have

$$\frac{\Delta V_{gas}}{\Delta t} - \frac{\Delta V_{drop}}{\Delta t} = \frac{\pi}{6}\frac{\Delta\Big(D^3\Big)}{\Delta t}. \tag{6.52}$$

In the limit as $\Delta t \to 0$, this gives the equation

$$\frac{dV_{gas}}{dt} - \frac{dV_{drop}}{dt} = \frac{\pi}{6}\frac{d}{dt}\Big(D^3\Big) = \frac{\pi}{2}D^2\frac{dD}{dt}. \tag{6.53}$$

From equation (6.50),

$$\Delta V_{gas} \;=\; \frac{\rho_{drop}}{\rho_{gas}}\,\Delta V_{drop}. \tag{6.54}$$

Substituting (6.54) into (6.53) the LHS becomes the expression

$$\frac{\rho_{drop}}{\rho_{gas}}\,\frac{dV_{drop}}{dt} - \frac{dV_{drop}}{dt} = \Big(\frac{\rho_{drop} - \rho_{gas}}{\rho_{gas}}\Big)\,\frac{dV_{drop}}{dt}. \tag{6.55}$$

A thermal energy balance for the heat energy absorbed into the droplet, relative to the energy required to convert a certain mass of liquid into vapour is given by the equation

$$\pi D^2 h_f (T_{gas} - T_{drop})\Delta t = \Delta h_v \rho_{drop} \Delta V_{drop}, \tag{6.56}$$

where Δh_v is the enthalpy of vaporisation of the moisture within the droplet and h_f is the heat transfer coefficient for a single droplet. Here, T_{air} and T_{drop} are the temperature of the air, and the evaporating droplet, respectively.

Equations (6.53) and (6.55) can then be combined with the thermal energy balance in (6.56), to produce the equation

$$\frac{dD}{dt} = \frac{2h_f(T_{gas} - T_{drop})(\rho_{drop} - \rho_{gas})}{\rho_{gas}\rho_{drop}\Delta h_v}. \tag{6.57}$$

To get an expression for $\gamma(x, z)$ from (6.57), we make use of the fact that for a droplet of volume x with diameter $D = (6x/\pi)^{1/3}$,

$$\gamma(x, z) = \frac{dx}{dt} = \frac{dx}{dD}\frac{dD}{dt} = \frac{\pi}{2}D^2 \times \frac{dD}{dt} = \frac{\pi^{1/3}}{2}(6x)^{2/3}\frac{dD}{dt}. \tag{6.58}$$

Since

$$h_f = \frac{k_{air}Nu}{D} = \frac{k_{air}Nu}{(6x/\pi)^{1/3}}, \tag{6.59}$$

this leads to the following equation for the evaporation rate:

$$\gamma(x, z) = -\frac{\pi^{2/3}(6x)^{1/3}k_{air}Nu\,(T_{air} - T_{drop})\,(\rho_{drop} - \rho_{gas})}{\Delta h_v \rho_{drop}\rho_{gas}}. \tag{6.60}$$

Here, k_{air} is the thermal conductivity of air and Nu is the Nusselt number. This evaporation rate describes the evaporation rate of spherical droplets within a liquid flow, and so is perfect for our purposes.

An example of the typical values taken by the parameters found in (6.60),

within a spray dryer, can be found in [57, Table 1]. Here, we have that:

$$k_{air} = 0.03\mathrm{W\,m^{-1}\,K}, \quad T_{air} = 286.35°\mathrm{C}, \quad T_{drop} = 92.35°\mathrm{C}, \quad \rho_{gas} = 0.615\mathrm{kg\,m^{-3}}$$
$$\rho_{drop} = 1566\mathrm{kg\,m^{-3}}, \quad \mu = 2.945 \times 10^{-5}\mathrm{kg/(ms)}, \quad \Delta h_v = 2.26 \times 10^{6}\mathrm{J\,kg^{-1}}.$$

The Nusselt number correlation used comes from [98] and takes the form

$$Nu = 2.0 + 0.6Re^{0.5}Pr^{1/3}, \quad \text{with} \quad Pr = \mu \times c_p/k_{air}, \tag{6.61}$$

where Pr is the Prandtl number and $c_p = 1006\mathrm{J\,kg^{-1}\,K}$ is the specific heat of the gas. Here, the Reynolds number takes the same form as (2.27), and so is given by the equation

$$Re = \frac{\rho_{air} d(x)\,|u(x,z) - u_{air}(z)|}{\mu}. \tag{6.62}$$

From these, we can see that

$$\gamma(x,z) \sim x^{1/3}.$$

Clearly, this means larger droplets will evaporate faster than their smaller counterparts. This is due to the fact they have larger surface areas, and thus a bigger surface in contact with the air, at which evaporation may take place.

6.2.2 Dimensionless growth-coagulation-advection equation

Before we proceed further, we first derive the non-dimensional form of equation (6.49), using the same steps taken in Section 2.2.1. In what follows, the constants N_0, V_0, x_0, K_0, and the non-dimensional variables $\bar{x}$, $\bar{y}$, $\bar{z}$, $\bar{u}$ and $\bar{v}$ are the same as those defined in (2.43) – (2.49). The dimensionless area $\bar{A}(\bar{z})$ can be found in

(2.53), the dimensionless number density $\bar{n}$ in (2.57) and the dimensionless kernel $\bar{K}(\bar{x},\bar{y},\bar{z})$ in (2.52). We again assume that coagulation is the dominant time-scale and, for the time variable, set $t = \bar{t}\,/\,N_0K_0$.

For the growth rate $\gamma(x,z)$, we have that

$$\gamma(x,z) = \frac{\partial x}{\partial t} = x_0 N_0 K_0 \frac{\partial \bar{x}}{\partial \bar{t}}. \tag{6.63}$$

These dimensionless variables can then be used to write equation (6.49) as follows:

$$\begin{aligned} N_0\,K_0\frac{\partial}{\partial \bar{t}}\Big[A_L\bar{A}(\bar{z})\frac{N_0}{x_0}\bar{n}(\bar{x},\bar{z},\bar{t})\Big] \;+\; \frac{1}{L}\frac{\partial}{\partial \bar{z}}\Big[A_L\bar{A}(\bar{z})u_0\bar{u}(\bar{x},\bar{z})\frac{N_0}{x_0}\bar{n}(\bar{x},\bar{z},\bar{t})\Big] \\ + \frac{1}{x_0}\frac{\partial}{\partial \bar{x}}\Big[A_L\bar{A}(\bar{z})\,x_0N_0K_0\,\bar{\gamma}(\bar{x},\bar{z})\,\frac{N_0}{x_0}\bar{n}(\bar{x},\bar{z},\bar{t})\Big] = \\ A_L\bar{A}(\bar{z}) \times \Big[\frac{1}{2}\int_0^{\bar{x}} K_0\bar{K}(\bar{x}-\bar{y},\bar{y},\bar{z})\frac{N_0}{x_0}\bar{n}(\bar{x}-\bar{y},\bar{z},\bar{t})\frac{N_0}{x_0}\bar{n}(\bar{y},\bar{z},\bar{t})\,x_0\,d\bar{y} \\ - \int_0^{\infty} K_0\bar{K}(\bar{x},\bar{y},\bar{z})\frac{N_0}{x_0}\bar{n}(\bar{x},\bar{z},\bar{t})\frac{N_0}{x_0}\bar{n}(\bar{y},\bar{z},\bar{t})\,x_0\,d\bar{y}\Big]. \end{aligned} \tag{6.64}$$

Grouping all the constants together, this becomes

$$\begin{aligned} \frac{A_LN_0^2K_0}{x_0}\frac{\partial[\bar{A}(\bar{z})\bar{n}(\bar{x},\bar{z},\bar{t})]}{\partial \bar{t}} + \frac{A_Lu_0N_0}{Lx_0}\frac{\partial[\bar{A}(\bar{z})\bar{u}(\bar{x},\bar{z})\bar{n}(\bar{x},\bar{z},\bar{t})]}{\partial \bar{z}} \\ + \frac{A_LK_0N_0^2\bar{A}(\bar{z})}{x_0}\frac{\partial}{\partial \bar{x}}\Big[\,\bar{\gamma}(\bar{x},\bar{z})\,\bar{n}(\bar{x},\bar{z},\bar{t})\Big] = \\ A_L\bar{A}(\bar{z}) \times \frac{K_0N_0^2}{x_0}\Big[\,\frac{1}{2}\int_0^{\bar{x}} \bar{K}(\bar{x}-\bar{y},\bar{y},\bar{z})\bar{n}(\bar{x}-\bar{y},\bar{z},\bar{t})\bar{n}(\bar{y},\bar{z},\bar{t})\,d\bar{y} \\ - \int_0^{\infty} \bar{K}(\bar{x},\bar{y},\bar{z})\bar{n}(\bar{x},\bar{z},\bar{t})\bar{n}(\bar{y},\bar{z},\bar{t})\,d\bar{y}\Big]. \end{aligned} \tag{6.65}$$

Simplifying (6.65), and using (2.55) for the specific cross-sectional area of the spray, produces the non-dimensional form of the combined growth, coagulation

and advection equation (6.49):

$$\frac{\partial}{\partial \bar{t}}\Big[\bar{z}^2\bar{n}(\bar{x},\bar{z},\bar{t})\Big]+\frac{u_0}{N_0K_0L}\frac{\partial}{\partial \bar{z}}\Big[\bar{z}^2\bar{u}(\bar{x},\bar{z})\bar{n}(\bar{x},\bar{z},\bar{t})\Big] + \bar{z}^2\frac{\partial}{\partial \bar{x}}\Big[\bar{\gamma}(\bar{x},\bar{z})\,\bar{n}(\bar{x},\bar{z},\bar{t})\Big] = \bar{z}^2\times\Big[\frac{1}{2}\int_0^{\bar{x}}\bar{K}(\bar{x}-\bar{y},\bar{y},\bar{z})\bar{n}(\bar{x}-\bar{y},\bar{z},\bar{t})\bar{n}(\bar{y},\bar{z},\bar{t})\,d\bar{y} - \int_0^{\infty}\bar{K}(\bar{x},\bar{y},\bar{z})\bar{n}(\bar{x},\bar{z},\bar{t})\bar{n}(\bar{y},\bar{z},\bar{t})\,d\bar{y}\Big]. \quad (6.66)$$

Dropping the bars for notational convenience, (6.66) can be written as

$$\frac{\partial}{\partial t}\Big[z^2n(x,z,t)\Big] + q_0\frac{\partial}{\partial z}\Big[z^2u(x,z)n(x,z,t)\Big] + z^2\frac{\partial}{\partial x}\Big[\,\gamma(x,z)\,n(x,z,t)\Big] = z^2\times\Big[\frac{1}{2}\int_0^{x}K(x-y,y,z)n(x-y,z,t)n(y,z,t)\,dy - \int_0^{\infty}K(x,y,z)n(x,z,t)n(y,z,t)\,dy\Big], \quad (6.67)$$

$$\text{where}\quad q_0=\frac{u_0}{N_0K_0L}\qquad\Big(=\frac{\text{Coagulation time-scale}}{\text{Advection time-scale}}\Big), \quad (6.68)$$

$$\text{and}\quad K(x,y,z)=C\times(x^{1/3}+y^{1/3})^2|v(x,z)-v(y,z)|. \quad (6.69)$$

Note that here, q_0 is the same ratio of coagulation and advection time-scales seen previously in (2.63) in Section 2.2.1.

6.2.3 Existing results for growth-coagulation-advection equations

At this stage, as in Chapter 3, we briefly investigate whether any existing analytic results may be applied to the system described by equations (6.67) – (6.69). Assuming that time is suitably large enough, such that a steady-state system has

been achieved, we can say that any steady-state solution to (6.67) must satisfy the equation:

$$q_0 \frac{\partial}{\partial z}\Big[z^2 u(x,z)n(x,z)\Big] + z^2 \frac{\partial}{\partial x}\Big[\gamma(x,z)\, n(x,z)\Big] = z^2 \times \Big[\frac{1}{2}\int_0^x K(x-y,y,z)n(x-y,z)n(y,z)\,dy - \int_0^\infty K(x,y,z)n(x,z)n(y,z)\,dy\Big]. \quad (6.70)$$

If we then set

$$c_s(x,s) = z^2 n(x,z) \quad \text{and} \quad k(x,y,z) = \frac{K(x,y,z)}{z^2}, \quad (6.71)$$

equation (6.67) becomes

$$q_0 \frac{\partial}{\partial z}\Big[u(x,z)c_s(x,z)\Big] + \frac{\partial}{\partial x}\Big[\gamma(x,z)\, c_s(x,z)\Big] = \Big[\frac{1}{2}\int_0^x k(x-y,y,z)c_s(x-y,z)c_s(y,z)\,dy - \int_0^\infty k(x,y,z)c_s(x,z)c_s(y,z)\,dy\Big]. \quad (6.72)$$

This can be further simplified by defining

$$f(x,z) = u(x,z)c_s(x,z), \;\; \widetilde{k}(x,y,z) = \frac{k(x,y,z)}{q_0 u(x,z)u(y,z)}, \;\; \text{and} \;\; \widetilde{\gamma}(x,z) = \frac{\gamma(x,z)}{q_0 u(x,z)}, \quad (6.73)$$

from which (6.72) can then be written in the form

$$\frac{\partial}{\partial z}\Big[f(x,z)\Big] + \frac{\partial}{\partial x}\Big[\widetilde{\gamma}(x,z)\, f(x,z)\Big] = \Big[\frac{1}{2}\int_0^x \widetilde{k}(x-y,y,z) f(x-y,z) f(y,z)\, dy - \int_0^\infty \widetilde{k}(x,y,z) f(x,z) f(y,z)\, dy\Big]. \quad (6.74)$$

The form of (6.74) is that of a standard Smoluchowski equation with an additional growth term, for which a limited number of analytical results are available within the literature.

In [99], analytic solutions are presented for combined nucleation, growth and aggregation of particles; however the results are limited to very specific growth rates (constant/linear) and coagulation kernels (sum/constant), and so cannot be applied to our spatially dependent coagulation kernel. Similar results are presented in [100], but once again we find that solutions are only shown for very specific combinations of coagulation kernel and growth rate.

The results in [68], detailed in Section 3.1 may also have proved useful, however again we are limited by the fact that these require our kernel to be bounded. Similarly, the results from [67] are not applicable here either, as they require the kernel to depend upon size alone, and so cannot be applied to a spatially dependent kernel.

Thus, in the absence of analytic solutions applicable to (6.70), we again look to a numerical approach to solve the case of combined growth and evaporation within our spray.

6.2.4 Discretised growth-coagulation-advection equation

To discretise the growth term from (6.67), we employ the moment-preserving second-order upwind scheme for growth that is presented in (6.36).

The growth term from equation (6.67) states that change in the droplet number density due to growth is given by the equation

$$z^2 \frac{\partial n(x,z,t)}{\partial t} = -\frac{\partial}{\partial x}\Big[z^2 \gamma(x,z)\, n(x,z,t)\Big]. \tag{6.75}$$

Integrating over the cell Ω_{ij}, we have

$$\int_{z_{j-1/2}}^{z_{j+1/2}} \int_{v_i}^{v_{i+1}} z^2 \frac{\partial n(x,z,t)}{\partial t}\, dxdz \;=\; -\int_{z_{j-1/2}}^{z_{j+1/2}} z^2 \int_{v_i}^{v_{i+1}} \frac{\partial}{\partial x}\Big[\gamma(x,z)\, n(x,z,t)\Big]\, dxdz. \tag{6.76}$$

The expression on the LHS of (6.76) can be approximated using the midpoint rule for the z integration. Doing so, the LHS of (6.76) becomes

$$\int_{z_{j-1/2}}^{z_{j+1/2}} \int_{v_i}^{v_{i+1}} \frac{\partial}{\partial t}\Big[z^2 n(x,z,t)\Big] dx\, dz \simeq \frac{d}{dt}\Big[V_j N_{ij}(t)\Big], \tag{6.77}$$

where

$$V_j \equiv \Delta z \times z_j^2. \tag{6.78}$$

Carrying out the x integration on the RHS of (6.76), we have

$$\text{RHS} = -\int_{z_{j-1/2}}^{z_{j+1/2}} z^2 \Big[\gamma(v_{i+1},z)\, n(v_{i+1},z,t) - \gamma(v_i,z)\, n(v_i,z,t)\Big]\, dz. \tag{6.79}$$

Using the midpoint rule for the z integration, this leads to the equation

$$\begin{aligned}\text{RHS} &= -(z_{j+1/2} - z_{j-1/2}) z_j^2 \Big[\gamma(v_{i+1}, z_j)\, n(v_{i+1}, z_j, t) - \gamma(v_i, z_j)\, n(v_i, z_j, t)\Big] \\ &= V_j \Big[\gamma(v_i, z_j)\, n(v_i, z_j, t) - \gamma(v_{i+1}, z_j)\, n(v_{i+1}, z_j, t)\Big]. \end{aligned} \tag{6.80}$$

Since the droplet number density is calculated at the representative droplet sizes x_i, we do not know the droplet number densities $n(v_i, z_j, t)$ at the cell edges that appear in the above and so these have to be approximated.

To begin the process, we let

$$\begin{aligned} GP_{ij}(t) &\simeq \gamma(v_{i+1}, z_j)\, n(v_{i+1}, z_j, t), \\ GM_{ij}(t) &\simeq \gamma(v_i, z_j)\, n(v_i, z_j, t). \end{aligned}$$

then approximate the $GP_{ij}(t)$ and $GM_{ij}(t)$ terms using the second-order upwind approximation from [95]. To achieve this, we set

$$\begin{aligned} GP_{ij}(t) &\simeq \gamma(v_{i+1}, z_j) \left[n_{ij}(t) + \frac{\Delta x_i}{2(x_i - x_{i-1})} \Phi(r_{ij}^+(t)) \Big(n_{i+1\,j}(t) - n_{ij}(t)\Big)\right], \\ GM_{ij}(t) &\simeq \gamma(v_i, z_j) \left[n_{i-1\,j}(t) + \frac{\Delta x_{i-1}}{2(x_{i-1} - x_{i-2})} \Phi(r_{i-1\,j}^+(t)) \Big(n_{ij}(t) - n_{i-1\,j}(t)\Big)\right], \end{aligned} \tag{6.81}$$

where

$$\Phi(r_{ij}^+(t)) = \frac{|r_{ij}^+(t)| + r_{ij}^+(t)}{1 + |r_{ij}^+(t)|}, \quad r_{ij}^+(t) = \frac{n_{ij}(t) - n_{i-1\,j}(t) + \epsilon}{n_{i+1\,j}(t) - n_{ij}(t) + \epsilon} \text{ and } n_{ij}(t) \simeq \frac{N_{ij}(t)}{\Delta x_i}. \tag{6.82}$$

Here, $\epsilon \ll 1$ is some arbitrary small number, and has been included to avoid division by zero. Combined, equations (6.80) – (6.82) give us the discrete growth

term for our spray equation

$$\widetilde{G}_{ij}(t) = V_j \times \Big[GP_{ij}(t) - GM_{ij}(t) \Big]. \tag{6.83}$$

Finally, we add this new growth term into our existing discrete system of equations for the spray (4.51). The existing discrete transport, birth and death terms, can be found in (4.23), (4.50) and (4.27) respectively. Combined with (6.83), they result in the coupled system of ordinary differential equations

$$\frac{d}{dt} N_{ij}(t) = \frac{1}{V_j} \Big[\widehat{B}_{ij}^{CA}(t) + \widetilde{D}_{ij}(t) - \widetilde{T}_{ij}(t) - \widetilde{G}_{ij}(t) \Big], \tag{6.84}$$

where

$$1 \leq i \leq I \ \text{ and } \ 1, \leq j \leq J. \tag{6.85}$$

This is our discrete approximation to equation (6.67).

The novel combination of numerical techniques found in (6.84) results in our discrete approximation being second-order accurate for all three of the processes being modelled — growth, transport and coagulation. As far as we are aware, this is also the first time that this particular combination of the cell average technique, the Kurganov-Tadmor scheme and the second-order upwind scheme for growth has been applied.

6.2.5 Test cases — evaporation in a spray dryer

Having established the discrete form of the spray equation (6.84), incorporating growth, coagulation and advection, we now go on to investigate the effects of varying various parameters found within the model. Here, we look at the case of a co-current dryer, spraying water into a flow of hot air, and run a series of test cases. Throughout these examples, we will use the realistic droplet velocities defined by (2.31) and the co-current airflow velocity defined by (2.23).

To allow for comparisons to be made when a physical variable is changed, we first define a base setting for the physical parameters in the model. These base settings are:

$$\begin{array}{ccc} \rho_{air} = 0.746\,\mathrm{kg\,m^{-3}}, & \rho_{drop} = 999.7\,\mathrm{kg\,m^{-3}}\ , & \mu = 2.577\times10^{-5}\ \mathrm{kg/(ms)}, \\ L = 1\,\mathrm{m}, & z_0 = 0.2\,\mathrm{m}, & \lambda = 0.75. \\ d_{min} = 100\,\mu\mathrm{m}, & d_{max} = 2080\,\mu\mathrm{m}, & \frac{\beta}{2} = \frac{\pi}{6}, \frac{\alpha}{2} = \frac{7\pi}{36} \\ \Delta h_v = 2.478\times10^{6}\mathrm{J\,kg^{-1}}, & u_{inlet} = 15\,\mathrm{m\,s^{-1}}, & u_{air}(z_0) = 7.5\,\mathrm{m\,s^{-1}}\ . \\ T_{air} = 200^{\circ}\mathrm{C}, & k_{air} = 0.038\mathrm{W\,m^{-1}\,K}, & T_{drop} = 10^{\circ}\mathrm{C}\ . \end{array}$$

The physical properties of water and air found in the above list are taken from the reference tables in [101, Appendix 1].

For simplicity, it is assumed that the internal temperature of all water droplets remains constant at T_{drop} for a droplet's entire residence within the dryer. Similarly, it is assumed that we have a constant air temperature T_{air} throughout the entire length of the drying tower.

In what follows, we solve (6.49) numerically, using the base settings above, and the inlet droplet distribution (5.6) with $N_{part} = 1\times10^{9}$, $x_{50} = 6.545\times10^{-12}$ m^3 and $\sigma = \log(1.75)$.

Case 1 - No evaporation

First, we present results for just transport. This allows for comparisons to be made when evaporation and coagulation are later switched on. Here, only the realistic droplet velocities affect the droplet number distribution throughout the length of the spray, and both coagulation and evaporation terms are set to zero.

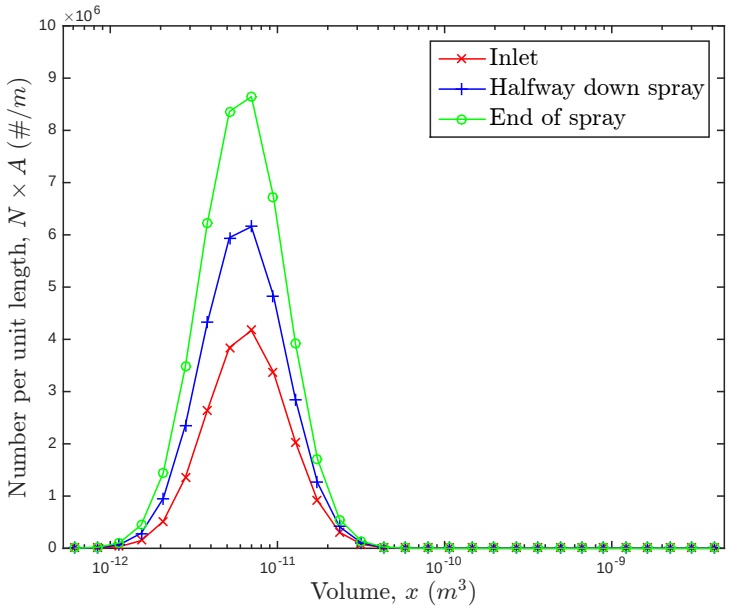

Figure 6.4: A reference run with realistic droplet velocities, but no evaporation or coagulation. The plot illustrates the resulting droplet number per unit length distribution throughout the length of the spray.

Case 2 - Physically realistic evaporation rate

Next we introduce the realistic evaporation rate from (6.60) and (6.61). The results of solving (6.49) numerically, with evaporation turned on, are illustrated in Figure 6.5. Here, an increase is observed in the number of smaller droplet sizes at the end of the spray when compared to the results seen in Figure 6.4 where evaporation is absent. Similarly, we see a small decrease in the number of larger droplets with

this example too. These observations are both in line with what we would expect to see for evaporating droplets.

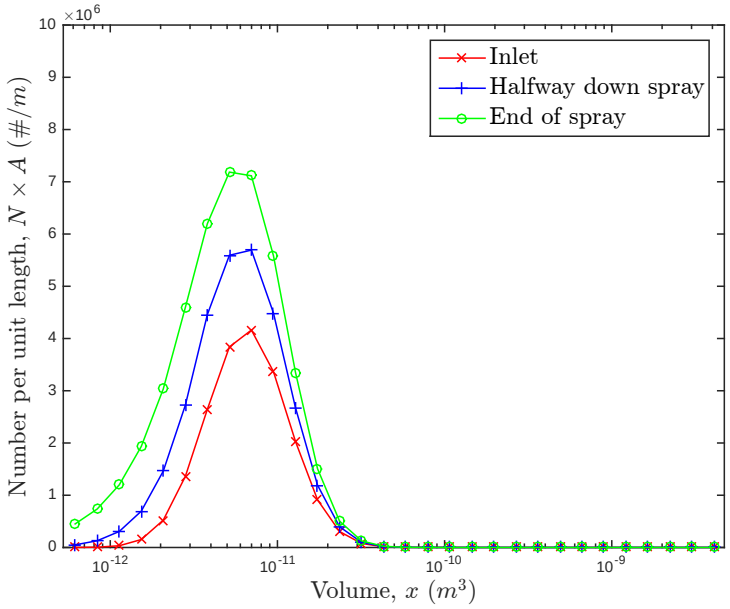

Figure 6.5: Effect of turning on evaporation, using the evaporation rate (6.60). The plot illustrates the droplet number per unit length distribution throughout the spray.

To illustrate the effect of evaporation on an individual droplet, we have also plotted the volume lost from a droplet during its residence time within the dryer tower in Figure 6.6. Clearly the volume lost is directly proportional to the droplet's initial volume, with the larger droplets shrinking more due to evaporation than the smaller ones. This is to be expected, as the larger drops have a larger surface area available for evaporation to take place over.

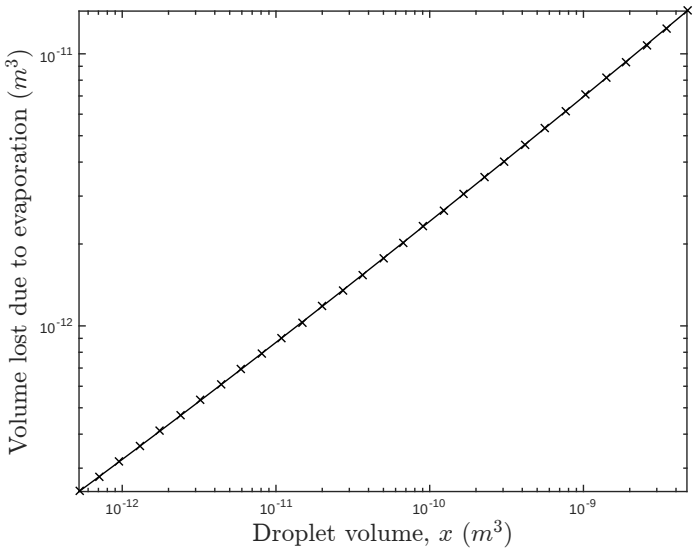

Figure 6.6: Plot of the theoretical volume lost due evaporation during a droplet's residence time within the dryer, using the evaporation rate from equation (6.60). All droplets are initially travelling at $15\mathrm{m\,s^{-1}}$, through co-current air with a temperature of 200°C, and initial air velocity $7.5\mathrm{m\,s^{-1}}$.

Case 3 - Effects of combined evaporation & coagulation

Now we look at the effect of adding coagulation into the equation. The results of solving (6.49) for combined coagulation, advection and evaporation are shown in Figure 6.7.

The results in Figure 6.7 clearly show that coagulation has caused a small increase in the number of larger droplets towards the end of the spray, compared to the results in both Figures 6.4 and 6.5. What can also be seen, although the difference is more subtle, is that there is also a small decrease in the number of small to medium size droplets, when compared to the results in Figure 6.5. This is in line with what we would expect when coagulation is occurring.

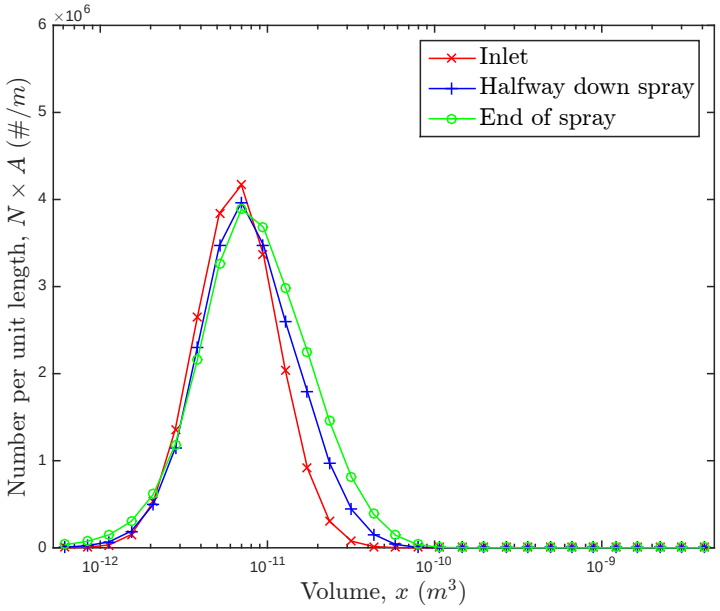

Figure 6.7: Combined effects of evaporation, coagulation and advection, as per the base settings. The plot illustrates the droplet number per unit length distribution within the spray.

Case 4 - Effects of varying air temperature

We now consider the effects of varying the air temperature within the drying tower. To achieve this, we increase the air temperature from $T_{air} = 200°\text{C}$ to $T_{air} = 300°\text{C}$. In doing so, we must also scale the values of the air's other physical quantities accordingly. The required values of these can again be found in [101, Appendix 1], and take the form:

$$\rho_{air} = 0.616\,\text{kg}\,\text{m}^{-3} \qquad \mu = 2.934 \times 10^{-5}\ \text{kg/(ms)},$$
$$k_{air} = 0.044\text{W}\,\text{m}^{-1}\,\text{K}, \qquad c_p = 1044\text{J}\,\text{kg}^{-1}\,\text{K}\ .$$

The results are shown in Figure 6.8, and this time we observe an increase in the total number of smaller particles, relative to Figure 6.7. This can be attributed to the higher air temperature creating more evaporation within the dryer, and thus

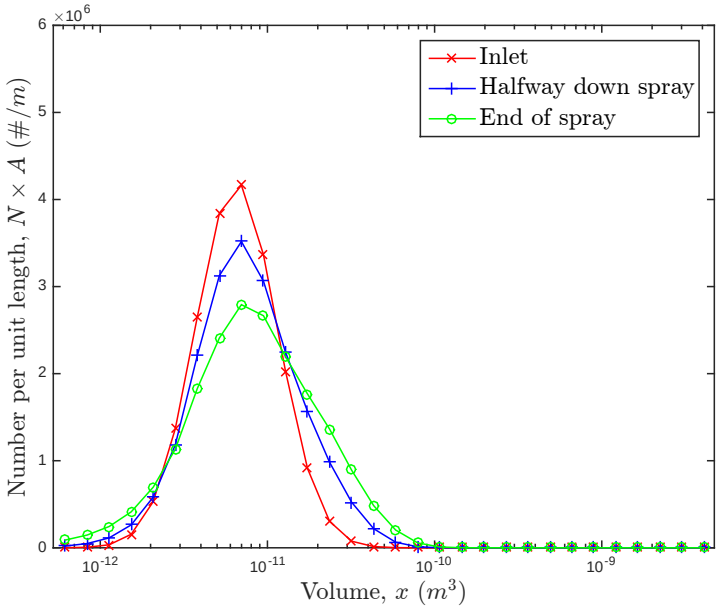

Figure 6.8: Results show the effect of increasing the air temperature to T_{air} = 300°C. The plot illustrates the droplet number per unit length distribution within the spray.

a shift in the number distribution towards more smaller droplets, and less larger ones.

Case 5 - Effects of varying droplet temperature

Here we increase the droplet's temperature from 10°C to 80°C, whilst returning the air's temperature, and other associated parameter values, to the base settings linked to T_{air} = 200°C.

From the results in Figure 6.9, it appears that increasing the droplet's initial temperature reduces the amount of evaporation taking place within the dryer. This appears to produce a decrease in smaller droplets, and an increase in the number of mid-size droplets compared to both Figures 6.7 and 6.8. For this particular case, it appears to narrow the range of the final droplet size distribution.

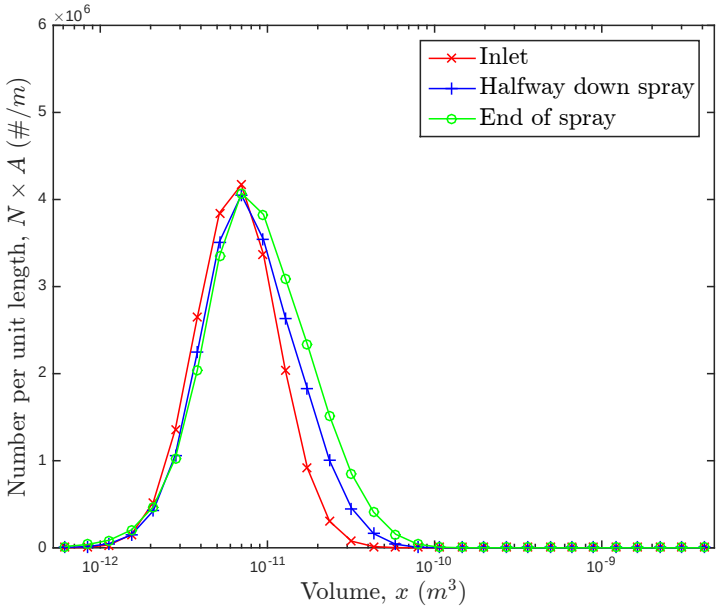

Figure 6.9: Results show the effect of increasing the droplet temperature to $T_{drop} = 80°C$. The plot illustrates the droplet number per unit length distribution within the spray.

Case 6 - Effects of varying droplet inlet velocity

Next we investigate the effect of increasing the droplet's inlet velocity from $u_{inlet} = 15\,\mathrm{m\,s^{-1}}$ to $u_{inlet} = 40\,\mathrm{m\,s^{-1}}$. Again, all other parameter values are returned to the base settings, and the results are plotted below.

The results are shown in Figure 6.10. Here, we can clearly see an increase in the number of mid to large size droplets, relative to Figure 6.7. This can be attributed to the increased inlet velocity causing a bigger difference between the velocities of the larger and smaller droplets further down the spray. This will cause more collisions, leading to an increase in coagulation within the dryer, and so more of the smaller droplets will coagulate with larger ones. Similarly, the larger droplets that maintain their momentum longer, will now have reduced residence times within the dryer, which in turn results in less evaporation from these particular droplets.

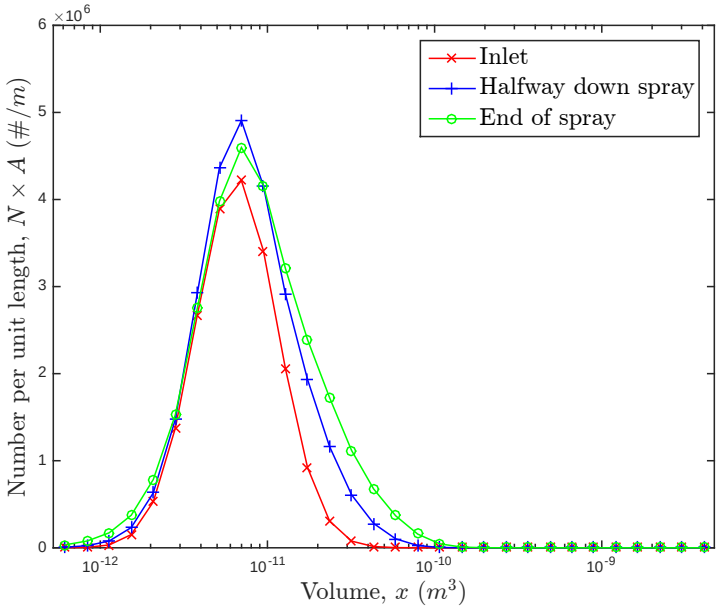

Figure 6.10: Results show the effect of increasing the droplet inlet velocity to u_{inlet} =40 m s^{-1}. The plot illustrates the droplet number per unit length distribution within the spray.

Case 7 - Effects of varying the spray angle

Finally, we look at the effects of increasing the spray's inner cone angle from $\beta = \frac{\pi}{3}$ to $\beta = \frac{\pi}{2}$, whilst keeping the spray's thickness constant at $\frac{\alpha}{2} - \frac{\beta}{2} = \frac{\pi}{36}$. The results are shown below in Figure 6.11 .

This time, we clearly see a large increase in the number of all droplet sizes through out the length of the spray. This will be due to the increased spray angle increasing the residence times of all droplets within the spray, which in turn will produce an increase in both evaporation and coagulation effects, as is illustrated in Figure 6.11.

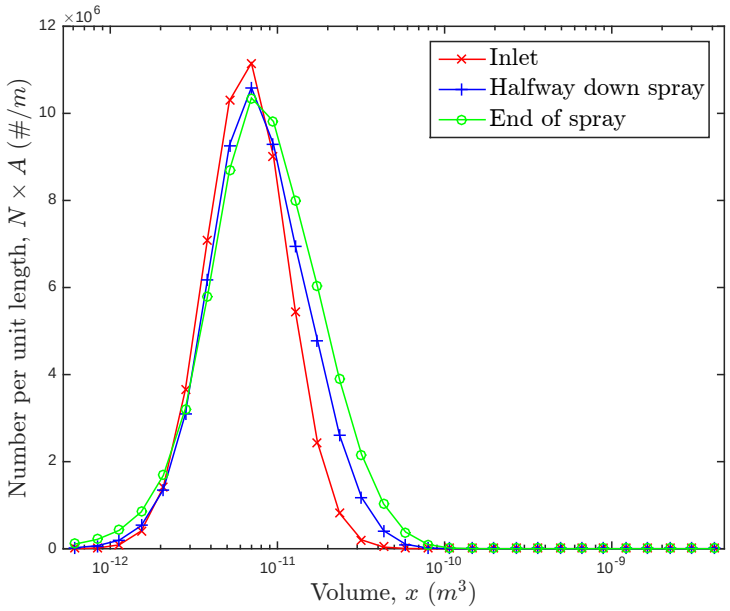

Figure 6.11: Results from increasing the spray's inner cone angle from $\beta = \frac{\pi}{3}$ to $\beta = \frac{\pi}{2}$. The plot illustrates the droplet number per unit length distribution within the spray.

Chapter 7

Experimental validation

In this chapter, we look to validate the model's predictions against experimental data provided by Procter and Gamble. Most of the data was obtained by the process engineers, however I was also given the opportunity to run my own series of small-scale atomisation rig trials at their innovation centre in Newcastle. So all of the data presented in Section 7.1 is data I collected myself from those trials. For the full-scale dryer, the data provides many of the model's input parameters; these include spray angle, slurry density and the inlet droplet size distribution (albeit not in number concentration form). It is also detailed enough to allow calculation of any input parameters that are missing, such as the droplet's inlet velocity. However, the coagulation efficiency λ of each slurry is still unknown and so it must be calibrated using parameter sweep techniques.

In what follows, we first outline how some of the data has been collected. We do so by using the example of a small-scale rig used by P&G to calculate the atomisation properties of prototype slurries. Next, since the experimental size distribution data is presented in terms of fractional volume distributions, we describe how these are converted into number concentration distributions for use

within our computational model. Finally, the model of the full-scale drying tower is solved numerically, and the coagulation efficiency λ is calibrated for two separate slurry trials. Once calibrated, the model's predicted droplet size distributions are shown to be in good agreement with those observed experimentally. These simulations are run twice - once with just coagulation and transport, and then again, incorporating evaporation.

7.1 Small-scale data acquisition

To help understand how the experimental data was obtained in the full-scale dryer, I was given the chance to carry out my own series of experimental trials on a smaller laboratory scale in Newcastle. The aim of these was to calculate the spray angle and droplet size distribution for various water sprays, using the same nozzles seen in the full-scale drying towers. These trials were carried out in the small-scale atomisation rig illustrated in Figure 7.1.

This consists of a perspex box, with a spray nozzle mounted inside, through which water (or slurry) can be fired. A high speed camera is mounted within the box, to film the spray and capture the spray angle, whilst a Malvern Spraytec laser diffraction system allows measurement of the droplet size distribution in real-time, at the point of complete sheet break-up. An image from one of the water trials is shown in Figure 7.2.

Atomisation rigs such as the one in Figure 7.1 are commonly used to quantify the atomisation qualities of new slurry mixes prior to trialling them within a full-scale dryer tower; in some cases, slurries may clog the nozzles or simply not atomize very well. So the rig trials mean they can be rejected early on, minimising waste

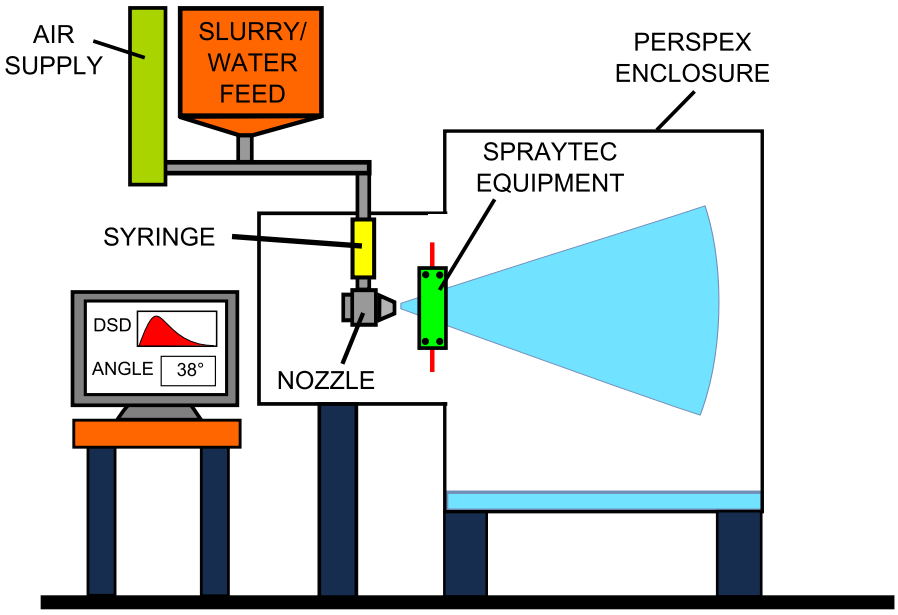

Figure 7.1: Outline of the rig used to measure atomisation properties for water and slurry trials. These measurements include the droplet size distribution (DSD) and spray angle.

slurry and reducing operational costs from running full-scale dryer trials.

The trial in Figure 7.1 used a spray of water, fired through one of the hollow-cone nozzles commonly used in a full-scale spray dryer. The operating conditions consisted of a nozzle pressure of 60.1 bar, a nozzle temperature of 71.5 °C and water flow rate of 0.96 t h^{-1} (tonnes per hour). From the video still, using ImageJ software, the spray angle was calculated to be 67.8°.

The droplet size distribution captured by the Malvern Spraytec, for the same trial, is shown in Figure 7.3. The system is capable of measuring droplets with diameters within the range from 0.1 – 2000 µm. Here, the measurements were taken at 20 cm from the spray nozzle, and the Sauter mean diameter of the droplet distribution was calculated to be $D_{32} = 98.43$ µm. Similarly, the diameter of the median droplet volume was found to be $D_{v0.5} = 137.80$ µm and the span of the

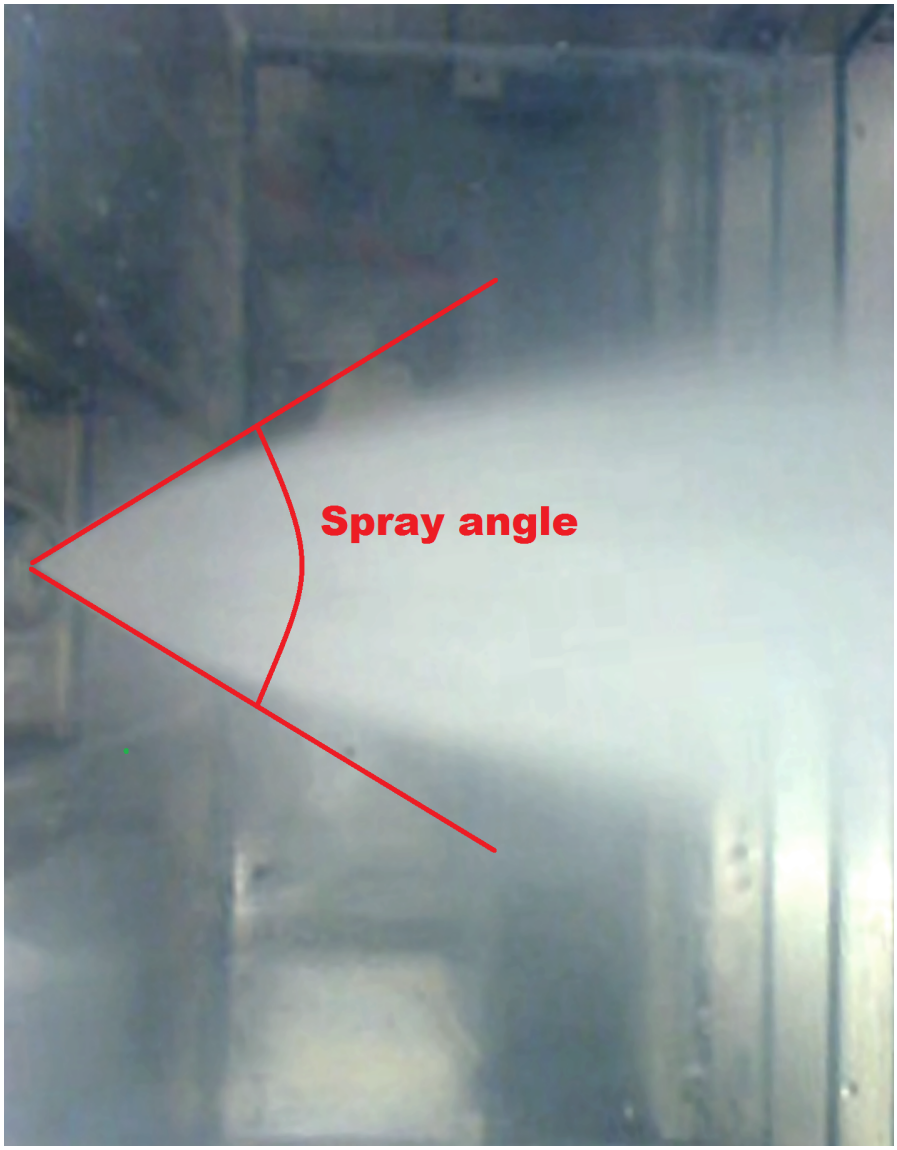

Figure 7.2: Video still capturing the shape of the spray produced during a trial conducted in the P&G atomisation rig.

volume distribution was calculated to be 0.96. The definitions of the Sauter mean and span can be found in (1.4) and (1.5), respectively.

Within the full-scale spray dryer, however, it is difficult to mount the Spraytec apparatus, and so the engineers use a sieve analysis technique instead — this is detailed in the next section.

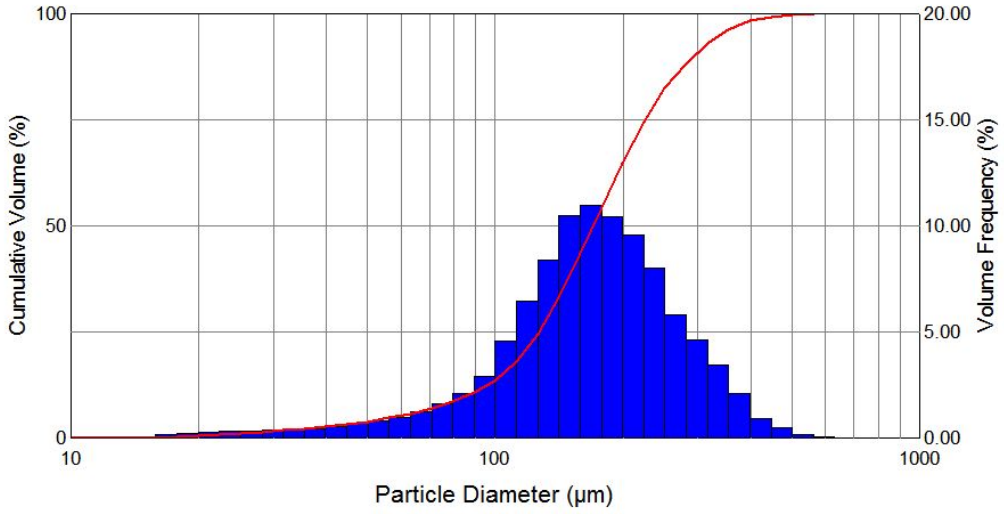

Figure 7.3: Droplet size distribution at 20 cm from the nozzle for a water spray trial conducted in the P&G atomisation rig. The red line is the corresponding cummulative droplet size distribution.

7.2 Full-scale dryer data

Having established some background knowledge of how the experimental data has been gathered, we now move on to analyse the experimental data for the full-scale dryer tower. The first challenge is to convert the data to a usable format that will allow us to calibrate the coagulation efficiency parameter λ. Once this has been achieved, we may then compare the predicted and experimental results to further validate the model's predictions.

7.2.1 Experimental data acquisition

The data we have comes from a series of trials that were carried out in a full-scale spray dryer at the P&G Newcastle Innovation Centre. These involved firing different slurry mixes through hollow cone nozzles at varying pressures, and recording

the characteristics of the atomised spray. The measurements taken include the fractional volume distribution of droplets at distances of 20 cm, 3 m and 6 m away from the nozzle. The spray angle was also recorded, along with the slurry density, nozzle pressure, slurry mass flow rate and nozzle type/dimensions.

A laser diffraction system was used to record the fractional volume distribution at the 20 cm distance. Then sieve analysis was used to calculate the fractional volume distribution of the spray at the 3 m and 6 m distances, as the sieving equipment can more easily be implemented within the constraints of the existing tower configuration. This technique involves collecting a sample of droplets/powder from the spray at the chosen height of interest. The sample is then filtered through a tower of sieves which are stacked vertically, in order of decreasing sieve thickness (smallest sieve size at the bottom). The size distribution can then be calculated by measuring the volume of droplets that are able to pass through each sieve. Here, the total volume of droplets that passes through one sieve, but not the next (finer) sieve, is then allocated to the droplet volume bin that ranges between the two sieve widths. This means sieve sizes can be fine tuned to focus on accuracy around a range of expected droplet volumes — for example, if most of the droplets are expected to fall within a particular range, then more sieves can be used across that volume range. The total volume of droplets sieved is also measured, by summing up over all bin sizes, and this then allows the fractional volume distribution to be calculated. The experimental data has around a $90 - 97\%$ volume recovery rate, as inevitably, some of the droplets are lost during the sieving process. These lost droplets may fall into gaps in the sieving apparatus or get blown away if they are too fine. The data provided lists of all the sieve sizes used, along with the fractional volume of droplets observed within each sieve size range. An example

of the corresponding fractional volume distribution can be seen in Figure 7.4.

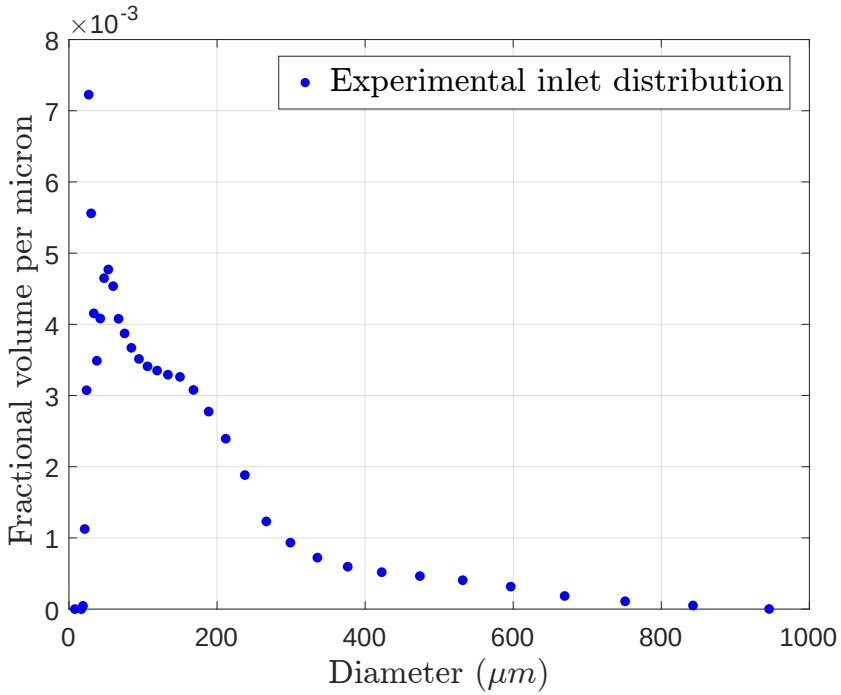

Figure 7.4: An example of the inlet droplet size distribution at 20 cm from an experimental trial.

7.2.2 Translation of experimental data

As is standard in the process engineering literature, the fractional volume distribution (see Figure 7.4) is given in terms of droplet diameter, rather than the droplet volume used in the computational model. Thus, before we can calibrate the computational model, these fractional volume distributions and droplet diameters need to be converted into number concentrations and droplet volumes, respectively. In the literature [102], it is highlighted that care should be taken when converting between different distribution bases (e.g. volume to number distribution), as significant error can be introduced. For example, if it were the case that the droplets

were formed of non-uniform clusters of particles, whose shapes are complicated in nature (similar to popcorn), then approximating their volume as though they were solid spheres, or some other uniform shape, would introduce a significant source of error to the calculations. However, since the droplets measured experimentally are near spherical and we assume all droplets are spherical in the conversion, this minimizes the potential source of error.

In the experimental data, the droplet volume range has been divided into bins of varying widths. For each of these bins, we are told the corresponding fraction of the total volume of droplets that lie within the bin. As such, in order to convert the measurements to number concentrations (number per unit volume in space), we proceed as follows. First, the width of every bin is calculated and a representative droplet diameter, D_{rep}, is assigned to each. Here, D_{rep} is simply set to be the mid-point of the bin. It is then assumed that the volume of droplets in a given bin is made up entirely of droplets of this representative size. Next, we assume that $V_T(z)$, the total volume of droplets at distance z down the spray is known. The total volume of droplets in a given bin is then calculated by multiplying the corresponding fractional volume figure by $V_T(z)$. Finally, the total number of droplets in each bin is calculated. Using the assumption that the droplets are perfectly spherical, the representative droplet diameters for the experimental bins can be converted into the corresponding representative volumes, x_{rep}. The number of droplets in a given bin is then simply the total volume of droplets in the bin divided by the representative droplet volume x_{rep}.

While the above is a straightforward calculation, it is based on the assumption that $V_T(z)$ is known. Although it was obviously known at some point in the gathering of the experimental results, $V_T(z)$ is not given explicitly in the data

provided. It is, however, possible to calculate its value from the known parameter values. The data contains the following: the spray angle, the mass flow rate into the nozzle (kg/s), the slurry density (kg/m^3), the dimensions of the nozzle itself (mm) and the pressure drop across the nozzle (bar). From these, the total volume of droplets $V_T(z_0)$ within a slice of the spray of thickness Δz at the inlet z_0 is calculated using the formula

$$V_T(z_0) = \frac{\dot{m}}{\rho_{drop}\, v_{axial}} \Delta z. \tag{7.1}$$

Here, $\dot{m}$ is the mass flow rate of the slurry through the nozzle and v_{axial} is the axial velocity at which the droplets leave the nozzle. Both $\dot{m}$ and ρ_{drop} are known, however the velocity v_{axial} is not, and so must first be calculated. To do this, we refer to [59], in which the following formula is presented for the inlet axial velocity of a spray

$$v_{axial} = \frac{Q}{\frac{\pi D_o^2}{4}\left[1 - \left(\frac{D_c}{D_o}\right)^2\right]}. \tag{7.2}$$

Here, D_o and D_c are the diameter of the nozzle orifice and air core, respectively, whilst Q is the volumetric flow rate of the slurry through the nozzle, and is defined by

$$Q = \frac{\dot{m}}{\rho_{drop}}. \tag{7.3}$$

Equation (7.2) introduces the air-core diameter D_c as a further unknown. However, the ratio D_c/D_o can be easily be obtained, using linear extrapolation, from the plot in [59, Figure 7], for any given combination of orifice diameter and spray angle.

As an illustration, for one particular slurry trial, a nozzle air core to orifice

diameter ratio of $D_c/D_o = 0.28$ was used. The pressure drop across the nozzle was set to be 60 bar for the trial, which created a spray angle of $\alpha = 44.7°$ and a normalised mass flow rate[1] of $\dot{m}/\dot{m}_A = 1$. The particular slurry used here had a density of $\rho_{drop} = 1588\,\mathrm{kg/m^3}$. Substituting these into (7.2), the axial velocity for this trial was found to be $v_{axial} = 48.96\,\mathrm{m\,s^{-1}}$.

Now that the axial velocity at the inlet can be calculated, equation (7.1) can be used to obtain $V_T(z_0)$. Combining this with the fractional volume distribution, the total volume of droplets $V_i(z_0)$ in the i^{th} droplet size bin can be calculated. Then, assuming all the droplets in the i^{th} volume bin have volume x_i, the total number of these droplets at z_0 is given by

$$\Psi_i(z_0) = \frac{\text{Total volume of drops in bin(i)}}{\text{Representative volume } x_i} = \frac{V_i(z_0)}{x_i}. \tag{7.4}$$

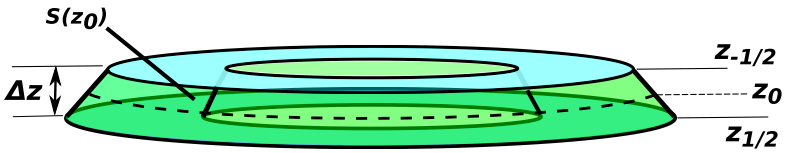

Figure 7.5: Here, the slice $S(z_0)$ of the spray is that enclosed between the surfaces $z_{j-1/2}$ and $z_{j+1/1}$.

If we want to convert between the total number of droplets $\Psi_i(z_0)$ and the numerical number concentration at the inlet, $N_i(z_0)$, we make use of the relationship

$$N_i(z_0) = \frac{\Psi_i(z_0)}{\Delta V(z_0)}, \tag{7.5}$$

[1]The mass flow rate has been normalised to protect commercially sensitive information. Here, $\dot{m}_A$ is the experimentally observed mass flow rate from Trial A, later introduced in Section 7.3.

where $\Delta V(z_0)$ is simply the volume of the slice $S(z_0)$ pictured in Figure 7.5, that was first introduced in Section 2.1.2.

7.2.3 Calculating a reference volume

Having established how to translate the experimental data into a usable format, the next step is to outline the calculation of the reference volume used in equation (7.5). This is the volume of the slice $S(z_j)$ of the spray pictured in Figure 7.6.

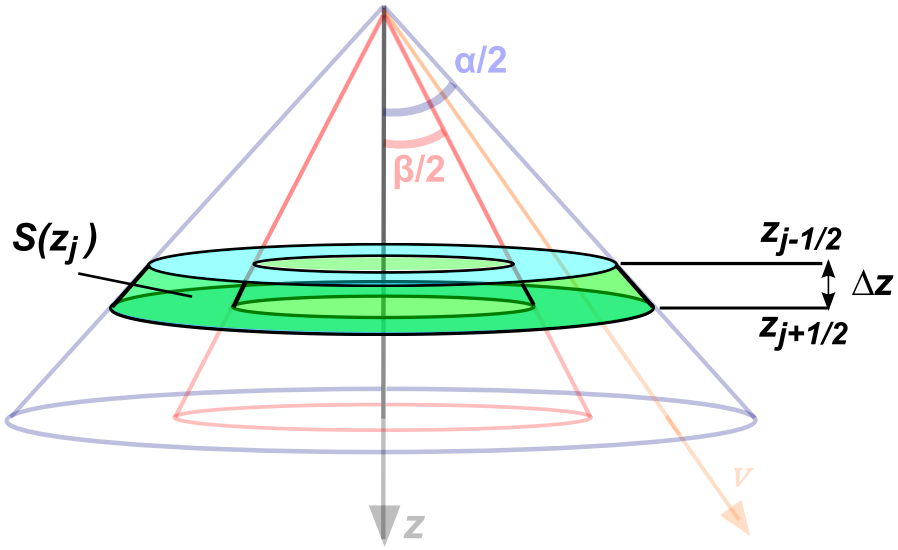

Figure 7.6: The geometry used to calculate the volume $\Delta V(z_j)$ of a slice $S(z_j)$ of the spray.

The volume $\Delta V(z_j)$ of this slice is given by the integral

$$\Delta V(z_j) = \int_{z_{j-1/2}}^{z_{j+1/2}} A(z)\,dz \;=\; \pi\left[\tan^2\frac{\alpha}{2} - \tan^2\frac{\beta}{2}\right]\int_{z_{j-1/2}}^{z_{j+1/2}} z^2\,dz.$$

Using the midpoint rule to approximate the z integral, the volume is then given by the equation

$$\Delta V(z_j) \simeq \Delta z\, \pi \Big[\tan^2 \frac{\alpha}{2} - \tan^2 \frac{\beta}{2}\Big]\; z_j^2 \;=\; \Delta z\, A(z_j). \tag{7.6}$$

This gives us the total volume of space, contained within the slice $S(z_j)$ and subsequently allows us to convert backwards and forwards between fractional volume distributions and the number per unit volume in space distribution that we use within our model. This volume also allows us to fit distribution curves to the inlet size distributions, and these in turn can be used as the inlet boundary condition for the model when using any arbitrary grid.

7.2.4 Generalising results for use on arbitrary grids

As touched upon above, the experimental data's distributions have one fundamental limitation — they are restricted to the bins used by the Malvern Spraytec laser diffraction system and the sieve analysis. Thus, in order to project the experimental data onto a more general grid, such as (4.2), we have chosen to fit either a log-normal (1.1) or a Rosin-Rammler (1.2) curve to the fractional volume distributions. An example of two fitted curves is shown in Figure 7.7; these have been produced using a nonlinear least squares technique. The use of these fitted distributions allows for much greater flexibility in the choice of grid used for the droplet size range. The corresponding droplet number concentrations for our chosen grid may then be calculated using the same technique described in Section 7.2.2.

The plot in Figure 7.7 also shows the median and Sauter mean diameter, along-

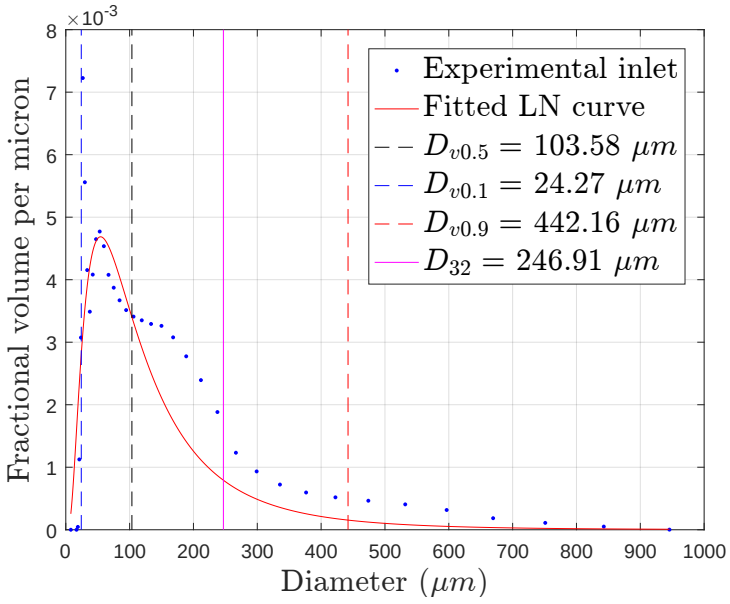

(a)

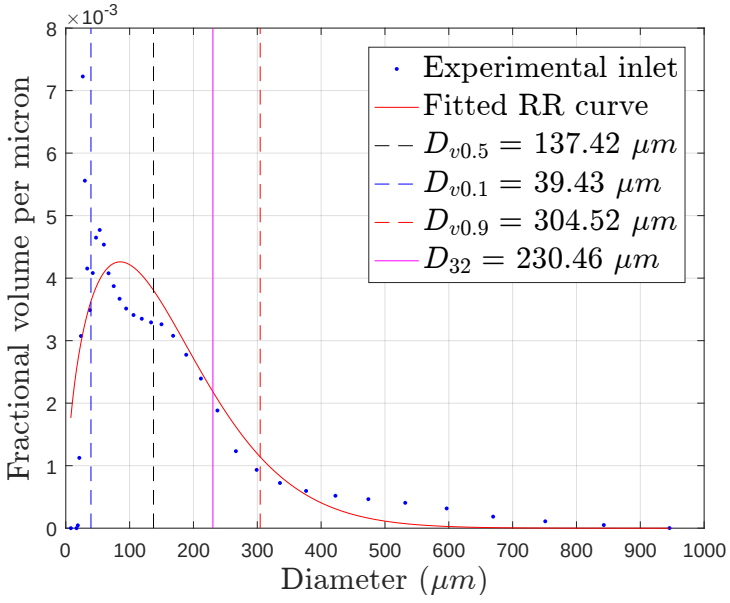

(b)

Figure 7.7: The experimentally observed inlet fractional volume distribution for slurry Trial A plotted against two curves which we have fitted (red lines) to the data. Here (a) shows a log-normal (LN) fit, as per equation (1.1), and (b) shows a Rosin-Rammler (RR) fit as per equation (1.2). Average diameters are also quoted for the fitted curve.

side the representative diameters $D_{v0.1}$ and $D_{v0.9}$ outlined earlier in Section 1.2.3. These have been included on all plots in this section, and allow for easier comparison between the different results. The values presented are for the curves which we have fitted to the inlet data.

7.3 Verification of mathematical model

In this section, the model of the full-scale drying tower is solved numerically for two slurry trials — referred to as Trial A and Trial B. In doing so, a parameter sweep is carried out to calibrate the coagulation efficiency parameter λ for each of the slurries. The results are then shown to be in good agreement with the experimental data. These simulations are initially run with just coagulation and transport, however they are repeated later, to incorporate evaporation as well.

7.3.1 Model input parameters and distribution

The model input parameters for each trial can be found in Table 7.1. The air flow velocity is assumed to be a constant counter-current velocity of $-0.25\,\mathrm{ms}^{-1}$ for both Trial A and Trial B. This is consistent with the experimental airflow used for these particular trials.

A Rosin-Rammler curve was fitted to the experimental fractional volume data at the inlet for both trials. This was chosen over the alternative log-normal curve as it appears to provide the best approximation to the droplet size distribution across the entire droplet size range. In contrast, the log-normal curve does a very good job for smaller droplet volumes, but underpredicts the number of larger droplets from around 100 µm in diameter, upwards. The Rosin-Rammler curve takes the

Parameter	Trial A	Trial B
Spray Angle, α	44.7°	36.7°
Slurry density, ρ_{drop}	$1588\,\mathrm{kgm}^{-3}$	$1727\,\mathrm{kgm}^{-3}$
Normalised mass flow rate, $\dot{m}/\dot{m}_A$	1	1.37
Pressure drop across nozzle	60 bar	80 bar
Nozzle air core to orifice diameter ratio, D_c/D_o	0.28	0.19
Axial inlet velocity, v_{axial}	$48.96\,\mathrm{ms}^{-1}$	$58.86\,\mathrm{ms}^{-1}$
Air Temperature, T_{air}	97.8 °C	93.1 °C
Slurry Temperature, T_{drop}	30 °C	30 °C

Table 7.1: Experimentally measured input parameters for slurry Trials A and B.

form (1.2), where

$$f(D) = \frac{k}{\lambda_{rr}}\Big(\frac{D}{\lambda_{rr}}\Big)^{k-1}\exp\Big[-\Big(\frac{D}{\lambda_{rr}}\Big)^{k}\Big]. \tag{7.7}$$

The best-fit distribution parameters were calculated using a nonlinear least squares approach and can be found in Table 7.2, along with a 95% confidence interval for each. Plots of these inlet distributions can then be found in Figures 7.7(b) and 7.8, for Trials A and B respectively. These curves are used to convert the fractional volume distribution into a number per unit volume in space distribution which is used as the inlet distribution at $z_0 = 20\,\mathrm{cm}$ when solving the spray model numerically.

The same approach was used to fit a log-normal curve (1.1) to the inlet data. However, whilst the fit was good, it appeared to significantly underpredict the larger droplets in comparison to the chosen Rosin-Rammler distribution. The corresponding plot for Trial A can be found in Figure 7.7(a), where $D_{ng} = 103.4$,

Parameter	Trial A	95% CI	Trial B	95% CI
λ_{rr}	175.2 µm	(149.9, 200.5)	196.8 µm	(178.4, 215.1)
k	1.51	(1.28, 1.73)	1.63	(1.47, 1.79)

Table 7.2: Rosin-Rammler parameters for the inlet curve for Trials A and B, along with the corresponding 95% confidence intervals.

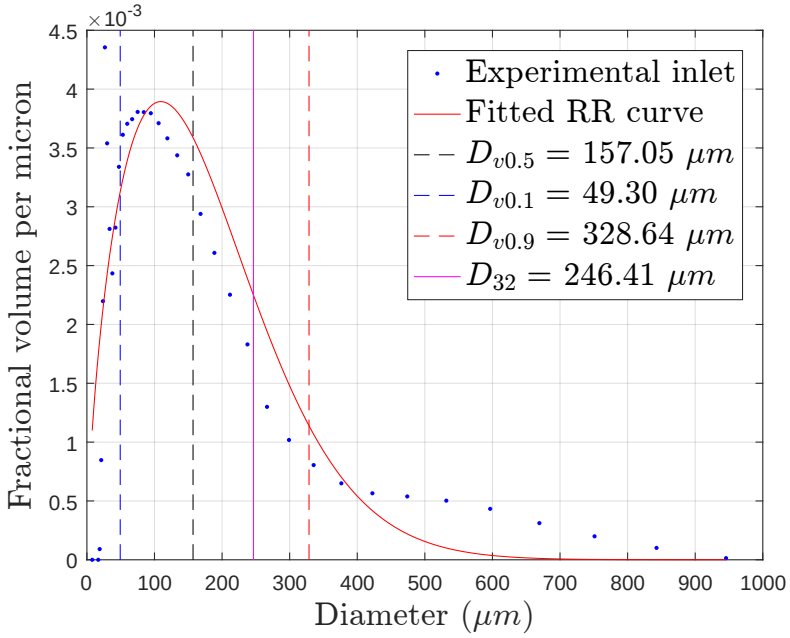

Figure 7.8: Rosin-Rammler curve fitted to the inlet droplet size distribution data for Trial B.

$S_g = 1.13$, and the corresponding 95% confidence intervals were (90.32, 116.5) and (0.97, 1.29), respectively. Here, D_{ng} and S_g are the mean droplet diameter and standard deviation for the log-normal distribution defined earlier in (1.1).

An alternative approach could have been to use the exact experimental data as the inlet distribution. However, that would mean being restricted to the grid defined by the sieve sizes used when collecting the original data. Instead, by using the fitted curves, we have much greater freedom to use any arbitrary grid, with

any number of grid points.

When solving the spray model numerically, the droplet volume grid was set to be the same geometrically stretched grid as that defined in (4.2) and (4.3), making use of $I = 40$ points and covering the volume range of droplets with diameters 15 – 2000 µm. The spatial range was covered by a uniformly spaced grid of $J = 80$ points, covering the distances from $z = 0.2$ – 6 m.

7.3.2 Fitted curves for 3 m and 6 m data

Next, we look to fit a similar curves to the outlet data we have for each of the spray trials. The experimental data at 3 m and 6 m is obtained using very few droplet diameter size bins — only 11 compared to the 37 provided for the inlet. This is a result of the two different measuring techniques used to obtain each distribution — the Spraytec laser diffraction system used at the inlet uses more size bins than the sieve analysis used at the outlet. As a result, we would be even more restricted if we were stuck using the outlet bin sizes as the grid for our model. So, we again fit log-normal and Rosin-Rammler curves to the data at these points, and then select the best fit for use on the geometric grid.

For both Trial A and Trial B, the best fit curve at both 3 m and 6 m comes from a log-normal distribution. The curve's equation can be found in (1.1), and the best fit parameters are presented in Tables 7.3 and 7.4, for Trial A and Trial B, respectively. The corresponding plots for Trial A are presented in Figures 7.10 and 7.11, whilst those for Trial B are plotted in Figures 7.13 and 7.14.

Parameter	Trial A (3 m)	95% CI	Trial A (6 m)	95% CI
D_{ng}	259.4 µm	(238.0, 280.7)	232 µm	(207.1, 257)
S_g	0.76	(0.68, 0.83)	0.58	(0.47, 0.68)

Table 7.3: Best fit log-normal parameters for the Trial A data at 3 m and 6 m, along with the corresponding 95% confidence intervals.

Parameter	Trial B (3 m)	95% CI	Trial B (6 m)	95% CI
D_{ng}	260 µm	(216.6, 303.4)	260 µm	(233.4, 286.6)
S_g	0.85	(0.70, 1.00)	0.74	(0.65, 0.54)

Table 7.4: Best fit log-normal parameters for the Trial B data at 3 m and 6 m, along with the corresponding 95% confidence intervals.

7.3.3 Model validation (no evaporation)

Having established the model's input parameters from the experimental data, we now move on to fit the coagulation efficiency parameter λ to the slurry used in each of the trials.

Here, a series of parameter estimation sweeps were performed. This involves running repeated simulations of the spray dryer model, varying the λ value used on each run, and plotting the output from each run onto the same figure. From this plot, the optimal value of λ can easily be pinpointed, and validated quantitatively using an error norm.

In what follows, the model is solved using only coagulation and transport and so the evaporation term is set to zero. Corresponding results when evaporation is switched on are presented later in Section 7.3.4.

Trial A

For slurry Trial A, the best fitting value of λ was found to be $\lambda = 0.51$, and the corresponding predicted droplet size distribution at the 3 m distance is shown in Figure 7.10. To evaluate the best fit for λ, the error between the predicted results and the experimentally observed data was calculated at the 3 m distance. In doing so, the following error norm was evaluated for each value of λ used in the parameter sweep:

$$E_\lambda = \sum_{i=1}^{I} \Delta D_i \times |FV_i^{Exp}(z_J) - \widetilde{FV}_i(z_J)|. \tag{7.8}$$

Here, $FV_i^{Exp}(z_J)$ is the curve fitted to the experimentally observed fractional volume per micron distribution at $z_J = 3$ m, as per Figure 7.10. Similarly, $\widetilde{FV}_i(z_J)$ denotes the numerically predicted fractional volume per micron distribution at z_J, and ΔD_i is the width of the i^{th} droplet diameter bin.

λ	0.35	0.40	0.45	0.50	0.51	0.52	0.55	0.60
E_λ (3 m)	0.3834	0.3637	0.3504	0.3404	0.3401	0.3403	0.3434	0.3567

Table 7.5: Results for evaluating the error (7.8) for each λ value for Trial A.

The results for evaluating the error (7.8) for Trial A can be found in Table 7.5, along with the plot in Figure 7.9, and provide quantitative evidence that $\lambda = 0.51$ is the best fitting value for the slurry used in Trial A.

From Figure 7.10, it is clear that the model's prediction is not the closest match to the experimental data at 3 m. Here, the peak of the predicted distribution lies in the right place, as do the distribution's tails, however there is a clear overprediction of the number if droplets for almost all sizes. In contrast, the model's predictions are a much better fit at the 6 m distance. For Trial A, a plot of these results is shown

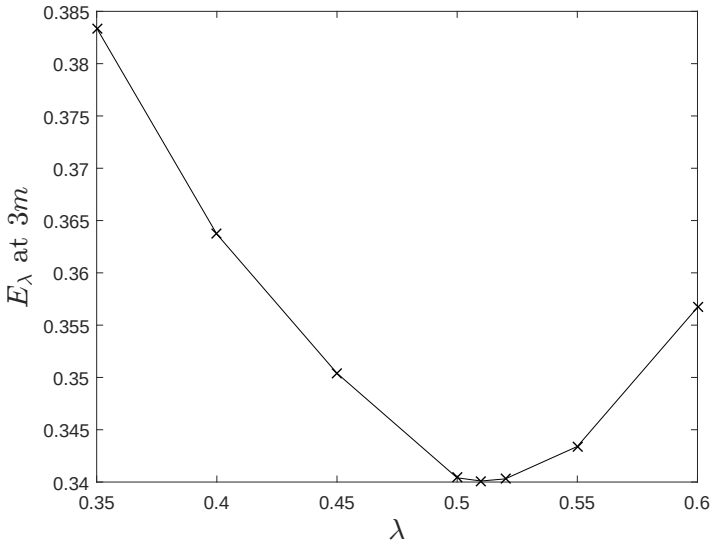

Figure 7.9: The error E_λ at 3 m plotted against λ for Trial A.

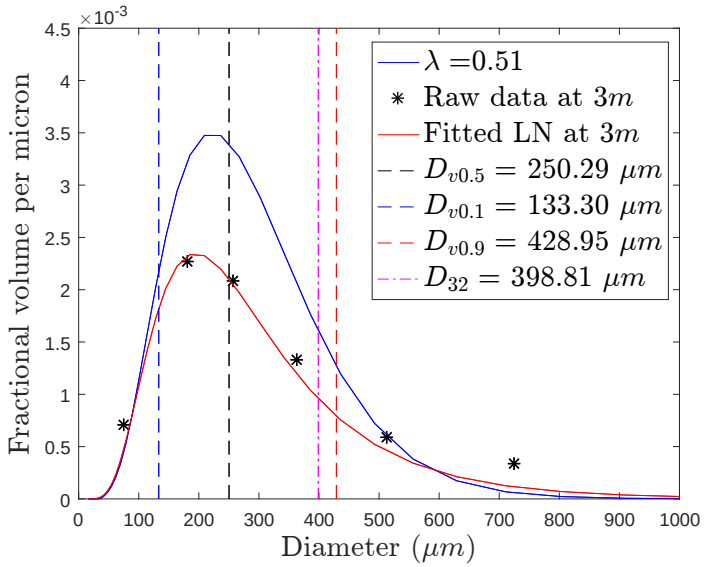

Figure 7.10: Model's predicted output (blue curve) plotted against the experimental data for Trial A at the 3 m distance, with no evaporation. Here, $\lambda = 0.51$.

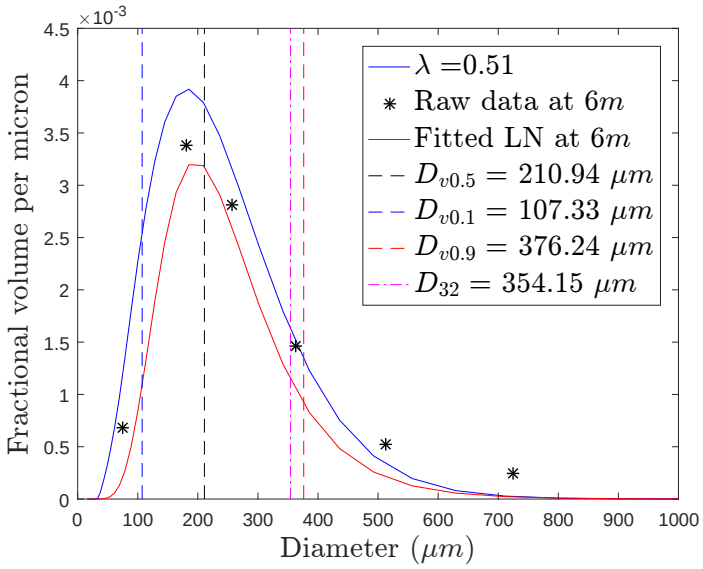

Figure 7.11: Model's predicted output (blue curve) plotted against experimental data for Trial A at the 6 m distance, with no evaporation. Here, $\lambda = 0.51$.

in Figure 7.11, and clearly the prediction is much closer fit to the experimental data at this distance. Whilst there is a slight overprediction of droplets below 400 µm in size, and an underprediction of those above, the shape of the curve is a good match to the experimental data.

Representative diameter	Numerically predicted		Experimental data	
	3 m	6 m	3 m	6 m
$D_{v0.5}$ (µm)	250.29	210.94	259.38	232.01
D_{32} (µm)	398.91	354.15	415.20	310.98

Table 7.6: Representative droplet diameters for Trial A. This table shows both the numerically predicted results, and those for the log-normal curves that have been fitted to the experimental data at both 3 m and 6 m.

The median ($D_{v0.5}$) and Sauter mean (D_{32}) diameters for the numerically pre-

dicted fractional volume distribution are presented in Table 7.6, alongside the corresponding values for the log-normal curves fitted to the experimental data at 3 m and 6 m.

From Table 7.6, it can be seen that the predicted size distribution captures both the median and Sauter mean diameters really well at the 3 m distance, however the predictions become slightly less accurate at the 6 m distance. It is also noted that the error E_λ actually decreased by the 6 m distance, compared to that at 3 m for the best fit value of $\lambda = 0.51$. At 6 m, this error dropped down to $E_\lambda = 0.2969$ compared to the 0.3401 value seen in Table 7.5. So in this case, the fit is consistently good throughout the length of the spray.

Trial B

λ	0.30	0.35	0.39	0.40	0.41	0.45
E_λ (3 m)	0.4157	0.3969	0.3926	0.3924	0.3928	0.4010

Table 7.7: Results for evaluating the error (7.8) for each λ value for Trial B.

On repeating the same steps for Trial B, the best fitting value for the coagulation efficiency parameter was found to be $\lambda = 0.40$. The error analysis used to verify this quantitatively is shown in Table 7.7, and Figure 7.12. The corresponding numerically predicted droplet size distributions at 3 m and 6 m can be found in Figures 7.13 and 7.14, respectively.

The fact that λ is smaller here than it was for Trial A will likely be a direct result of the different slurries used for each trial. Trial B uses a heavier density slurry, which may mean it contains more solid particles and less liquid binder than the slurry in Trial A. This could potentially make the slurry of Trial B less sticky,

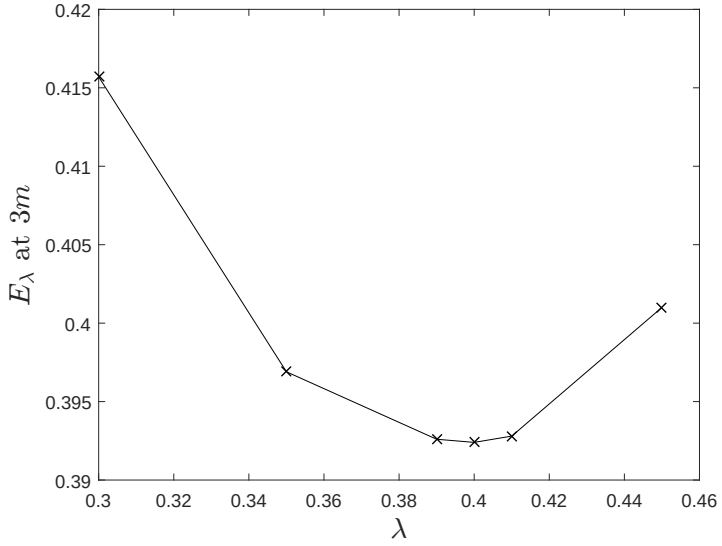

Figure 7.12: The error E_λ at 3 m plotted against λ for Trial B.

which could in turn explain the smaller value of λ.

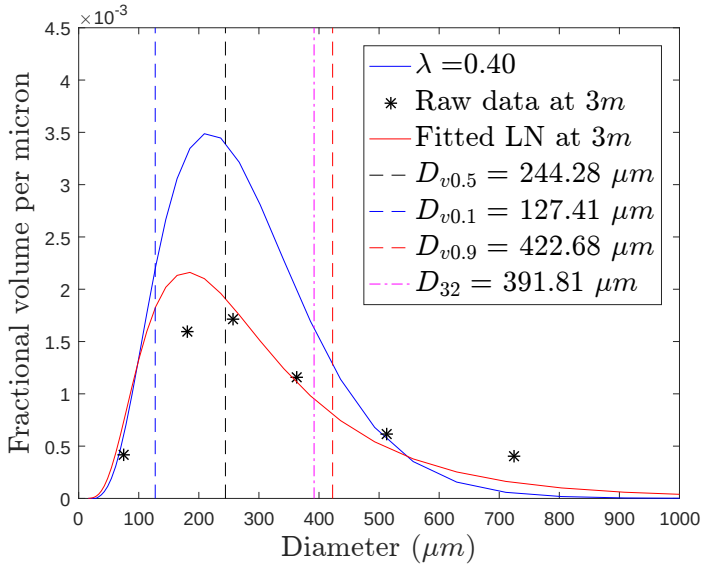

Figure 7.13: Model's predicted output (blue curve) plotted against experimental data for Trial B at the 3 m distance, with no evaporation. Here, $\lambda = 0.40$.

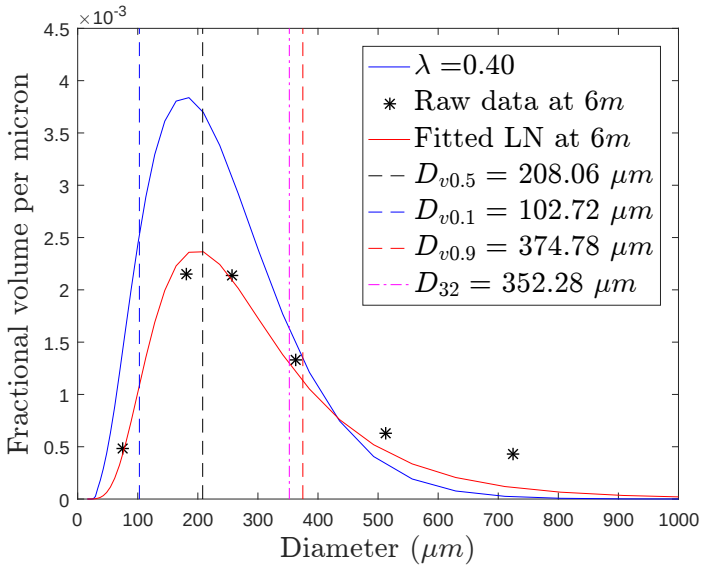

Figure 7.14: Model's predicted output (blue curve) plotted against experimental data for Trial B at the 6 m distance, with no evaporation. Here, $\lambda = 0.40$.

From Figure 7.13, the model's predictions show another good fit to the experimental data. Again, we see a slight overprediction for droplets below 50 µm in diameter, and an underprediction of those above; however the peak of the distribution lies almost on top of the peak of the experimental data.

Similar results can be seen at the 6 m distance in Figure 7.14. This time the spread of the model's predicted curve appears to narrow, and again the predictions show a very good agreement with the experimental data. On evaluating the error (7.8) at 6 m, $E_\lambda = 0.3938$, which is marginally smaller than the value of 0.3924 observed at the 3 m distance, and shown in Table 7.7.

The median and Sauter mean diameters for the numerically predicted fractional volume distribution can be found in Table 7.8, alongside those for the log-normal curves fitted to the experimental data at 3 m and 6 m. As was the case for Trial

Representative diameter	Numerically predicted		Experimental data	
	3 m	6 m	3 m	6 m
$D_{v0.5}$ (µm)	244.28	208.06	260.00	260.00
D_{32} (µm)	391.81	352.28	467.43	410.50

Table 7.8: Representative droplet diameters for Trial B. This table shows both the numerically predicted results, and those for the log-normal curves that have been fitted to the experimental data at both 3 m and 6 m.

A, the predicted results for median and Sauter mean diameters are both more accurate at the 3 m point than at 6 m. Here the numerically predicted median droplet diameter at 3 m shows a good match to the experimentally observed value, whilst the predicted Sauter mean results are not quite as close to those observed experimentally this time.

The results above all provide validation that, once calibrated for a particular slurry, the simple one-dimensional model can in fact produce good predictions of the droplet size distribution within the spray drying tower.

7.3.4 Model validation with coagulation and evaporation

Trial A

Finally, the calibrated coagulation efficiency parameters from Section 7.3.3 were used to assess the predictions of the model for Trials A and B when both coagulation and evaporation are turned on.

For Trial A, the temperature of the airflow was 97.8 °C, and for modelling purposes, we have assumed that the slurry temperature was 30 °C for both Trials A and B.

Results at 3 m and 6 m are shown in Figures 7.15 and 7.16, respectively. For Trial A, the errors in these results were found to be $E_\lambda = 0.3424$ and $E_\lambda = 0.2968$ at 3 m and 6 m respectively. When compared to Figures 7.10 and 7.11 (no evaporation), the new results in Figures 7.15 and 7.16 are still a good fit to the experimental data.

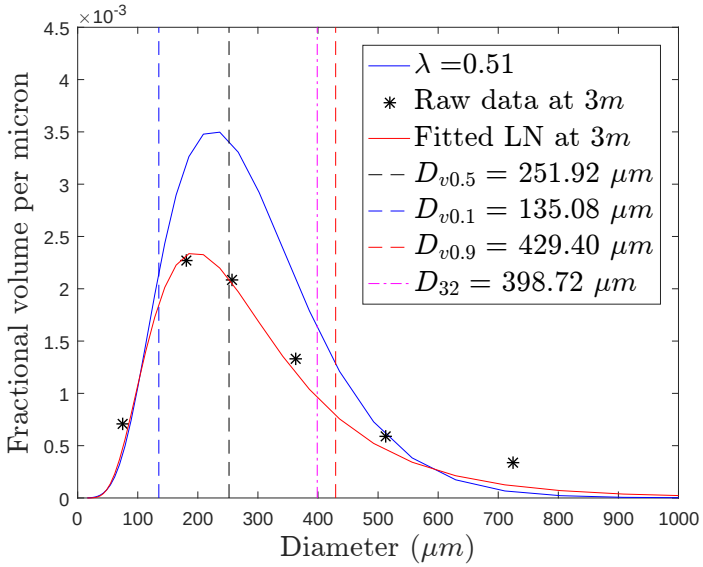

Figure 7.15: Model's predicted output (blue curve) plotted against experimental data for Trial A at the 3 m distance, when evaporation is turned on. Here, $\lambda = 0.51$.

The numerically predicted average diameters for Trial A, with evaporation turned on, can be found in Table 7.9. These are presented alongside those for the experimental data, as well as the earlier numerical results for no evaporation. It is clear that, with the addition of evaporation, the numerical results for the median droplet diameter at each distance in the spray are both a slightly better fit than those produced without evaporation.

Since these results show minimal difference to those produced without evapora-

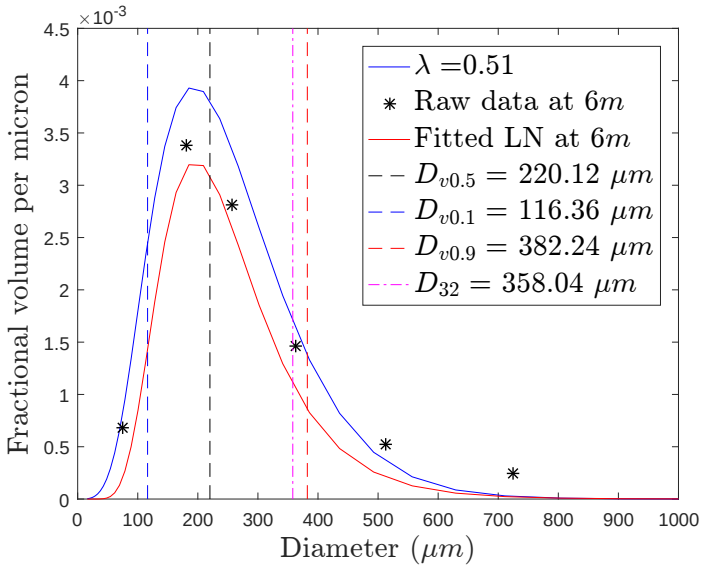

Figure 7.16: Model's predicted output (blue curve) plotted against experimental data for Trial A at the 6 m distance, when evaporation is turned on. Here, $\lambda = 0.51$.

	Numerically predicted results					
	No Evaporation		Evaporation		Experimental data	
Diameter	3 m	6 m	3 m	6 m	3 m	6 m
$D_{v0.5}$ (μm)	250.29	210.94	251.92	220.12	259.38	232.01
D_{32} (μm)	398.91	354.15	398.72	358.04	415.20	310.98

Table 7.9: Representative droplet diameters for Trial A. This table shows the numerically predicted results, both with and without evaporation, alongside those for the log-normal curves that have been fitted to the experimental data at both 3 m and 6 m.

tion, it would seem that coagulation is the dominant physical effect. However, the addition of evaporation does have a small effect, and moves the predicted median droplet diameter closed toward the experimentally measured value.

Trial B

For Trial B, the temperature of the airflow was 93.1 °C and we again assumed the slurry temperature was 30 °C. Results at 3 m and 6 m are shown in Figures 7.17 and 7.18, respectively. For this trial, the errors in these results were found to be $E_\lambda = 0.3978$ and $E_\lambda = 0.3850$ at 3 m and 6 m, respectively.

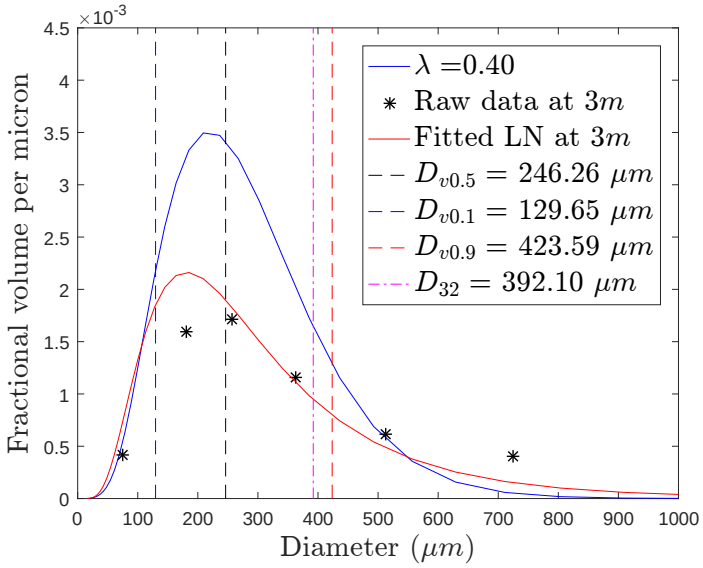

Figure 7.17: Model's predicted output (blue curve) plotted against experimental data for Trial B at the 3 m distance, when evaporation is turned on. Here, $\lambda = 0.40$.

From the results in Figures 7.17 and 7.18, we again see a slight improvement compared to the results presented earlier, where evaporation was not present. Compared to the corresponding plots in Figures 7.13 and 7.14, the predicted size distributions are near identical.

Table 7.10 shows the predicted representative diameters for Trial B, with evaporation turned on. Again, we find that both the predicted median and Sauter diameters a slightly better match to the experimental data when evaporation is

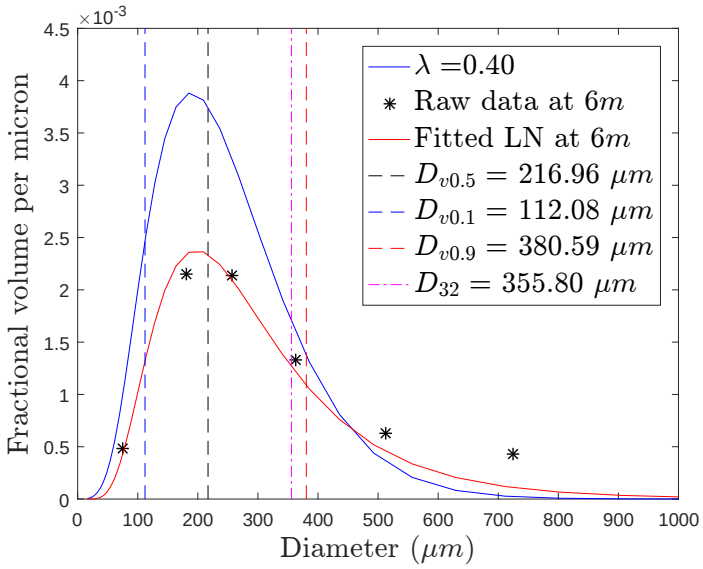

Figure 7.18: Model's predicted output (blue curve) plotted against experimental data for Trial B at the 6 m distance, when evaporation is turned on. Here, $\lambda = 0.40$.

	Numerically predicted results					
	No Evaporation		Evaporation		Experimental data	
Diameter	3 m	6 m	3 m	6 m	3 m	6 m
$D_{v0.5}$ (μm)	244.28	208.06	246.26	216.96	260.00	260.00
D_{32} (μm)	391.81	352.28	392.10	355.80	467.43	410.50

Table 7.10: Representative droplet diameters for Trial B. This table shows the numerically predicted results, both with and without evaporation, alongside those for the log-normal curves that have been fitted to the experimental data at both 3 m and 6 m.

incorporated in the model. This is true at both the 3 m and 6 m distances.

From Figures 7.10–7.18, it is clear that the simple one-dimensional model does a reasonable job of predicting the droplet distribution throughout the length of the spray. Whilst the predicted size distribution is not an exact match for the

experimental data, the general shape of the predicted distributions, along with the location of their peak/tails, are all close to those of the experiential data. Similarly, the predicted Sauter mean and median diameters show a good agreement with the experimental data, and improve further when evaporation is incorporated into the model. Thus, whilst the size distribution may suffer from some overprediction, the one-dimensional model is clearly a useful tool for estimating the representative diameters.

Chapter 8

Conclusions and future work

8.1 Conclusions

This thesis has demonstrated that, once calibrated, a simple one-dimensional model can successfully predict the droplet size distribution throughout the length of a spray within a drying tower. The model's predictions have been validated against both real-world experimental data from a spray dryer, and known analytic solutions for simplified cases.

The initial model was shown to produce excellent agreement with analytic results for pure coagulation, pure advection and combined advection/coagulation problems. The results were accurate for both the droplet size distribution and the evolution of the first two moments. Then, later on, the extension of the model to incorporate evaporation was shown to produce excellent agreement with available analytic results for the growth-coagulation equations as well.

To our knowledge this is the first time that the cell-average technique has been applied to model coagulation in the context of a spray drying operation. It is also the first time that this unique combination of the cell-average technique, and the

Kurganov-Tadmor scheme for advection have been coupled to describe a drying tower. It is clear that this novel pairing leads to excellent predictions of the droplet distributions within the tower.

It has been observed that the amount of coagulation occurring within the spray may be increased by each of the following; increasing the spray angle, reducing the spray sheet's thickness, increasing the density of the droplets or increasing the efficiency parameter λ. Similarly, minimal coagulation is observed if the droplet's inlet velocity is increased — a perhaps obvious result of the droplet's decreased residence time within the dryer, which leaves less available time for coagulation.

For the cases we have looked at, it would also seem that coagulation has a greater bearing on the final droplet size distribution than evaporation does. However, the incorporation of evaporation effects has been shown to further increase the agreement of the model's predictions with experimental data in Chapter 7.

Despite the many assumptions and simplifications made during the model's derivation, the results it produces are excellent. The end result is an efficient computational tool, proving fast and accurate predictions of the droplet size distribution throughout a spray. Whilst the predictions do not match the experimentally observed size distributions perfectly, they are accurate enough to allow engineers to quickly estimate the median droplet diameter for a given combination of slurry and operating conditions. This will be a much welcome addition to their research and development toolkit, as the alternative CFD simulations may take several hours to model the problem.

8.2 Future work and modifications to the model

Moisture content and droplet material properties

The slurries used in spray drying are multiphase mixtures, made up of various solids and liquids. However, the model presented here makes no provision to account for the moisture content contained within the droplets. In reality, the moisture content of a droplet will affect its stickiness, which in turn will affect its likelihood of successful coagulation. Subsequently, the coagulation kernel could be adapted to be a function of moisture, as well as size and velocity, in order to account for this.

The moisture content of the droplets will generally reduce as the droplets spend more time evaporating within the dryer. Therefore, two dryer droplets may be less likely to coagulate than more moist ones that have just entered the dryer. This could again be accounted for within the coagulation kernel. The moisture content of the droplets entering the dryer could then be optimized to produce the desired final droplet size distribution. This could be achieved by fine tuning the input parameters such as spray angle, slurry temperature, and inlet velocity. The moisture content of the final product could also be optimized, to ensure that it is flowable and easy to handle, by avoiding it being too sticky so that it simply clumps together.

Spray shape

Within the model presented, the spray angles α and β are assumed to remain constant throughout the length of the spray. In reality, these will usually decrease as z increases, due to the influences of aerodynamic drag and gravity — see Figure

7.2 for an example. These forces lead to a deceleration of the droplets and cause the spray to become bell shaped further away from the nozzle. This is something that could be incorporated into the model by making both α and β functions of z. The form of these could, for example, be decided by fitting the inner and outer surface curves to experimental data. Alternatively, $\alpha(z)$ and $\beta(z)$ could be chosen to follow the theoretical parabolic paths traced out by the trajectory of the largest and smallest droplets respectively.

Fragmentation

Whilst spray drying is based around the idea of droplets coagulating, it is also possible that collisions may result in droplets fragmenting into smaller droplets. This process has been ignored in the current model. However it is something that could be added into the model in the future.

Droplet-air momentum balance

The one-dimensional model makes no explicit provision to account for momentum transfer between the slurry droplets and the airflow within the spray dryer. It simply uses inertial deceleration of the droplets to pre-define the droplet's velocity as z-increases, along with a pre-defined airflow velocity, whereas, in reality, the droplets will be decelerating the airflow as well.

The model could be adapted to include momentum conservation of the air-droplet interaction by incorporating both a momentum balance for the air in steady state, as well as the existing momentum balance used to pre-define droplet velocities. If the mass flux of air entering the spray is calculated, and a mass balance

derived for the entire system of droplets within the spray, these could then be solved to steady state, to give a more comprehensive picture of the entire system.

However, care has to be taken not to make the model too computationally expensive as a result, as then the "computationally-inexpensive" benefits over a full CFD simulation may be lost.

Turbulence and droplet recirculation

In a real world spray dryer, there can often be zones of turbulent airflow or flows of recirculating air/droplets within the dryer tower. These are both complicated physical phenomena that the model makes no attempt to capture. Thus, finding a simple way in which these could be incorporated could further improve the model's predictions.

Application to other industries

The model presented has obviously been developed with a focus on spray drying. However, there is no reason it could not be further generalised and applied to other fields in which sprays are involved. Examples might include fuel injector sprays within engines, or agricultural crop dusting systems.

Future analytical work

The mathematical models, and numerical schemes, presented in this thesis are clearly all heavily influenced by the presence of coagulation within the spray-drying process. This leads to nonlinear integro-differential equations of the Smoluchowski type playing a fundamental role within the modelling. Despite the availability of

a substantial number of analytical results for these types of equations, very few of these results can actually be applied when the kernel is spatially or temporally dependant. Instead, these existing results generally focus on kernels that depend only upon on the size of the coagulating droplets. Thus, as touched upon in Chapters 3 and 6, none of the existing results can be applied to the coagulation kernel used in our model.

The same is true for even the simpler steady-state equations. For example, we showed that the steady-state version of (6.67) could be rewritten as a non-autonomous Smoluchowski equation with an additional evaporation term — see (6.74), where z plays the role of the time variable. However there are very few existing results that can be exploited on such equations, and once again, none of them are applicable to (6.74).

As a result, there is clearly scope for future analytical work to investigate the existence and uniqueness of solutions to equations of the form (6.67) and (6.74).

Incorporation into a larger CFD model

One final possibility is the incorporation of the coagulation model into a much larger, fully-comprehensive model of a spray dryer. As such, the coagulation model presented here could be incorporated as a sub-model, with other sub-models dealing with separate processes such as evaporation and bubble formation. The resulting model would be highly computer intensive, but extremely detailed and capable of comprehensively simulating the physics within an entire spray drying tower.

Appendix A

Exact moments for specific kernels

This appendix focuses on pure coagulation, with no z dependence, in an isotropic system of particles governed by the continuous coagulation equation (1.15) and outlines derivations of simple expressions for the exact zeroth, first and second moments of the number density function for the cases of constant and sum coagulation kernels, respectively. It also considers the exact solution of the moments for the case of specific initial conditions. Analytic solutions for both the number density and moments of these specific cases are widely available in the literature; see [39, 48].

A.1 Exact moments for the constant kernel

Zeroth moment

To find the zeroth moment for the constant kernel case, we set $\nu = 0$ and $K(x, y) = 1$ in (1.23) to get the equation

$$M_0'(t) = -\frac{1}{2}\int_0^\infty \int_0^\infty n(x,t)n(y,t)\,dx\,dy = -\frac{1}{2}M_0^2(t). \tag{A.1}$$

This is easily solved to obtain,

$$M_0(t) = \frac{2}{t + C}, \tag{A.2}$$

$$\text{where } C = \frac{2}{M_0(0)} = \frac{2}{\int_0^\infty n_0(x)dx} \text{ and } n(x,0) = n_0(x). \tag{A.3}$$

First moment

The first moment for the constant kernel is found in exactly the same way as the zeroth moment — this time setting $\nu = 1$ and $K(x,y) = 1$ in (1.23) to get the equation

$$M_1'(t) = 0.$$

$$\implies M_1(t) = M_1(0) = \int_0^\infty x n_0(x)dx, \tag{A.4}$$

showing that the first moment (and total mass of droplets) is constant for all time, as expected.

Second moment

Finally, the second moment of the number density function for the constant kernel case is found by setting $\nu = 2$ and $K(x,y) = 1$ in (1.23). This leads to the equation

$$M_2'(t) = \int_0^\infty x n(x,t)dx \int_0^\infty y n(y,t)dy = M_1^2(t) = M_1^2(0),$$

where we have made use of (A.4) to simplify the RHS. It then follows that

$$M_2(t) = M_1^2(0)t + M_2(0). \tag{A.5}$$

Moments for an exponential initial condition

We now investigate these three moments for a specific initial particle size distribution — namely the negative exponential initial condition given by

$$n_0(x) = n(x, 0) = e^{-x}.$$

This is of particular interest as we use this initial distribution when comparing the performance of the fixed pivot and cell average numerical techniques to analytic solutions. In this case, we have that

$$M_0(0) = \int_0^\infty e^{-x} dx = 1,$$

and, on using (A.2) and (A.3), we arrive at

$$M_0(t) = \frac{2}{t+2}. \tag{A.6}$$

Similarly, from (A.4), for the first moment we have that

$$M_1(t) = M_1(0) = \int_0^\infty x e^{-x} dx = 1, \ \forall\, t \geq 0.$$

Finally, we consider the second moment. From (A.5) we have that

$$M_2(t) = M_1^2(0)t + M_2(0).$$

Using the negative exponential initial condition,

$$M_2(0) = \int_0^\infty x^2\, e^{-x} dx = 2, \tag{A.7}$$

and so for this specific case, the second moment is given by

$$M_2(t) = t + 2. \tag{A.8}$$

A.2 Exact moments for the sum kernel

We now consider the case of the sum kernel, when $K(x, y) = x + y$. The first moment is again constant, as in the constant kernel case, due to mass conservation.

Zeroth moment

To find the zeroth moment for the sum kernel, we set $\nu = 0$ and $K(x, y) = x + y$ in (1.23) to get the equation

$$\begin{aligned} M_0'(t) &= -\frac{1}{2}\int_0^\infty \int_0^\infty (x+y)\, n(x,t) n(y,t)\, dx\, dy, \\ &= -\frac{1}{2}\left[\int_0^\infty n(y,t)\, M_1(t)\, dy + \int_0^\infty n(x,t) M_1(t)\, dx\right], \\ &= -M_1(0) M_0(t)\,, \text{ from (A.4)} \\ \implies M_0(t) &= M_0(0) e^{-M_0(0)t}, \end{aligned} \tag{A.9}$$

which clearly decreases with time, as expected in a system of pure coagulation. The decay in M_0 here is also considerably faster than the decay seen in (A.2) when the constant kernel is used. This is a result of the large increase in the

likelihood of larger particles successfully coagulating that occurs when the sum kernel is used instead of the constant kernel. Consequently the total number of particles decreases at a much faster rate.

In the case of the negative exponential initial condition, where $M_0(0) = 1$, the exact solution for the zeroth moment is $M_0(t) = e^{-t}$.

Second moment

To calculate the second moment for the sum kernel, we set $\nu = 2$ and $K(x, y) = x + y$ in (1.23). This gives the following equation

$$\begin{aligned} M_2'(t) &= \frac{1}{2}\int_0^\infty \int_0^\infty 2xy\,(x+y)\,n(x,t)n(y,t)\,dx\,dy \\ &= \int_0^\infty x^2\,n(x,t)\,dx \int_0^\infty yn(y,t)\,dy + \int_0^\infty x\,n(x,t)\,dx \int_0^\infty y^2 n(y,t)\,dy \\ &= M_2(t)\,M_1(t) + M_1(t)\,M_2(t) = 2M_1(0)M_2(t) \\ \implies M_2(t) &= M_2(0)e^{2M_1(0)t}. \end{aligned} \tag{A.10}$$

Clearly this increases exponentially with time, and so $M_2(t)$ increases more quickly than in the constant kernel case. The increased likelihood of the larger particles coagulating when the sum kernel is used results in the size of the largest particle increasing at a far quicker rate than that seen with the constant kernel — clearly resulting in the variance about the mean particle size increasing at a quicker rate too. For the specific negative exponential initial condition, using (A.7) implies that $M_2(0) = 2$, and thus $M_2(t) = 2e^{2t}$.

Bibliography

[1] M. J. Crosby, L. M. De Juan, E. Martin, and G. Montague, "Particle size control of detergents in mixed flow spray dryers," *The Journal of Engineering*, vol. 2015, pp. 102—107, 03 2015.

[2] T. Langrish and D. Fletcher, "Prospects for the modelling and design of spray dryers in the 21st century," *Drying Technology*, vol. 21, no. 2, pp. 197–215, 2003.

[3] D. Fletcher, B. Guo, D. Harvie, T. Langrish, J. Nijdam, and J. Williams, "What is important in the simulation of spray dryer performance and how do current CFD models perform?," *Applied Mathematical Modelling*, vol. 30, no. 11, pp. 1281–1292, 2006.

[4] I. Zbicinski and R. Zietara, "CFD model of counter-current spray drying process," *Proceedings of the 14th International Drying Symposium*, vol. A, pp. 169–176, 2004.

[5] A. Gharsallaoui, G. Roudaut, O. Chambin, A. Voilley, and R. Saurel, "Applications of spray-drying in microencapsulation of food ingredients: An

overview," *Food Research International*, vol. 40, no. 9, pp. 1107–1121, 2007.

[6] C. Anandharamakrishnan, *Computational Fluid Dynamics Applications in Food Processing*. Springer, 2013. ISBN: 978-1461479895.

[7] A. Lefebvre, *Atomization and Sprays*. CRC Press, 1988. ISBN: 978-0891166030.

[8] "SDX spray drying — product guide," *Delavan Spray Technologies 2004*, 2004.

[9] N. Dombrowski and W. Johns, "The aerodynamic instability and disintegration of viscous liquid sheets," *Chemical Engineering Science*, vol. 18, no. 3, pp. 203–214, 1963.

[10] W. Sirignano and C. Mehring, "Review of theory of distortion and disintegration of liquid streams," *Progress in Energy and Combustion Science*, vol. 26, no. 4–6, pp. 609–655, 2000.

[11] P. Rosin and E. Rammler, "The laws governing the fineness of powdered coal," *Journal of the Institute of Fuel*, vol. 7, pp. 29–36, 1933.

[12] E. Babinsky and P. Sojka, "Modeling drop size distributions," *Progress in energy and combustion science*, vol. 28, no. 4, pp. 303–329, 2002.

[13] R. Mugele and H. Evans, "Droplet size distribution in sprays," *Industrial & Engineering Chemistry*, vol. 43, no. 6, pp. 1317–1324, 1951.

[14] P. B. Kowalczuk and J. Drzymala, "Physical meaning of the sauter mean diameter of spherical particulate matter," *Particulate Science and Technology*, vol. 34, no. 6, pp. 645–647, 2016.

[15] J. Collet, "Some modelling issues in the theory of fragmentation-coagulation systems," *Communications in Mathematical Sciences, Supplemental Issue*, no. 1, pp. 35–54, 2004.

[16] D. Southwell and T. Langrish, "Observations of flow patterns in a spray dryer," *Drying Technology*, vol. 18, no. 3, pp. 661–685, 2000.

[17] J. Hecht, J. Stamper, and D. Giles, "Pneumatic atomization of laundry detergent slurries as affected by solid particle size and concentration," in *ILASS Americas, 20th Annual Conference on Liquid Atomization and Spray Systems*, 2007.

[18] D. H. Huntington, "The influence of the spray drying process on product properties," *Drying technology*, vol. 22, no. 6, pp. 1261–1287, 2004.

[19] M. J. Hanus and T. A. G. Langrish, "Re-entrainment of wall deposits from a laboratory-scale spray dryer," *Asia-Pacific Journal of Chemical Engineering*, vol. 2, no. 2, pp. 90–107, 2007.

[20] T. Langrish and I. Zbicinski, "The effects of air inlet geometry and spray cone angle on the wall deposition rate in spray dryers," *Chemical engineering research & design*, vol. 72, no. A3, pp. 420–430, 1994.

[21] L. Ozmen and T. Langrish, "An experimental investigation of the wall deposition of milk powder in a pilot-scale spray dryer," *Drying Technology*, vol. 21, no. 7, pp. 1253–1272, 2003.

[22] V. Francia, L. Martín, A. E. Bayly, and M. J. H. Simmons, "The role of wall deposition and re-entrainment in swirl spray dryers," *AIChE Journal*, vol. 61, no. 6, pp. 1804–1821, 2015.

[23] T. Langrish, "Multi-scale mathematical modelling of spray dryers," *Journal of food engineering*, vol. 93, no. 2, pp. 218–228, 2009.

[24] D. E. Oakley, "Spray dryer modeling in theory and practice," *Drying Technology*, vol. 22, no. 6, pp. 1371–1402, 2004.

[25] R. A. Goffredi and E. J. Crosby, "Limiting analytical relationships for prediction of spray dryer performance," *Industrial & Engineering Chemistry Process Design and Development*, vol. 22, no. 4, pp. 665–672, 1983.

[26] C. Baker and K. McKenzie, "Energy consumption of industrial spray dryers," *Drying Technology*, vol. 23, no. 1-2, pp. 365–386, 2005.

[27] S. Papadakis, R. Bahu, K. McKenzie, and I. Kemp, "Correlations for the equilibrium moisture content of solids," *Drying Technology*, vol. 11, no. 3, pp. 543–553, 1993.

[28] L. Ozmen and T. Langrish, "A study of the limitations to spray dryer outlet performance," *Drying technology*, vol. 21, no. 5, pp. 895–917, 2003.

[29] K. Clement, A. Hallström, H. Dich, C. Le, J. Mortensen, and H. Thomsen, "On the dynamic behaviour of spray dryers," *Chemical Engineering Research & Design*, vol. 69, no. A, pp. 245–252, 1991.

[30] D. Fletcher, B. Guo, D. Harvie, T. Langrish, J. Nijdam, and J. Williams, "What is important in the simulation of spray dryer performance and how do current CFD models perform?," *Applied Mathematical Modelling*, vol. 30, no. 11, pp. 1281–1292, 2006.

[31] T. Langrish and D. Fletcher, "Spray drying of food ingredients and applications of CFD in spray drying," *Chemical Engineering and Processing: Process Intensification*, vol. 40, no. 4, pp. 345–354, 2001.

[32] B. Guo, D. Fletcher, and T. Langrish, "Simulation of the agglomeration in a spray using Lagrangian particle tracking," *Applied Mathematical Modelling*, vol. 28, no. 3, pp. 273–290, 2004.

[33] M. Gavaises, A. Theodorakakos, G. Bergeles, and G. Brenn, "Evaluation of the effect of droplet collisions on spray mixing," *Proceedings of the Institution of Mechanical Engineers, Part C: Journal of Mechanical Engineering Science*, vol. 210, no. 5, pp. 465–475, 1996.

[34] R. Verdurmen, J. Straatsma, and M. Gunsingv, "Simulation of agglomeration in spray drying installations: The EDECAD project," *Drying technology*, vol. 22, no. 6, pp. 1403–1461, 2004.

[35] M. Sommerfeld, "Validation of a stochastic Lagrangian modelling approach for inter-particle collisions in homogeneous isotropic turbulence," *International Journal of Multiphase Flow*, vol. 27, pp. 1829–1858, 2001.

[36] Y. Sano and R. Keey, "The drying of a spherical particle containing colloidal material into a hollow sphere," *Chemical Engineering Science*, vol. 37, no. 6, pp. 881–889, 1982.

[37] M. V. Smoluchowski, "Drei vortrage uber diffusion, Brownsche bewegung und koagulation von kolloidteilchen," *Physik. Zeit.*, vol. 17, pp. 557–585, 1916.

[38] M. Smoluchowski, "Versuch einer mathematischen theorie der koagulationskinetik kolloider lösungen," *Pisma Mariana Smoluchowskiego*, vol. 2, no. 1, pp. 595–639, 1917.

[39] J. Wattis, "An introduction to mathematical models of coagulation-fragmentation processes: A discrete deterministic mean-field approach," *Physica D: Nonlinear Phenomena*, vol. 222, no. 1–2, pp. 1–20, 2006.

[40] R. Drake, "A general mathematical survey of the coagulation equation," *Topics in current aerosol research (Part 2)*, vol. 3, pp. 201–376, 1972.

[41] S. Chandrasekhar, "Stochastic problems in physics and astronomy," *Reviews of Modern Physics*, vol. 15, pp. 1–89, Jan 1943.

[42] H. Müller, "Zur allgemeinen theorie ser raschen koagulation," *Fortschrittsberichte über Kolloide und Polymere*, vol. 27, no. 6, pp. 223–250, 1928.

[43] H. Müller, "Die theorie der koagulation polydisperser systeme," *Colloid & Polymer Science*, vol. 38, no. 1, pp. 1–2, 1926.

[44] D. Smit, M. Hounslow, and W. Paterson, "Aggregation and gelation—i. analytical solutions for CST (continuous stirred tank) and batch operation," *Chemical Engineering Science*, vol. 49, no. 7, pp. 1025–1035, 1994.

[45] D. Aldous, "Deterministic and stochastic models for coalescence (aggregation and coagulation): a review of the mean-field theory for probabilists," *Bernoulli*, vol. 5, pp. 3–48, 1999.

[46] W. T. Scott, "Analytic studies of cloud droplet coalescence I," *Journal of the Atmospheric Sciences*, vol. 25, pp. 54–65, 1967.

[47] M. Hounslow, R. Ryall, and V. Marshall, "A discretized population balance for nucleation, growth, and aggregation," *AIChE Journal*, vol. 34, no. 11, pp. 1821–1832, 1988.

[48] F. Leyvraz, "Scaling theory and exactly solved models in the kinetics of irreversible aggregation," *Physics Reports*, vol. 383, no. 2, pp. 95–212, 2003.

[49] J. Banasiak and M. Mokhtar-Kharroubi, *Evolutionary equations with applications in natural sciences*. Springer, 2015. ISBN: 978-3319113210.

[50] P. G. J. Van Dongen and M. H. Ernst, "Dynamic scaling in the kinetics of clustering," *The American Physical Society*, vol. 54, no. 13, pp. 1396–1399, 1985.

[51] P. G. J. Van Dongen and M. H. Ernst, "Scaling solutions of Smoluchowski's coagulation equation," *Journal of Statistical Physics*, vol. 50, no. 1, pp. 295–329, 1988.

[52] N. Fournier and P. Laurençot, "Well-posedness of Smoluchowski's coagulation equation for a class of homogeneous kernels," *Journal of Functional Analysis*, vol. 233, no. 2, pp. 351–379, 2006.

[53] N. Fournier and P. Laurençot, "Existence of self-similar solutions to Smoluchowski's coagulation equation," *Communications in Mathematical Physics*, vol. 256, no. 3, pp. 589–609, 2005.

[54] A. Boehm, "A scaling theory for number-flux distributions generated during steady-state coagulation and settling and application to particles in Lake Zurich, Switzerland," *Journal of Colloid and Interface Science*, vol. 254, pp. 266–273, 2002.

[55] H. Masuda, K. Higashitani, and H. Yoshida, *Powder technology: Fundamentals of particles, powder beds, and particle generation*. CRC Press, 2006. ISBN: 978-1420044102.

[56] R. Patel, M. Patel, and A. Suthar, "Spray drying technology: An overview," *Indian Journal of Science and Technology*, vol. 2, no. 10, pp. 44–47, 2009.

[57] M. Ali, T. Mahmud, P. J. Heggs, M. Ghadiri, D. Djurdjevic, H. Ahmadian, L. M. de Juan, C. Amador, and A. Bayly, "A one-dimensional plug-flow model of a counter-current spray drying tower," *Chemical Engineering Research and Design*, vol. 92, no. 5, pp. 826–841, 2014.

[58] D. Ramkrishna, *Population balances: Theory and applications to particulate systems in engineering*. Academic press, 2000. ISBN:978-0125769709.

[59] P. A. Nelson and W. F. Stevens, "Size distribution of droplets from centrifugal spray nozzles," *AIChE Journal*, vol. 7, no. 1, pp. 80–86, 1961.

[60] K. C. Chang, M. R. Wang, W. J. Wu, and C. H. Hong, "Experimental and theoretical study on hollow-cone spray," *Journal of Propulsion and Power*, vol. 9, no. 1, pp. 28–34, 1993.

[61] T. Langrish and K. Kota, "A comparison of collision kernels for sprays from one and two-nozzle atomisation systems," *Chemical Enginering Journal*, vol. 126, pp. 131–138, 2007.

[62] H. Holterman, *Kinetics and evaporation of water drops in air*, vol. 2012. IMAG, 2003. ISBN: 978-9054062349.

[63] A. Williams, "Combustion of droplets of liquid fuels: A review," *Combustion and Flame*, vol. 21, no. 1, pp. 1–31, 1973.

[64] L. Schiller and A. Naumann, "Uber die grundlegenden berechnungen der schw-erkraftaufbereitung (fundamental calculations in gravitational processing)," *Z. Ver. Deut. Ing.*, vol. 77, pp. 318–320, 1933.

[65] J. Abrahamson, "Collision rates of small particles in a vigorously turbulent fluid," *Chemical Enginering Science*, vol. 30, pp. 1371–1379, 1975.

[66] M. Kostoglou, "On the constant kernel Smoluchowski equation: fast algorithm for solution with arbitrary initial conditions," *Computer Physics Communications*, vol. 173, pp. 34–40, 2005.

[67] P. B. Dubovskiĭ, *Mathematical theory of coagulation.* Lecture Notes 23. Seoul: Global Analysis Research Center, 1994.

[68] H. Amann, "Coagulation-fragmentation processes," *Archive for Rational Mechanics and Analysis*, vol. 151, pp. 339–366, Apr 2000.

[69] D. J. McLaughlin, W. Lamb, and A. C. McBride, "Existence and uniqueness results for the non-autonomous coagulation and multiple-fragmentation equation," *Mathematical Methods in the Applied Sciences*, vol. 21, no. 11, pp. 1067–1084, 1998.

[70] Z. A. Melzak, "A scalar transport equation. ii.," *Michigan Math. J.*, vol. 4, no. 3, pp. 193–206, 1957.

[71] J. Banasiak and W. Lamb, "Analytic fragmentation semigroups and continuous coagulation–fragmentation equations with unbounded rates," *Journal of Mathematical Analysis and Applications*, vol. 391, no. 1, pp. 312–322, 2012.

[72] A. Kurganov and E. Tadmor, "New high-resolution central schemes for nonlinear conservation laws and convection-diffusion equations," *Journal of Computational Physics*, vol. 160, pp. 241–282, 1999.

[73] H. Nessyahu and E. Tadmor, "Non-oscillatory central differencing for hyperbolic conservation laws," *Journal of Computational Physics*, vol. 87, pp. 408–463, 1990.

[74] P. K. Sweby, "High resolution schemes using flux limiters for hyperbolic conservation laws," *SIAM Journal on Numerical Analysis*, vol. 21, no. 5, pp. 995–1011, 1984.

[75] R. J. LeVeque, *Finite volume methods for hyperbolic problems*, vol. 31. Cambridge university press, 2002. ISBN: 978-7506266352.

[76] R. M. Beam and R. Warming, "An implicit finite-difference algorithm for hyperbolic systems in conservation-law form," *Journal of Computational Physics*, vol. 22, no. 1, pp. 87–110, 1976.

[77] P. Lax and B. Wendroff, "Systems of conservation laws," *Selected Papers Volume I*, pp. 263–283, 2005.

[78] S. Kumar and D. Ramkrishna, "On the solution of population balance equations by discretization - i. a fixed pivot technique," *Chemical Engineering Science*, vol. 51, pp. 1311–1332, 1996.

[79] F. Filbet and P. Laurençot, "Numerical simulation of the Smoluchowski coagulation equation," *SIAM Journal on Scientific Computing*, vol. 25, no. 6, pp. 2004–2028, 2004.

[80] J. Kumar, M. Peglow, G. Warnecke, S. Heinrich, and L. Mörl, "Improved accuracy and convergence of discretized population balance for aggregation: The cell average technique," *Chemical Engineering Science*, vol. 61, pp. 3327–3342, 2006.

[81] J. Kumar, *Numerical approximations of population balance equations in particulate systems*. PhD thesis, Otto-von-Guericke-Universität Magdeburg, Universitätsbibliothek, 2006.

[82] R. Courant, K. Friedrichs, and H. Lewy, "Über die partiellen differenzengleichungen der mathematischen physik," *Mathematische Annalen*, vol. 100, no. 1, pp. 32–74, 1928.

[83] C. B. Laney, *Computational gasdynamics*. Cambridge University Press, 1998. ISBN: 978-0521625586.

[84] M. M. Attarakih, H. J. Bart, and N. M. Faqir, "Numerical solution of the spatially distributed population balance equation describing the hydrodynamics of interacting liquid–liquid dispersions," *Chemical Engineering Science*, vol. 59, no. 12, pp. 2567–2592, 2004.

[85] A. K. Giri and E. Hausenblas, "Convergence analysis of sectional methods for solving aggregation population balance equations: The fixed pivot technique," *Nonlinear Analysis: Real World Applications*, vol. 14, no. 6, pp. 2068–2090, 2013.

[86] J. Kumar, M. Peglow, G. Warnecke, and S. Heinrich, "An efficient numerical technique for solving population balance equation involving aggregation, breakage, growth and nucleation," *Powder Technology*, vol. 182, no. 1, pp. 81–104, 2008.

[87] T. E. Ramabhadran, T. W. Peterson, and J. H. Seinfeld, "Dynamics of aerosol coagulation and condensation," *AIChE Journal*, vol. 22, no. 5, pp. 840–851, 1976.

[88] S. Qamar and G. Warnecke, "Numerical solution of population balance equations for nucleation, growth and aggregation processes," *Computers & Chemical Engineering*, vol. 31, no. 12, pp. 1576–1589, 2007.

[89] P. Middleton and J. Brock, "Simulation of aerosol kinetics," *Journal of Colloid and Interface Science*, vol. 54, no. 2, pp. 249–264, 1976.

[90] F. Gelbard and J. H. Seinfeld, "Numerical solution of the dynamic equation for particulate systems," *Journal of Computational Physics*, vol. 28, no. 3, pp. 357–375, 1978.

[91] P. Marchal, R. David, J. Klein, and J. Villermaux, "Crystallization and precipitation engineering—i. an efficient method for solving population balance in crystallization with agglomeration," *Chemical Engineering Science*, vol. 43, no. 1, pp. 59–67, 1988.

[92] S. Kumar and D. Ramkrishna, "On the solution of population balance equations by discretization—iii. nucleation, growth and aggregation of particles," *Chemical Engineering Science*, vol. 52, no. 24, pp. 4659–4679, 1997.

[93] R. Kumar, J. Kumar, and G. Warnecke, "Moment preserving finite volume schemes for solving population balance equations incorporating aggregation, breakage, growth and source terms," *Mathematical Models and Methods in Applied Sciences*, vol. 23, no. 7, pp. 1235–1273, 2013.

[94] M. Kostoglou, "Extended cell average technique for the solution of the coagulation equation," *Journal of Coloid and Interface Science*, vol. 306, pp. 72–81, 2007.

[95] J. Kumar and G. Warnecke, "A note on moment preservation of finite volume schemes for solving growth and aggregation population balance equations," *SIAM Journal on Scientific Computing*, vol. 32, no. 2, pp. 703–713, 2010.

[96] B. van Leer, "Towards the ultimate conservative difference scheme. ii. monotonicity and conservation combined in a second-order scheme," *Journal of Computational Physics*, vol. 14, pp. 361–370, 1974.

[97] M. Song, A. Steiff, and P. M. Weinspach, "Direct-contact heat transfer with change of phase: A population balance model," *Chemical Engineering Science*, vol. 54, no. 17, pp. 3861–3871, 1999.

[98] W. E. Ranz and W. R. Marshall, "Evaporation from drops," *Chemical Engineering Progress*, vol. 48, no. 3, pp. 141–146, 1952.

[99] Z. Pinar, A. Dutta, G. Bény, and T. Özis, "Analytical solution of population balance equation involving growth, nucleation and aggregation in terms of auxiliary equation method," *Applied Mathematics & Information Sciences*, vol. 9, no. 5, pp. 2467–2475, 2015.

[100] F. Gelbard and J. Seinfeld, "Coagulation and growth of a multicomponent aerosol," *Journal of Colloid and Interface Science*, vol. 63, no. 3, pp. 472–479, 1978.

[101] Y. Çengel, *Heat Transfer: A Practical Approach*. McGraw-Hill series in mechanical engineering, McGraw-Hill, 2003.

[102] A. Rawle, "The basic principles of particle size analysis," *Surface Coatings International Part A: Coatings Journal*, vol. 86, pp. 58–65, 2003.